FLEXURE OF THE OCEANIC LITHOSPHERE IN THE VICINITY OF THE MARQUESAS ISLANDS

by

PAUL EDWARD FILMER

B.Sc. with Honors, Geophysics
California Institute of Technology
(1985)

SUBMITTED TO THE DEPARTMENT OF EARTH, ATMOSPHERIC AND
PLANETARY SCIENCES IN PARTIAL FULFILLMENT OF
THE REQUIREMENTS FOR THE DEGREE OF

DOCTOR OF PHILOSOPHY

at the

MASSACHUSETTS INSTITUTE OF TECHNOLOGY

November 1991

Signature of author______________________________
Department of Earth, Atmospheric and Planetary Sciences

Certified by______________________________
Marcia K. McNutt
Department of Earth, Atmospheric and Planetary Sciences

Accepted by______________________________
Thomas H. Jordan
Chairman, Department of Earth, Atmospheric and Planetary Sciences

DEDICATION

'Where shall I begin, please your Majesty?' he asked. 'Begin at the beginning,' the King said gravely, 'and go on till you come to the end: then stop.'

Lewis Carroll
Alice in Wonderland, ch. 11

This thesis is dedicated to the memory of my aunt, Agnes Waldron, who died six weeks before I defended. When I was young, I regarded her with fear: her unswerving wit and acerbic tongue were, for me and many others, like facing the Red Queen. Now that she is gone, I realize that she was really only Alice after all.

TABLE OF CONTENTS

APPENDIX B

APPENDIX C

APPENDIX D

LIST OF FIGURES

CHAPTER ONE

CHAPTER TWO

CHAPTER THREE

CHAPTER FOUR

CHAPTER FIVE

APPENDIX B

APPENDIX D

LIST OF TABLES

CHAPTER TWO

CHAPTER THREE

CHAPTER FOUR

CHAPTER FIVE

ACKNOWLEDGEMENTS

From quiet homes and first beginning,
Out to the undiscovered ends,
There's nothing worth the wear of winning,
But laughter and the love of friends.

Hilaire Belloc
Dedicatory Ode

Even though I have decided to place the acknowledgements in the prefatory material, they form one of the last pieces of writing I have had to do. Having finished the thesis, and defended it, what now? What of the thesis? On its startlingly white, acid-free paper, it descends into the archives, to be placed among all the other theses. It will sit unread, all the pretentiously chosen quotes never to be seen by anyone but admiring family, who with their own private copies will glance at the figures, scan the equations and wonder at its weight, never fully understanding that part of that weight will always rest on me, as well as on their hands.

I have always needed to read before sleeping, and never more so than during the last few months. During the last few weeks that I wrote this, I read *War and Peace*. Tolstoy wrote of things I was to experience. Not in a simplistic sense of physical struggle, but in the sense of an inner war and peace. At some point, I realized that this degree was something I would soon finish, and that I could sense myself beginning to feel a happiness I had not felt in years. Somewhere, in that last month, and during the last few pages of *the novel*, I realized that like Pierre Bezuhov, I had passed into a peace of my own, and I again looked forward to working on my thesis. Much like the strange, detached feeling that I had when I first came to interview my future advisor, I felt that I was a spectator, hovering excorporeally, and listening to a conversation which I mysteriously controlled.

In a moment of idleness, I once added up the costs of my education. I don't remember the total I reached, but I do recall realizing that if my future income were equivalent to my colleagues' in academia, it would take over six years to repay the amount without spending a cent on anything else. Twenty-two years of private education was awfully expensive, and very near the point of diminishing returns. Though the returns were diminishing in a coldly economic sense, they were highly rewarding returns in a personal sense. The people I met and befriended here were those with whom I felt I had the most in common: they were curious, thoughtful, broad-minded, well read, well travelled, and well spoken. They also had a strange desire to test their well-being by going to graduate school.

Most importantly, I should like to thank my parents. They always encouraged me to pursue my true interests, and always supported my decisions, even when that meant my staying in school for another six (!) years. They gave me the opportunity to leave home when I was eleven, an experience which I highly recommend. Most of all, what I have received from them is a constant love, something which I discover more of each passing year as I grow to know them as friends. I thank them for the opportunities I have been lucky enough to receive, and I thank them for letting me go when they must have borne the brunt of loneliness when I left Colombia.

I thank Kathryn for enduring my attempts at answering the repeated question "When will you be done?" It's a question I can't even answer today with precision. As Tigger's button said, "Soon." Very soon. Without Kathryn's gentle prodding, I doubt I would be as close to finishing as I am today. While I am certainly glad to be finishing, I do regret that Kathryn was exposed to some of the darker moments in a graduate student's career. I hope I have been as good a companion in difficult times for her as she has been for me.

My advisor, Marcia McNutt, was a model of endurance for me during a time when my troubles paled compared to her own. While I stayed out of her office perhaps more than I should have, I was able to enjoy the great freedom she gives her students. I was free to beat my head against problems by myself. It makes for a sore head, but it does feel better when the problem is solved. I was also completely free to *define* my own problems; a circumstance that made for rather slow progress, but resulted in greater satisfaction. Marcia was quick to praise, and perhaps more usefully, quick to dismiss.

Matthew Cordery was my office-mate and pseudo house-mate for the last few months here. A true friend, a sounding board for my stupidity, a dedicated sparring partner (sorry about the blow to the head that day...), and a collaborator in many plots. He provided a fine foil for my sense of humour, withstanding full broadsides of my abuse without flinching. It's amazing what an over-developed sense of self-confidence can withstand. Matthew spurred me to finish by actually starting to write his own thesis.

Steve Daly and Linda Meinke, my first office-mates, proved very tolerant of neophytes. I learnt an undying enthusiasm for geophysics and the graciousness to thank people for their codes from Steve, and gained a healthy respect for operating system quirks and an appreciation of the baodhran and fiddle from Linda. Mavis Driscoll and Adam Freedman were liberal with their encouragement, and assured me that wanting to jump ship was just a passing phase.

Garrett Ito has been a great office-mate for my last stage at MIT. He was just crazy enough to keep me going by providing continuous (and unconscious) amusement. In an anonymous vote among friends, we decided he reminded us of Tom Hanks in the movie "Big". His request for a second's worth of diskette time while I was typing my thesis was fairly typical: after removing the diskette he muttered, "Gee, I wonder if there was a virus on that..."

Javier Escartín was usually about during the small hours, fighting Matlab and non-linear inverse problems from Ted's class. He is responsible for my developing a guttural 'j' and appreciating *Loquillo:* ...la voy a matar... ...cuidado con la Policía... ...esto no es Hawaii...

Gerald Zeininger is one of my finest friends, and kept up with my progress from thousands of miles away, and was always ready to discuss anything and everything, from his latest project to points of humour in Russell. I have always enjoyed his company, and regret that a continent now separates us.

I owe a great deal of my character to Doris and Les Ives, who cared for me during the years I was in Toronto. They always had a warm welcome and a house full of love, something that certainly helped during the first few Canadian winters. The Streeters, Coxes and Angers', all gave me support while I was in New England.

Perry Bonnani, Fernando Chamberlain, Pietro Dova, Gerd Fritsch, Paul and Elizabeth Graven, Blake Jacobs, Harri and Sirkku Kytömaa, Julie LaPointe, Mike Machado, and Greg Rutledge: some of you are probably to blame for my cirrhosis, but you are also responsible for my surviving these six years. I'm sure Great Scott's has hit hard times since our Thursday night Prairie Fire and Long Island Ice Tea parties.

My latest house mates, David Ferris, Hannah Goodwin and Adriana Ponce, began to teach me the difference between the piano playing of early and late Cortot, although when the conversation proceeded beyond that I was still quite lost. Dinners with musicologists and divinity students were a world apart from the 3 p.m. teas in the Ida Green lounge...

Peter Lacovara at the Egyptology Department of the Museum of Fine Arts, Anita Killian at EAPS HQ, Noel Knight at the Center for Democracy, Mauricio Román with the Colombian Association of MIT, Walt Specht with the Caltech Alumni Association, and everyone at the Teatro Español all provided various ways for me to evade writing my thesis. Monica Posada very kindly kept me supplied with *café nacional*, which saved me from the rancid machine in the marine map lab, and kept me going during my 36 hour marathons.

I have enjoyed being with many other people here: Mike Bergman, Chris Bradley, Roger Burns, Al Cangahuala, Greg Chamitoff, Bob Cicerone, Dave Dinter, Kurt Feigl, Duncan Fisher, Karen Fischer, Chris Forrest, Joanne Fredrich, Connie Hart, Andrew Gunstensen, Mark Handel, Steve Hickman, Richard Holme, Yu Jin, Tom Juster, Peter Kaufman, Ro Kinzler, Sarah Kruse, Sang Mook Lee, Dan Lizarralde, Randy Mackie, Dave McCormick, Pat McGovern, Mark Murray, Radoslav Nakov, Jason Phipps-Morgan, Peter Puster, Nilton Renno, Justin Revenaugh, Beth Robinson, Joao and Jose Rosa, Carolyn Ruppel, Arcangelo

Sena, Mark Simons, Anne Sheehan, D'Arcy Straub, Paula Waschbusch, Will Wilcock, Cecily Wolfe, and Deb Zervas. Bruce Cabral was always behind the scenes. I'm sure I never saw half of what he does for all of us. Apologies for omissions - I'm amazed I remembered all these...

I thank the officers and crew of the *R/V Thomas Washington* for their help in collecting this data, and Michel Diament for his preliminary interpretation of the sonobuoy data. Loren Shure was extremely helpful in the initial development of codes, and Karen Cianculli compiled bathymetry and produced a base map included in my dataset. Wiki Royden very kindly gave me the basis for my successive overrelaxation codes, and Alain Bonneville was always there to hear my latest puzzles and to help me run differential subsidence codes or to decypher French abbreviations. Fred Frey and Tim Grove provided me with helpful constants and discussions. Ted Madden had the good sense to tell me to re-write my original acknowledgements, and is one of the best defencemen I ever tended net behind. It is always a pleasure to watch him calmly fend off frantic fraternity forwards by slowly circling, just out of reach.

Several members of my family died while I was at MIT, and did not live to see me graduate, and that I truly regret. For Grandad, Uncle Jimmy, Uncle Tom, and especially Aunt Agnes, I wish I had truly gathered my wits earlier, and finished for you all.

Yes, my acknowledgements are bittersweet, but I will not apologize for that. Most graduate lives are bittersweet. If the reader hasn't finished their degree yet, take heart: it really does come to an end. I am already looking forward to the day when I can remember all this fondly.

PF was supported by an NSF graduate fellowship

¡Carajo! Al fín terminé esta vaina.

CURRICULUM VITÆ

Not that I had any special reason for hating school. Strange as it may seem to my readers, I was not unpopular there. I was a modest, good-humoured boy. It is MIT that has made me insufferable.

after Max Beerbohm
Going Back to School

Date of Birth

22 . III . 1963, Bogotá, Colombia

Education

VI . 1985	B.Sc., Caltech, Pasadena, California
XI . 1991	Ph.D., Massachusetts Institute of Technology, Cambridge, Massachusetts

Awards and Fellowships

VI . 1984	Hall Geology Prize, Caltech
II . 1985	Robert Noland Leadership Prize, Caltech
VI . 1985	Honors Graduation, Caltech
VI . 1986	National Science Foundation Graduate Fellowship

Field Experience

Sample collection in the Carpathians, Tyrolean Alps, Pyrenées, Atlas and Anti-Atlas mountains, 1984

Sample collection and stratigraphic surveys in Baja California, 1983, 1984

Sea Experience

Crossgrain Leg 2, on R/V *Thomas Washington* (SIO), 1987

Publications

Kirschvink, J.L., C.A. Peterson, M. Chwe, P.E. Filmer, and B. Roder, An attempt to replicate the spinning chair experiment, in *Magnetite biomineralization and magnetoreception in organisms: a new Biomagnetism,* Kirschvink, J.L., D.S. Jones, and B.J. MacFadden, eds., Topics in Geobiology, v. 5, Plenum Press, NY, pp. 605–608.

Filmer, P.E., and J.L.Kirschvink, A paleomagnetic constraint on the Late Cretaceous paleoposition of northwestern Baja California, Mexico, *Journal of Geophysical Research,* v. 94, no. B6, pp. 7332–7342, 1989.

Filmer, P.E., and M.K. McNutt, Geoid anomalies over the Canary Islands group, *Marine Geophysical Researches*, v. 11, pp. 77-78, 1989.

Hagstrum, J.T., and P.E. Filmer, Paleomagnetic and tectonic constraints on the Late Cretaceous to early Tertiary northward translation of the Baja California Peninsula, *Geofísica Internacional, 29,* 175-184, 1990.

Hay que hablar claro de las piedras claras,
de las piedras oscuras,
de la roca ancestral, del rayo azul
que quedó prisionero en el zafiro,
del peñasco estatuario en su grandeza
irregular, del vuelo submarino,
de la esmeralda con su incendio verde.

Ahora bien, el guijarro
o la mercadería fulgurante,
el relámpago virgen del rubí
o la ola congelada de la costa
o el secreto azabache que escogió
el brillo negativo de la sombra,
pregunto yo, mortal, perecedero,
de qué madre llegaron, de qué esperma
volcánica, oceánica, fluvial,
de qué flora anterior, de cuál aroma,
interrumpido por la luz glacial?
Yo soy de aquellos hombres transitorios
que huyendo del amor en el amor
se quedaron quemados, repartidos
en carne y besos, en palabras negras
que se comió la sombra:
no soy capaz para tantos misterios:
abro los ojos y no veo nada:
toco la tierra y continúo el viaje
mientras fogata o flor, aroma o agua,
se transforman en razas de cristal,
se eternizan en obras de la luz.

Pablo Neruda
Las piedras del cielo, xxix

FLEXURE OF THE OCEANIC LITHOSPHERE IN THE VICINITY OF THE MARQUESAS ISLANDS

by

PAUL EDWARD FILMER

Submitted to

the Department of Earth, Atmospheric and Planetary Sciences,
Massachusetts Institute of Technology

on November 20th, 1991
in partial fulfillment of the requirements for
the Degree of Doctor of Philosophy

ABSTRACT

While the visible portion of the Marquesas Islands is much smaller than that of the Hawaiian Islands, modelling of the shipboard gravity collected during the *Crossgrain 2* expedition indicates that the rate of magma production by the two hotspots must be similar. The difference in effective elastic plate thickness beneath the two island chains causes the Marquesas to subside to a greater extent, allowing only the late alkalic caps to emerge from the ocean. Since the tholeiitic shields remain immersed, the gravitationally induced stress remains low, and well developed rift zones do not appear. The archipelagic apron surrounding the islands is composed of lava flows from the initial stages of volcanism, and of debris from slumps and catastrophic collapses of the later volcanic edifices. The flexural moat has been completely filled, and the lateral extent of the apron is controlled by flexural uplifting of abyssal hills.

Data from the alignment of seamount major axes and dikes observed on the SEABEAM archive plots from the *Crossgrain* 2 expedition to the Marquesas Islands area are determined to be randomly distributed for seamounts above 500 m in height. For smaller seamounts, the seamount major axes are aligned with the seafloor lineations produced at the mid-ocean ridge. There is no observable correlation between the major axis alignment and dike trends at any seamount height, and no evidence of dike clustering about any direction in the manner observed in the Hawaiian rift zones.

Sediments forming the archipelagic apron are observed by single channel seismics to extend out to 250 km from the islands, and to be dammed by uplifted abyssal hills. Ponded sediments can be observed up to 50 km further, burying the low relief between the abyssal hills. The sediments are determined to be at least 1350 m thick near the islands, and to thin to 250 m, the depth of the regional pelagic sediments, at the distal ends of the apron. Velocities for the two units observable in the refraction profiles are estimated at 3.1 km/s and 5.9 km/s. Two of the three units identified in the seismic sections correspond to units seen in similar work in Hawaii, however the completely infilled moat has caused the merging of the offlapping and ponded units observed in Hawaii into a single smooth unit in the Marquesas. The volume of the sediments is estimated to be 118,000 km^3, with tens to hundreds of the largest mass wasting events supplying most of the material in the Marquesas as well as in Hawaii. Thick calcareous sedimentary packages fill the inter-island basins, being shed from the steeper slopes of the islands by turbidite flows. The extent of the archipelagic apron is controlled by the geometry of the load and the shape of the flexural arch that dams the turbidite flows.

An acoustically opaque layer is observed to extend from the island of Fatu Hiva to the northern wall of the Marquesas fracture zone ridge. From the presence of small volcanic cones observed on the SEABEAM swaths and a dredged pillow lava, the layer is inferred to be lava erupted by a distributed vent system before coalescing into a few central sources. The absence of this layer on the south side of the fracture zone ridge would seem to indicate that the hotspot presently lies below the ridge itself.

Best-fitting models of free-air gravity, determined by minimization of residuals, indicate that an elastic plate thickness of 20 km and a mean density of 2590 kg/m^3 is appropriate for the central and northern lines. Although there is a trend in the best fitting elastic plate thicknesses from the south to the north, it is very slight and estimated to be within the error of the model. The 20 km thickness can model both the central and northern lines acceptably. The deflection of the pre-existing seafloor indicates that the moat is composed of volcaniclastic debris from mass wasting events and volcanic flows in equal proportions. Data from the southernmost line cannot be explained by simple flexural models due to the presence of a long wavelength component in the gravity that obscures any flexural moat.

Magnetic lineations indicate that the seafloor in the area is 55 to 58 million years old. The appropriate elastic plate thickness for lithosphere of this age is 30 km. The 4 to 8 million year lifetime of the islands is sufficient for plate weakening to the observed 20 km by simple heat conduction in the central and northern regions, but is insufficient to weaken the plate to the 10 km thickness observed under the Marquesas Fracture Zone Ridge. The energy from the cooling and solidification of magmas injected into the lithosphere is also insufficient to weaken the plate, implying that the observed thickness under the fracture zone ridge may date from the locking of the transform fault at the observed 12 Ma offset age. If the fracture zone ridge is of a recent volcanic origin, other mechanisms of plate weakening must be invoked to explain the extreme weakening observed. The total magma production rate of the Marquesas is estimated to be 0.18 km^3/y, similar to that of the Hawaiian hotspot. Because the elastic plate thickness under the Marquesas is half that under Hawaii, most of the Marquesan volcanic output has subsided below the surface, and exists as an extremely thick volcanic pile. Since only the alkalic stage emerges from the ocean, the Marquesas never develop the large gravitational stresses that are necessary to develop preferred orientations for rift zones. An island of intermediate size, Réunion, exhibits some slight preference in the orientation of dikes in the form of some poorly developed rift zones.

Thesis advisor	:	Dr. Marcia K. McNutt
Title	:	Griswold Professor of Geophysics Department of Earth, Atmospheric and Planetary Sciences Massachusetts Institute of Technology Cambridge, Massachusetts

Examining committee:	Dr. Donald Forsyth, Brown University Dr. Frederick Frey, MIT Dr. Theodore Madden, MIT, Chairman Dr. Marcia McNutt, MIT, Thesis Advisor

CHAPTER ONE

THE MARQUESAS ISLANDS

Believe me, my young friend, there is nothing -absolutely nothing- half so much worth doing as simply messing about in boats.

Kenneth Grahame
The Wind in the Willows, ch 1.

When we view the tremendous explosion in the amount of knowledge we have gathered about the worlds around us, it is quite surprising to find that we still know less about the shape of the seafloor on Earth than we do about the surfaces of the Moon, Mars, and recently, of Venus. Much like the surface of Venus, the Earth's seafloor is cloaked by a layer that has foiled simple attempts at direct observation. To see the surface of Venus we have had to dig out Arecibo and launch the Mariner, Venera, Pioneer, Vega, and Magellan probes. To see the detail of the sea floor, we have had to design complex instruments that afford us more information than just the depth to the bottom directly beneath the ship.

The use of instruments that measure the magnetic field and the amount of heat rising through the sediments, combined with the sounding of the seafloor below the sediment layer has slowly yielded up the keys to a relatively new science. These observations enabled the discovery of a vast pattern of movement of the seafloor that eventually led to the birth of the science of plate-tectonics. We now know that the interaction of the dynamic interior of the earth with the more rigid outer layers has produced the ridges, trenches, arcs, fractures, and island chains that are observed at sea, and that this interaction is also responsible for the major features on the continents.

During the first twenty years of the science, observations of the symmetry of magnetic lineations about mid-ocean ridges and the alignments of fracture zones, when coupled with the discovery of age progressions along linear island chains, led to a rigorous understanding of the motions of the oceanic plates and to the theory of hotspots. The creation of hot seafloor at shallow ridges, observations of its slow subsidence as it cooled and progressed horizontally over the underlying asthenosphere, and its eventual subduction in trenches all led to a preliminary understanding of the thermal structure of the plates. Presently, marine geophysics is mostly concerned with the details of the overall picture: studies of perturbations to the basic patterns produce most of the new science.

The subject of the present thesis concerns several aspects of just such a perturbation. The Marquesas Islands form a small chain in the South Pacific, similar to the Hawaiian Islands far to the north, but dissimilar in that there is virtually no previous geophysical data for these islands. In comparison to Hawaii, the Marquesas are virtually unknown. Rather than a long, thousand kilometer progression from incipient seamount to drowned atoll, the Marquesas present an abrupt beginning and end to their geographic and temporal distribution, and do so on a geographic trend that is not compatible with other Pacific chains.

The second perturbation is in a wider sense: the Marquesas lie just to the north of an area of anomalously shallow seafloor that has been termed the 'Superswell' [*McNutt and Fischer,* 1987]. We do not yet fully understand why the Marquesas fracture zone is a sharp boundary between the normal seafloor of the north, and the abnormally shallow seafloor to the south, but the position of the Marquesas on the boundary may provide some new data for the resolution of this problem.

1.1. SETTING OF THE SURVEY AREA

The Marquesas Islands form a linear chain over 355 km long of twenty or more major volcanic islands and seamounts in the south-central Pacific (see Figures 1.1 and 1.2), lying on seafloor formed at the Pacific-Farallon rise 45 to 65 m.y. ago [*Kruse,* 1988]. The islands are

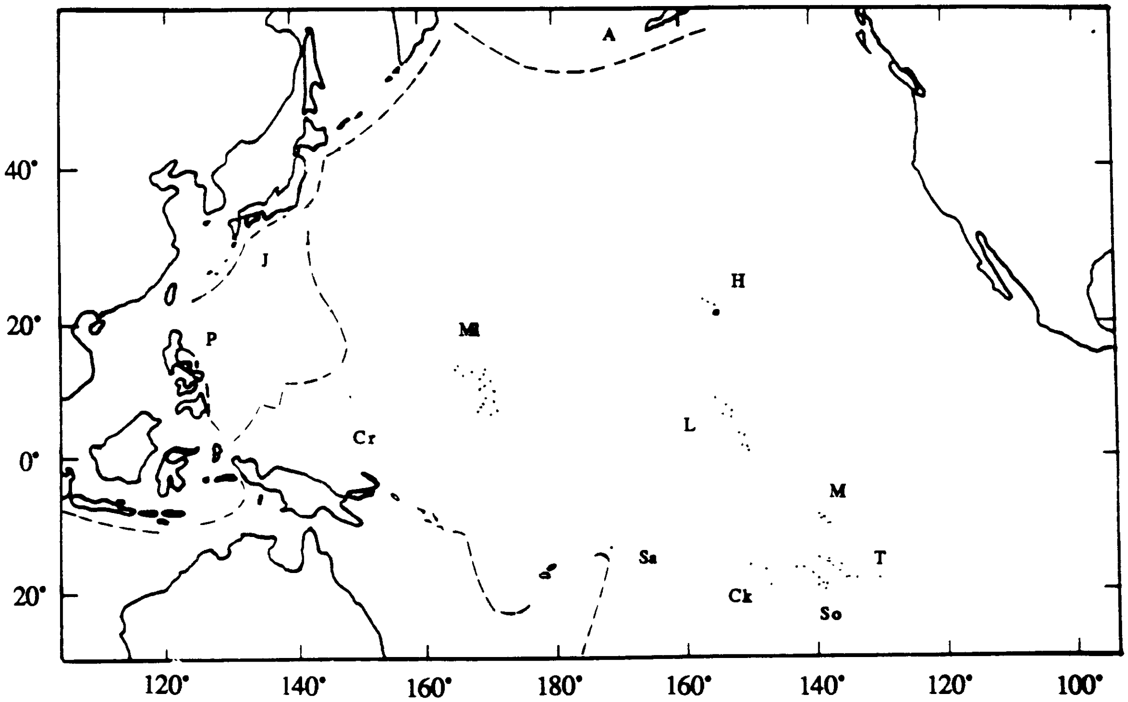

Figure 1.1. The Pacific Ocean and the location of the Marquesas Islands. The Marquesas (M) form a volcanic island chain in the southern Pacific which is thought to represent the trace of a hotspot along the seafloor. Several other volcanic chains are shown: the Hawaiian (H), Marshall (Ml), Caroline (Cr), Line (L), Samoan (Sa), Cook (Ck), Society (So), and Tuamotu (T) Islands. Other groups, such as the Aleutians (A), Philippine (P) and Japanese (J) island chains are classified as back-arc island chains rather than as hotspot traces. Trenches are indicated by the dashed lines.

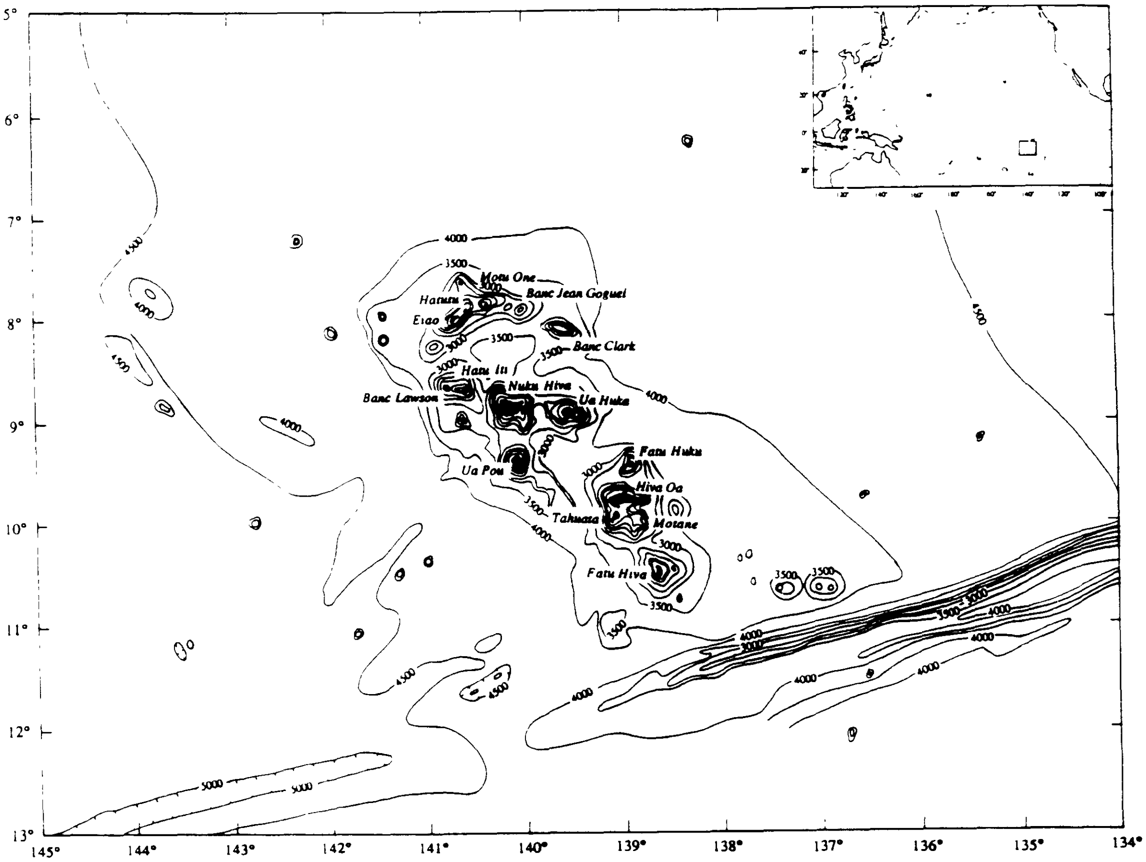

Figure 1.2. The Marquesas Islands. The island group is composed of seven major islands, six smaller islands, many isolated rocks and pinnacles, and various shallow banks. The area has not been fully surveyed, so many seamounts remain to be discovered. Visible in the area is the fracture zone, expressed as a deep in the west, and as a ridge in the east. Contours are in meters. Based on a map and notes compiled by Karen Cianculli. INSET: Figure 1.1 with area of the Marquesas outlined by the small box.

surrounded by a bathymetric swell between 0.5 and 1 km in height which extends nearly 600 km from the islands, rising from unperturbed seafloor depths of 4500 to 5000 meters [*Crough and Jarrard,* 1981*; Fischer et al.,* 1986]. Potassium-argon dating of rocks from the islands has demonstrated an age progression from 5.33±0.07 Ma on Eiao (8°00'S 141°27'W) to 1.61±0.03 Ma on Fatu Hiva (10°35'S 138°35'W) (recalculated data of *Brousse and Bellon* [1974], *Duncan and MacDougall* [1974], using the later decay and abundance constants of *Steiger and Jäger* [1977], from the compilation of *Brousse et al.* [1990]). Given the islands' age progression and their northwesterly trend, it is generally accepted that these islands form part of a hotspot trace on the seafloor.

The divergence between the apparent trend of the Marquesas Islands, N42°W, and the direction of absolute plate motion in the area, N66°W [*Minster and Jordan,* 1978], has been used to argue for inter–hotspot motion [*Chase and Sprowl,* 1984*; Pollitz,* 1986], and a change in the post 10 Ma pole of rotation for the Pacific [*Cox and Engebretson,* 1985]. The absence of a linear chain of guyots and seamounts to the northwest of the Marquesas has also been used to argue for the existence of short-lived, or intermittent hotspots [*Jarrard and Clague,* 1977]. Whereas the Marquesas hotspot seems to cease, or at least diminish, eruptive activity upon encountering the Marquesas fracture zone, other hotspots, including the Society and Pitcairn hotspots, and possibly the MacDonald hotspot, seem to show an increase in eruptive activity.

The presence of the Marquesas Fracture Zone Ridge, an apparently volcanic feature lying along the strike of the Marquesas Fracture Zone, has been used to suggest that the Marquesas hotspot is only able to penetrate the lithosphere at points of pre-existing weakness. The portion of the ridge abutting the Marquesas swell subtends about 275 km in the direction of plate motion, and the swath defined by the ridge contains all of the Marquesas Islands, suggesting that the islands' divergent trend may be explained by some pre-existing line of weakness in the lithosphere, rather than motion of the Marquesas hotspot relative to the other Pacific hotspots [*McNutt et al.,* 1989]. Although not all hotspots have produced ridges when crossing fracture zones, the Marquesas hotspot seems to have produced them along the Galapagos and

Clipperton Fracture Zones as well as along the Marquesas Fracture Zone [*McNutt et al.,* 1989]. There is some evidence that the Musicians and South Hawaiian seamounts were formed along the Murray and Molokai Fracture Zones, but a spreading direction change provides the tectonic mechanism for weakening the fractures [*Sager and Pringle,* 1987]. Evidence from surface observations of bathymetry and gravity, along with Geosat radar altimetry data across the fracture zone would seem to indicate that the Marquesas Fracture Zone is indeed weak, or 'unlocked' along most of its length, being unable to support the shear stresses caused by differential subsidence and thermal cooling effects [*Christeson and McNutt,* 1991]. If the weakness is in the lithosphere to the north of the fracture zone, and is controlled by the fabric of the lithosphere created at the ridge crest, then the width of the zone normal to the crest affected by the hotspot is 190 to 250 km wide [*Brousse et al.,* 1990].

Estimates for the relative velocity between the lithosphere and the hotspot come from two classes of calculation: K-Ar measurements of volcanic progression with time, yielding values of 99 mm/yr along the great circle through Fatu Hiva and Eiao (N48°W) [*Duncan and MacDougall,* 1974], and best fits to sets of Pacific hotspot data, yielding values of 106±1 mm/yr along N66°W for a pole (61.7°N 82.8°W, 0.96°/Myr) [*Minster and Jordan,* 1978], 110±2 mm/yr along N77°W, from a pole (70°N 101°W, 1°/Myr) [*McDougall and Duncan,* 1980], and 107.5 mm/yr along N69°W, from a pole (60.60°N 95.10°W, 0.985°/Myr) [*Pollitz,* 1986], all calculated for a point at 9°S 140°W in the Marquesas area. The isotopic data of *Duncan and MacDougall* [1974] do not constrain the magnitude of the velocity very well, and the azimuth for the isotopic trend is based entirely on morphological arguments, a particularly tenuous approach since the subaerial portion of the islands fans out from Fatu Hiva in directions between N10°W and N55°W. This spread of directions accounts for the various estimates of mean trend for the islands in the literature.

1.2. ORGANIZATION OF THE THESIS

This thesis represents a partial synthesis of the data gathered during leg 2 of the *Crossgrain* expedition, carried out aboard the R/V *Thomas Washington* of the Scripps Institution of Oceanography, San Diego. Equipment on board included a SEABEAM swath mapper, a Bell BGM–3 gravimeter, and a Geometrics proton precession magnetometer. Seismic equipment included a 3.5 kHz profiler, single channel seismic acquisition with an 80 in^3 water gun, and sonobuoys with a 550 in^3 air gun source for refraction studies. Navigation was controlled by SATNAV and GPS satellite fixes, with gyro and Doppler constrained interpolation. We collected gravity, magnetic, SEABEAM, and seismic profiles in the vicinity of the Marquesas Islands (Figure 1.3), laid out to cross the island chain and its associated swell at different locations in the hotspot track. The magnetic data have been used to constrain the age of the seafloor [*Kruse,* 1988] (Figure 1.4), and in combination with the gravity data, to constrain the formation of the Marquesas Fracture Zone Ridge [*McNutt et al.,* 1989].

The second chapter consists of statistical analysis I performed on data gathered from the SEABEAM archive plots of the *Crossgrain 2* expedition. Sizes and directional alignments from seamounts, ridges, fracture zone scarps, and lineations in the abyssal hill fabric form the dataset which I examined for relations between the various measurements. I examined the directions exhibited by the seamount major axes and radial dikes for a preferred orientation, in view of the evidence that many volcanic dikes in back-arc environments provide good indicators of regional stresses [*Nakamura,* 1977; *Nakamura et al,* 1977]. To test the data for dependence on gravity induced stress patterns like those observed in the Hawaiian islands [*Fiske and Jackson,* 1972], I examined the dike orientations for correlation with the edifice major axes. The data from the seamount dimensions of height and width is compared with the more elaborate analysis of *Jordan et al.* [1983] and *Smith and Jordan* [1988] for relations governing the slope of the seamounts.

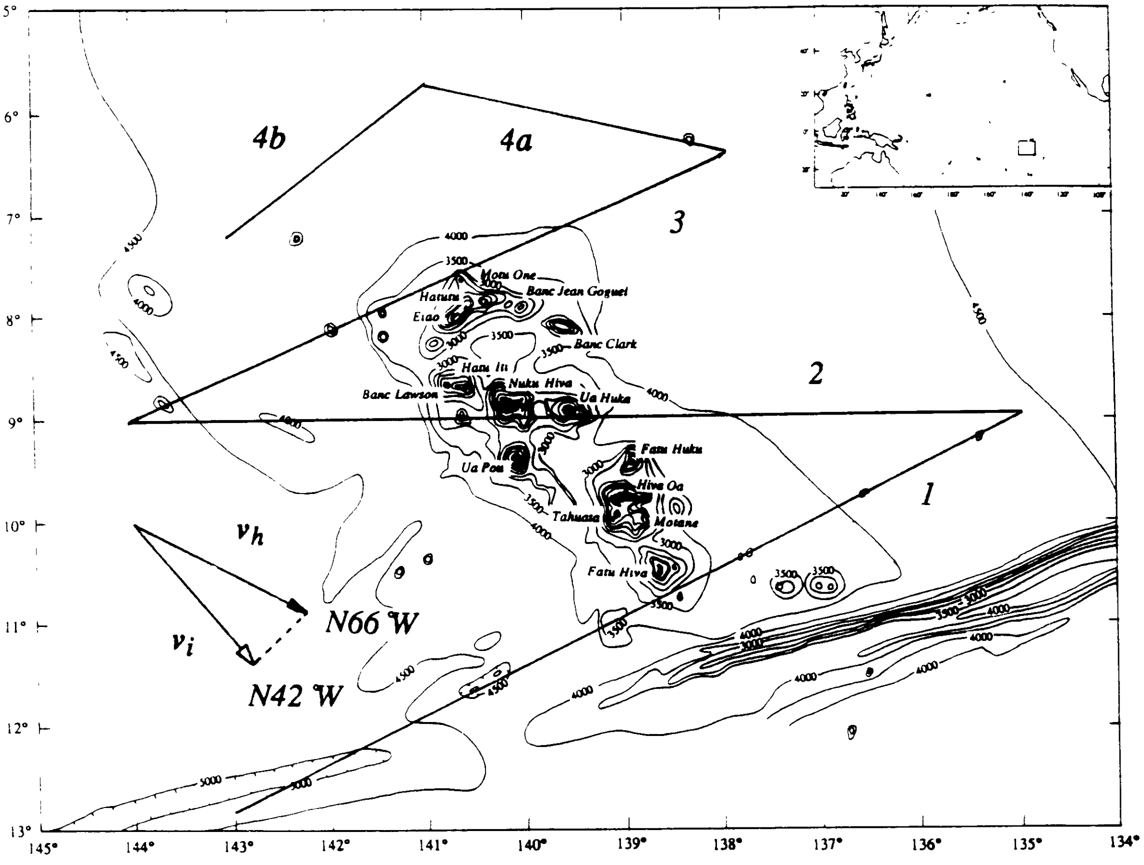

Figure 1.3. Geophysical survey lines and bathymetry of the Marquesas Islands area. Survey lines sailed are indicated by the solid line. The trend of the islands, N42°W, is indicated by the open–headed vector v_i. The expected hotspot velocity relative to the seafloor for the area is indicated by the vector v_h, 106 mm/yr at N66°W. Bathymetry is indicated with 500 m contour intervals, where the hachured contours enclose depressions. Italic numbers indicate the survey lines.

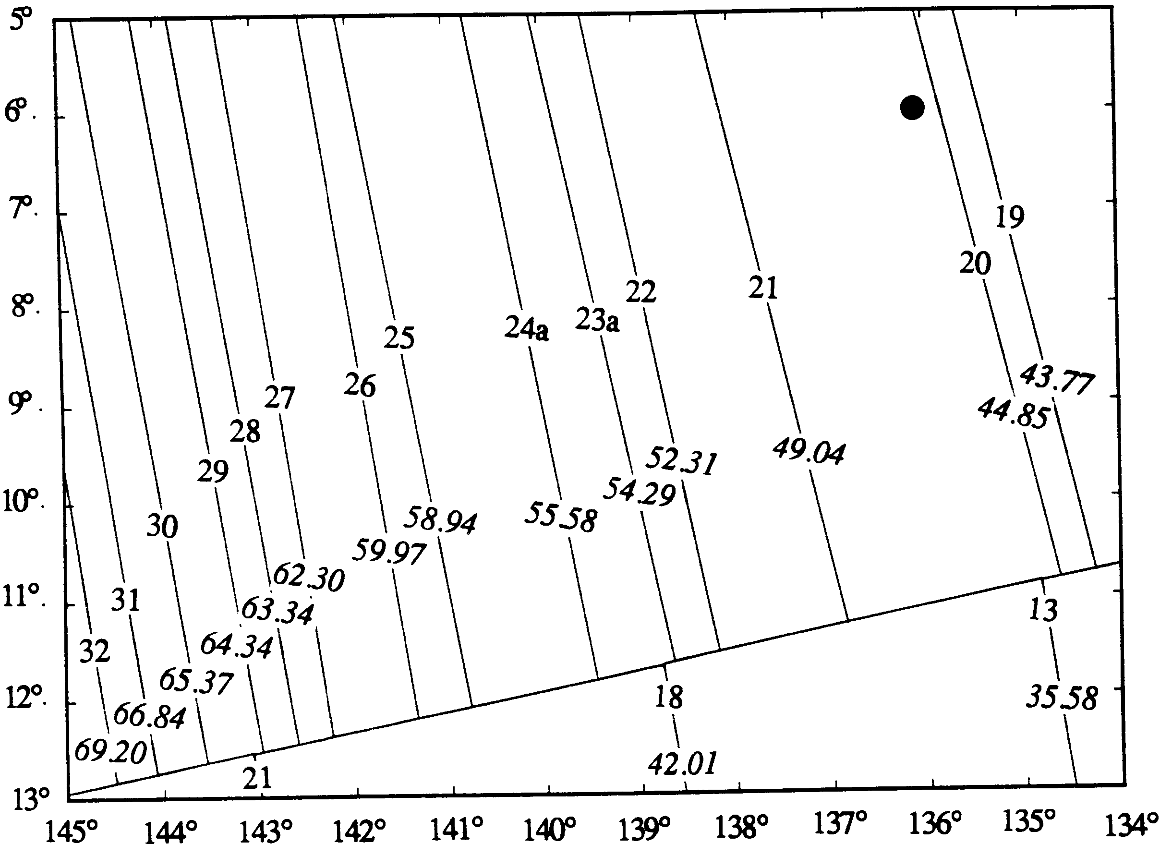

Figure 1.4. Marquesan Isochrons. Isochrons north of the fracture zone are from *Kruse* [1988], ranging from anomaly 32 to 19, or from 69.20 to 43.77 Ma, on the time scale of *LaBrecque et al.* [1977]. Isochrons to the south of the fracture zone are from *Rosa and Molnar* [1988], from anomaly 21 to 13, or 49.55 to 35.58 Ma on the time scale of *Berggren et al.* [1985]. Assigned ages are indicated in italics. Dot is the site of DSDP hole 74 dated at 45.0 +6.9 -4.9 Ma [*van Andel and Bukry,* 1973].

The third chapter presents the seismic data from the cruise, gathered by reflection and refraction techniques. The general morphology and description of the seafloor and the sediment cover is shown by the reflection data, and in conjunction with the previously described SEABEAM data, provides a good dataset for the description of various stages of volcanic island chain construction that are in evidence along the Marquesas. The refraction data provides some constraint on the depth of the sediment layers, and also gives the speed of the seismic wave in the material, giving an idea of the composition and state of compaction in the material composing the archipelagic apron. The Marquesas data is searched for evidence of the same processes observed in the Hawaiian apron: onlap and offlap patterns in the sediments, evidence of smooth and chaotic reflectors, and evidence for large scale mass wasting in the form of slumps and debris flows from the flanks of the islands.

Chapter Four is concerned with the gravity data collected on the cruise, and the different methods employed to model the data. To calculate the gravity profiles, I used models of two and three dimensions, as well as frequency domain, or spectral techniques. For the three dimensional analyses, I produced a new digital map of the area that merged the bathymetric data from the *Crossgrain 2* cruise with several other datasets. The gravity data constrains the average density of the material composing the islands and the moat, and constrains the elastic plate thickness of the lithosphere supporting the load of the islands. Since the shiptrack crosses the island chain at various distances from the presumed present-day location of the hotspot beneath the fracture zone, the gravity data afford the possibility of detecting a change in the effective elastic plate thickness with time since reheating.

The fifth and final chapter deals with the implications that all of the previously described data have for the evolution of the Marquesas as a volcanic island chain forming in an environment close to the Marquesas Fracture Zone, and adjacent to the abnormally shallow seafloor of the 'Superswell'. The total amount of erupted material is calculated as a function of the load and infill densities, along with the rate of eruption, and a lower bound on the total amount of heat produced by the hotspot during this time is estimated and compared with the much more well known data of Hawaii.

Throughout this thesis, when the mathematics used for analysis of the model interfered with a clear exposition of the science involved, I have moved the mathematics into the appendices. I apologize for any inconvenience, but this may be a convenience to those who wish to view the mathematics unencumbered by the science.

1.3. PUBLICATION OF RESULTS

Selected results from Chapter 4, and parts of Chapter 3 have been presented at AGU meetings. The remaining material from Chapter 3 and the entirety of Chapters 2 and 5 remain unpublished to this date (November, 1991).

CHAPTER TWO

THE ALIGNMENT OF SEAFLOOR FEATURES

What the sage poets taught by th' heavenly Muse,
Storied of old in high immortal verse
Of dire chimeras and enchanted isles
And rifted rocks whose entrance leads to Hell, –
For such there be, but unbelief is blind.

Milton
Comus, 1, 515

2.1. INTRODUCTION

Geographic trends for volcanism in the Marquesas area can be detected at two, or possibly three levels. The primary trend of the chain has a mean direction of N42°W, and a width of approximately 250 km (see Figure 2.1). The secondary trend, about 75 km in width along N75°W, consists of the island groups Clark Bank - Jean Goguel Bank - Hatutu, and Ua Huka - Nuku Hiva - Hatu Iti - Lawson Bank, and possibly Fatu Hiva and two undated seamounts 130 and 180 km to the East. The tertiary, and tentative trend that can be observed lies along N5°W and is also about 75 km wide, and consists of the island groups Lawson Bank/Hatu Iti - Eiao/Hatutu, Ua Pou - Nuku Hiva, and Fatu Hiva - Motane - Tahuata/ Hiva Oa - Fatu Huku. It is intriguing to note that the secondary lineation is very close to the plate direction, N66°W, and tertiary lineation is very close to the alignment of the magnetic lineations, N12°W, and presumably the alignment of the fabric in the sheeted dike complexes produced at the Pacific-Farallon Ridge.

It has been proposed that the divergence of the primary trend of the Marquesas from the local plate motion direction is due to weaknesses in the lithosphere that control the locus of

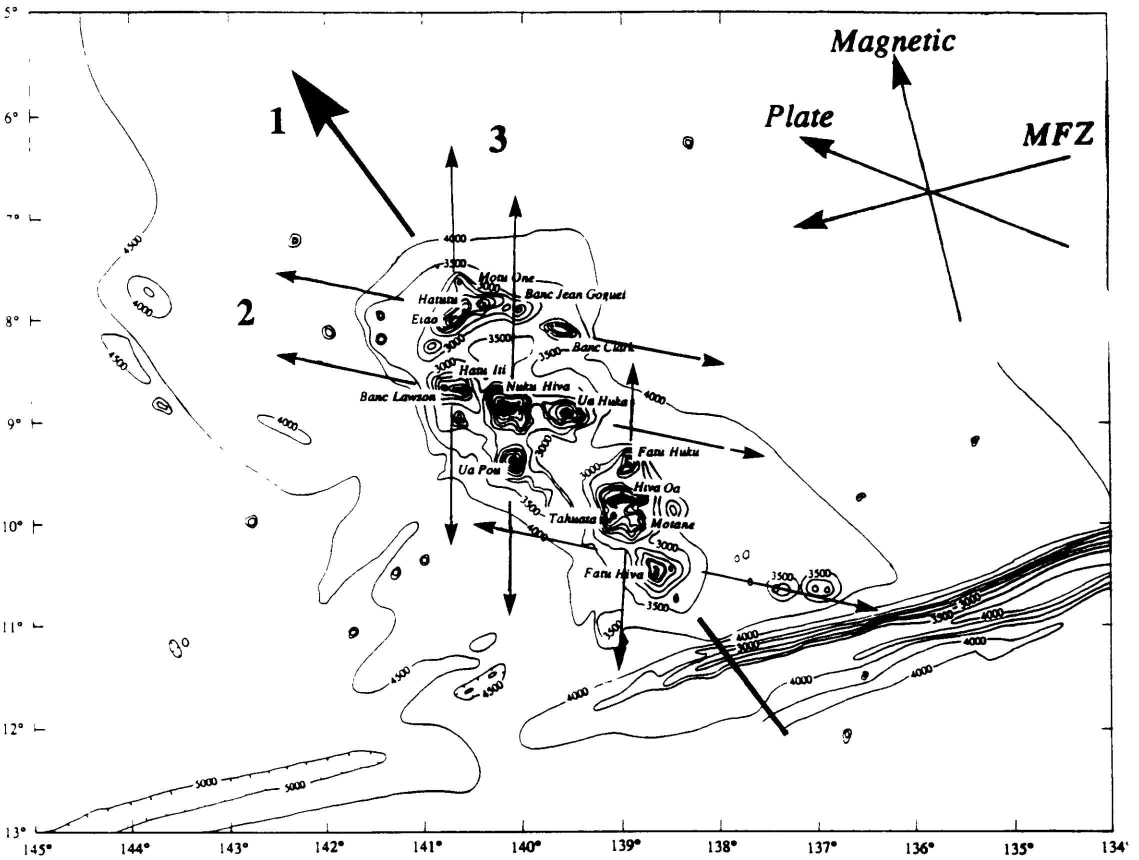

Figure 2.1. Geographic trends for volcanism in the Marquesas Islands. The primary trend of the islands is shown by the large arrow, and represents the direction that is used to argue for motion between hotspots. The secondary and tertiary trends are indicated by the lighter arrows. Also shown are the trends for the fracture zone, local plate motion, and the local magnetic lineations.

eruptive activity [*McNutt et al.,* 1989; *Brousse et al.,* 1990]. Isotropy in the strength of the seafloor should be expressed in various ways: if the strength of the seafloor controls the direction of dike formation and rift propagation, then this isotropic direction should be compatible with the statistically derived mean direction for such features, and if the cumulative process of erupting along particular trends is the major source of growth for a seamount, then the seamount major axes themselves should express this same alignment.

Dike alignment has been used as an indicator of tectonic stress in various areas, primarily in the form of flank eruptions or fissures on the slopes of polygenetic volcanoes in back-arc environments [*Nakamura,* 1977, 1987; *Nakamura et al.,* 1977], but also to explain the dike pattern around igneous intrusive bodies [*Muller and Pollard,* 1977]. From theoretical arguments, the dikes should form radially in the immediate area of the conduit, and then curve in the far field to asymptotically approach the regional stress field. If the oceanic crust approximates a homogeneous medium, the dikes are more likely to form along the direction normal to the minimum horizontal compression, and so indicate the plane of the maximum and intermediate stress [*Nadai,* 1963; *Timoshenko and Goodier,* 1970]. Should there be a regional tectonic stress, and an isotropic structure to the strength of the seafloor, it is reasonable to assume that the dikes injected into the seafloor will statistically reflect the horizontal direction of the maximum stress.

The trends of the major rifts in the Hawaiian islands are more closely correlated to the state of stress induced by the slope of the older, underlying shield rather than to the local underlying fabric of the seafloor attributed to ridge processes [*Fiske and Jackson,* 1972]. Data from the inflation and deflation of Mauna Loa and Kilauea volcanoes on Hawaii seems to indicate that the magma chambers and the dike origins lie within the volcano edifice itself, about 2 to 6 km below the Mokuaweoweo and Kilauea calderas [*Swanson et al.,* 1976b], and above the crust and any regional or predetermined directional preferences. This result suggests that even if there is some fabric or local tectonic stress under Hawaii that has an influence on small-scale eruptive processes, the evidence of these alignments (if they exist) is quickly lost both under the lava edifices, and is lost statistically in the larger scale stress controlled directions that result as the island edifice grows in size and weight. One might expect to see some shift from an alignment consistent with the abyssal hill fabric in the smaller sized eruptive features to an alignment consistent with the maximum axial stress caused by the loading in larger features. The main difficulty lies first in differentiating the two populations, and then in sampling these two populations in great enough number to determine statistically significant results.

2.2. DATA COLLECTION

The shiptrack for the *Crossgrain 2* expedition passes through the Society islands, the Tuamotus, and the Marquesas (see Figure 2.2). The data gathered by the SEABEAM system along this track allows us to observe various characteristic features of the fracture zone and of the seafloor that the fracture zone separates. First, we may observe the alignment of the fracture zone itself on two scales, one derived from crossings of the fracture zone at widely separated locations, and a smaller scale estimate of the fracture zone alignment from the trends that are observed in the swath from a single crossing. Second, the lineations in the seafloor formed by the abyssal hill fabric created at the ridge-crest form a strong pattern that can be detected by statistical study of many single observed trends. This mean trend may not necessarily be the same from one side of the fracture zone to the other, since the alignment of the ridge crest may change from spreading segment to segment. Third, the seamounts themselves exhibit various characteristics that we may quantify. Along with the obvious characteristics of height and radius, seamounts exhibit elongations that may be quantified in terms of alignment and major and minor semi-axis sizes and ratios.

The irregular shape of many seamounts is caused by the sub-aqueous eruption of lava along dikes that propagate radially from the seamount, forming observable 'ribs', or rifts, that can be characterized by their propagation direction. The height and radius measurements can be made on each seamount that is fully resolved (i.e. both the summit and base were observed) and can be estimated for many of the features whose bases or summits are not directly resolved

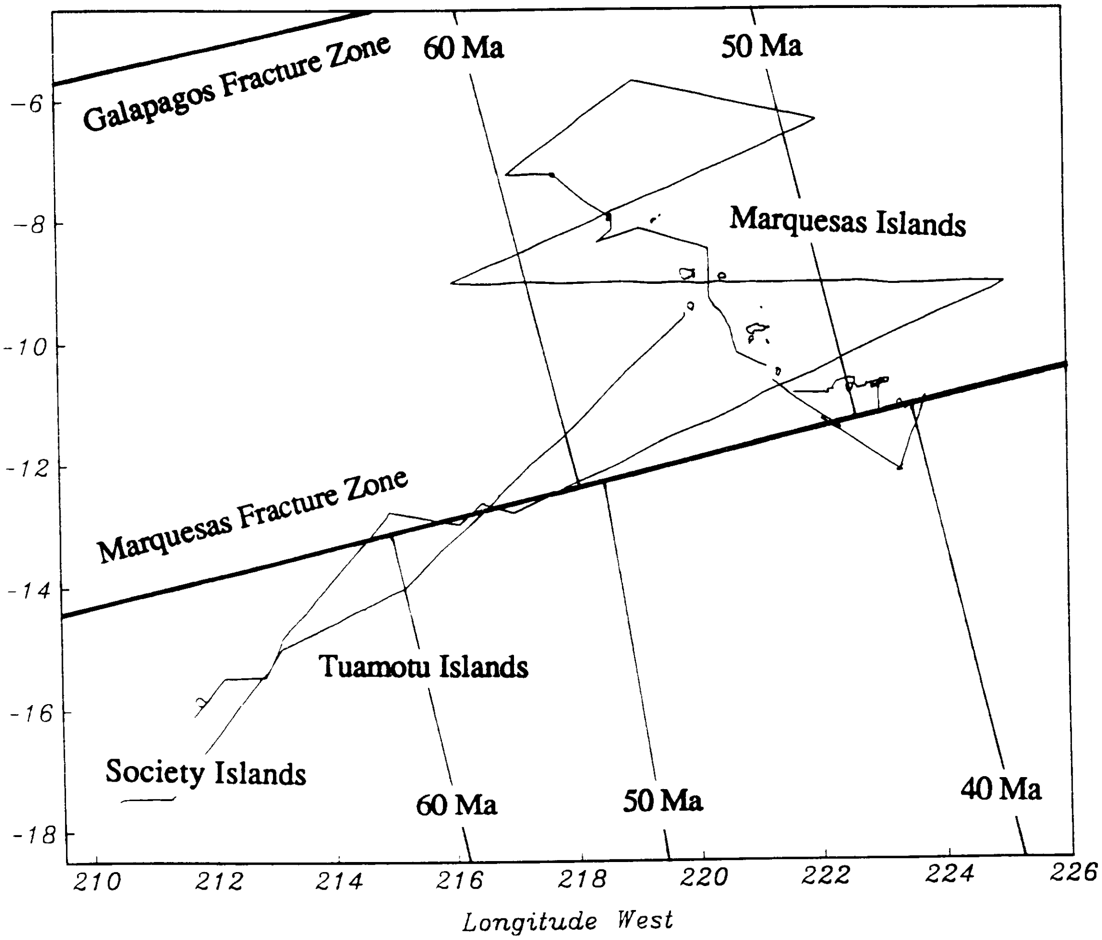

Figure 2.2. Major tectonic features of the Marquesas region. The shiptrack for *Crossgrain 2* is shown as a line which begins in the Society Islands, crosses the Tuamotu Islands to the Marquesas, and returns again to the Societies. Thick lines are the Marquesas and Galapagos Fracture Zones, with the thinner perpendicular lines representing isochrons.

by the SEABEAM swath, while measurements of the direction of propagation of dikes can be made from both full and partial coverage of features.

In this chapter I present the results from 133 different features picked off the SEABEAM archive plots, and over 1,000 measurements taken from these features. The features are analyzed for their mean trends, and the implications discussed in light of the previous discussion of isotropic seafloor strength and the state of stress induced by the island load itself. Swath charts for the entire cruise have been compiled into archive plots by Ute Albright at the Scripps Institute of Oceanography and by Karen Cianculli of MIT, using facilities kindly donated by the University of Rhode Island. I have used large scale renderings of this data to select the features presented in this chapter.

2.3. SEAFLOOR FEATURES

There are several types of feature visible in the SEABEAM archive plots that I have chosen to measure and list in Table 2.1. The center beam bathymetry for the passes over these features is given in Figure 2.3 for the entire cruise, with the corresponding feature numbers. Since the ship might not pass directly over the top of the feature, and also might not sail in a straight line (for example while circling or dredging a seamount), the depths in Figure 2.3 are complex representations of the individual features. It is unfortunately not practical to include all the archive plots in the thesis, but Figures 2.4 through 2.6 illustrate typical examples of the features that are included in the dataset of Table 2.1. The resolution of the SEABEAM system is sufficient to produce maps contoured at a 10 m interval, and so has ample resolution for the features included in this dataset. The feature numeration is not strictly in order of sailing, since the features were picked from the compilation of all SEABEAM data, and may come from widely separated times in the cruise, even though the features may actually be geographically adjacent.

Figure 2.3.a-h. The following four pages show the center beam bathymetry along the *Crossgrain 2* shiptrack. Numbers correspond to the feature number of Table 2.1. Feature may have multiple peaks or other irregularities in this representation because of the line sailed. Major features are named (MFZR = Marquesas Fracture Zone Ridge).

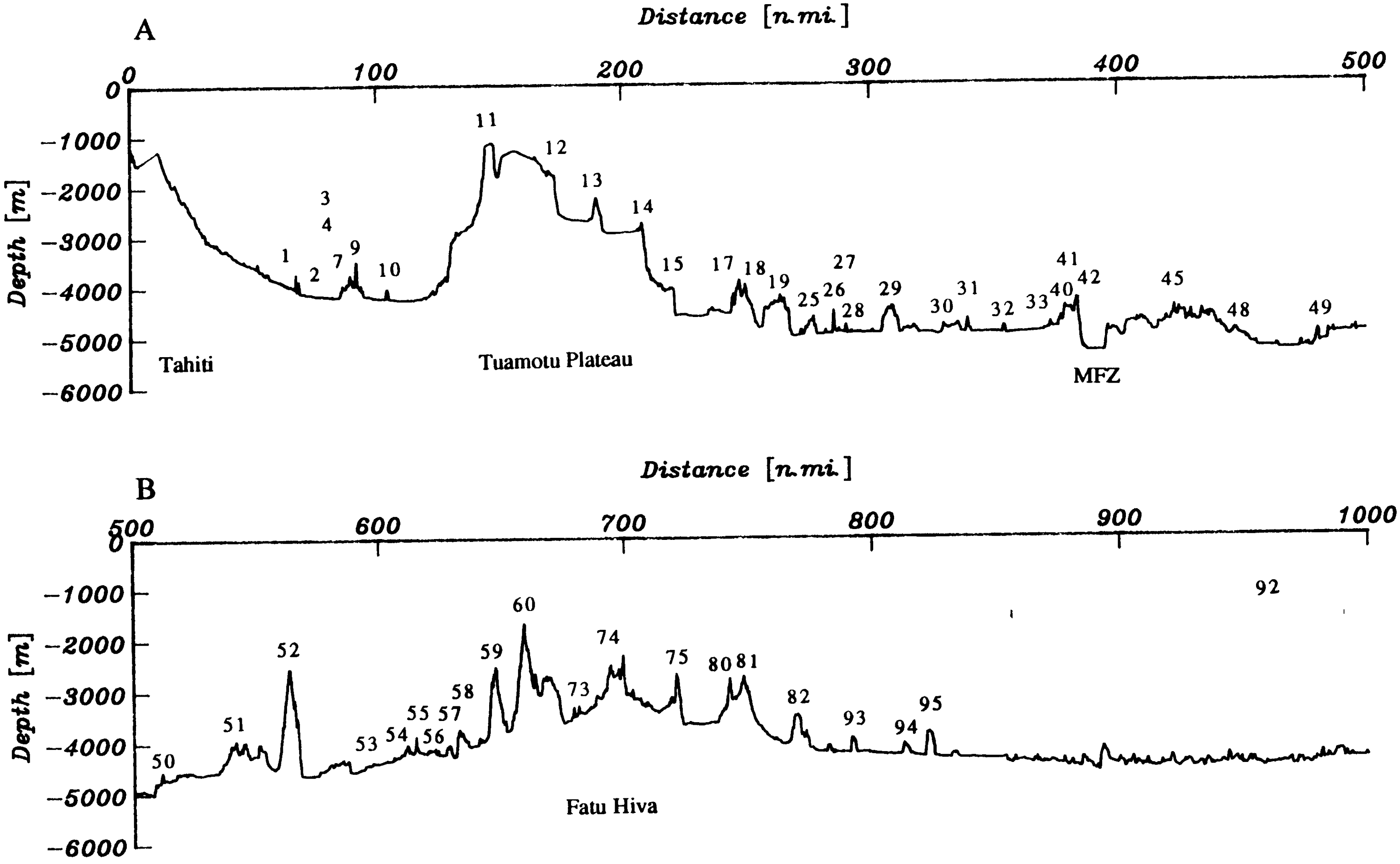
A
Distance [n.mi.]
0
100
200
300
400
500
Depth [m]
0
−1000
−2000
−3000
−4000
−5000
−6000
1
2
3
4
7
9
10
11
12
13
14
15
17
18
19
25
26
27
28
29
30
31
32
33
40
41
42
45
48
49
Tahiti
Tuamotu Plateau
MFZ
B
Distance [n.mi.]
500
600
700
800
900
1000
Depth [m]
0
−1000
−2000
−3000
−4000
−5000
−6000
50
51
52
53
54
55
56
57
58
59
60
73
74
75
80
81
82
92
93
94
95
Fatu Hiva

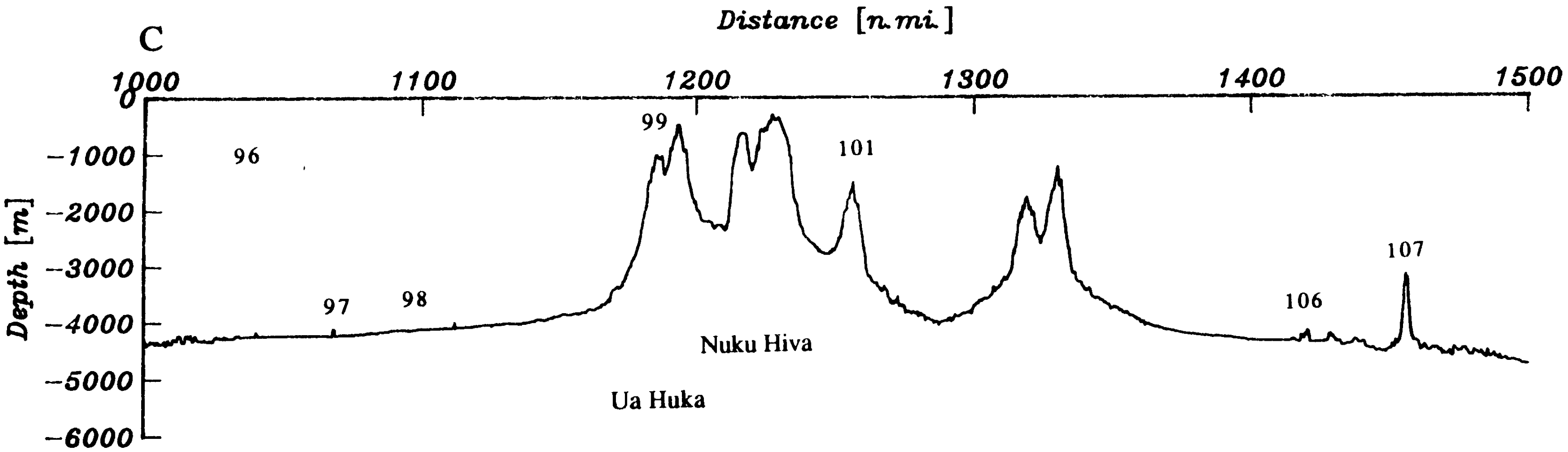
C
Distance [n.mi.]
1000
1100
1200
1300
1400
1500
0
-1000
-2000
-3000
-4000
-5000
-6000
Depth [m]
96
99
101
107
106
97
98
Nuku Hiva
Ua Huka

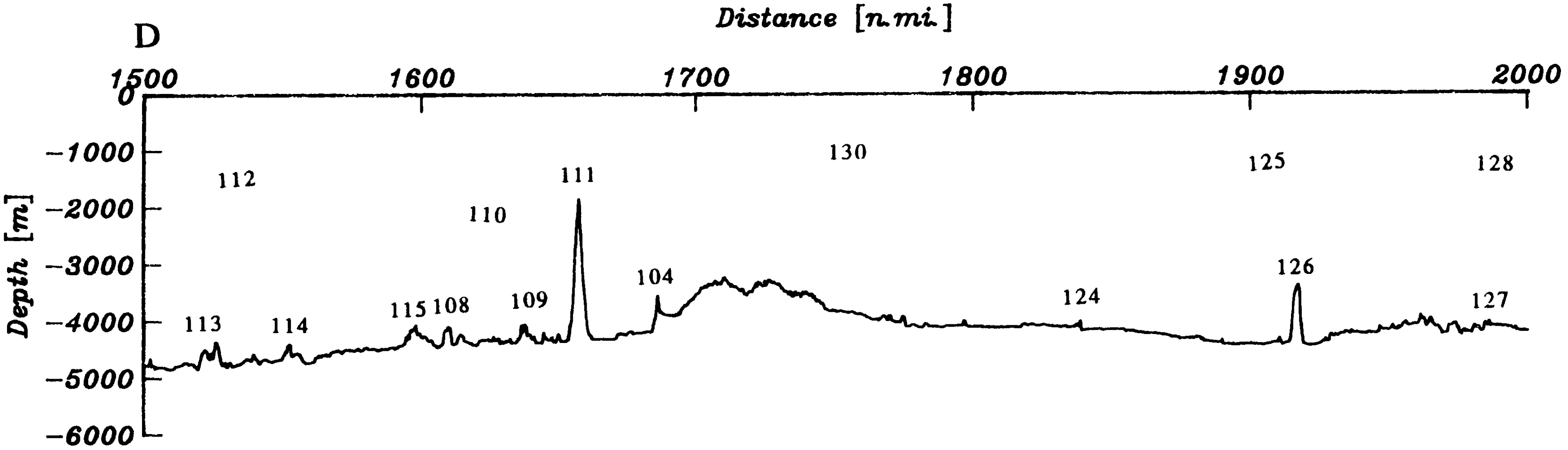
D
Distance [n.mi.]
1500
1600
1700
1800
1900
2000
0
-1000
-2000
-3000
-4000
-5000
-6000
Depth [m]
130
125
128
112
111
110
104
126
124
127
113
114
115
108
109

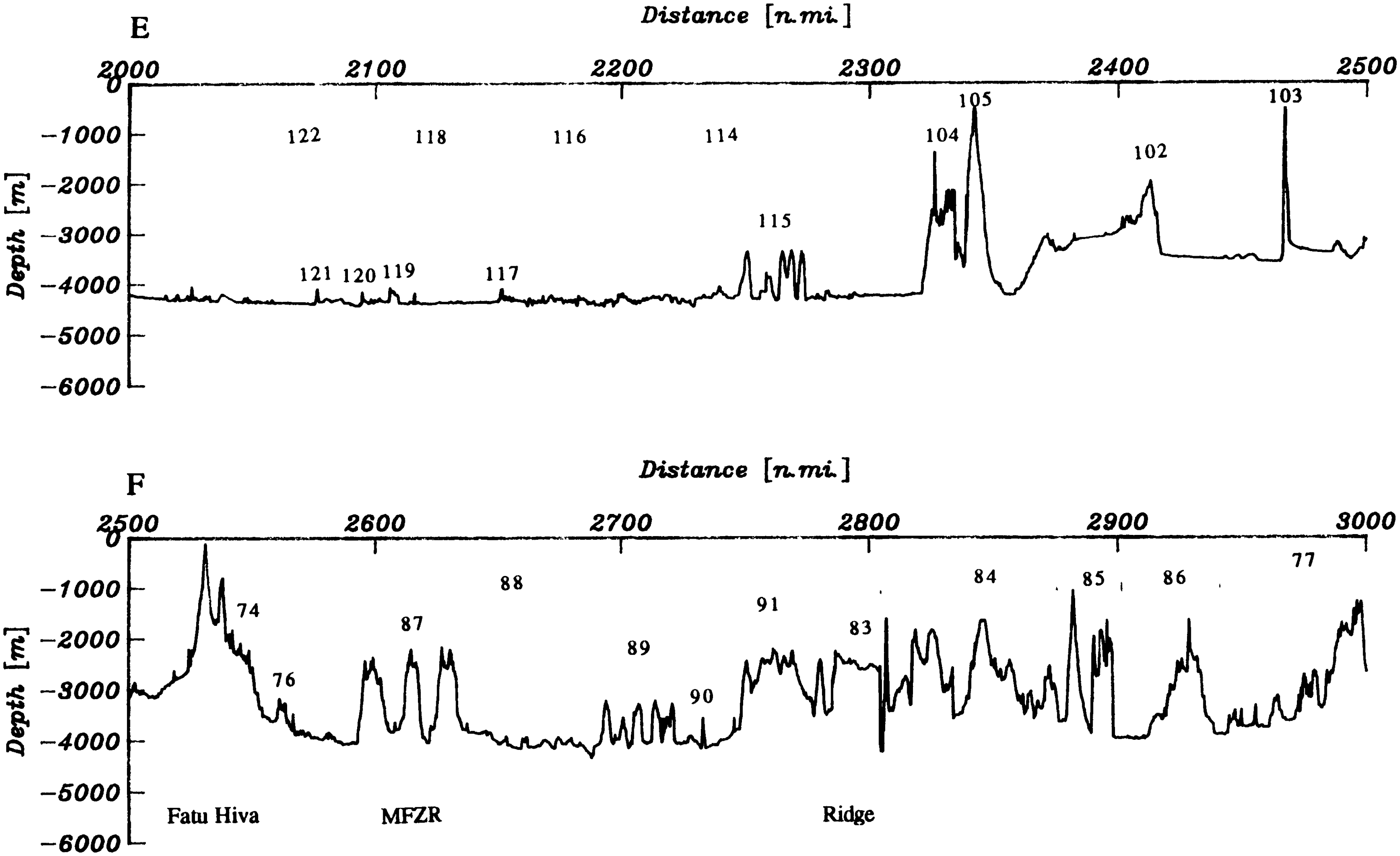
E
Distance [n.mi.]
2000
2100
2200
2300
2400
2500
Depth [m]
0
−1000
−2000
−3000
−4000
−5000
−6000
122
118
116
114
104
105
102
103
115
121
120
119
117
F
Distance [n.mi.]
2500
2600
2700
2800
2900
3000
Depth [m]
0
−1000
−2000
−3000
−4000
−5000
−6000
74
76
87
88
89
90
91
83
84
85
86
77
Fatu Hiva
MFZR
Ridge

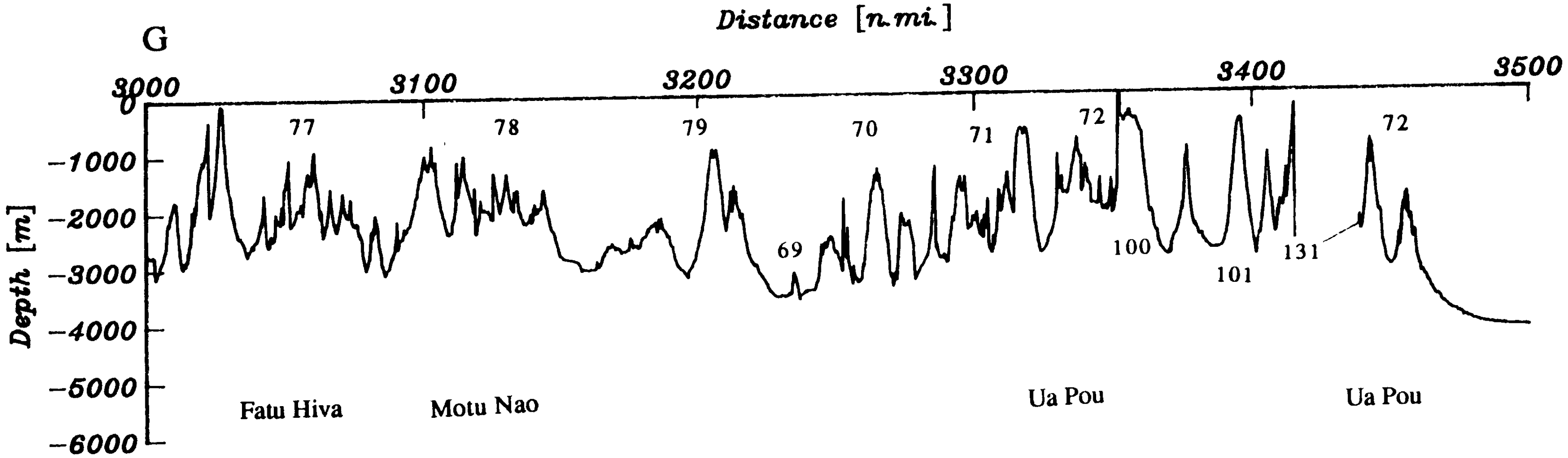
G
Distance [n.mi.]
3000
3100
3200
3300
3400
3500
0
-1000
-2000
-3000
-4000
-5000
-6000
Depth [m]
77
78
79
70
71
72
72
69
100
101
131
Fatu Hiva
Motu Nao
Ua Pou
Ua Pou

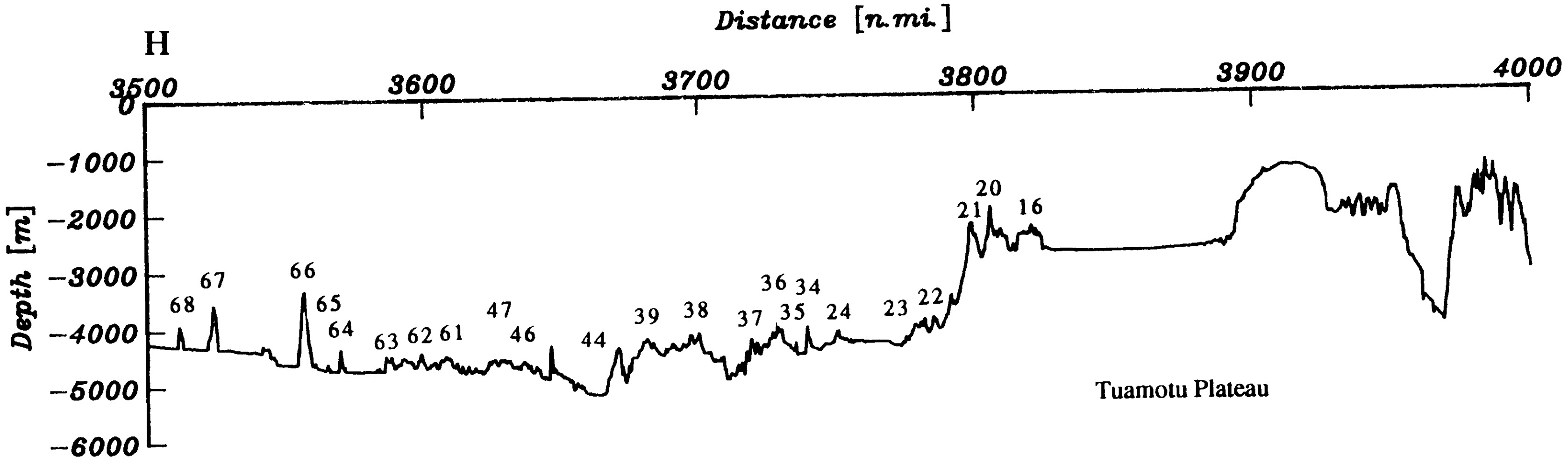
H
Distance [n.mi.]
3500
3600
3700
3800
3900
4000
0
-1000
-2000
-3000
-4000
-5000
-6000
Depth [m]
68
67
66
65
64
63
62
61
47
46
44
39
38
37
36
35
34
24
23
22
21
20
16
Tuamotu Plateau

2.3.1. Feature type

Features listed in Table 2.1 are the following: seamounts, designated by an 'S' in the second column; ridges, designated by an 'R'; lineations, designated by an 'L'; fracture zone features, designated by an 'F'; and plateau features, such as edges, designated by 'P'. Where the distinction between feature types is not clear, or the feature identification is tentative, I include a question mark (?) with the 'Feature Type' designation.

2.3.1.1. Seamounts

I choose to define a seamount as a feature on the archive plots that displays closed contours with over 200 m of relief. This value for relief is very low, near the mean value for the relief of the abyssal hills themselves, but any such contour is an arbitrary choice. Values for the characteristics of the seamounts whose summits or bases were not fully resolved by the swaths can sometimes be estimated from the shape of the imaged portion, although this is admittedly an arbitrary procedure. I have indicated all features for which estimated values of the axes are given in Table 2.1 by a question mark (?) in the axis columns, and by notations in the comment column. Where the base is not resolved, the comment reads 'bnr', and where the summit is not resolved, I use 'snr'. I leave the designation 'sbnr' to the reader.

On the basis of fully resolved versus partially resolved features, I have divided the tabulated dataset into two classes, one containing only the fully resolved data, and the other containing the estimates as well. The estimated values are therefore included in the statistical analysis of the full dataset, but are excluded from the analysis of the partial dataset. An example of a fully resolved seamount is shown in Figure 2.4, which corresponds to feature number 104 in Figure 2.3d and Table 2.1.

2.3.1.2. Ridges and lineations

The distinction between 'ridges', 'lineations', and 'seamounts' is one of number, not of size, and as such, contains elements of an arbitrary decision on my part. Where there is a

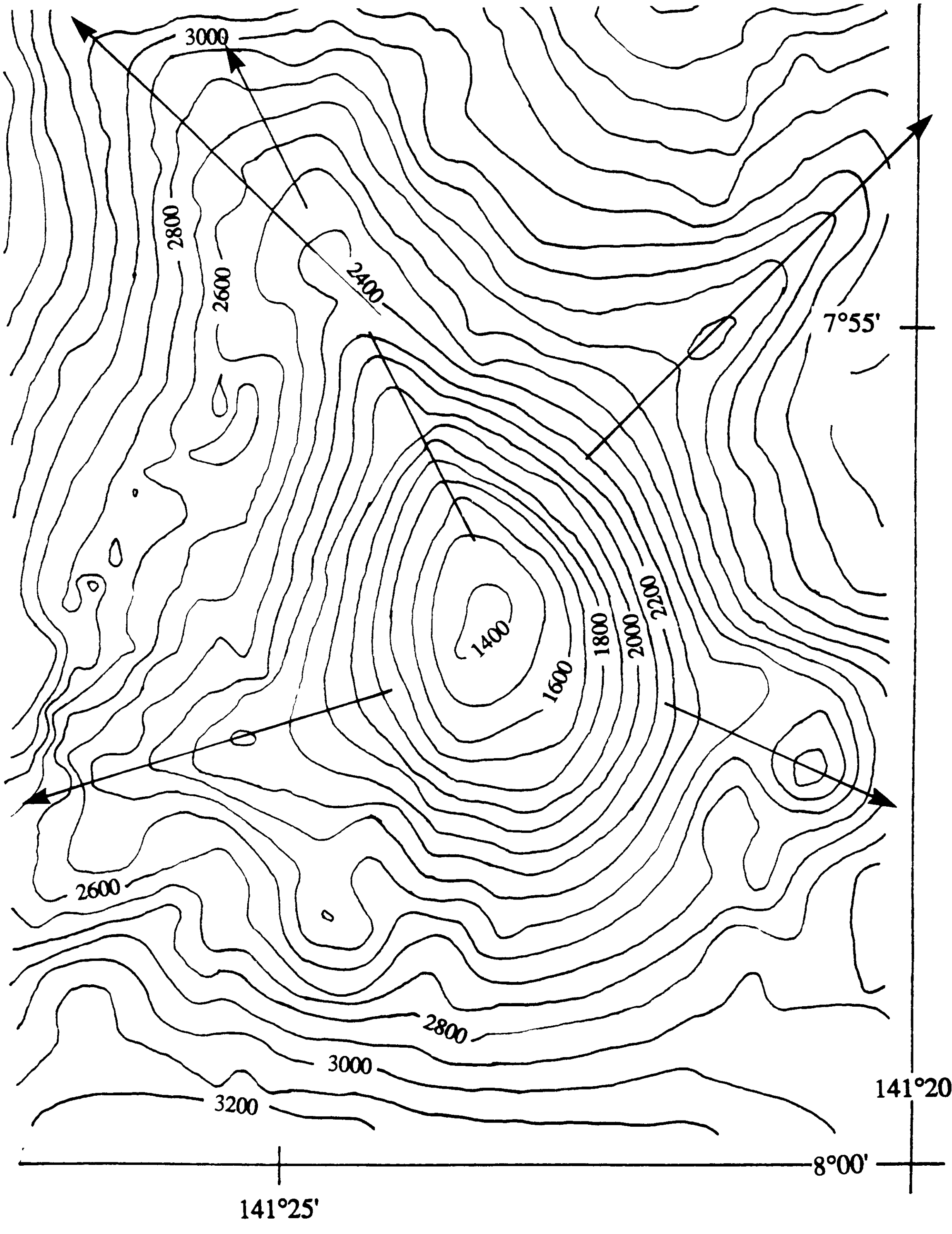

Figure 2.4. SEABEAM swath over a typical seamount. Seamount shown is feature number 104 from Table 2.1 and Figure 2.3d, with alignment of major axis and dike trends indicated by the arrows. Contours are in meters, and axis lengths are measured to the 1/*e* height of the seamount, in this case 5.6 and 5.8 kilometers. Height is 2800 meters, based on contours outside this section of the swath.

lone feature over 200 m high of fairly regular height that extends through both sides of the swath, I have designated it a ridge, although major axis lengths of infinite extent are an obvious exaggeration. Where there are many features of 50 to 100 meter relief that cross the swath over shiptrack distances of 50 to 100 km, I have designated these 'lineations'. The 'lineations' are probably the abyssal hills generated at the ridge crest. Feature number 96 from Figure 2.3 and Table 2.1 from the SEABEAM data is shown in Figure 2.5 as an example of the lineations observed beyond the archipelagic apron.

2.3.1.3. The Tuamotu Plateau

The shiptrack passes directly over the Tuamotu plateau, and I have designated the edges of this feature separately to avoid including them in the statistical analysis. The plateau is clear in Figure 2.3 as an elevated area bounded by steep scarps. The trends derived from these scarps are not directly relevant to the discussion, but I have included them for two reasons. The first being a result of the method I used to choose features, in that I did not consult the overall trackplot for an idea of the general location of each feature before choosing it. This was an attempt to minimize any unconscious bias on my part to pick specific features from specific areas. The second reason is simply for completeness. I have chosen to include all features I measured.

2.3.1.4. The Marquesas Fracture Zone

The Marquesas Fracture Zone features are themselves of two classes, corresponding to the two expressions that were observed. To the west, the fracture zone is observed as a sudden change in bathymetry across the fracture, dropping from the shallow 50 Ma seafloor of the Superswell in the south to the deeper 69 Ma seafloor of the north. The features here are those of a scarp: the alignments of the scarp itself, and of the trough to the north. The fracture zone is illustrated in Figure 2.6, where the SEABEAM swath crossed the fracture zone, and corresponds to features 41 - 49 in Figure 2.3a and h.

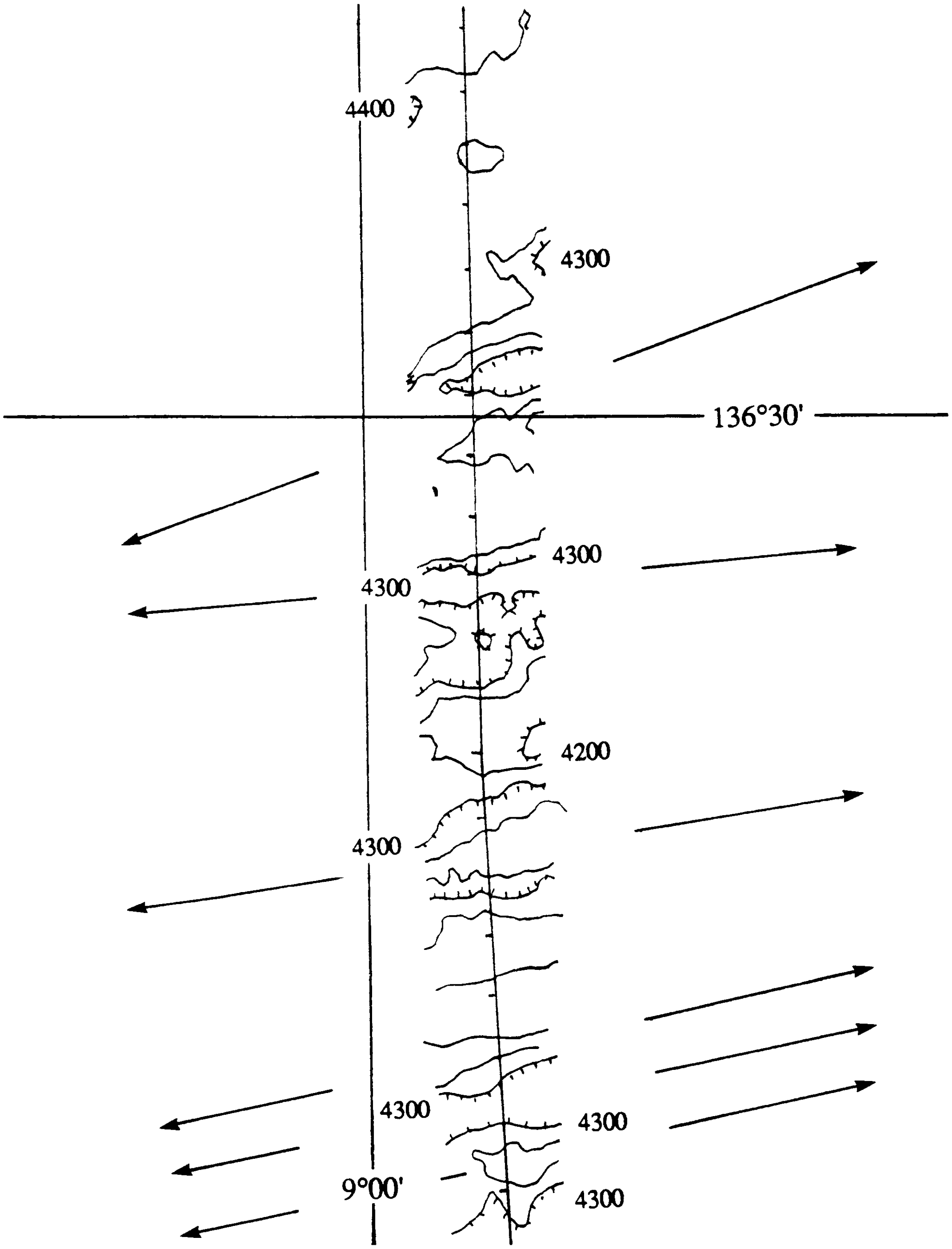

Figure 2.5. SEABEAM swath over lineations to the east of the Marquesas islands. Feature shown is number 96 from Figure 2.3c and Table 2.1. Low amplitude hills on the seafloor are aligned along directions indicated by the arrows. North is to the left of the figure.

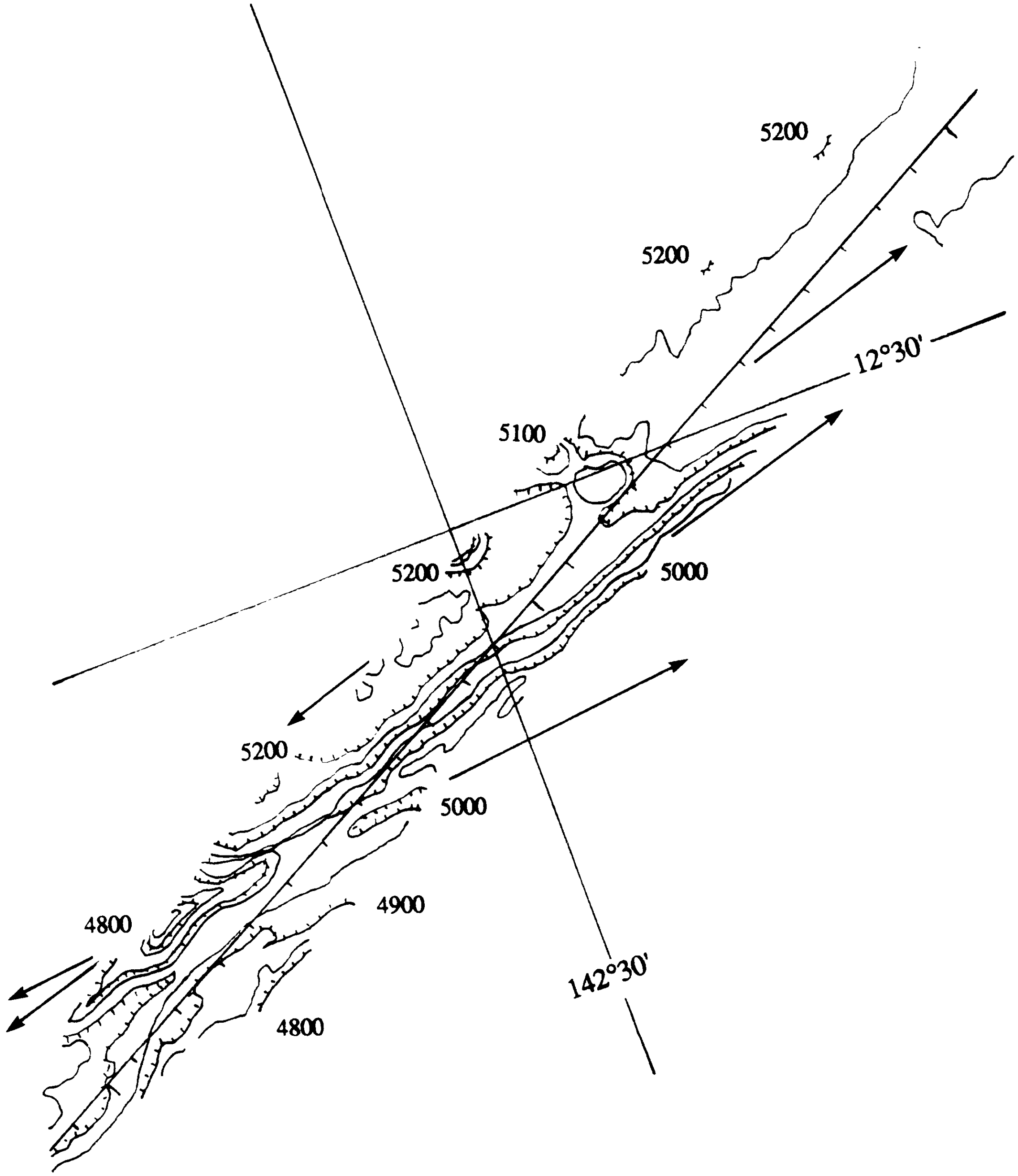

Figure 2.6. SEABEAM swath over the Marquesas Fracture Zone. Feature shown is number 42 from Figure 2.3a and Table 2.1, with alignments shown by arrows. The fracture zone is characterized by the abrupt change in depth from the shallow seafloor of the 'Superswell' in the south to the normal seafloor in the north.

To the east, and along the predicted hotspot trend from the Marquesas themselves, a 20 km wide, 1.5 km high ridge extends at least 300 km along the fracture zone. This feature is not illustrated here in map view, but it corresponds to features number 83, 87, and 91 in Figure 2.3. The fracture zone ridge is described more fully by *McNutt et al.* [1989].

2.3.2. Latitude and longitude of features

The latitude and longitude of the features are straightforward, and express the location of the feature within one minute as determined from the SEABEAM archive plots. In the case of the lineation entries, which occur over a wide area, the latitude and longitude represent the center of the area covered by the listed lineations.

2.3.3. Depth and height of features

The depth is taken as the deepest point in the area immediately surrounding the feature, which in most cases is the depth of the even seafloor from which the feature rises. For lineations, this figure represents an average depth over the area, since the feature is very large, and the relief of the feature itself is of the same order as the variation in depth of the seafloor itself. Height is simply the difference in depth between the deepest point and the shallowest point of the feature.

2.3.4. Axial lengths and trends

Most of the features on the SEABEAM archive plots have a definite elongation in one direction, and I have chosen to define this direction as the major axis of the feature. A corresponding minor axis is generally perpendicular to this direction, but on highly irregular features this is not necessarily the case. The length of the semi-axes is defined as the horizontal distance from the shallowest point to the contour defining the $1/e$ height for the feature. This particular definition is chosen for the ease which it affords modelling the feature with a Gaussian surface.

The definition of the major axis also allows the measurement of the azimuth of the elongation. The entry under the "Axial Trend" heading in Table 2.1 reflects the alignment of the major axis for seamounts, ridges and lineations, or the scarp in the case of plateau and fracture zone features.

2.3.5. Dike and rift zone trends

Figure 2.4 illustrates the fact that many of the seamounts exhibit a stellate cross-section, due to the collapse of less resistant flows between the denser radial dikes [*Moore et al.,* 1989; *Lénat and Labazuy*, 1990]. In this chapter I use the term 'dike' loosely for these radial structures, although it should be understood that the features are a result of repeated dike intrusions, rather than a single, large dike. In the case of Hawaii, where the process of eruption is still active, these structures are termed 'rift zones' principally in their subaerial portion, although their submarine extensions, or 'ridges', have now been recognized as also being volcanically active, as in the East Rift Zone of Kilauea which leads to Puna Ridge off Cape Kumukahi on the main island [*Moore,* 1987].

The rift zones do not necessarily radiate in a straight line or from the center of the structure, so their trends are measured along the longest extent visible on the SEABEAM swath. All seamounts were not surveyed the full 360° around their bases, so the trends *for these seamounts* do not represent an unbiased sampling of the dike azimuths. When full coverage of a seamount was obtained, it was usually as a result of the seamount being a dredge site. Partial coverage was obtained for those seamounts that coincidentally lay under the line of sailing, and since this is essentially a random process, there is no reason to expect that there is a preference for mapping one side of a seamount over another. The observed dike trends should present the best approximation to an unbiased sample *for the entire seamount population* that I can obtain from the SEABEAM swaths.

TABLE 2.1.Seafloor feature locations, sizes and trends from the Society, Tuamotu and Marquesas Islands

Feature Number	Feature Type	Latitude	Longitude	Depth (m)	Height (m)	Min. Axis (km)	Maj. Axis (km)	Axial Trends	Dike Trends	Comments
1	S	17°08'	148°30'	4050	350	.8	1.1	010°	-	-
2	S	17°07'	148°31'	4050	250	.6	1.1	350°	-	-
3	S	16°48'	148°17'	4150	450	1.0	1.5	353°	320°	-
4	S	16°47'	148°16'	4150	300	.6	.8	001°	-	-
5	S	16°46'	148°15'	4200	200	.3	.4	000°	-	-
6	S	16°44'	148°12'	4200	250	.4	1.7	358°	230°	-
7	S	16°41'	148°11'	4200	250	.4	1.4	008°	055°	-
8	S	16°40'	148°10'	4200	350	1.0	1.4	359°	231°	-
9	S	16°39'	148°09'	4200	600	.8	1.5	352°	043°,058°	-
10	S	16°26'	147°57'	4200	200	.8	5.7	006°	232°	-
11	S	15°36'	147°20'	4200+	1700	13.4?	16.1?	347°	234°	snr
12	P	15°02'	146°55'	2600	700	-	-	124°	-	edge
13	R?	14°40'	146°44'	2900	400	3.9	∞	089°	002°	-
14	P	14°20'	146°25'	2900	1200	-	-	-	352°,351°	edge
15	P	14°07'	146°15'	2900	600	-	-	281°	-	edge
16	P?	14°25'	145°45'	2900	400	-	-	244°	170°,171°	edge
17	S?	13°45'	145°55'	4550	650+	1.7?	3.9?	040°	174°	snr
18	S	13°38'	145°49'	4900	1050	5.0	5.0?	008°	358°	-
19	S?	13°24'	145°35'	4300	350+	-	-	-	002°,357°	snr
20	S	14°20'	145°31'	2900+	950+	2.9?	2.9?	337°	-	bnr
21	S	14°17'	145°24'	4300+	2100+	7.8?	7.8?	-	014°	sbnr
22	S	14°11'	145°12'	4300+	900+	1.7?	2.8?	018°	023°	bnr
23	S?	14°10'	145°06'	4400	800+	2.4?	6.7?	065°	335°,355°, 008°,025°	-
24	S	13°55'	144°42'	4350	500?	1.5?	5.0?	040°	-	snr
25	R	13°12'	145°25'	4950	450	2.0	∞	348°	021°, 026°	-
26	S	13°02'	145°16'	4950	500	1.0	2.5?	336°	-	-
27	S	13°00'	145°15'	4900	300	1.5	2.4	043°	317°	-
28	S	12°56'	145°10'	4950	200	-	-	-	349°, 309°	irregular
29	S	12°47'	144°55'	4950	650	3.8	6.4	355°	332°,078°	-
30	S	12°52'	144°35'	4950	700	1.1	1.1	-	-	circular

TABLE 2.1. Continued...

Feature Number	Feature Type	Latitude	Longitude	Depth (m)	Height (m)	Min. Axis (km)	Maj. Axis (km)	Axial Trends	Dike Trends	Comments
31	S	12°55'	144°23'	4950	700+	1.5?	2.2?	102°	325°	snr
32	S	12°51'	144°07'	4950	650	1.3	1.7	322°	032°	-
33	S	12°54'	143°49'	4900	350	1.1	1.1	353°	301°,121°	
34	S	13°40'	144°29'	4500	450	1.5	1.1	030°	250°,079°	-
35	S	13°38'	144°26'	4500	200	.6	1.1	342°	-	-
36	S	13°32'	144°21'	4350	300	1.0	2.2	356°	-	-
37	S	13°31'	144°20'	4250	250	.6	2.2	353°	-	-
38	L	13°20'	144°10'	-	-	-	-	338°,336°, 347°,349°, 336°,341°, 349°,340°, 349°,347°, 347°,347°, 338°,222°, 273°,355°, 324°	-	-
39	R	12°53'	143°35'	4250+	200+	-	-	036°	-	bnr
40	S	12°49'	143°43'	4750+	500+	1.7?	1.8?	007°	-	bnr
41	S	12°46'	143°40'	4550	450	1.0	1.3	012°	-	-
42	S	12°44'	143°39'	5300	1150	3.9	3.9	294°	066°,015°, 250°	-
43	S	12°37'	143°28'	5300	500+	1.3?	1.3?	349°	-	snr
44	L	12°40'	143°25'	-	-	-	-	264°,088°, 072°,081°, 284°,231°, 322°,222°, 350°,223°, 037°,016°	-	-

TABLE 2.1. Continued ...

Feature Number	Feature Type	Latitude	Longitude	Depth (m)	Height (m)	Min. Axis (km)	Maj. Axis (km)	Axial Trends	Dike Trends	Comments
45	L	12°43'	142°50'	-	-	-	-	353°,358°, 336°,340°, 352°,355°, 342°,000°, 344°,353°, 340°,302°, 002°	-	-
46	S	12°20'	143°05'	4900	600	1.1	1.7	310°	302°,355°	-
47	S	12°10'	142°55'	4700	200	.7	1.4	063°	337°	-
48	F	12°35'	142°35'	-	-	-	-	-	074°,088°, 074°,075°	Figure 2.6
49	L	12°20'	142°05'	-	-	-	-	338°,336°, 335°,348°, 347°	-	-
50	S	12°06'	141°35'	5000	350	1.1	2.0	339°	340°	-
51	S?	11°53'	141°05'	4600	900+	4.4?	9.2?	063°	336°,032°	-
52	S	11°40'	140°44'	4650	2400	5.0	9.7	021°	323°,006°	-
53	S	11°27'	140°12'	4400	300	.7	1.1	080°	-	moat
54	S	11°20'	139°58'	4200	250	1.1	2.0	070°	000°	-
55	S	11°19'	139°54'	4200	500+	1.1?	2.8?	019°	097°	snr
56	S	11°15'	139°46'	4200	500+	1.7?	2.0?	065°	120°	snr
57	S	11°13'	139°40'	4200	750+	2.2?	3.1?	093°	-	snr
58	S	11°11'	139°35'	4200	750+	2.9?	5.7?	068°	346°,019°	snr
59	S	11°06'	139°24'	4000+	1450	2.0?	2.5?	019°	063°,054°	bnr
60	S	11°00'	139°11'	3800+	2150	3.9?	3.9?	018°	260°	bnr
61	L	11°50'	142°35'	4700	-	-	-	349°,348°, 342°,335°	-	-
62	L	11°40'	142°20'	4700	-	-	-	329°,347°, 355°,342°, 337°,348°, 348°,350°, 356°	-	-

TABLE 2.1. Continued ...

Feature Number	Feature Type	Latitude	Longitude	Depth (m)	Height (m)	Min. Axis (km)	Maj. Axis (km)	Axial Trends	Dike Trends	Comments
63	S	11°30'	142°10'	4700	300	.8	1.1	028°	007°	-
64	S	11°15'	141°55'	4700	500	1.4	2.6	303°	274°	-
65	L	11°10'	141°50'	4700	200	-	-	322°,347°	-	-
66	S	11°02'	141°43'	4700	1400	3.7	4.4	352°	-	-
67	S	10°30'	141°10'	4300	800+	2.8?	3.5?	073°	294°	snr
68	S	10°20'	141°00'	4300	700+	2.0?	2.0?	-	293°,261°	snr
69	S	10°05'	139°30'	3600	900+	1.5?	2.5?	088°	140°,239°	snr
70	S	09°50'	139°37'	-	-	-	-	-	285°,089°, 126°,343°, 204°,202°, 232°,004°	sbnr
71	S	09°35'	139°45'	3400	2750	8.8	10.6	002°	060°,060°, 040°,173°, 204°,185°, 162°,127°, 076°	-
72	S	09°25'	140°05'	3700	4100	14.4	17.8	345°	342°,048°, 086°,012°, 094°,044°, 286°,091°, 096°,236°, 239°,212°, 238°,237°, 245°,267°, 235°,244°, 243°,291°, 267°,278°	Ua Pou
73	R	10°47'	138°50'	3600	250	.7	∞	329°	312°,327°, 247°	-
74	S	10°42'	138°38'	3300	1000	-	-	-	029°,027°, 267°,097°, 298°	-

TABLE 2.1. Continued ...

Feature Number	Feature Type	Latitude	Longitude	Depth (m)	Height (m)	Min. Axis (km)	Maj. Axis (km)	Axial Trends	Dike Trends	Comments
75	R	10°31'	138°12'	3600	1200	2.0	∞	000°	337°,292°	-
76	S	10°56'	138°20'	3800	400	.9	1.3	000°,341°, 340°,340°, 093°,350°, 008°,048°, 020°,041°, 357°,344°	-	various small seamounts
77	S	10°30'	138°35'	3800	4100	20.9	20.9	354°	037°,040°, 316°,092°, 116°,204°, 198°,189°, 239°,242°	Fatu Hiva
78	S	10°23'	138°25'	3800	3800	10.4	10.4	-	014°,051°, 180°,235°, 291°	Motu Nao
79	S	10°05'	139°05'	3600	2700	7.0	-	-	228°,165°, 182°	-
80	S	10°21'	137°52'	3600	800	2.5	4.50	093°	164°	-
81	S	10°20'	137°45'	3900	1350	7.9	7.9	095°	352°,326°, 326°	-
82	R	10°08'	137°25'	4100	700	2.8	∞	015°	150°	-
83	F	11°00'	137°05'	4100	1600	-	-	251°	-	-
84	S	10°40'	137°00'	4200	2600	5.2	5.6	068°	331°,155°	-
85	S	10°41'	137°26'	3900	2900	5.3	6.7	059°	354°,344°, 327°,343°	-
86	S	10°49'	137°51'	3500	2000	5.6	5.6	358°	334°	-
87	F	11°20'	137°50'	4000	1700	7.8	∞	255°	254°	-
88	L	11°35'	137°20'	4100	300	-	-	357°,349°, 349°	-	-
89	S	12°05'	136°42'	4000	800	2.5	3.3	078°	117°,236°, 137°	-
90	S	11°35'	136°32'	4100	600	.8	1.7	355°	115°	-

TABLE 2.1. Continued ...

Feature Number	Feature Type	Latitude	Longitude	Depth (m)	Height (m)	Min. Axis (km)	Maj. Axis (km)	Axial Trends	Dike Trends	Comments
91	F	11°00'	136°30'	4000+	1800+	6.1?	∞	257°,258°, 259°,258°, 257°	096°	height varies
92	S	09°15'	135°35'	4600	600	2.9	3.9	352°	-	-
93	S	09°58'	137°02'	4200	350	1.8	2.5	330°	-	-
94	R?	09°47'	136°42'	4250	250	1.7	∞	247°	071°	-
95	S	09°44'	136°33'	4300	550	2.2	3.2	046°	345°	-
96	L	09°00'	136°45'	4300	-	-	-	353°,354°, 349°,347°, 339°,356°, 352°,347°, 348°,350°, 335°,349°	-	Figure 2.5
97	S	08°59'	137°30'	4200	200	.8	1.0	284°	-	-
98	S	09°01'	137°52'	4100	300	.7	1.4	333°	-	-
99	S	08°55'	139°35'	3700	4000	24.5	24.5	265°	120°,150°, 231°,249°	Ua Huka
100	S	08°50'	140°10'	2700	3300	-	-	089°	217°,252°, 268°	Nuku Hiva
101	S	09°05'	140°38'	2700	2200	6.7	6.7	060°	348°,274°, 302°	-
102	S	08°10'	140°40'	3400	1800+	-	-	-	150°,194°, 217°,148°	snr
103	S	08°46'	139°55'	3500	3000	12.2	12.2	203°	335°,350°	-
104	S	07°55'	141°25'	4200	2800	5.6	5.8	238°	358°,044°, 113°,233°, 313°	Figure 2.4
105	S	08°09'	141°23'	4200	3700	11.1	11.1	005°	187°,150°, 351°,238°, 209°,322°, 167°,288°	-
106	S	09°00'	142°05'	4300	300	.7	1.4	349°	281°,347°	-

TABLE 2.1. Continued

Feature Number	Feature Type	Latitude	Longitude	Depth (m)	Height (m)	Min. Axis (km)	Maj. Axis (km)	Axial Trends	Dike Trends	Comments
107	S	08°58'	142°45'	4500	1400	3.3	3.3?	-	200°,268°	-
108	S	08°27'	142°43'	4400	500	2.2	2.8	077°	-	-
109	S	08°13'	142°15'	4350	450	.8	1.1	039°	343°	-
110	L	08°15'	142°23'	-	-	-	-	352°,343°, 344°,343°, 340°,349°, 337°	-	-
111	S	08°06'	141°56'	4300	2500	3.9	3.9	291°	041°,328°, 089°,266°	Tua Ivi Totahi
112	L	09°00'	143°25'	4500	-	-	-	000°,342°, 348°,348°, 351°,350°, 340°,343°, 339°,350°, 349°,328°, 343°,340°, 349°		-
113	S	09°00'	143°55'	4800	500	1.7	2.4	334°	330°,285°, 304°	-
114	S	08°50'	143°40'	4650	850+	1.7?	2.5?	067°	125°,164°	snr
115	R	08°32'	142°55'	4450	450	-	-	308°	124°,151°, 335°,184°	-
116	L	07°20'	142°30'	4300	-	-	-	355°,353°, 354°,349°, 354°,359°, 001°,358°, 354°,349°, 347°,351°, 352°	-	-

TABLE 2.1. Continued ...

Feature Number	Feature Type	Latitude	Longitude	Depth (m)	Height (m)	Min. Axis (km)	Maj. Axis (km)	Axial Trends	Dike Trends	Comments
117	S	07°13'	142°19'	4300	900	2.5	2.5	320°	241°,254°, 192°,305°, 349°	-
118	L	07°00'	142°40'	4300	-	-	-	350°,336°, 354°,354°, 323°,347°, 349°,354°, 354°,355°, 354°,350°, 356°,355°, 002°,349°, 355°,342°, 346°,344°, 344°,353°, 339°,341°, 346°,341°	-	-
119	S	06°04'	142°12'	4300	300	1.4	2.2	341°	076°,077°	-
120	L	06°13'	141°55'	4400	-	-	-	-	355°,352°, 352°,348°, 348°,347°	-
121	R	06°00'	141°28'	4300	300	3.3	∞	353°	352°,036°	-
122	S	05°52'	141°17'	4400	300	.8	1.3	338°	358°	-
123	S	05°41'	140°58'	4400	350	1.0	1.4	012°	-	-

TABLE 2.1. Continued ...

Feature Number	Feature Type	Latitude	Longitude	Depth (m)	Height (m)	Min. Axis (km)	Maj. Axis (km)	Axial Trends	Dike Trends	Comments
124	L	05°48'	140°45'	4300	-	-	-	012°,009°, 356°,345°, 005°,355°, 340°,347°, 352°,357°, 348°,351°, 350°	-	-
125	L	06°00'	139°35'	4300	-	-	-	345°,355°, 014°,335°, 352°,351°, 347°,352°, 345°,015°, 356°,015°, 358°,017°, 015°,010°, 006°,352°	-	-
126	S	06°48'	138°59'	4200	250	.6	.8	252°	-	-
127	L	06°22'	138°30'	4400	-	-	-	348°,342°, 005°	-	-
128	S	06°15'	138°17'	4400	1200	3.3	4.5	010°	-	-
129	S	07°15'	140°02'	4100	200	2.1	2.2	327°	-	-
130	L	07°12'	139°55'	4100	-	-	-	095°,083°, 093°,104°, 085°	-	-
131	S	09°11'	140°37'	3200+	3200+	8.7?	8.7?	358°	178°,188°	-

TABLE 2.1. Continued ...

Feature Number	Feature Type	Latitude	Longitude	Depth (m)	Height (m)	Min. Axis (km)	Maj. Axis (km)	Axial Trends	Dike Trends	Comments
132	L	09°15'	135°45'	4500	-	-	-	346°,345°, 342°,319°, 007°,342°, 351°,353°, 349°,331°, 341°,347°, 348°,352°, 351°,343°, 346°,346°, 346°,345°, 347°,359°, 341°,006°, 338°		
133	S	05°52'	140°07'	4300	250	.8	1.3	355°	-	-

S: Seamount; R: Ridge; P: Plateau edge; L: Lineation; F: Fracture zone; snr: summit not resolved; bnr: bottom not resolved; Question marks indicate estimates for the axial measurements, tentative identifications for the feature types. All notation is discussed in the text.

TABLE 2.2. Circular statistics for trends of seafloor features

Sample	Symbol	N	R	r	$s2$	$\overline{\varphi}$	$\delta\overline{\varphi}$	$\tilde{\kappa}$	$\delta\tilde{\kappa}$	P	V
lineation	Λ	208	162.17	0.8134	0.323	349°	4°	3.0	$2.6\leq\kappa\leq3.3$	<<.001	-
seamount	Σ	74	28.40	0.3838	1.232	359°	24°	0.8	$0.6\leq\kappa\leq1.3$	<.001	-
ridge	P'	7	2.54	0.3629	1.274	353°	90°	0	0	.413	1.354
dike	Δ	202	17.01	0.0842	1.832	001°	90°	0.2	$\kappa\leq0.3$	z=1.432	1.655
dike	*Δ*	166	15.96	0.0962	1.808	*351°*	90°	0.2	$\kappa\leq0.3$	.243	-
estimates included	Σ'	97	32.49	0.3250	1.350	004°	27°	0.7	$0.4\leq\kappa\leq0.9$	<.001	-
	Σ'+P'	104	34.92	0.3358	1.328	004°	22°	0.7	$0.4\leq\kappa\leq0.8$	<.001	-
MFZ	-	12	11.92	0.9740	0.052	078°	6°	19.5	$\kappa\gg5$	<.001	-
southern & northern sub-samples	SΛ	45	24.16	0.5369	0.926	352°	22°	1.2	$0.8\leq\kappa\leq1.8$	<.001	-
	NΛ	163	145.01	0.8896	0.221	349°	4°	4.9	$\kappa\geq3.8$	<<.001	-
	SΣ	18	13.34	0.7408	0.518	000°	22°	2.2	$1.3\leq\kappa\leq3.3$	<<.001	-
	NΣ	56	15.06	0.2690	1.462	358°	40°	0.5	$0.2\leq\kappa\leq0.9$	.024	-
	SΔ	29	10.83	0.3736	1.253	025°	44°	0.8	$0.2\leq\kappa\leq1.3$	.017	2.319
	NΔ	171	14.10	0.0825	1.835	343°	90°	0.2	$\kappa\leq0.3$	.385	1.568
	SΔ	24	4.28	0.1785	1.643	*351°*	90°	0	$\kappa\leq0.7$	.470	-
	NΔ	140	13.24	0.0945	1.811	*353°*	90°	0.2	$\kappa\leq0.4$	.317	-
	SΣ'	28	19.34	0.6907	0.619	005°	20°	1.9	$1.3\leq\kappa\leq2.7$	<.001	-
	NΣ'	69	13.24	0.1918	1.616	004°	84°	0.6	$\kappa\leq0.7$	.110	2.181
	SP'	1	-	-	-	-	-	-	-	-	-
	NP'	6	3.54	0.5897	0.821	341°	85°	1.0	$\kappa\leq2.6$	.123	2.021
	S(Σ'+P')	29	18.35	0.6329	0.734	008°	22°	1.6	$1.1\leq\kappa\leq2.4$	<.001	-
	N(Σ'+P')	75	16.58	0.2212	1.558	002°	52°	0.4	$0.2\leq\kappa\leq0.7$	.047	2.646

N: Number of measurements in sample; R: Length of resultant vector; r: Length of mean vector; s^2: angular variance; $\overline{\varphi}$: Mean azimuth of sample; $\delta\overline{\varphi}$: 95% confidence interval for mean azimuth; $\tilde{\kappa}$: estimated concentration parameter; $\delta\tilde{\kappa}$: 90% confidence interval for concentration parameter; P: Critical level, or significance probability under a uniform distribution; V: V-test statistic under uniform distribution and $\theta_0 = \overline{\varphi}_\Lambda$. Symbols and mean angles in italics refer to samples that are **not** measured w.r.t. geographic North. See text for full explanation.

2.4. FEATURE TRENDS AND SIZES

The circular statistics derived from the trend data of Table 2.1 are listed in Table 2.2. Following convention, I have designated each sample of directions by a Greek capital letter. Each sample contains all the measurements of trends under the corresponding Latin capital entry in Table 2.1. Thus, all lineation trends "L" in table 2.1 are contained in the sample Λ, all seamount axial trends "S" are contained in the sample Σ, and ridges "R" are in P. The exceptions to this are: the dike trends, entered with each accompanying seamount in Table 2.1, but listed as a separate sample Δ in Table 2.2; an entry *Δ* for the dikes in the reference frame of the seamount major axes; and the trends from the fracture zone, which are considered separately under the entry 'MFZ', with no symbol. I have excluded the features measured on the edge of the Tuamotu plateau from the analysis.

Samples that are primed (') include trends from the features which have estimated dimensions, or where the designation of the feature type was tentative. I did not include estimates in any sample for seamount axis trends in cases where there was an uncertain trend. For this reason, the number of entries under each letter in Table 2.1 will not precisely correspond to the number of measurements in the corresponding sample, *N*, listed in Table 2.2. When dealing solely with trends, I may include the primed samples in any estimate of a mean direction, while when I am dealing with any calculation involving the axial lengths, I exclude the samples that contain estimated data. Since there is no clear difference between seamounts and ridges as defined in sections 2.3.1.1/2, I have also included an entry for the union of the two samples, under Σ'+P'. The samples *Δ*, *NΔ*, *SΔ*, and their corresponding mean trends are in italics to highlight the fact that the directions are in the seamount axis frame of reference, and not the geographic frame of reference. The lower half of Table 2.2 presents the statistics for the same samples subdivided into northern and southern sub-samples, divided by the Marquesas fracture zone, and the corresponding combination of the ridge and seamount axis trend samples.

Samples are illustrated in frequency distribution diagrams in Figures 2.7 through 2.18. In these figures, the radius is the number of observations, and the angle is the azimuth of the observation, and all samples are binned at a 1° interval. The lineations are clearly clustered around a direction, whereas the other samples are not so clearly aligned. To determine in a quantitative sense the directions indicated by these samples, I calculate the circular statistics for the various samples to determine the mean directions of the trends, and determine the confidence intervals that accompany each sample. There is a certain amount of terminology that accompanies the statistical analysis of periodic variables, and in what follows, I assume that the reader is at least familiar with the basic terms. Appendix A contains a slightly more detailed introduction than the brief notes included here.

The resultant vector of the sample, $\boldsymbol{R}$, is formed by adding unit vectors in each of the N directions composing the sample. The magnitude of the resultant vector, $R = |\boldsymbol{R}|$, indicates how closely the N observations come to indicating a single direction. If all the observations are equal, then R equals N. The magnitude of the mean vector $\boldsymbol{m}$ is $r = |\boldsymbol{m}| = R/N$, allowing comparisons between samples with different numbers of observations to be made.

I have modelled all the observed samples with the von Mises distribution [*von Mises*, 1918], which is a conditional distribution of the normal, or Gaussian distribution under the restriction that the variables lie on a circle. The von Mises distribution seems to describe the distribution of random observations for most circular variables, and appears to approximate the distribution of estimations of the parameters of most other circular distributions [*Watson*, 1961,1983; *Fisher et al.*, 1987]. The precision parameter κ of the von Mises distribution is a measure of the dispersion of the sample, just as σ^2 functions on the linear case. The parameter has the range $0 \leq \kappa \leq \infty$, the extremes indicating uniform and point distributions respectively. The angular variation s^2 also indicates dispersion, but has the range $0 \leq s^2 \leq 2$.

A careful inspection of Table 2.1 reveals that there are two types of measurement for trends. Trends for axial features like lineations and seamount axes have an inherent ambiguity in their azimuth, while features like dikes are unambiguous in their direction. As discussed in

Appendix A, these two measurements correspond to the two types of circular variables, *axial* and *vector circular variables*. For axial variables, a measurement 45° could just as easily be expressed as 225°. The two numbers are equivalent geometrically, but not statistically. If I were to include the reciprocal bearing of each measurement in the sample, there would be 100% correlation between the two modes of the distribution. Ideally, the measurements about the two modes of a distribution drawn from a bimodal parent are independent in the sense that while they share the same axis and precision parameter, the observations near each mode are independent of observations at the other mode. However, I cannot be sure that the process of measuring will provide an unbiased distribution between the two modes, so I have chosen to express all the axial measurements as azimuths between 270° and 90°, so that a measurement of 180° reads as 000° in Table 2.1. I determine the direction $\overline{\varphi}$ of the mean vector by determining the resultant vector from an addition of unit vectors in the tabulated directions. Because all the measurements fall in one half of the circle, the magnitude of this resultant vector is overestimated. To correct for this, I use the magnitude of the *second* moment of the distribution for the magnitude of the mean vector rather than the first moment.

A unimodal distribution will have a non-zero first moment, and a second moment smaller than the first, while a bimodal distribution will have a near zero first moment, and a non-zero second moment. The use of the second moment is standard for axial variables, but in our case, where the measurements were made as if the variable was unimodal, the use of the second moment is technically correct, but probably an underestimation of the value if there were observations equally distributed between the two modes. Any estimation of the angular confidence intervals $\delta\overline{\varphi}$ for these samples will then be conservative, and I may assume that the 'true' 95% confidence interval lies within my calculated 95% bounds.

The situation for the observations of the dike trends is simple: since I observe trends over the full circle, I may use either the first or second moments, depending on whether I desire to test for unimodal or bimodal tendencies in the distribution. If the dike trends are controlled by the fabric of the seafloor, I am looking for a bimodal distribution, while if the dike trends are controlled by internal stresses caused by loading, I can expect to see either a uniform distribution, or a distribution correlated with some edifice feature. In this chapter, I test for uniformity, for a bimodal distribution, and the correlation between the seamount axis azimuths and the dike trends.

In Table 2.2, I also list point estimates, $\tilde{\kappa}$, for the precision parameter κ, and 90% confidence intervals. The confidence level for the precision parameter is different from that of the mean direction only because tables of the intervals at the 95% level for $\tilde{\kappa}$ were not available. Except for the interval for $\tilde{\kappa}$, all figures and tests in this chapter are at the $\alpha = 0.05$, or 5% level of significance, or equivalently, a 95% confidence level. Also listed for each sample is the critical level, or significance probability, P, under the Rayleigh test for randomness. The critical level gives the smallest significance level by which a null hypothesis can be rejected. For the P values listed, the null hypothesis is that the parent distribution for the samples is uniform, and the P value then gives the probability that the observed distribution could have resulted from a uniform parent. Where $P > \alpha$, the possibility cannot discounted that the observed sample is in fact uniform, or random. For values that are close to α, or exceed it, I have also given values of the test statistic $u = \sqrt{2N}\, r \cos(\overline{\varphi} - \theta_0)$, in the more stringent *V*-test, which is more powerful than the Rayleigh test at detecting randomness if there is a reason to suspect an *a priori* direction for the mean.

For the *V*-test of the dike trends in the seamount frame of reference, I have used two *a priori* directions that are natural to the geometry of the problem: the direction $\theta_0 = 0°$, along the major axis, and the direction $\theta_0 = 90°$, along the minor axis. For the geographic trends of the samples, I have used the mean direction of the lineations, $\theta_0 = \overline{\varphi}_\Lambda$, as the *a priori* direction. As outlined in more detail in Appendix A, the *V*-test is often misused to indicate deviation from the *a priori* direction, when the null hypothesis is actually one of uniformity, rather than distribution about a specific direction. As such, it should be understood that since the test can only reject the possibility of randomness, the use of the mean direction for the lineations is not a form of 'circular argument'. The *V*-test is obviously not used on the lineation sample itself.

2.4.1. Lineation statistics

As could be expected from Figures 2.7, 2.8, and 2.9, the results of these two tests indicate that I may reject a uniform distribution at the 95% confidence level for the lineations Λ and the sub-samples $N\Lambda$ and $S\Lambda$ from north and south of the Marquesas fracture zone. There is no statistical difference in the mean trends between the sub-samples, so the lineation trend can be said to be the same on both sides of the fracture zone at the 95% confidence level.

2.4.2. Seamount and ridge major axis statistics

Results from the seamount and ridge samples are more complex. The seamount major axis azimuth samples Σ and Σ', and the sample $\Sigma'+P'$ including the ridge trends, are all significantly different from a uniform distribution, while the sample P', and the sub-samples SP' and NP', all fail the Rayleigh test. SP' is composed of one observation, and so automatically fails, while the removal of this observation from the sample P' to form NP' improves the statistics of NP' to the point that even though it still fails the Rayleigh test, there is marginal significance under the V-test.

The sub-samples $N\Sigma$, $S\Sigma$, $N(\Sigma'+P')$, and $S(\Sigma'+P')$ are all significantly non-uniform, but cannot be said to differ across the fracture zone, while the sub-samples $N\Sigma'$ and $S\Sigma'$ differ only in that the addition of the seamounts with estimated axis lengths improves $S\Sigma'$ but worsens $N\Sigma'$, so that $N\Sigma'$ fails the Rayleigh test, but has marginal significance under the V-test. The sub-samples $N\Sigma'$ and $S\Sigma'$ do not differ significantly across the fracture zone. The frequency distribution of samples Σ', $N\Sigma'$, and $S\Sigma'$ is shown in Figures 2.10, 2.11, and 2.12.

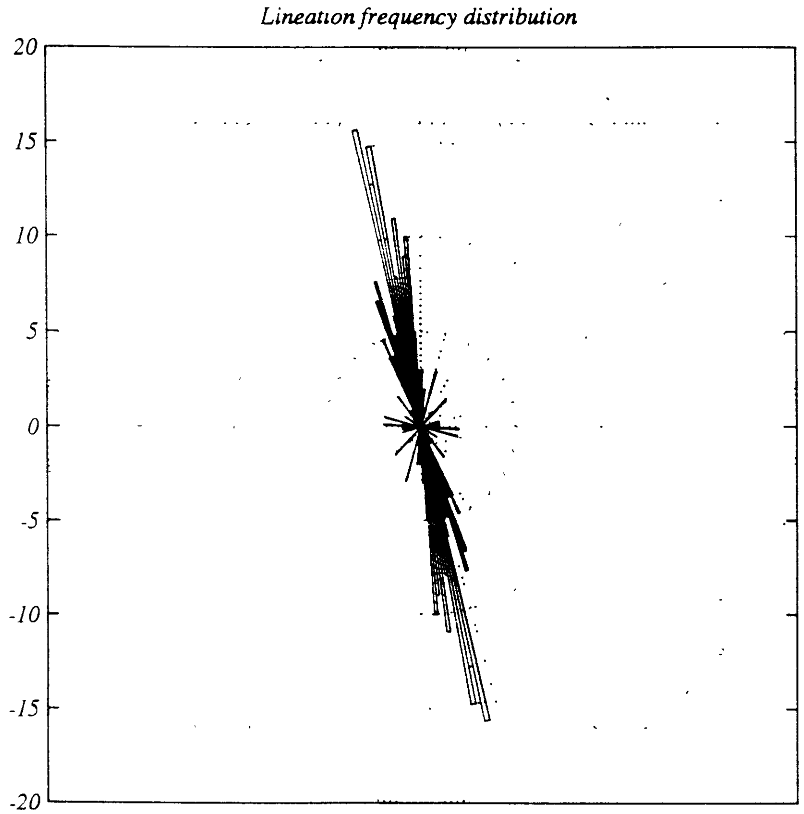

Figure 2.7. Frequency distribution of all lineations. Measured lineation trends are shown as bars through the origin, with the length of the bar reflecting the number of observations along the trend indicated by the angle of the bar to the vertical, or geographic North (000°). Dotted circles are in units reflected at the side of the box, and the dotted square reflects the maximum count. This distribution has a total count of $N = 208$, and a mean direction of 349°, with a 95% confidence interval of 4°. There is less than a 0.1% chance that this distribution could be observed from a uniform parent distribution.

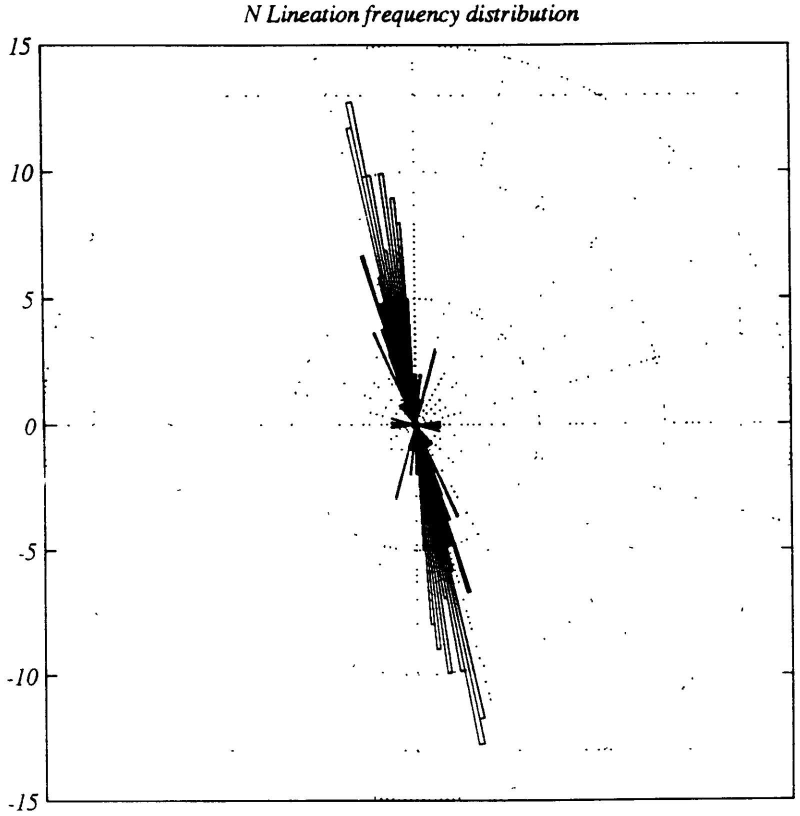

Figure 2.8. Frequency distribution of lineations north of the Marquesas Fracture Zone. Measured lineation trends are shown as bars through the origin, with the length of the bar reflecting the number of observations along the trend indicated by the angle of the bar to the vertical, or geographic North (000°). Dotted circles are in units reflected at the side of the box, and the dotted square reflects the maximum count. This distribution has a total count of N = 163, and a mean direction of 349°, with a 95% confidence interval of 4°. There is less than a 0.1% chance that this distribution could be observed from a uniform parent distribution.

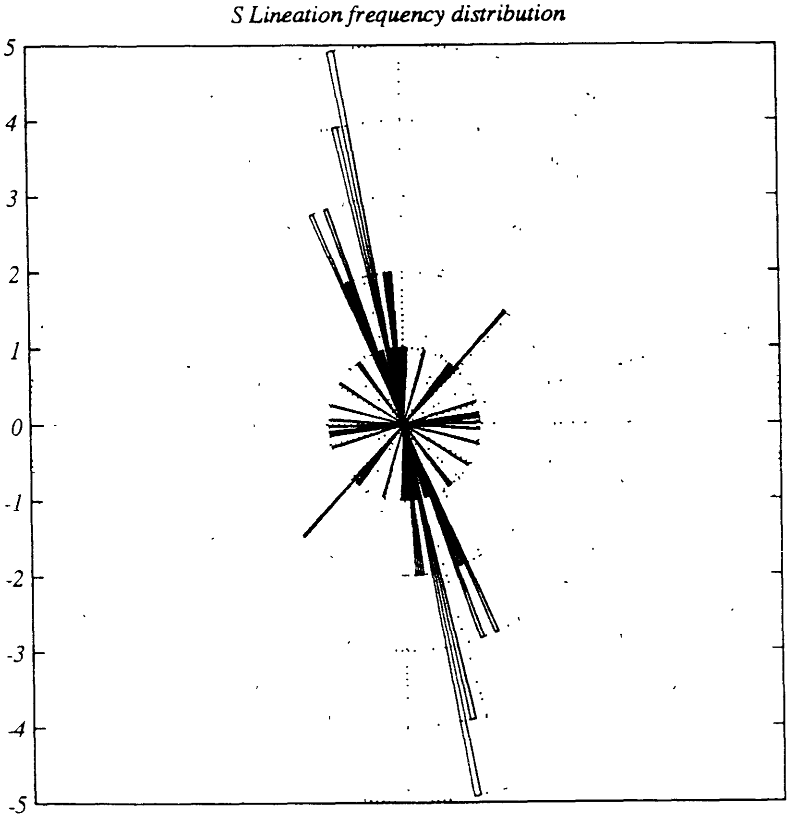

Figure 2.9. Frequency distribution of lineations south of the Marquesas Fracture Zone. Measured lineation trends are shown as bars through the origin, with the length of the bar reflecting the number of observations along the trend indicated by the angle of the bar to the vertical, or geographic North (000°). Dotted circles are in units reflected at the side of the box. This distribution has a total count of $N = 45$, and a mean direction of 352°, with a 95% confidence interval of 22°. There is less than a 0.1% chance that this distribution could be observed from a uniform parent distribution.

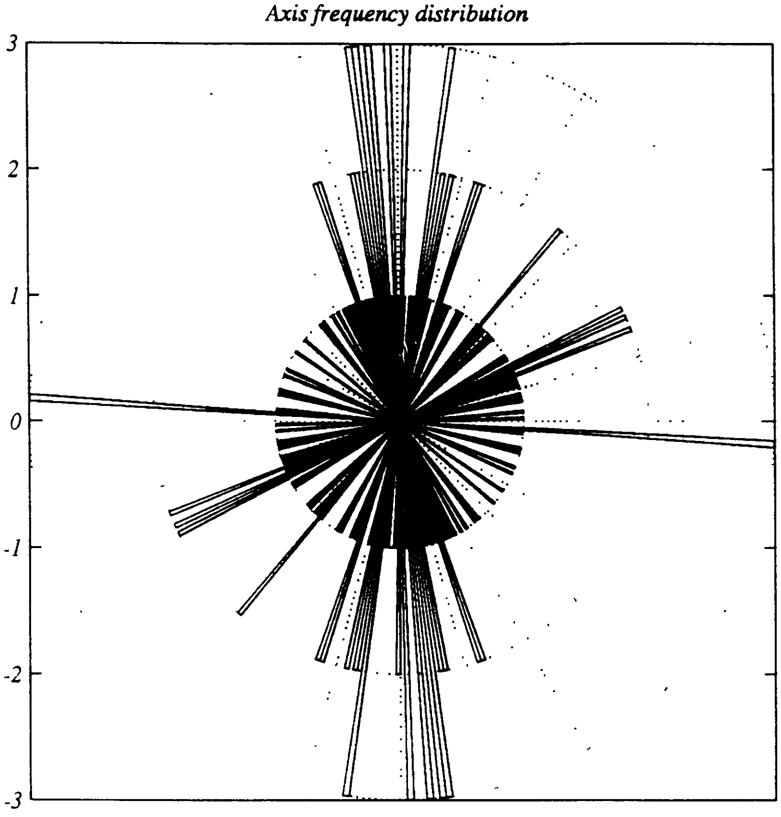

Figure 2.10. Frequency distribution of all seamount major axes. Measured major axis trends are shown as bars through the origin, with the length of the bar reflecting the number of observations along the trend indicated by the angle of the bar to the vertical, or geographic North (000°). Dotted circles are in units reflected at the side of the box. This distribution has a total count of $N = 97$, and a mean direction of 004°, with a 95% confidence interval of 27°. There is less than a 0.1% chance that this distribution could be observed from a uniform parent distribution.

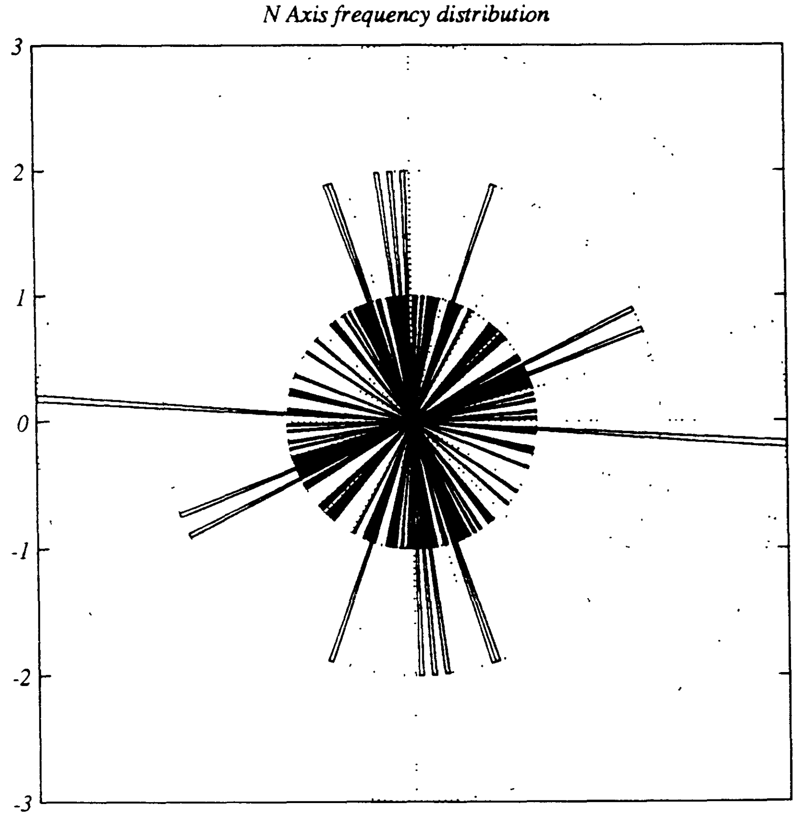

Figure 2.11. Frequency distribution of seamount major axes north of the Marquesas Fracture Zone. Measured axis trends are shown as bars through the origin, with the length of the bar reflecting the number of observations along the trend indicated by the angle of the bar to the vertical, or geographic North (000°). Dotted circles are in units reflected at the side of the box. This distribution has a total count of N = 56, and a mean direction of 358°, with a 95% confidence interval of 40°. There is a 2.4% chance that this distribution could be observed from a uniform parent distribution.

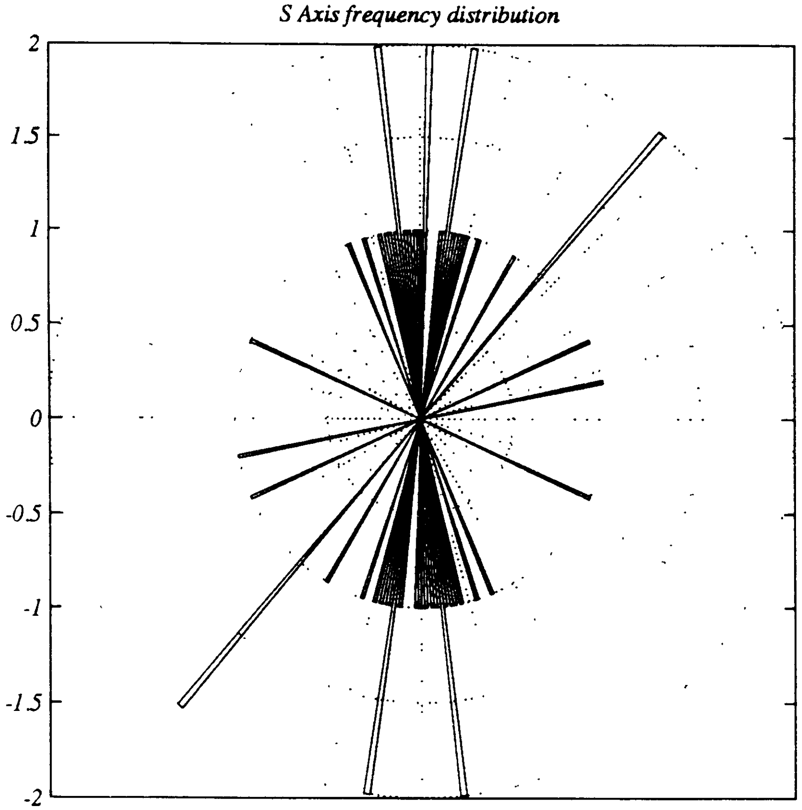

Figure 2.12. Frequency distribution of seamount major axes south of the Marquesas Fracture Zone. Measured axis trends are shown as bars through the origin, with the length of the bar reflecting the number of observations along the trend indicated by the angle of the bar to the vertical, or geographic North (000°). Dotted circles are in units reflected at the side of the box. This distribution has a total count of $N = 18$, and a mean direction of 000°, with a 95% confidence interval of 22°. There is less than a 0.1% chance that this distribution could be observed from a uniform parent distribution.

2.4.3. Dike trend statistics

The dike samples are simpler than the seamounts and ridges, but no less interesting. The sample Δ fails the Rayleigh test (where I have used the test statistic $z = Nr^2$ since $N>200$), but marginally passes the *V*-test, as a result of the contribution from the southern sub-sample, SΔ. When I divide the dikes into the northern and southern sub-samples (discounting two dikes that occur on the fracture zone ridge itself), I find that the sub-sample SΔ cannot be said to be random, while NΔ fails both the Rayleigh test and the *V*-test. Since the northern sub-sample has a confidence interval of 90°, I cannot say whether or not the mean directions differ across the fracture zone. The frequency distribution for these samples is shown in Figures 2.13, 2.14, and 2.15.

I have also formed samples of the dike trends with reference to the seamount major axes, and whose frequency distributions are shown in Figures 2.16, 2.17, and 2.18. The trend of the corresponding seamount major axis is subtracted from the observed geographic dike trend to give the dike trend in the seamount frame. This new sample, designated by the symbol *Δ*, and its sub-samples *SΔ* and *NΔ* all fail the Rayleigh test, so that we cannot discount the possibility that the dike trends are randomly distributed in the seamount frame. All samples fail the *V*-test for the *a priori* direction of *90°*, perpendicular to the major axes of the seamounts, while only *Δ* passes the *V*-test for an *a priori* direction of *0°*, parallel to the major axes of the seamounts. Since all sub-samples failed the tests, no information is available to determine if differences exist across the fracture zone.

2.4.4. Seamount dimensions

To understand other factors that may affect the mean directions calculated above, I now turn to the other characteristics listed in Table 2.1 for the measured features, including the height and axial lengths of the seamounts themselves. A basic characteristic of the seamount is the ratio of height to radius, which has been previously investigated by *Jordan et al.* [1983], and *Smith and Jordan* [1988] in a more formal sense than is attempted here. I simply note that

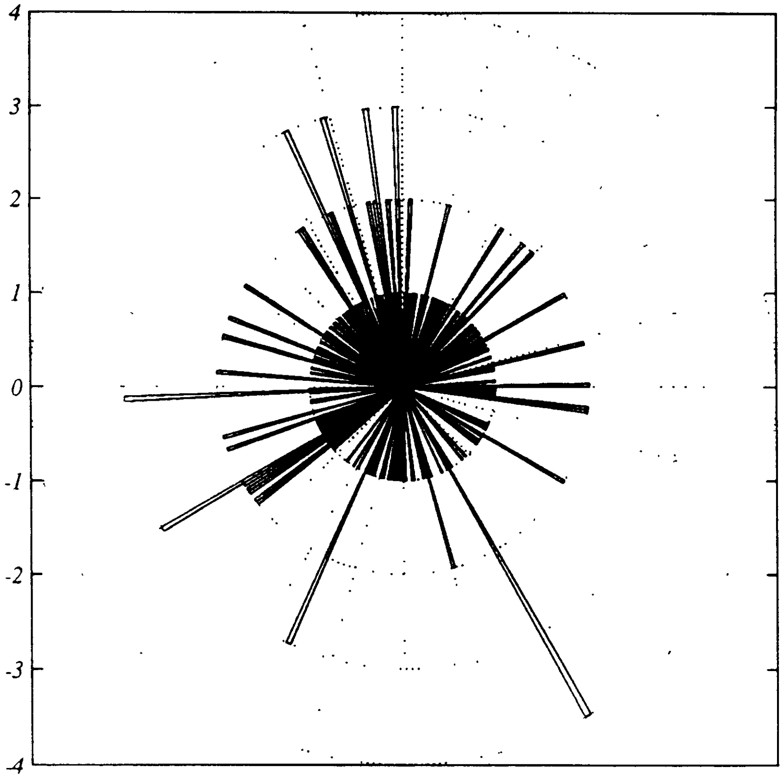

Figure 2.13. Frequency distribution of all dikes. Measured dike trends are shown as bars radiating from the origin, with the length of the bar reflecting the number of observations along the trend indicated by the angle of the bar to the vertical, or geographic North (000°). Dotted circles are in units reflected at the side of the box. This distribution has a total count of N = 202, and a mean direction of 001°, with a 95% confidence interval of 90°. There is marginal statistical evidence that this distribution is non-uniform.

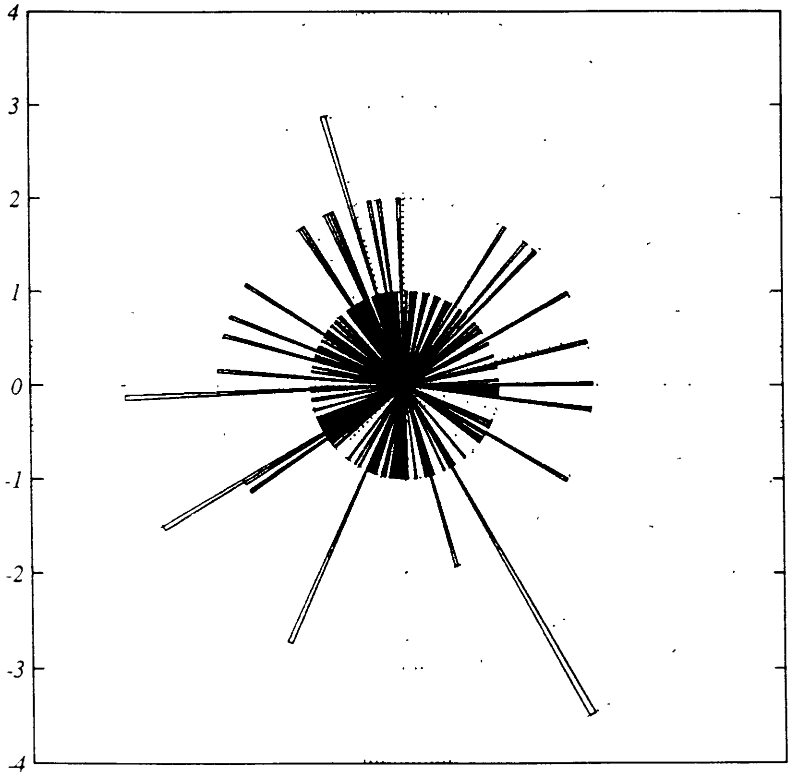

Figure 2.14. Frequency distribution of dikes north of the Marquesas Fracture Zone. Measured dike trends are shown as bars radiating from the origin, with the length of the bar reflecting the number of observations along the trend indicated by the angle of the bar to the vertical, or geographic North (000°). Dotted circles are in units reflected at the side of the box. This distribution has a total count of $N = 171$, and a mean direction of 343°, with a 95% confidence interval of 90°. There is no statistical evidence that this distribution is non-uniform, since there is a 38.5% chance that it could be observed randomly.

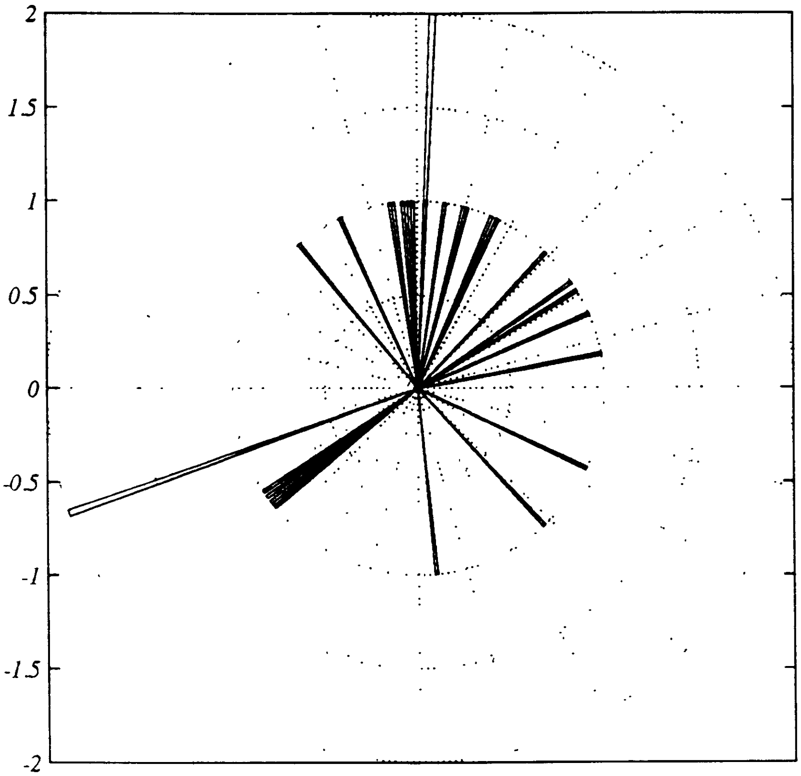

Figure 2.15. Frequency distribution of dikes south of the Marquesas Fracture Zone. Measured dike trends are shown as bars radiating from the origin, with the length of the bar reflecting the number of observations along the trend indicated by the angle of the bar to the vertical, or geographic North (000°). Dotted circles are in units reflected at the side of the box. This distribution has a total count of N = 29, and a mean direction of 025°, with a 95% confidence interval of 44°. There is less than a 1.7% chance that this distribution could be observed from a uniform parent distribution.

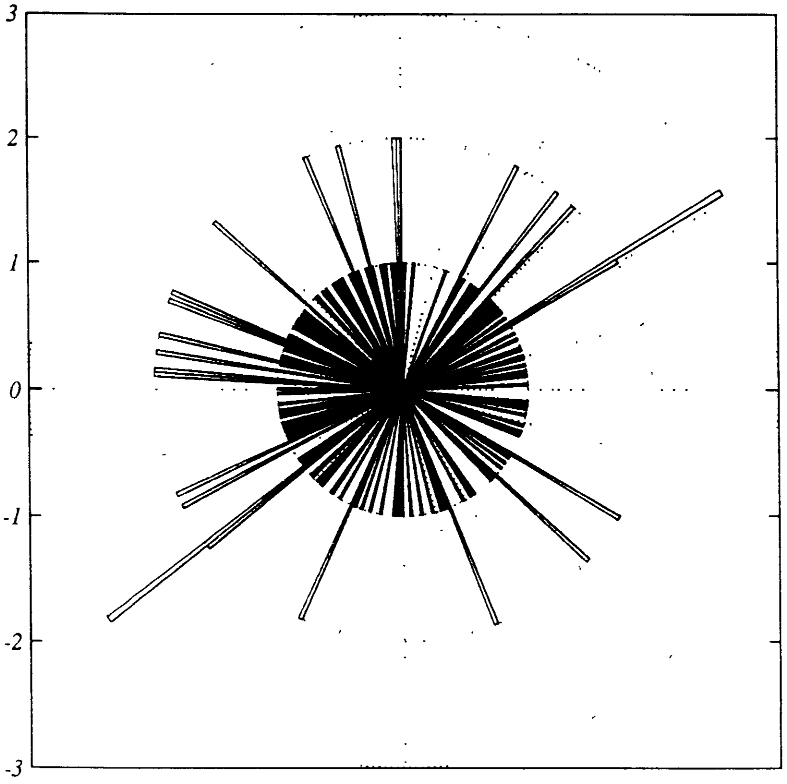

Figure 2.16. Dike frequency distribution in seamount frame of reference. Measured dike trends are shown as bars radiating from the origin, with the length of the bar reflecting the number of observations. The angle of the bar to the vertical indicates the angle to the major axis of the seamount. Dotted circles are in units reflected at the side of the box. This distribution has a total count of $N = 166$, and a mean direction with respect to the major axis of *351*°, with a 95% confidence interval of 90°. There is no statistical evidence that this distribution is non-uniform, since there is a 24.3% chance that it could be observed randomly.

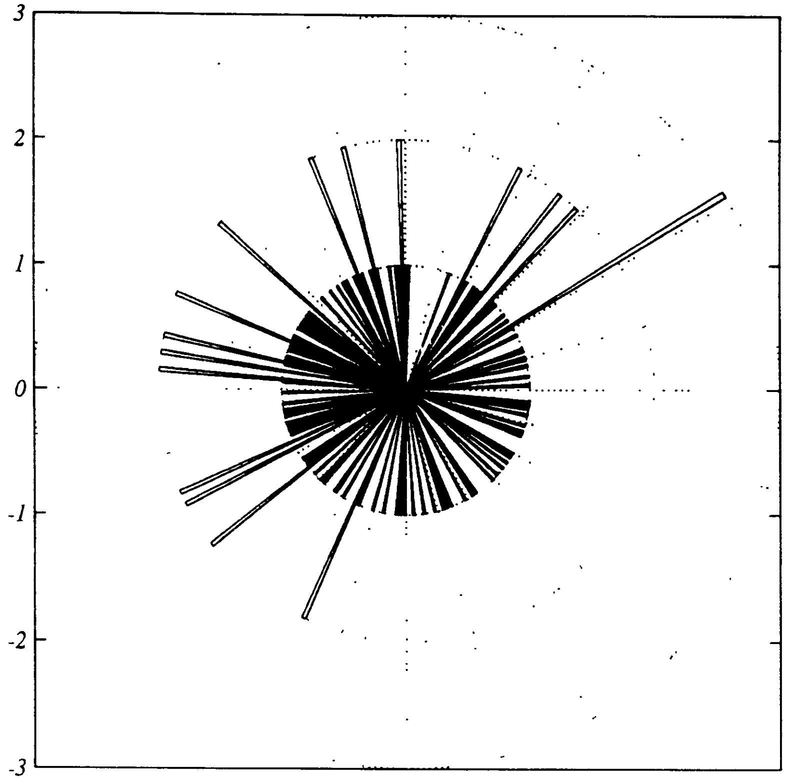

Figure 2.17. Dike distribution in seamount frame of reference, north of the Marquesas Fracture Zone. Measured dike trends are shown as bars radiating from the origin, with the length of the bar reflecting the number of observations. The angle of the bar to the vertical indicates the angle to the major axis of the seamount. Dotted circles are in units reflected at the side of the box. This distribution has a total count of N = 140, and a mean direction with respect to the major axis of 353°, with a 95% confidence interval of 90°. There is no statistical evidence that this distribution is non-uniform, since there is a 31.7% chance that it could be observed randomly.

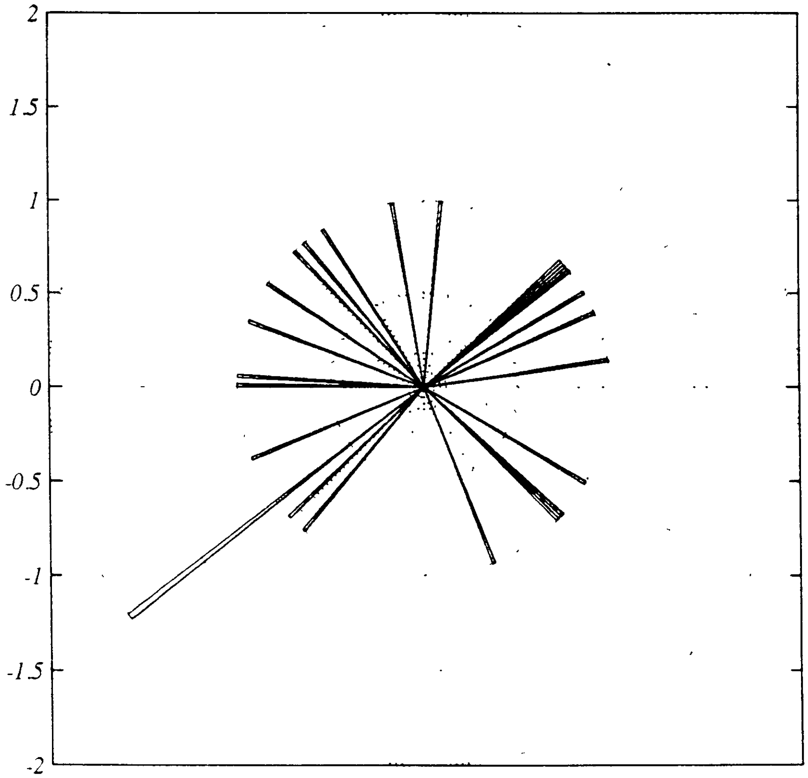

Figure 2.18. Dike distribution in seamount frame of reference, south of the Marquesas Fracture Zone. Measured dike trends are shown as bars radiating from the origin, with the length of the bar reflecting the number of observations. The angle of the bar to the vertical indicates the angle to the major axis of the seamount. Dotted circles are in units reflected at the side of the box. This distribution has a total count of $N = 24$, and a mean direction with respect to the major axis of 351°, with a 95% confidence interval of 90°. There is no statistical evidence that this distribution is non-uniform, since there is a 47.0% chance that it could be observed randomly.

in order to compare the ξ' derived from the present dataset with their height to radius ratio $\xi = 0.21$, I must account for the fact that I have measured two radii for each seamount, which must be combined into a single value. In order to conserve the volume of the seamount, I use the geometric mean rather than the average of the two figures. Figure 2.19 displays the data, with the means indicated by the crosses, and the axial values indicated by dots. The dashed line is the fit through the mean radii by simply averaging all values in the dataset, as done by *Jordan et al.* [1983], yielding $\xi' = 0.30$, while a least squares fit, shown with the solid line, yields $\xi' = 0.24$.

The difference between the values for ξ has to do with subtle differences in definitions: *Jordan et al.* [1983] define ξ as $2h/d_1$, where h is the height and d_1 is the basal radius (they also define d_2 as the summit radius of a flat-topped seamount), whereas I have defined ξ' as $h/\sqrt{r_1 r_2}$, where r_1 and r_2 are the major and minor axis lengths, respectively, measured at the $1/e$ height. Since my $1/e$ radii are smaller than the corresponding basal radii, my ξ' will be large compared with *Jordan et al.* [1983], and *Smith and Jordan* [1988]. The factor by which they differ can be found quite simply after an initial assumption.

If the slope of the Gaussian at the $1/e$ height is taken as the slope of the seamount, then it is a rather trivial exercise to find the basal radius corresponding to this slope. For $\sigma = \sqrt{r_1 r_2}$, the estimated basal radius r is $3\sigma/2$, which means that the ξ' estimates from this data must be corrected by a factor of 2/3 before being compared directly with the *Jordan et al.* [1983] and *Jordan and Smith* [1988] $\xi = 0.21$ estimate. The value of ξ' derived from this dataset using the same method, $\xi' = 0.30$, therefore compares well with the $\xi = 0.21$ estimate.

The difference between the two estimates for ξ' that come from the data of Table 2.1, derived through either simple averaging or a least-squares approach, is related to the weighting of the various points. While the average weights all points equally, the least-squares fit weights the larger radius-height points more than the smaller points. The maximum likelihood estimate for ξ' could be calculated if we knew the joint distribution of heights and radii, but we only know the marginal distributions. Since they are dependent (precisely through ξ), direct

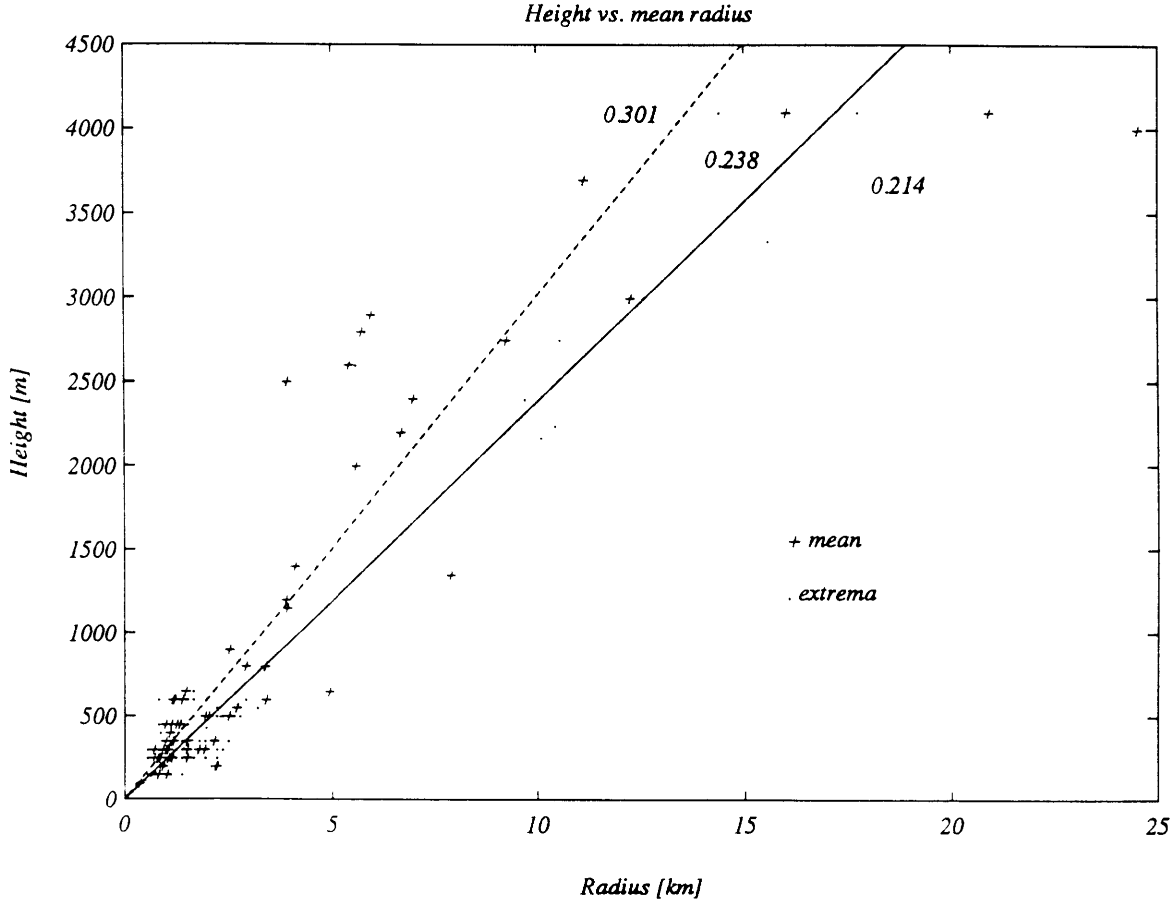

Figure 2.19. Seamount height as a function of mean radius. The mean radius of a seamount is defined as the geometric mean of the major and minor axis lengths at the 1/*e* height. This mean is displayed as a '+' symbol between the axis lengths, which are displayed as dots. Lines represent various height-to-radius ratios, as follows: the solid line is the least-squares fit to the mean radii, the dashed line is the average of all the radius to height ratios, and the dotted line is the ratio derived by *Jordan et al.* [1983], and *Smith and Jordan* [1988]. Differences are discussed in the text.

calculation of the joint distribution is unfortunately not a simple quotient of the marginal distributions.

2.5. DISCUSSION

The mean trends and confidence intervals are summarized in Figures 2.20 and 2.21. While the mean trends of the dikes and ridges are not well constrained in either diagram, it is interesting to note the general characteristics of the other features. I have shown the mean trend for the Marquesas fracture zone on both plots as both a reference and as a 'member' of both sample sets.

2.5.1. Fabric lineations and magnetic lineations

The lineations are roughly perpendicular to the fracture zone, with an angle of $101^\circ \leq \theta \leq 81^\circ$ separating the trends at roughly the 95% confidence level (an approximation since we are adding and subtracting angles...). While not all lineations produced at a ridge crest are necessarily perpendicular to the associated fracture zones, there is an independent piece of evidence that suggests these features are associated with the ridge crest process. During the *Crossgrain 2* cruise, magnetic data was also collected, and interpreted by *Kruse* [1988]. From seven anomalies identified at a wide enough spacing to permit a long line to be drawn between them, I have calculated a mean trend for the magnetic lineations of 349°. The magnetic distribution is illustrated in Figure 2.22. Since the 95% confidence interval of the magnetic lineations overlaps that of the fabric lineations, the directions are similar at the 95% level, and the fabric lineations are very likely to be associated with the same process that created the magnetic lineations, i.e. the original ridge.

While the above is intuitive, the directional statistics of the seafloor fabric could also be used in the Cretaceous quiet zone, where magnetic reversals are absent, or where the structure is not so simple, for example in regions where there was a complex reorganization of ridges, or the failure of one ridge system and the initiation of another. These latter areas tend to be

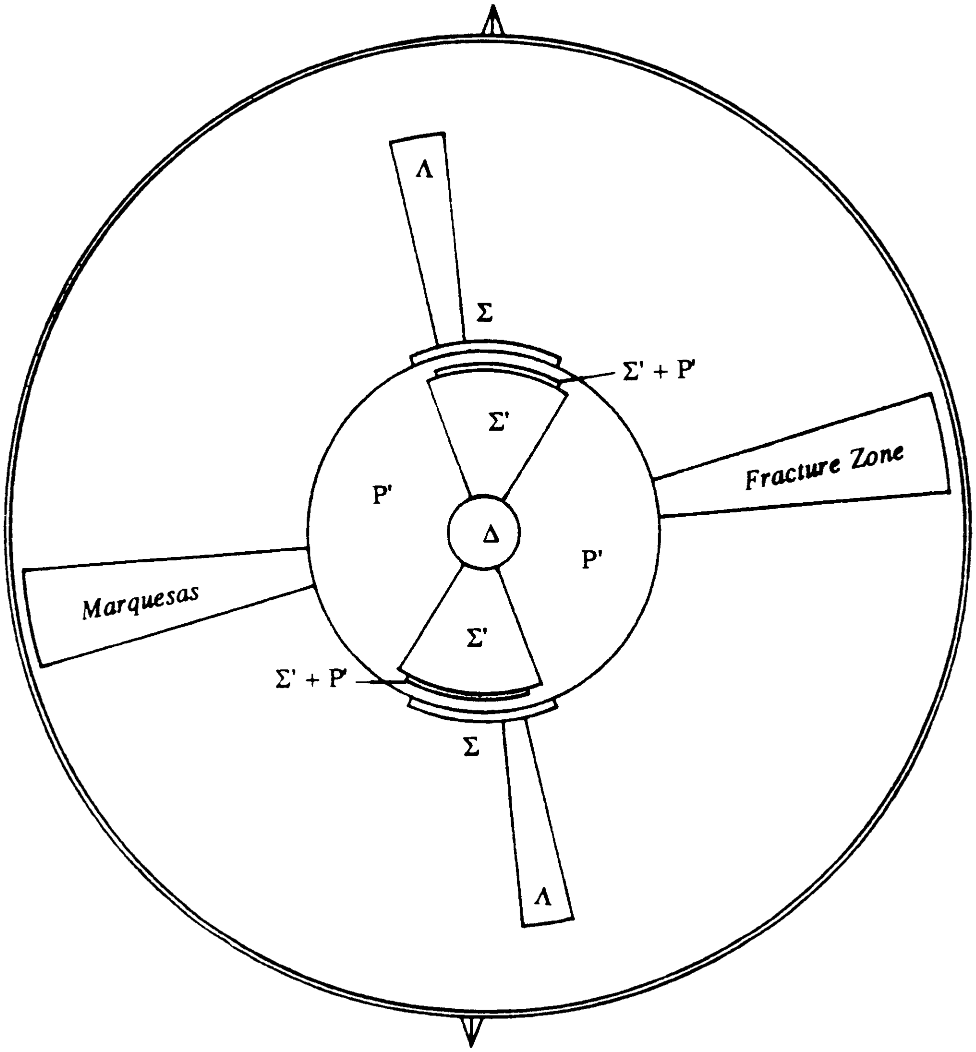

Figure 2.20. Confidence interval diagram for all trend data. Data is shown as sectors centered about the mean trends and their reciprocal bearings, with the angular width of the sectors reflecting the 95% confidence interval of the mean directions, while the radii of the sectors reflect the magnitude of the second moment of the samples. Complete circles represent mean trends with no useful confidence interval, i.e. $\delta\overline{\varphi} = 90°$. Greek capitals refer to the feature type: Λ are the lineation trends, Σ are the seamount major axis trends, Ρ are the ridge trends, and Δ are the dike trends. Primes indicate estimated data is included in the sample, and + signs indicate the union of samples.

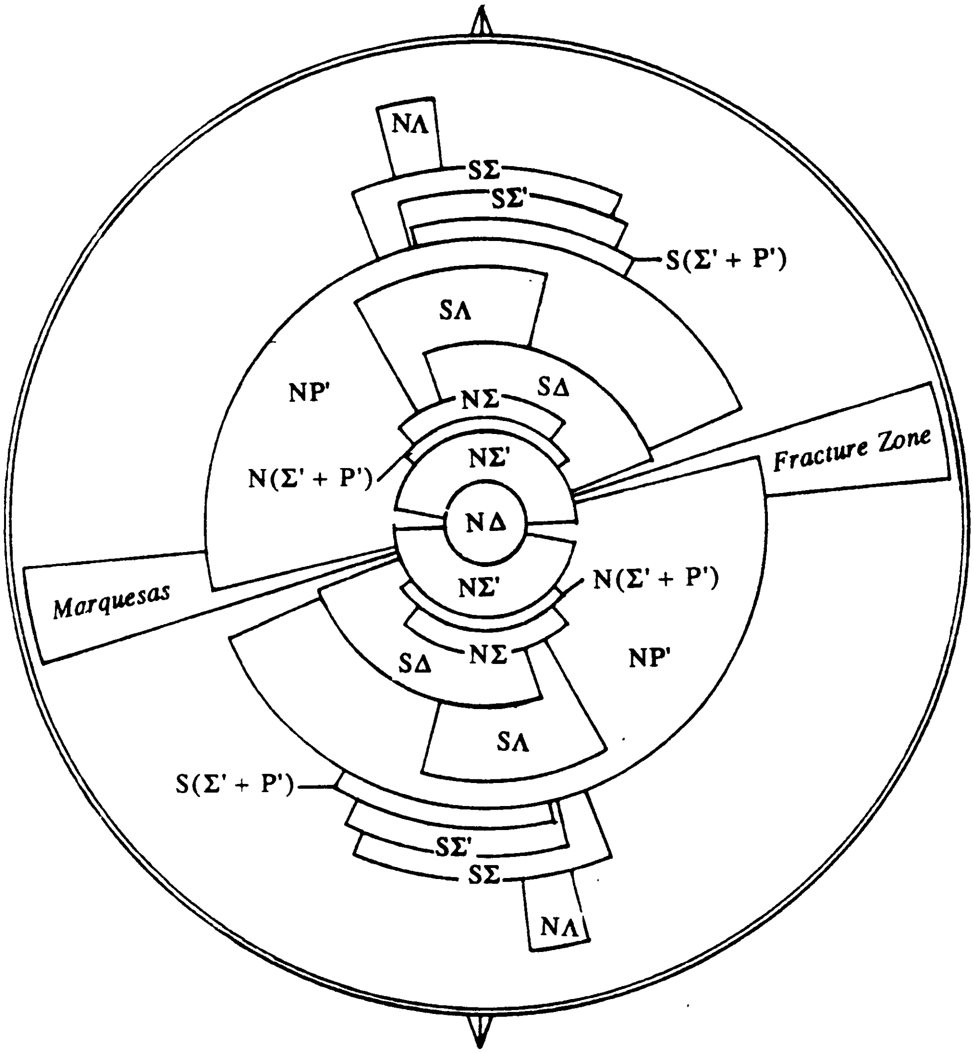

Figure 2.21. Confidence interval diagram for trend data north and south of the Marquesas Fracture Zone. Data is shown as sectors centered about the mean trends and their reciprocal bearings, with the angular width of the sectors reflecting the 95% confidence interval of the mean directions, while the radii of the sectors reflect the magnitude of the second moment of the samples. Complete circles represent mean trends with no useful confidence interval, i.e. $\delta\overline{\varphi} = 90°$. Greek capitals refer to the feature type, while preceding Latin capitals refer to the sub-sample area: L are the lineation trends, S are the seamount major axis trends, R are the ridge trends, and Δ are the dike trends, while the prefixes N and S refer to data to the north and south of the fracture zone respectively. Primes indicate estimated data is included in the sample, and + signs indicate the union of samples.

tectonically very complex, and difficult to interpret due to the nature of magnetic data. While the fabric will be as complex as the magnetic intensity, the fabric is easier to interpret in the sense that measuring trends is much easier than identifying and matching anomalies on separate shiptracks. In a sense, tectonic maps of these areas are already interpretations of the mean fabric trends that have been derived by eye.

2.5.2. Seamount major axis alignment

The mean direction of the seamount major axes is the same at a 95% confidence level as the lineation directions, for both the composite sample and the northern and southern sub-samples. This implies that there might well be some factor that controls the growth direction for seamounts that is connected with the lineation fabric. There are, however, several statistical problems that may lead to this apparent correlation.

If the data from Table 2.1 contains many small seamounts that are actually part of the abyssal hill fabric, then this may bias the mean direction of the samples Σ and Σ' towards the lineation direction, since smaller seamounts are more likely to have been produced at the ridge crest [*Smith and Jordan,* 1988]. In Figure 2.23, I plot seamount height versus major axis azimuth. There seems to be some clustering about the lineation trend of 347° for small sizes of seamount (-013° in Figure 2.23), although the sample number is very small ($N = 63$). Using the Rayleigh test on successively smaller datasets that are limited by an increasing lower height bound, I determined that for seamounts above 500 meters in height, the distribution loses significance, and is essentially random. The calculated mean for the seamount directions is therefore biased by the smallest seamounts.

From Figure 2.24, we can see that the most elongated seamounts are also the smallest, another indication that perhaps the smallest seamounts are in fact abyssal hills that are biasing the mean direction. At an axial ratio of one, for a circular seamount, the entire range of heights is observed. The mean and median of the axial ratio are 0.7, but the distribution cannot be symmetric, since ratios of one are much more likely than ratios of zero. The axial ratio is also

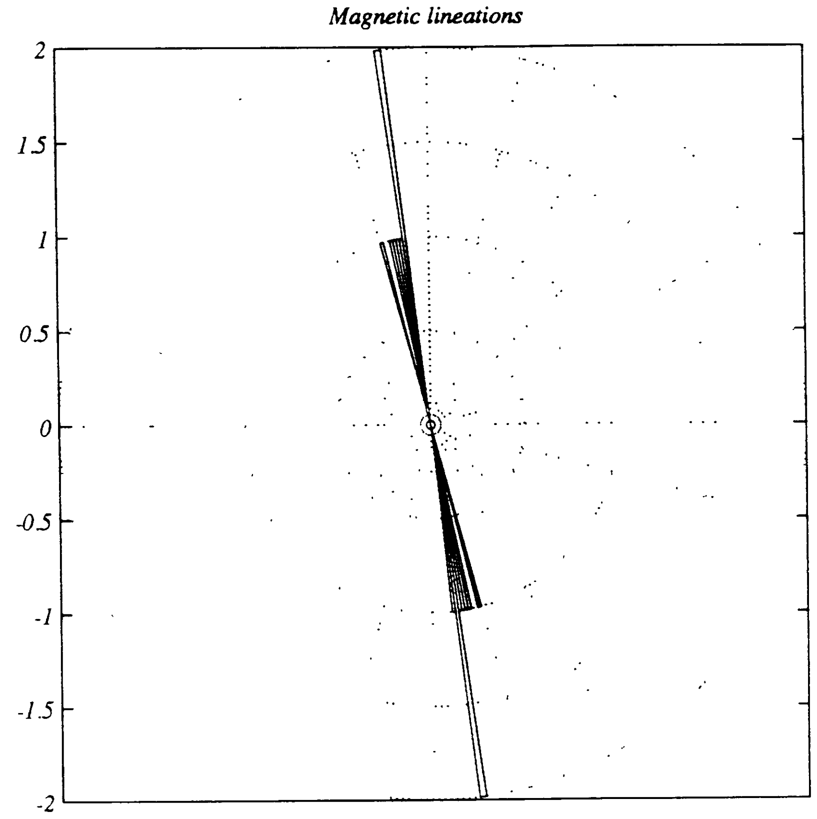

Figure 2.22. Magnetic lineation distribution in the Marquesas Islands area. Measured lineation trends are shown as bars through the origin, with the length of the bar reflecting the number of observations along the trend indicated by the angle of the bar to the vertical, or geographic North (000°). Dotted circles are in units reflected at the side of the box. This distribution has a total count of $N = 7$, and a mean direction of 349°, with a 95% confidence interval of <1°. There is less than a 0.1% chance that this distribution could be observed from a uniform parent distribution.

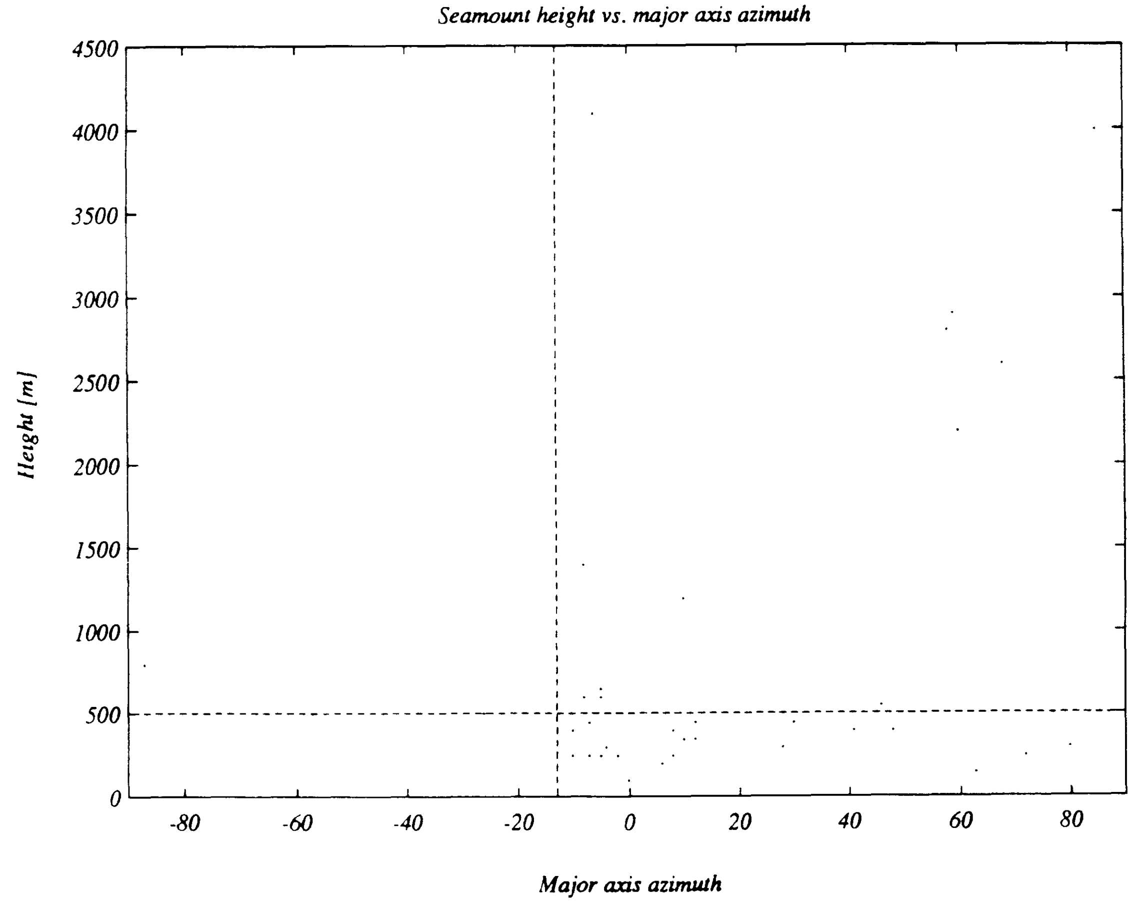

Figure 2.23. Seamount height as a function of major axis azimuth. The azimuth has been rectified to the [-90, 90] interval to approximately center the greatest concentration of points. The vertical dashed line is the mean azimuth of the lineations, while the horizontal dashed line indicates the height at which the sample loses significance. Inclusion of points below this line are necessary for the sample to pass the Rayleigh randomness test, and indicate that the sample direction is biased by the smallest seamounts, which are more likely to be related directly to the tectonic or volcanic processes at the ridge than to the secondary volcanic events associated with hotspot magmatism.

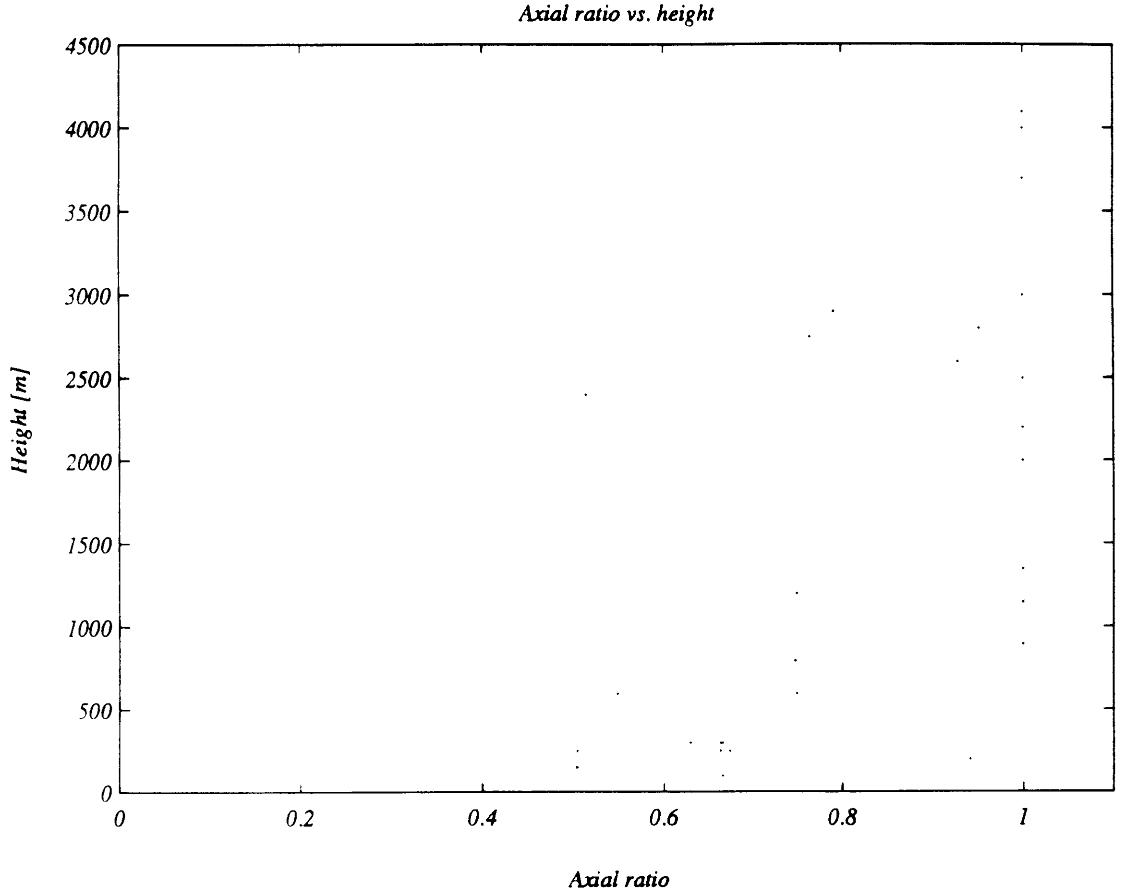

Figure 2.24. Minor to major axial ratio as a function of seamount height. While circular seamounts with axial ratio of one are observed at all heights, only the smallest seamounts are observed to have very low ratios indicating a greater degree of elongation.

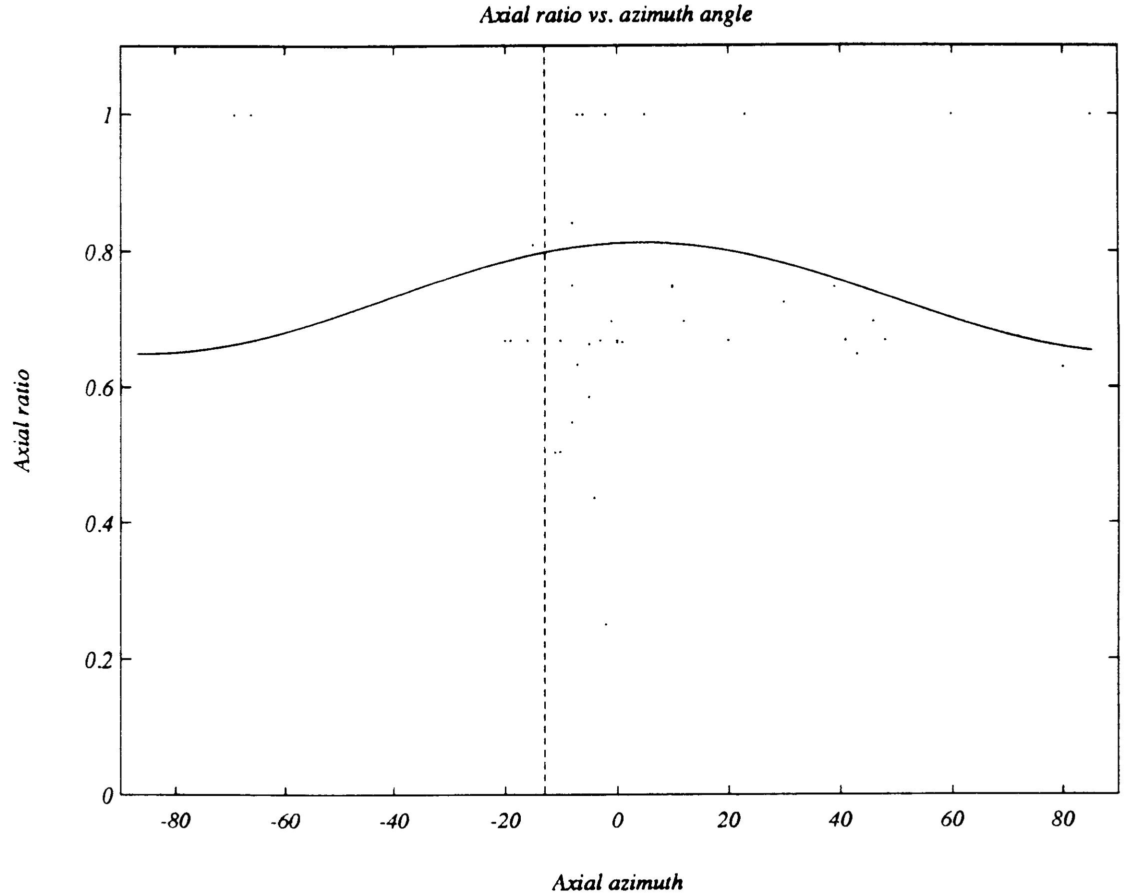

Figure 2.25. Seamount axial length ratio as a function of azimuth angle. The azimuth has been rectified to the [-90, 90] interval to approximately center the greatest concentration of points. The vertical dashed line is the mean azimuth of the lineations, at -013°. Sinusoid represents the best fit of axial ratio to azimuth, however the Nr^2 test determines that there is no statistical evidence in the data of axial ratio depending on the azimuth at the 95% confidence level.

independent of the azimuth, as seen in Figure 2.25. A least squares periodic regression is shown, and I test the correlation for significance using the Nr^2 statistic of Appendix A, calculated for the data at 5.5961. Under the null hypothesis that the two variables are independent, the statistic is distributed for $N > 20$ approximately as χ^2 with two degrees of freedom, and here indicates that the two variables are independent at above the 95% confidence level, since the tabulated value of the critical value P for this value of χ^2, 0.063, exceeds the level of significance, $\alpha = 0.05$.

There would seem to be no evidence that seamounts grow in any direction that is related to the pre-existing fabric of the seafloor. Above a 500 meter height, the distribution of the seamount major axes is essentially random, although the decreasing sample size with seamount height is a statistical problem that can only be solved with a larger dataset.

2.5.3. Dike alignments

The problem of seamount growth mechanisms was addressed by *Fiske and Jackson* [1972] in an attempt to explain the alignment of the major rift zones in the Hawaiian islands. By injecting colored dyes into large gelatin models, they found that in a homogeneous body, dikes will form parallel to the longest axis of the body, reflecting the alignment of the intermediate and maximum stress axes induced by gravity on the body. To map the positions of deeper and older dense dikes in the Hawaiian islands, *Fiske and Jackson* [1972] used Bouguer gravity maps to detect elongations in the shape of the gravity field, and found that the elongations indeed indicated that later dike directions were controlled by the alignments of the major axes of pre-existing edifices. New rift zones formed parallel to the slopes of the preceding shields that they passed through. Even though on a small scale volcanoes are far from homogeneous, the behavior of the rifts indicates that on this scale at least, volcanoes can be considered homogeneous structures.

Since *Fiske and Jackson* [1972] injected their dyes into a *pre-formed*, homogeneous body, a question of order arises: what came first, the rift, or the volcanic edifice? A better posed question might be one concerning control: do rifts control the growth of the edifice, or does the edifice control the direction of the rifts? In order to attempt to answer these questions, we may observe the modes by which a volcano attains its overall shape. There are two major modes of construction: eruptions from the summit, or eruptions from the rift zones. Both these modes are observed on Hawaii, and at least in Kilauea volcano, often alternate, with flank eruptions progressing outwards along the rift zones after central deflation and sometimes the draining of lava lakes in the caldera [*Holcomb,* 1987; *Klein et al.,* 1987]. Eruptions from the rift zones tend to elongate the volcano, while eruptions from the central caldera tend to fill out the volcano, making the shape more regular by mantling areas with steeper gradients. Another major force shaping the volcanoes is the process of mass wasting, in the form of large slumps or debris avalanches, which tend to occur on the oversteepened slopes, contributing to the elongation of the volcano [*Moore et al.,* 1989]. Mass wasting in the Marquesas and Hawaii is discussed further in the following chapter.

If summit eruptions versus flank eruptions and mass wasting are the factors controlling volcano growth, then the shape of the volcano should indicate the predominant process. The historically accepted age progression of the five Hawaiian volcanoes seems to indicate that as volcanoes are built upon successively larger preceding shields, they tend to be more elongate. Kohala and Hualalai are perhaps contemporaneous [*Clague and Dalrymple,* 1987, Appendix 1.1], and developed short, arcuate rift zones. The much larger shield of Mauna Kea was built along three short radial rift zones, and presents a nearly circular plan in topography and in the radial direction of the Laupahoehoe volcanic flow series (see *Peterson and Moore,* 1987, Figure 7.3). Buttressed to the north by the mass of Mauna Kea, Mauna Loa has developed a distinctively 'longer' shape, forming almost 40% of the island's total bulk (subsidence not accounted for) [*Peterson and Moore,* 1987, Table 7.2]. Continued growth of Mauna Loa along the Southwest Rift Zone is attributed to the sealing of the Northeast Rift Zone by the weight of the next volcano, Kilauea [*Holcomb,* 1987]. Kilauea, as the youngest of the subaerial volcanoes, is also the most elongate, formed along two major rift zones that lie against the shields of Mauna Kea and Mauna Loa (see Figure 2.26). From the volumetric data estimated for the historical eruptions of Kilauea, it would seem that the largest volumes are erupted from the central caldera [*Peterson and Moore,* 1987, Table 7.3], but the topographic extent of the volcano along the rift zones contradicts this observation. It is quite possible that the 240 years of eruptive activity and observations during the historical period represent a statistically insignificant portion in the estimated 400,000+ year history of the volcano.

In comparison, the islands of the Marquesas show very little development of rift zones, and the elongate forms of the islands are attributed to catastrophic collapse of the edifices [*Brousse et al.,* 1990]. It should be noted that as far as erosion and planform comparisons, the Marquesas should be compared more strictly with Hawaiian islands of a similar age: Fatu Hiva (1.6 Ma [recalculated data of *Brousse et al.,* 1990]) with the West Maui - East Molokai - Lanai complex (1.4 to 1.6 Ma [*Clague and Dalrymple,* 1987]), and Eiao (5.3 Ma [recalculated data of *Brousse et al.,* 1990]) with Niihau (5.4 Ma [*Clague and Dalrymple,* 1987]), with corresponding islands inbetween.

The age of the lithosphere beneath Hawaii at the time of loading was approximately 80 Ma [*Clague and Dalrymple,* 1987], while beneath the Marquesas the age was approximately 50 Ma [*Kruse,* 1988]. This difference in age allows the volcanoes of the Marquesas chain to subside to a greater extent, an effect constrained by the gravity data of Chapter Four. Because the shields in the Marquesas are submerged, the gravitational stresses induced by the edifices are not as great, and even though the average inter-volcano spacing is less in the Marquesas than Hawaii [*ten Brink,* 1991], each Marquesan volcano has developed in comparative isolation from the stresses imposed by its predecessor, allowing a relatively circular plan to develop for most of the edifices, and inhibiting the development of rift zones.

This lack of preferential orientation for dikes is observed in the data from the SEABEAM swaths. No difference from a randomly distributed set was observed either in the geographic or seamount frame of reference, which is expected if the seamounts develop essentially in isolation from their neighbors, and in the absence of a regional stress field. By comparison

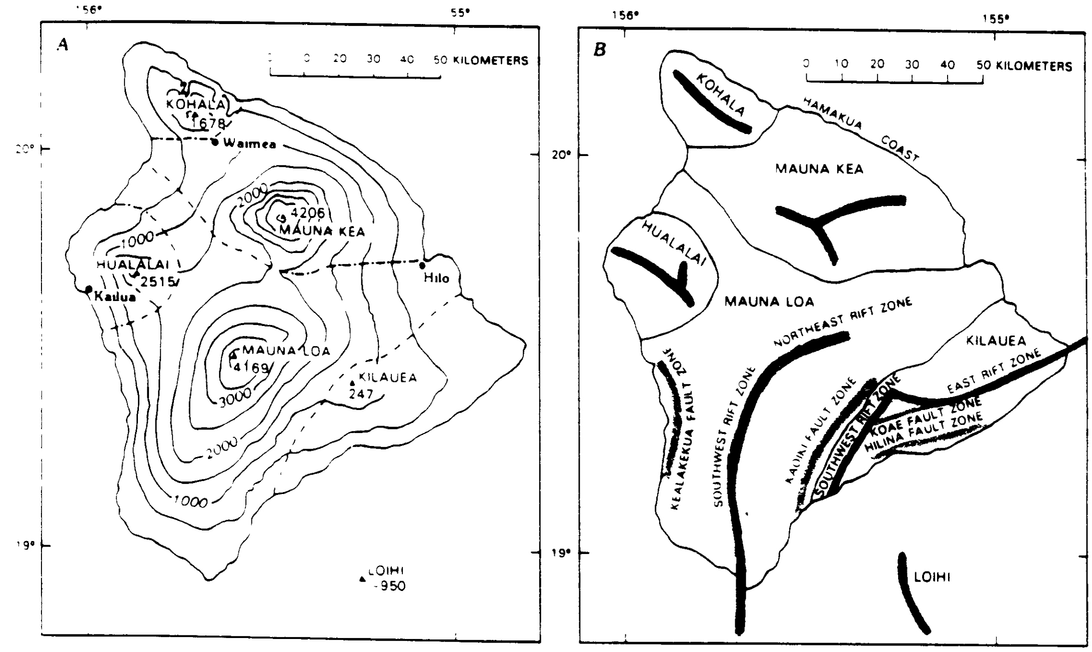

Figure 2.26. The volcanoes and rift zones of the Hawaiian Islands. Rift zones are marked by the thicker lines radiating from the volcanic centers of each island. Figure is from *Peterson and Moore* [1987].

with Hawaii, it appears that the volume that is erupted subaerially will also control not only the size of the volcano, but its grossest morphology. Greater subaerial eruption volumes will create larger gravitational stresses, especially when a portion of the shield itself is emergent, and 'gains' an extra 1000 kg/m^3 of density. The building of large subaerial shields in succession may control the appearance of well-developed rift zones, with a critical subaerial size for the shield lying between the Marquesan and Hawaiian sizes.

A transitional size may be represented by the island of Réunion, in the Indian Ocean. The emergent portion of the island is approximately a 60 by 45 km oval, rising 7 km from a 220 km diameter base from to heights of 2000 m in two peaks: Piton des Neiges, an extinct or quiescent volcano, and Piton de la Fournaise, an active volcano formed on the southeast flank of the Piton des Neiges [*Lénat et Labazuy,* 1990] (see Figure 2.27). From evidence that historical subaerial eruptions along two fairly well defined topographic trends drain the central magma reservoir of Piton de la Fournaise [*Delorme et al.,* 1989], and gravimetric evidence over submarine ridges lying off Piton des Neiges [*Lénat and Labazuy,* 1990], it is reasonable to suppose that these features are analogous to the better developed rift zones of the Hawaiian volcanoes.

To compare Réunion with the Marquesas and Hawaii, I must consider another factor controlling the building of shields: the plate velocity. For very small plate velocities, a small magma production rate will suffice to build a large shield, while for greater velocities, a correspondingly larger rate is necessary for an equal sized shield. If u_0 is the velocity of the plate relative to the hotspot, and ϕ is the magma production rate, then the volume emitted per unit distance, Q, is simply

$$Q=\frac{\phi}{u_0} \qquad (2.1).$$

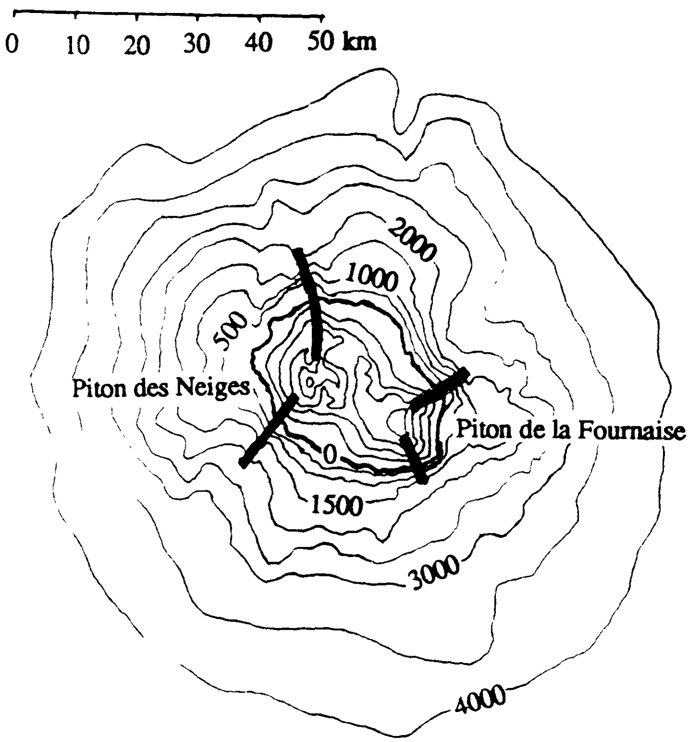

Figure 2.27. Volcanoes and rift zones of Réunion Island, Indian Ocean. The volcano Piton des Neiges is quiescent, while Piton de la Fournaise exhibits continued eruptions. The rift zones shown on land are deduced from the abundance of injected dikes and eruptions from these areas, while the submarine extensions are deduced from gravimetric studies [*Lénat and Labazuy,* 1990].

A little reflection yields the fact that Q is an area, and should correspond to the cross-sectional area of the volcanic material produced by the hotspot, both in the form of material actually erupted, eroded material, and intruded material which never reaches the surface.

For Hawaii, the plate velocity is much the same as at the Marquesas, 10 cm/yr. The magma supply rate for Kilauea is estimated at 0.1 km^3/yr [*Frey et al.,* 1990], yielding a Q of 1×10^9 m^2, which compares well with the 1.2×10^9 m^2 cross-section for Hawaii estimated from multi-channel seismic data [*Watts and ten Brink,* 1989, Fig. 9]. For Réunion, the plate velocity is estimated at 3 cm/yr [*Bonneville et al.,* 1988], and the erupted magma is estimated at 9.5×10^{-3} km^3/yr [*Lénat,* 1987]. Since the eruption rate is a lower bound for the *production* rate, a lower bound on Q for Réunion is 3×10^8 m^2. For the Marquesas, the eruption rate is unknown, but the cross-section Q can be estimated to be 1.8×10^9 m^2 (this is done in Chapter 5), giving a predicted ϕ of 0.18 km^3/yr . If the value for Q at Réunion is similar to that of Hawaii and the Marquesas, the intermediate value of the elastic plate thickness at time of loading, 28±4 km [*Bonneville et al.,* 1988] would agree well with the observed intermediate development of rift zones.

2.5.4. Other concerns

The fact that each seamount used was not sampled in its entirety may be a factor in these results. If there is a bias in the sampling directions of seamounts, then this is directly reflected in the counts for the observed dike azimuths. However, the fact that the dikes are indistinguishably random both in the geographic and seamount axis frame of reference is evidence that the seamounts were well sampled as a group.

2.6. CONCLUSIONS

In this chapter I have determined that the mean direction of the seafloor lineations is, as expected, the same as the direction derived from the magnetic lineations. The seamount major axes seem to be aligned with this direction, but an investigation of the variation of significance of the seamount axis direction with seamount height casts doubt on the idea that there is a correlation between the major axis alignment for the seamounts larger than 500 meters in height and the seafloor lineations. In keeping with this observation, the 'dikes' or radial rifts on the observed seamounts are randomly distributed in the geographic frame. The dikes are also randomly distributed in the local frame of reference for each seamount, indicating that there is little structural effect visible at these scales other than a radial pattern that is not affected by the axial ratio of the seamount. The subaerial eruptive volume produced by the Marquesas hotspot is not significant enough for subsequent volcanos to be constructed high on the flanks of preceding volcanoes, where gravitational stresses begin to control the orientation of dike intrusion and rift zone formation. If there are rift zones, they should be present on volcanoes that are on the flanks of the larger shields, for example on Ua Pou, which lies on the flank of Nuku Hiva, and on Tahuata and Motane, which lie on the flanks of Hiva Oa. In this survey, only Ua Pou was sufficiently sampled, and failed to show any significant rift structures.

The gross geographic trends for Marquesan volcanism are not expressed in the mean directions for the features, unless there is some significance to the tertiary trend falling within the confidence interval of the seamount major axes. However, with seamounts of height less than 500 meters removed, the confidence intervals for this data increase to the maximum 90° value, and no significance can be attached to any particular direction. There is no evidence in the mean directions of either the dike or the seamount major axis alignments that can support a hypothesis that the seafloor is more susceptible to dike intrusions in the direction of the seafloor lineations for structures above 500 meters in height, or that there is a regional stress field that would cause dike eruptions in an orientation different from the abyssal hill fabric.

Whether the change in alignment with size is due to reorientation of the minimum axis of stress with increasing edifice weight is a question not answerable with this data. The features below 500 meters in height may have been produced at the crest or in later events, and without dates for these features, I cannot tell the difference, and so confirm or refute a modified hypothesis that only for later, *small* features is the seafloor fabric alignment significant.

CHAPTER THREE

ISLAND VOLCANISM AND ARCHIPELAGIC APRONS

ποντίον τε κυμάτον ἀνήριθμον γέλασμα
...multitudinous laughter of ocean waves

Aeschylus
Prometheus Bound, 88

3.1. INTRODUCTION

Various early marine researchers noted that while some islands and seamounts are surrounded by seafloor that slopes toward them, others have a slowly deepening, smooth topography that slopes away from them [*Vening Meinesz*, 1948; *Menard and Dietz*, 1951; *Dietz et al.*, 1954]. The Marquesas are among the group that exhibit no surrounding moat, and became the type locale for what *Menard* [1956] termed an 'archipelagic apron'. The apron extends for several hundred kilometers, and buries the abyssal hills completely up to 250 km from the islands. The channeled features in the proximal apron, and the very smooth nature and low slopes of the distal apron were all features that pointed to subaqueous lava flows from fissures and turbidite flows as the origin for the apron [*Menard*, 1956].

Later collection of multi-channel seismic data over the Hawaiian apron has revealed several aspects of that volcanic chain's history. The most prominent aspect of the history is the sheer size of the apron itself: manifested as a thick wedge of sediments that thickens from the peripheral bulge surrounding the islands to the deepest part of the moat, the apron is over 2 km thick off the north flank of Oahu [*ten Brink and Watts,* 1985; *Watts et al.,* 1985; *Watts and ten Brink,* 1989]. If the profile of the apron off Oahu is representative of the whole, the 157

km^2 cross-sectional area [*ten Brink and Watts,* 1985] implies a volume of 279,000 km^3 for the apron in the vicinity of the Hawaiian islands alone. As *Menard* [1956] noted, this volume of sediment cannot be derived solely from pelagic sources, nor solely from the erosion of the sub-aerial portion of the islands as extrapolated from the slope breaks. The apron must include other material, in the from of submarine lava flows and intrusions, or in the form of repeated weathering of a structure that is constantly replenished by volcanic activity.

3.1.1. Mass wasting

Data from submersibles, side-scan and multi-beam sonars, and both single-channel and multi-channel seismic surveys indicates that mass wasting, in the form of large slumps and catastrophic collapses, forms an integral part of a volcanic island's history. While the idea that large faults were present in an island volcano is not new, the faults were invoked primarily to explain the large sea cliffs of Nuuanu Pali on Oahu, East Niihau, the Napali coast of Kauai, and northern Molokai [*Dana,* 1890]. The active faults of the Hilina Pali on the main island were proposed as headwalls of a large landslide carrying the steeper slopes of Kilauea southeastward into the sea [*Stearns and Macdonald,* 1946], a suggestion which was supported by geodetic data that could be explained by the forceful intrusion of magma into the rift zones and the butressing of the Mauna Loa shield to the north [*Swanson et al.,* 1976a]. There have been two modes suggested for the displacement of the south flank of Kilauea: dike injections directly into faults, as observed in the Koae fault system, and the simple scarp failures of the Hilina fault system [*Duffield et al.,* 1982]. The displacement from the injections is estimated as 4 m in the S20°E direction during the 20th century [*Swanson et al.,* 1976a], while the November 29th 1975 magnitude 7.2 earthquake on Kilauea's south flank alone had displacements up to 3.5 m vertically and 8 m horizontally over tens of kilometers along the Hilina fault system [*Tilling et al.,* 1976]. The hypocenter of the foreshock was at a depth of 10 km, indicating the probable depth of the sole [*Lipman et al,* 1985]. Both of these modes belong to what is now recognized as a slumping process that takes place on extremely large scales and over long periods of time. These movements are large, wide (100 km), thick (10 km), and are characterized by transverse blocky ridges and steep toes [*Moore et al.,* 1989]. This morphology has been observed in the Waianae slump off southwestern Oahu, the Hana slump off northeastern Maui, and the Hilina slump itself off Hawaii [*Moore et al.,* 1989].

There is also a large body of evidence that supports suggestions of fast, catastrophic collapses of various sizes, ranging from the small sand-rubble flow of Papa'u (39 km^3) [*Fornari et al.,* 1979] to the giant slides of Nuuanu and Wailau off Oahu and Molokai, with estimated volumes of 5,000 and 1,000 km^3 respectively [*Moore et al.,* 1989], and the Alika and Ka Lae avalanches off the southwest flank of Mauna Loa, also with estimated volumes of 5,000 km^3 [*Lipman et al.,* 1988]. These features are characterized by well defined amphitheaters, thin deposits (0.05 to 2 km), and hummocky distal ends extending up to 230 km from the headwall. The presence of contemporaneous tsunami deposits on neighboring Lanai [*Lipman et al.,* 1988; *Moore and Moore,* 1984] indicates that these enormous slides occur within seconds to minutes, producing catastrophic damage. Examples of these fast debris avalanches abound, and are also found in combination with the slow, slumping type, where local oversteepening of a fault block causes a sudden collapse, as in the debris toe of the Waianae slump off southern Oahu [*Moore et al.,* 1989]. Recent surveys off the east coast of Réunion Island in the Indian Ocean suggest that the Grand-Brûlé scar is in fact the subaerial part of an avalanche amphitheater that created the large plateau of deposits offshore [*Lénat and Labazuy*, 1990] (see also Figure 2.27).

From observations of Loihi seamount off Hawaii, it is clear that this mass wasting process begins early in a volcano's history. This seamount is just beginning to erupt the characteristic tholeiitic magmas of the main shield building phase [*Frey and Clague,* 1983], and already over half its surface has been modified by avalanche scars [*Malahoff,* 1987; *Fornari et al.,* 1988]. Slope failures continue throughout the main shield building stage, as evidenced by the presence of post-failure benches that indicate subsequent eruptions and subsidence of the edifice [*Moore* *et al.*, 1989]. Failures probably continue well into the erosional stage, since the pelagic sediment cover over the older slides of Kauai and Niihau is extremely thin [*Moore et al.*, 1989]. In terms of volume, slope failures during the 'erosional' stage remove more material from the edifice than simple subaerial and subaqueous erosional processes.

While from the observations of Loihi it is apparent that mass wasting is occurring before a volcano reaches the surface, there are several reasons to believe that the process is accelerated when the volcano emerges from the sea. The most dramatic of these is of course the difference in density contrast between submarine and subaerial lavas, which affects not only the state of stress in the edifice as a whole, but the progress of a lava flow downhill: not only does a lava flow lose 1,000 kg/m^3 of density contrast and driving force, but it is also quenched upon reaching the water. The reduced flow rate and the quenching at the shore lead to the production of steep rims that are recognizable in the bathymetry off Hawaii and Réunion, and are presumably the source for many of the initial slope failures [*Fornari et al.*, 1979; *Lénat and Labazuy*, 1990]. It is reasonable to assume that the major portion of the landslides will occur during the peak of lava production, and that the major contribution of avalanche debris to the moat sediments will also occur during this period.

3.1.2. Subsidence, mass wasting, and the sediments of the apron

While debris avalanches are filling the moat, another process is deepening the moat. Slow subsidence of the islands occurs as the increasing weight of the volcanic pile causes relaxation of the lower plate through ductile flow [*Goetze and Evans*, 1979; *Bodine et al.*, 1981]. Subsidence of the islands over timescales of 10^4 to 10^5 years causes the surrounding flexural bulge and moat to migrate inwards, while the ongoing process of mass wasting serves to distribute the weight of the volcanoes over a greater area, and so to broaden the flexural moat around the chain. The position of the moat and bulge is then the result of two competing processes: subsidence and mass-wasting [*Moore et al.*, 1989; *Rees et al.*, 1991]. During the deposition of the majority of the moat sediments, this process should be expressed as an onlapping sequence towards the flexural bulge, while during the later stages when mass wasting is not as voluminous, an offlapping sequence develops as subsidence begins to dominate [*ten Brink and Watts,* 1985; *Moore et al.,* 1989; *Watts and ten Brink,* 1989; *Rees et al.,* 1991].

Using multi-channel seismic reflection data, *Rees et al.* [1991] have defined four units observable in the sediments of the northern Hawaiian apron. The basal unit is of uniform thickness, and drapes over the highly reflective basement, and is interpreted as the pelagic sediments that predate Hawaiian volcanism. The second, and thickest unit, is an onlapping wedge with layers that are acoustically chaotic. *Rees et al.* [1991] interpret these layers as debris avalanche material. A third unit is composed of highly coherent and continuous offlapping reflectors interpreted as turbidite flows that occur late in the sequence. A very thin unit of ponded sediments in the deeps of the moat makes up the final unit of the sequence around Hawaii.

Since the processes of mass wasting and subsidence are expected to occur in the Marquesas as well as in Hawaii, there should be some evidence of large slumps or debris avalanches in the Marquesas, as well as features similar to the previously described units in the sediment sections of the surrounding moat. The *Crossgrain 2* expedition collected three usable forms of seismic data: single channel reflection profiles using an 80 cubic inch water gun as a source, refraction data collected using sonobuoys and a 550 cubic inch air gun source, and the SEABEAM data described in Chapter 2. The data from the 3.5 kHz profiler was not considered due to its generally poor quality. I have used the single channel data to identify seismically similar areas, and to delineate the extent of the volcanic flows and the archipelagic apron. The sonobuoy data is used to constrain the velocities and thickness of the sediment layer, although the records are of variable quality due to the limited size of the air gun.

3.2. REFRACTION LINES

Nine of thirteen sonobuoys launched had useable signals. The use of a single air gun as a source made the recordings very noisy. The results are summarized in Table 3.1, and the locations of the launches are indicated on Figure 3.1. Sonobuoys 0 and 1 were launched on line 1, sonobuoys 2 through 10 on line 2, while sonobuoys 11 and 12 were launched to the northwest of the islands, on line 3. Sonobuoys 4 and 8 provide a direct and reversed profile. Sonobuoys 0, 5, 6, and 7 failed to transmit any signals, and I therefore omit them. Clear refracted arrivals were received only on sonobuoys 4, 10, 11, and 12. I assign four qualities to the traces on the records, with 'a' being a well defined trace, 'b' a medium trace, 'c' a poor trace, and 'd' a tentative identification of a very weak signal, or a trace close to the sampling grain of the record.

The grain arises from the sampling interval of the signal, 0.025 sec, and the sweep width of the recorder. These two factors combine to give the record from the sonobuoy a 'grain' that lines up when viewed from appropriate directions. I calculate only the first order (1:1) diagonal grain, since this grain falls closest to possible slopes from refracted arrivals. Poor and tentative quality arrivals that fall close to this value may well be artifacts.

I calculate all depths and velocities using a water velocity V_1 of 1495±5 m/s, and use the direct arrival to deduce a reference zero time and distance, since the start time for the recording is unknown. I compare the depths derived from the first reflected arrivals with the depths from the single channel reflection profiles and the center beam of SEABEAM for consistency, and I have corrected all numbers for the depth of the hydrophone, 150±10 meters, and for the dip of the interfaces, where the dip could be observed. Columns from the single channel profiles generally consist of a thin, acoustically transparent layer overlying a well stratified set of sediments, and in some areas a deeper basement is detected.

Preliminary interpretation of the sonobuoy data was done by Michel Diament while onboard the *Washington*. I have taken the original records and used them to identify new refracted arrivals and to recalibrate all previous measurements and estimates. All calculations

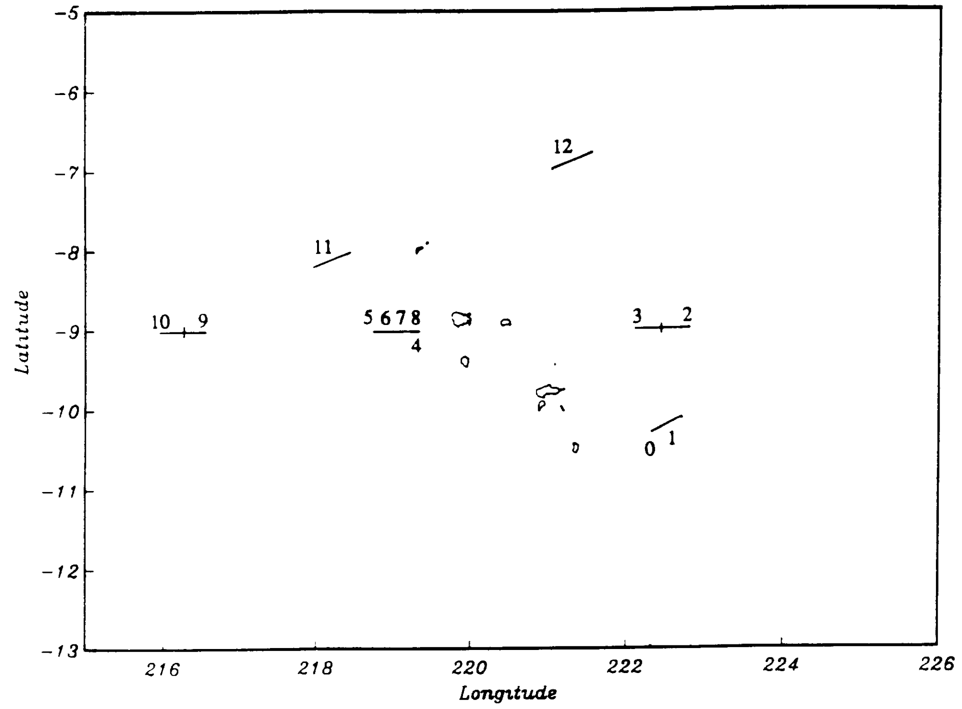

Figure 3.1. Locations of the refraction lines. Numbers correspond to the entries in Table 3.1. Sonobuoys 0, 5, 6, and 7 either showed no arrivals or were defective. Sonobuoys 4 and 8 were run on direct and reversed profiles respectively.

TABLE 3.1. Sonobuoy results

Sonobuoy number	ϕ † (deg)	SEABEAM‡ depth (m)	SC Reflection◊ depth (m)	h_1 (m)	V_{alias}¤ (m/s)	V_2 (m/s)	V_3 (m/s)	h_2 (m)
1	-1.0±0.4°			3730±40	1.68	-	5.1±0.2^{c}	-
2	0	4200^{+}	4200	4190±20	-	-	9.4±0.3^{d}	-
3	0	4200^{+}	4190	4180±20	3.33	2.6±0.1^{c}	13.4±0.6^{d}	-
						3.9±0.1^{c}		
4	+1.0°			3880±60	3.40	3.1±0.1^{c}	6.1±0.2^{a}	1350±60
8	-0.3°			3720±20	1.67	2.7±0.1^{c}	6.2±0.9^{d}	2980±280
4 & 8	-			3880±60	3.40	3.2±0.2	6.1±0.5	
9	-0.2°	4775	4765	4780±80	1.54	2.7±0.1^{c}	5.8±0.2^{b}	260±40
10	+0.2±0.6°	4825	4807	4840±20	1.65	3.1±0.1^{d}	6.0±0.1^{a}	770±50
11	0	4300	4326	4350±20	3.35	2.6±0.1^{b}	5.6±0.3^{a}	960±100
12	0	4100	4165	4190±20	3.49	3.7±0.1^{b}	6.4±0.1^{a}	990±20

†: slope of the seafloor; ‡: center beam depth; ◊: Single-channel reflection depth; ¤: Aliasing velocity from sampling frequency; a b c d: high, medium, poor, and tentative quality refraction traces respectively.

are made using the simplest of assumptions: there are no velocity gradients in the layers, and no low velocity zones. The first assumption is obviously incorrect for the sediments, but the absence of any detectable concavity in the refracted arrival traces indicates that any compaction, and therefore velocity gradient, in the sediments is either small or occurs at a shallow depth. The second assumption is valid because low velocity zones do not usually occur within the depths that were penetrated, and there are also no discontinuities in the traces. The thickness and velocity of the first layer is calculated from the simply derived formula:

$$h_1 = \frac{1}{2} T_R V_1 \tag{3.1}$$

where h_1 is the water depth, T_R is the vertical two-way travel time, and V_1 is the velocity of sound in water, as above. The reciprocal slope of the first refracted arrival gives the velocity of the second layer, V_2, which can be checked with

$$V_2 = \frac{T_R V_1}{\sqrt{T_R^2 - \tau_2^2}} \tag{3.2}$$

where τ_2 is the zero-time intercept of the first refracted trace, or simply the vertical two-way travel time. The velocity of the third layer, V_3, is estimated again from the slope of the second refracted arrival trace, and is used to estimate the thickness of the second layer with

$$h_2 = \frac{V_2 V_3}{2\sqrt{V_3^2 - V_2^2}} \left(\tau_3 - \frac{2h_1}{V_1 V_3} \sqrt{V_3^2 - V_1^2} \right) \tag{3.3}$$

where τ_3 is the zero-time intercept of the second refracted trace. No records showed more than two refracted arrival traces. Errors are propagated with standard formulæ.

For sonobuoys 4 and 8, which are direct and reversed profiles over a sloping surface, I may use the formula

$$V = 2 \cos \varphi \frac{V_d V_r}{V_d + V_r} \tag{3.4}$$

where V is the seismic velocity of the layer under consideration, and where V_d and V_r are the uncorrected velocities calculated for the direct and reversed profiles, and φ is the observed slope angle.

3.2.1. Sonobuoy record interpretation

Sonobuoy 1 was deployed about 100 km east of Fatu Hiva, over the irregular downward 1° slope of feature number 81 of Chapter 2 from the depth of 3775 m to 4000 m. The slope has 50 m undulations that are covered with a thin (0.01 s) layer of transparent sediment that showed one reflector over the basement. One poor refracted arrival yields a velocity V_3 of 5.1 km/s, rather high for basement, considering the values of 4.37 km/s and 4.65 km/s found for the Society and Tuamotu island basements respectively [*Talandier and Okal,* 1987]. Since no refracted arrival was observed for the sediments, I cannot calculate the depth h_2 of the sediment layer, but after assuming the average velocity for the sediments from all other traces, 3.1 km/s, I estimate the layer to be less than 20 m thick.

Sonobuoy 2, launched over the eastern apron just after feature 97 of Chapter 2, shows a tentative refraction, but the calculated velocity is 9.4 km/s so the trace is clearly spurious. The single channel profile shows a very even sediment layer, with only 5 m undulations of a highly reverberative top layer. The 4190 m depth derived from the first reflected arrival agrees well with the 4200 m from SEABEAM and the single channel profile.

Sonobuoy 3, launched immediately after sonobuoy number 2 about 200 km east of Ua Huka, shows three refracted arrivals: two poor signals and one tentative trace. Possible velocities for the sedimentary layer are 3.9 and 2.6 km/s. The third trace yields a velocity of 13.4 km/s, again a spurious result, precluding the calculation of the thickness of the sedimentary layer. The single-channel profile shows a surface slightly more irregular than number 2, with 10 m hummocks of roughly circular appearance in the SEABEAM swath.

Sonobuoy 4 was launched on the west flank of Nuku Hiva while the *Washington* backtracked to cover a gap in the gravity record, over a slope of approximately 1 degree. The reflection profile shows a surface that is composed of 20 to 50 m hillocks with various ponds of more well defined reflectors. The sonobuoy record and its interpretation are shown in Figure 3.2. A poor refracted arrival gives a velocity of 3.1 km/s for the sediments, and a good arrival yields a velocity of 6.1 km/s for the basement. The depth of the sediment layer here is 1350±60 m, just on the outer edge of the main volcanic edifice, seaward of feature 101 from Chapter 2.

Sonobuoy 8 provides a reverse profile 3.3 km north of number 4, and about 100 km west of Nuku Hiva. The seafloor is slightly smoother than for sonobuoy 4, with relief of 20 m on a slope of 0.3 degrees. The reflection profile shows reverberative layer overlying 0.03 to 0.04 s of transparent sediments, and a fairly clear basement layer. The refractions give velocities of 2.7 and 6.2 km/s for the sediment layer and basement, both from poor traces which yield a depth of 2980 m for the sediments, suspiciously high, especially when compared with the lower figure only 3.3 km to the south from sonobuoy 4. The combined profile of numbers 4 and 8 yields velocities of 3.2 and 6.1 km/s.

Sonobuoy 9 was launched 350 km west of Fatu Hiva over abyssal hill sediments that show three well defined reflectors on the single channel profile. The area corresponds to feature 112 from Chapter 2. Velocities derived from the poor and medium traces are 2.7 and 5.8 km/s respectively, yielding a sediment depth of 260 meters. There is no evidence of the transparent layer, although it is fairly clear on the reflection profile.

Sonobuoy 10, illustrated in Figure 3.3, was launched immediately after sonobuoy number 9, over slightly more irregular terrain. The refracted arrivals yield velocities of 3.1 and 6.0 km/s and a sediment thickness of 770 meters. The first refracted arrival is a tentative identification of a very faint trace.

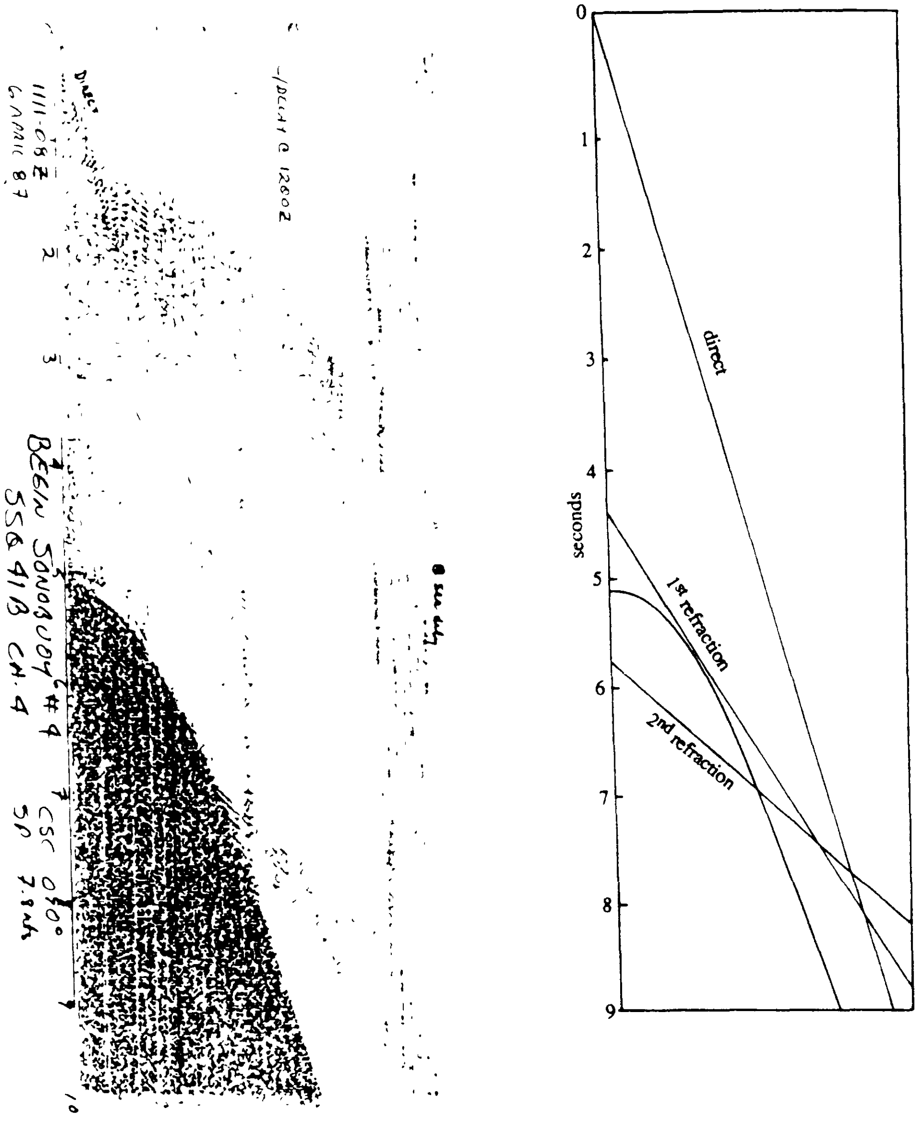

Figure 3.2. Sonobuoy record number 4 and interpretation. Long diagonal is the direct arrival, hyperbola is the single reflection arrival, and the intersecting diagonals are the first and second refracted arrivals. The first refracted arrival is only evident as it grazes the hyperbola.

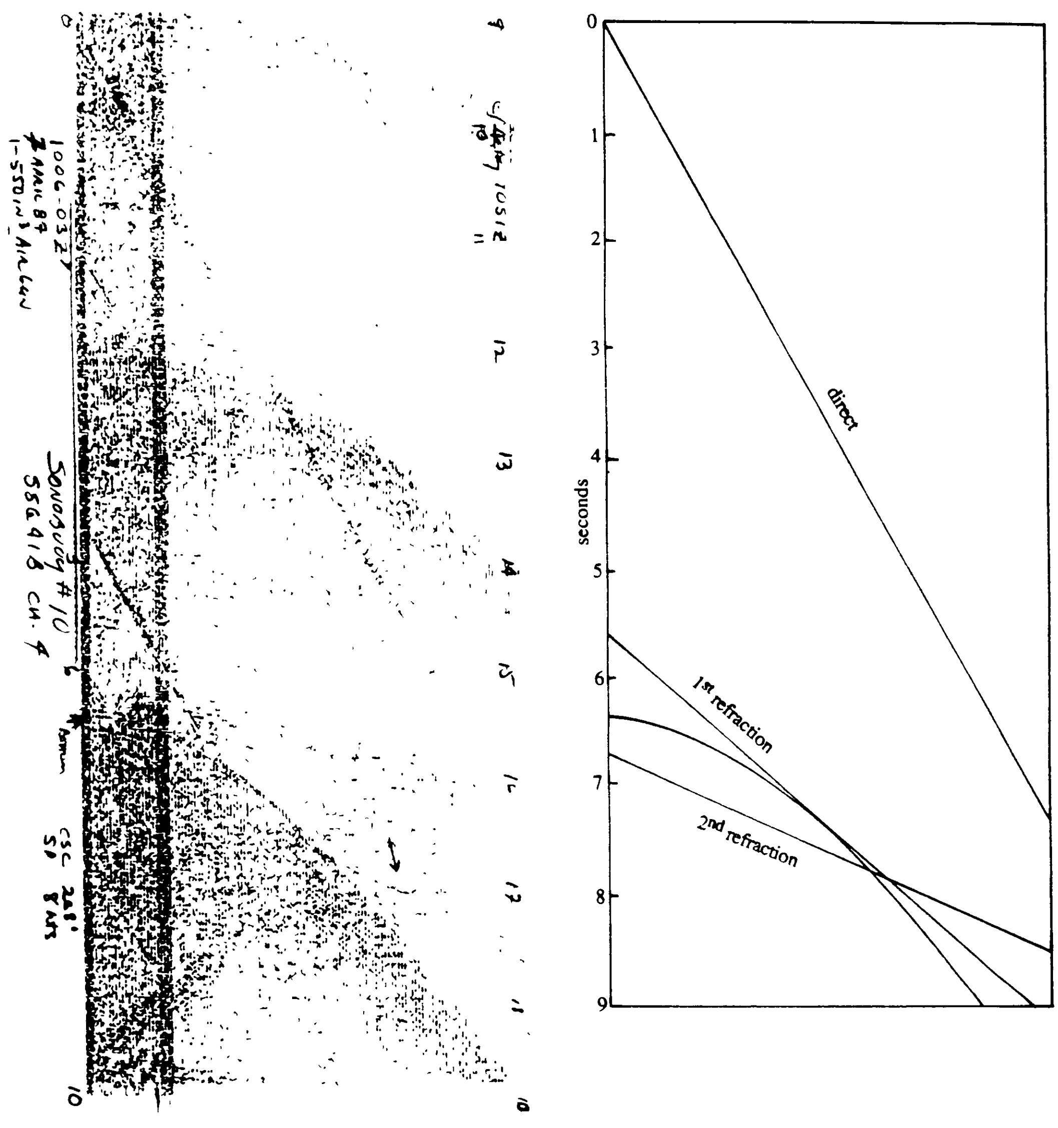

Figure 3.3. Sonobuoy record number 10 and interpretation. Long diagonal is the direct arrival, hyperbola is the single reflection arrival, and the intersecting diagonals are the first and second refracted arrivals. The first refracted arrival is only evident as a very faint trace just above the second refracted arrivals.

Sonobuoy 11 was launched 100 km west of Eiao, over level sediments that show several clear reflectors. Refracted arrivals of medium and good quality are present for two layers, giving velocities of 2.6 and 5.6 km/s, which yield a sediment thickness of 960 meters.

The final sonobuoy, number 12, was launched 160 km north-east of Banc Jean Goguel over a level surface that progresses into an irregular slope. Well defined layers are discernible in the reflection profile, and the refracted arrivals are both fair, yielding velocities of 3.7 and 6.4 km/s, and a sediment thickness of 990 meters.

From the meager sonobuoy results, I may tentatively state that pelagic sedimentation in the area has been responsible for at least 260 m of the sediment cover. Up to 1.5 km of consolidated sediments with velocities in the 3.1 km/s range form the bulk of the apron, and are probably composed of volcaniclastic and avalanche debris, ash fall, and turbidites. These sediments overlie basement with velocities in the 5.9 km/s range.

3.3. REFLECTION PROFILES

The single channel profiles from *Crossgrain* 2 show features observed by the *Capricorn* and *Mid-Pacific* expeditions [*Capricorn*, 1953; *Menard*, 1956], which is not surprising, since the shiptracks from all three expeditions nearly coincide along the eastern portion of line 2 and along the inbound leg of *Crossgrain 2*. I have divided the profiles up into areas of similar morphology and seismic character, and compiled the data into a schematic map, shown as Figure 3.4.

3.3.1. Abyssal hills and pelagic sediment cover

Abyssal hills are present throughout the deepest sections of the survey with several 100 meters of relief and 2 to 3 km spacing, and are capped by fairly transparent sediments up to 0.3 seconds thick. Figure 3.5 shows the abyssal hills from the eastern part of line 2, which correspond to feature number 92 of Chapter 2. The average depth for this set of hills is 4500 m, and the hills themselves have a mean height of 100 m. The sediment cover here consists of a nearly completely transparent cover, probably up to 0.01 s thick, interpreted as ten meters of pelagic ooze, underlain by denser and more reflective sediment layer up to 75 m thick.

3.3.2. Sediment ponds and apron turbidites

The first evidence of acoustically opaque apron turbidites appears at about 300 km distance from the islands, in the sediment ponds formed in the basins between abyssal hills. Figure 3.6 illustrates the sediment ponds, which in comparison to the abyssal hills of Figure 3.5, have clear areas of smooth sediment cover that buries the lower relief. The extent of the sediment ponds around the islands is indicated in Figure 3.4. The continuous apron, illustrated in Figure 3.7, appears to be dammed by uplifted abyssal hills at about 250 km distance from the islands. The smooth apron is composed of long continuous reflectors that lie fairly evenly on the ocean floor, with only the summits of a few abyssal hills rising steeply from an otherwise undisturbed plain. The apron is generally composed of three identifiable units: U_1, a thin transparent unit sometimes composed of a single layer, U_2, a highly reflective, continuous unit, and U_3, a unit which in some segments of the apron may exhibit offlapping (see Figure 3.8). The third unit is also characterized by internal chaotic layers similar to those found by *Rees et al.* [1991] in their 'Debris Flow Unit'. Unfortunately, the seismic penetration is insufficient to determine the character of any units below the third. The greatest thickness reached by the apron is unresolved, although from similar environments in Bermuda, Hawaii, and Bikini [*Officer et al.,* 1952; *Raitt*, 1952; *Gaskell,* 1954; *ten Brink and Watts*, 1985] and calculations outlined in Chapter 4, the apron thickness is estimated to be 2 km or more. The maximum areal extent of the apron is shown in Figure 3.4.

3.3.3. Inter-island sediments

Figures 3.9, 3.10, and 3.11 illustrate the thick sediments that are present between the islands. These thick sediment packages are present off Ua Pou, Hiva Oa, and along the ridge

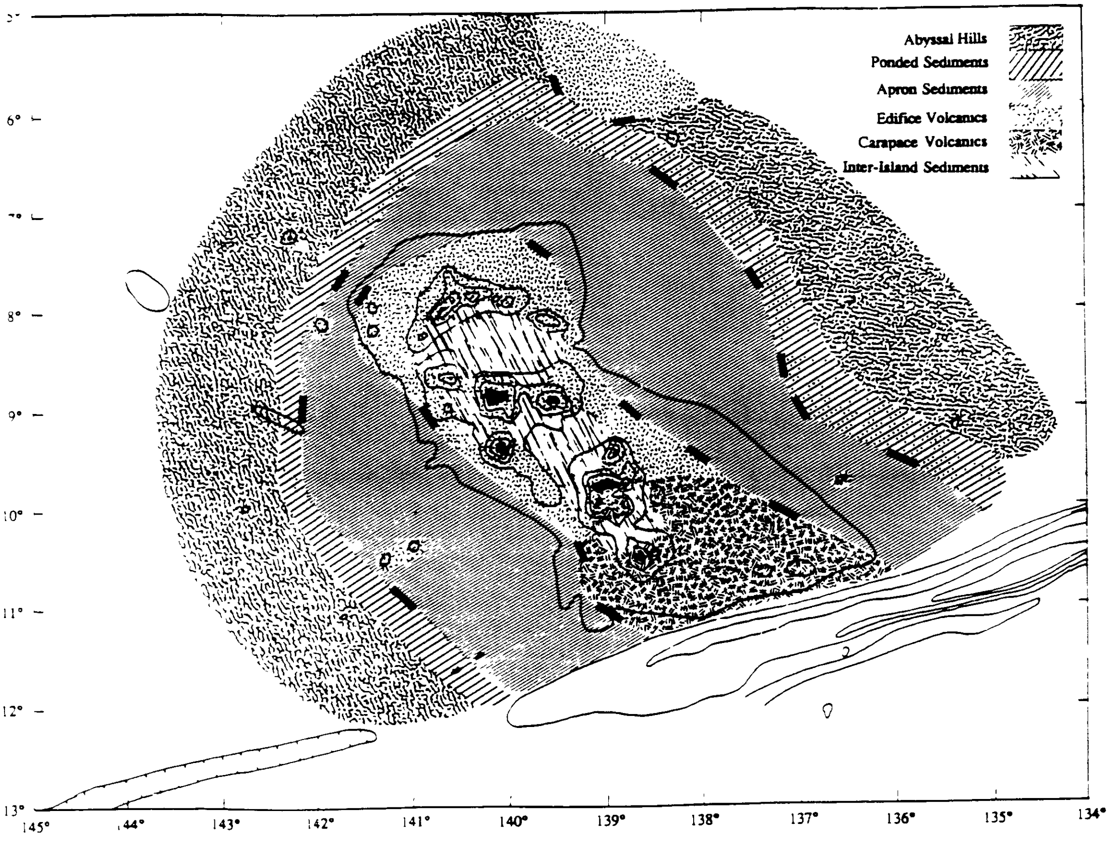

Figure 3.4. Schematic map of the sediment cover in the Marquesas area. Various types of seafloor are indicated: abyssal hills, ponded sediments, apron sediments, inter-island sediments, edifice volcanics, and carapace volcanics. Dark lines indicate positions where the boundary between sediments and volcanics has been observed, omitting the observed boundaries in the central area and small features for clarity. Boundaries in all other areas are hypothetical. The edifice and carapace volcanics differ only in the general slope and the presence of many small cones, with the boundary between the two being entirely artificial: there is a progression from one type to the other. Inter-island sediments are likewise highly generalized, indicating only the major basins between the islands. Observed boundaries not on the *Washington* shiptrack are from the R/V *Ewing* cruise EW9103 [*McNutt and Mutter,* 1991]. Contours interval is 1000 m, and the islands are indicated in black.

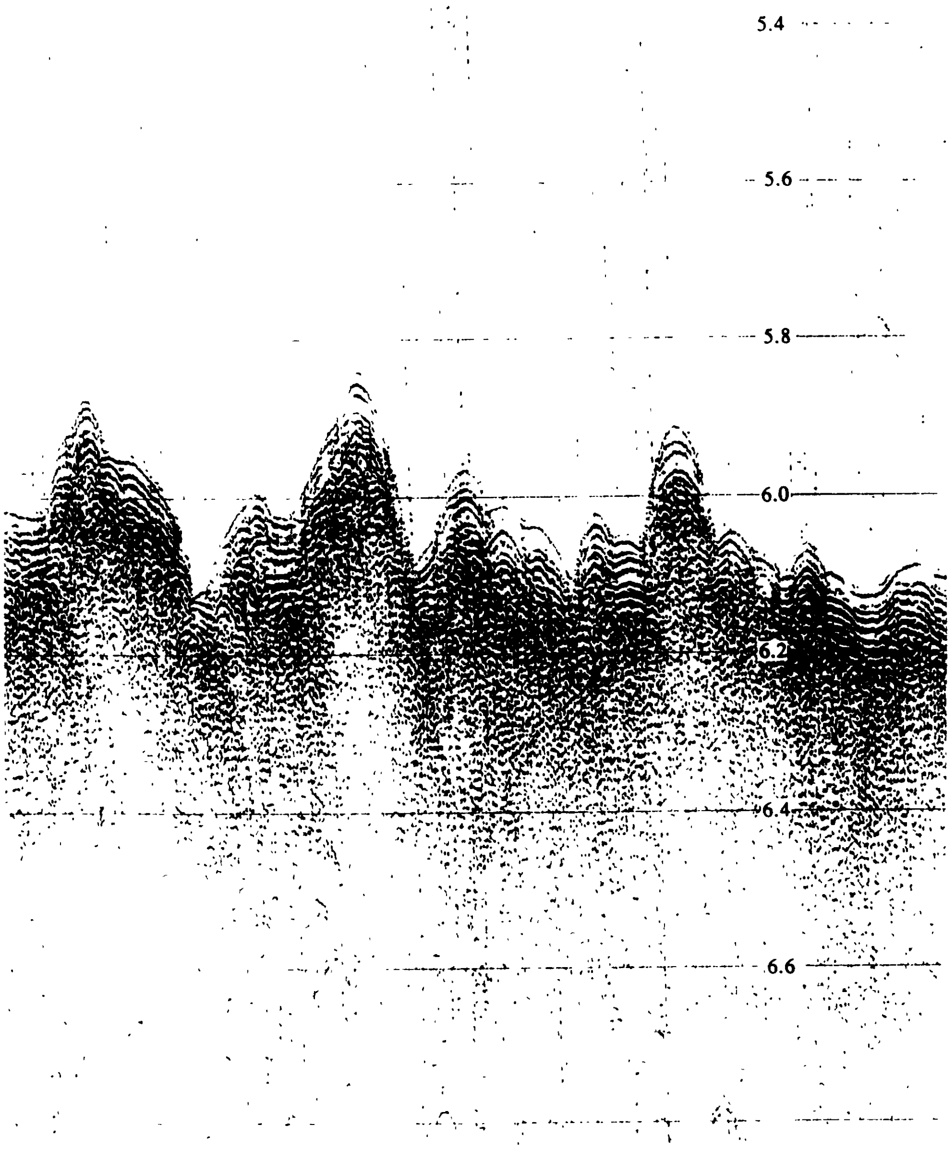

Figure 3.5. Single channel seismic profile of abyssal hills and pelagic sediment cover at 9°07'S, 135°10'W, feature 92 of Chapter 2. Average depth of hills is 4650 m, average height is 75 m. Sediment cover is a thin transparent layer overlying a more reverberative layer of total thickness 150 meters. Numbers on horizontal lines are seconds of two-way travel time.

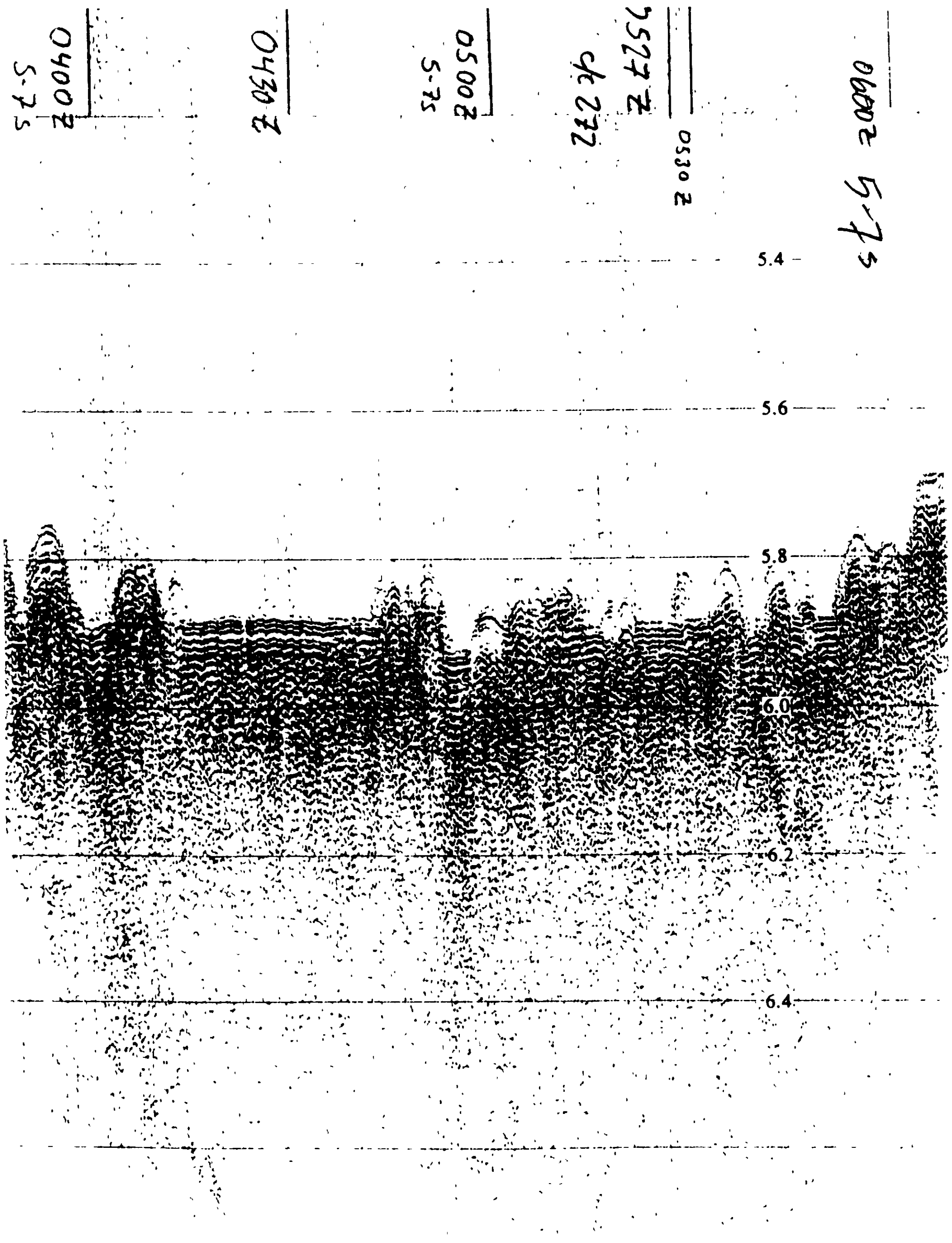

Figure 3.6. Single channel seismic profile over sediment ponds formed in abyssal hill basins. The sediments are acoustically similar to the sediments of the apron (see Figure 3.7), with a very thin transparent cover overlying a highly reverberative layer, and extend to an average distance of 300 km from the islands. Numbers on horizontal lines are seconds of two-way travel time. Handwritten notations are the time marks and comments from the watchstanders during the cruise itself.

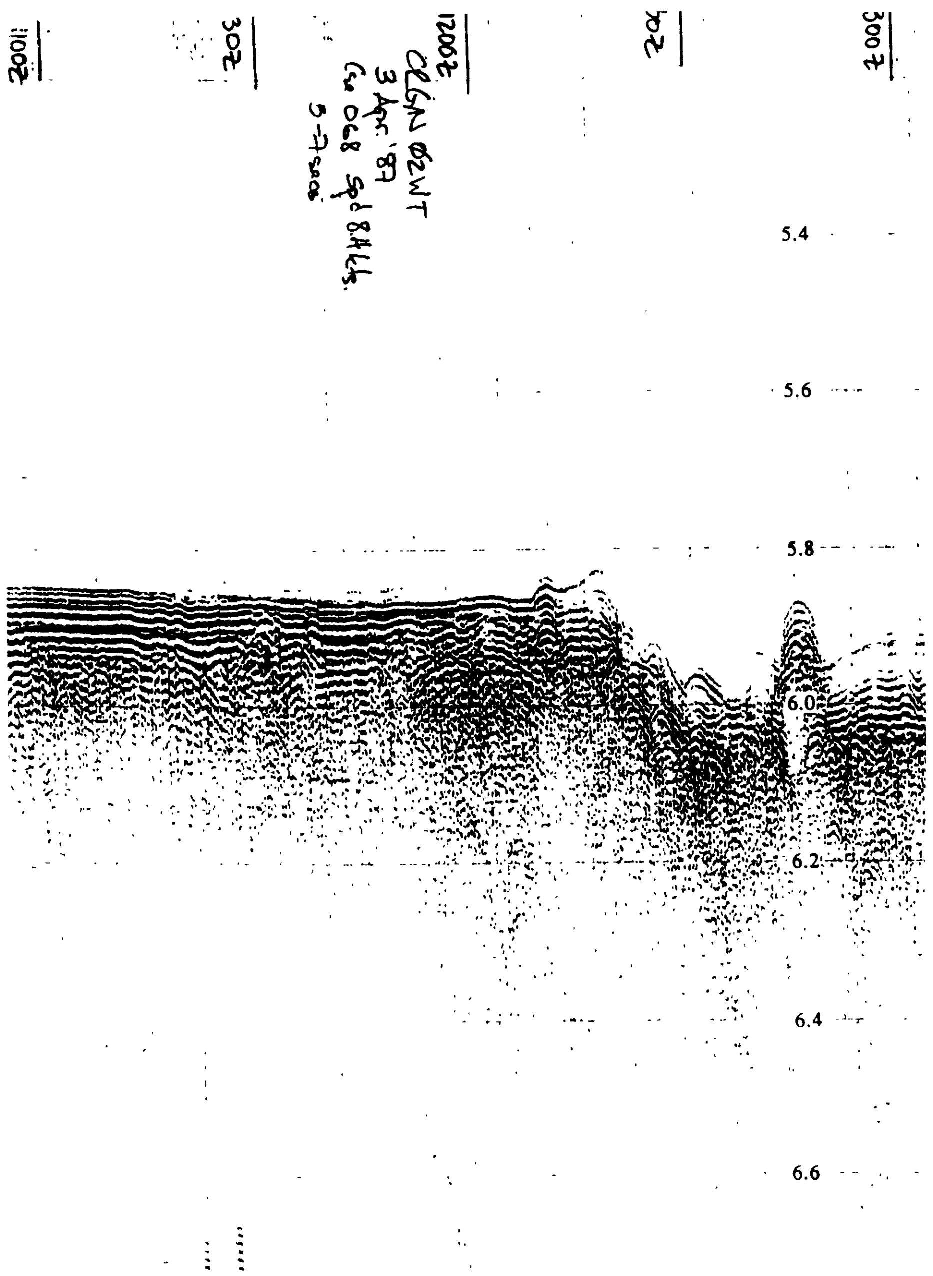

Figure 3.7. Single channel seismic profile over the archipelagic apron and turbidite dam on the eastern side of the Marquesas Islands. Turbidite flows from the islands are dammed by the uplifted abyssal hills on the flexural bulge created by the load of the islands, at an average distance from the islands of 250 km. Numbers on horizontal lines are seconds of two-way travel time. Handwritten notations are the time marks and comments from the watchstanders during the cruise itself.

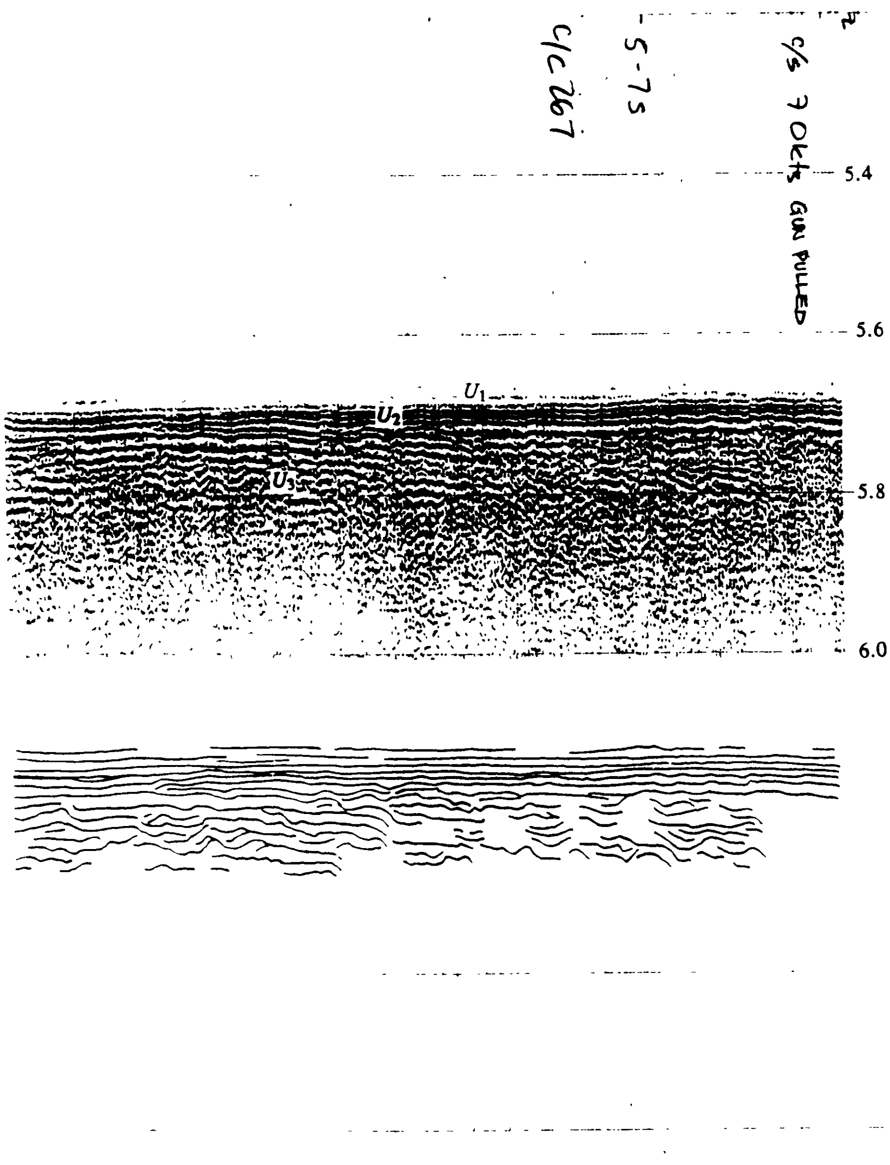

Figure 3.8. Three seismic units in the apron off the east flank of Fatu Huku. The first unit, U_1, is very thin and acoustically transparent, barely visible on the record. The second unit, U_2, is highly reflective and appears throughout the apron and ponded sediments. The third unit, U_3, displays some offlapping (visible here), although this is not widespread. There are also chaotic reflectors in this unit that may indicate an avalanche as the origin of the deposit. Numbers on horizontal lines are seconds of two-way travel time. Handwritten notations are the time marks and comments from the watchstanders during the cruise itself.

to the southeast of Ua Pou, and presumably between the other major structures. The recovery of a gravity core with foraminiferal sand off Ua Pou from the sediments in Figure 3.10 showed that at least the shallowest unit is calcareous. The fact that these islands are in a highly productive tropical zone suggests that there may be a large contribution to the sediment column from calcareous turbidite flows originating on the steeper flanks of the islands [*Natland and McNutt,* 1987]. The presence of the highly reflective unit U_2 is visible in Figure 3.9, and while there is no offlapping visible in U_3, there are clearly visible chaotic cores. In contrast, the layering visible in Figure 3.10 is extremely regular, and indicates that this area has not been subject to the largest debris flows that deposit acoustically chaotic layers. Figure 3.11 represents the section to the south of Motu One, in a particularly large sediment package. The three different units are clearly visible, with U_1 and U_2 overlying a thick section of unit U_3 that exhibits no offlapping but a fair amount of chaotic cores and disturbed sections.

The large thickness of the columns (>0.2 sec) compared to the apron can be attributed to the geometry of the islands: amphitheaters for avalanches surround the sites, whereas the apron only has amphitheaters feeding the debris from one direction, yielding less sediment input. This is geometry is particularly relevant for the section in Figure 3.11.

3.3.4. Volcanic carapace

Suggesting two possible sequences of development for archipelagic aprons, *Menard* [1956] observed that only one of the two sequences had been observed (see his Fig. 7). His sequence A-B_1-C_1-D, where the rough seafloor was first depressed by the building of a large volcano and then subsequently covered by lava flows and sediments, was interpreted to have been observed since lone seamounts with no apron and seamounts with a surrounding moat were known. However, his sequence A-B_2-C_2-D, where first a lava plain formed and subsequently volcanoes grew on the plain, had not been observed.

It is fitting, and ironic, that the Marquesas do exhibit precisely this type of sequence. From Fatu Hiva southwards to the Marquesas fracture zone ridge, the usual pattern of abyssal hills or

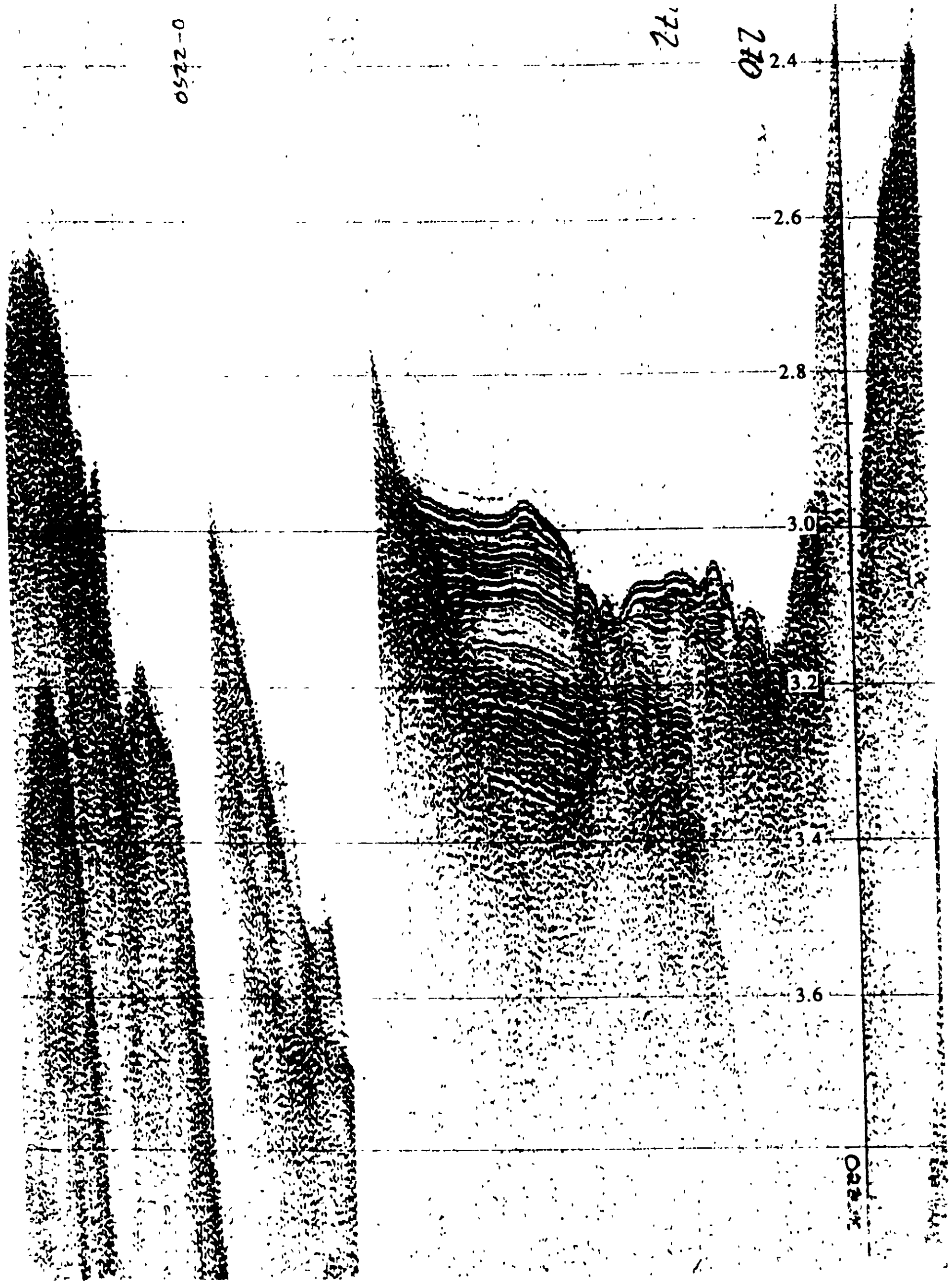

Figure 3.9. Single channel seismic profile of sediments between Nuku Hiva and Ua Huka. Units U_1, U_2 and U_3 are visible, with U_3 exhibiting some layers with chaotic cores. Numbers on horizontal lines are seconds of two-way travel time. Handwritten notations are the time marks and comments from the watchstanders during the cruise itself.

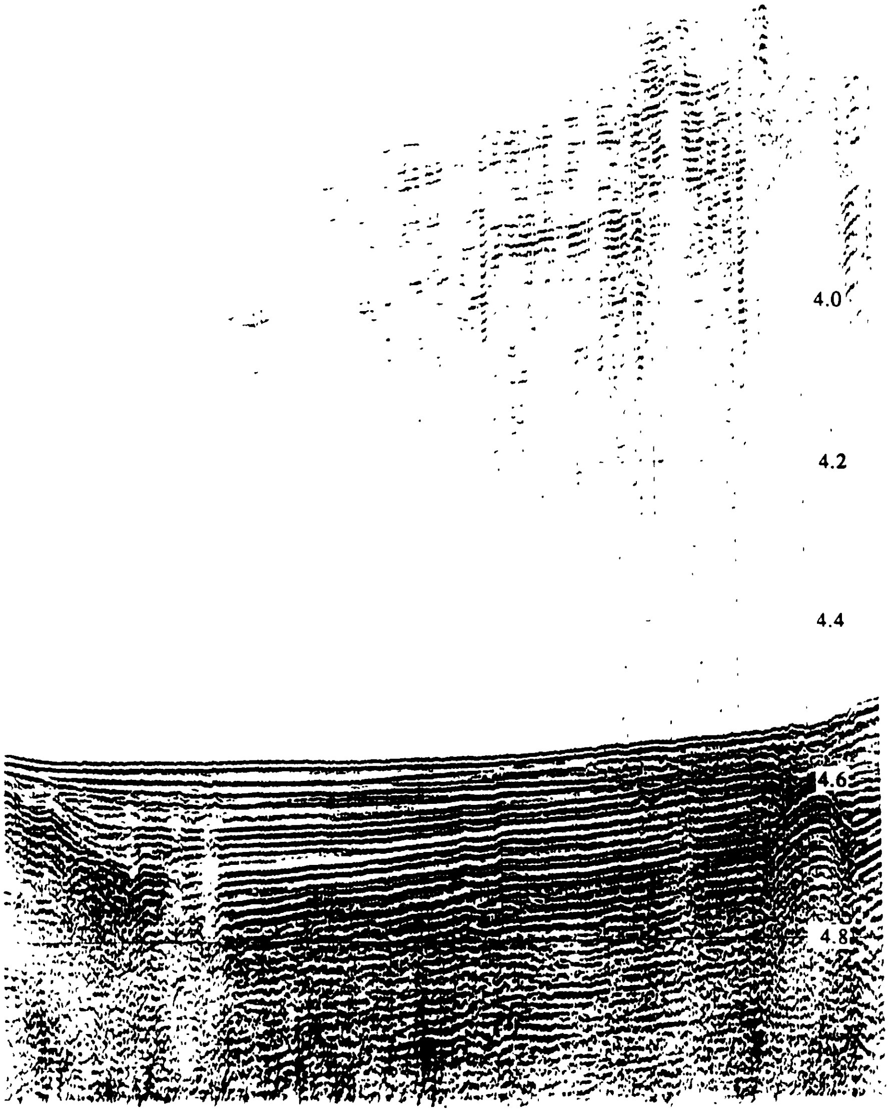

Figure 3.10. Single channel seismic profile of sediments directly east of Ua Pou and directly south of Ua Huka. A gravity core recovered from these sediments was composed of foraminiferal sand. The acoustic character of these sediments is similar to those of the U_2 unit in the apron, implying that U_2 is probably composed of turbidites that originate on the island flanks [*Natland and McNutt,* 1987]. Numbers on horizontal lines are seconds of two-way travel time.

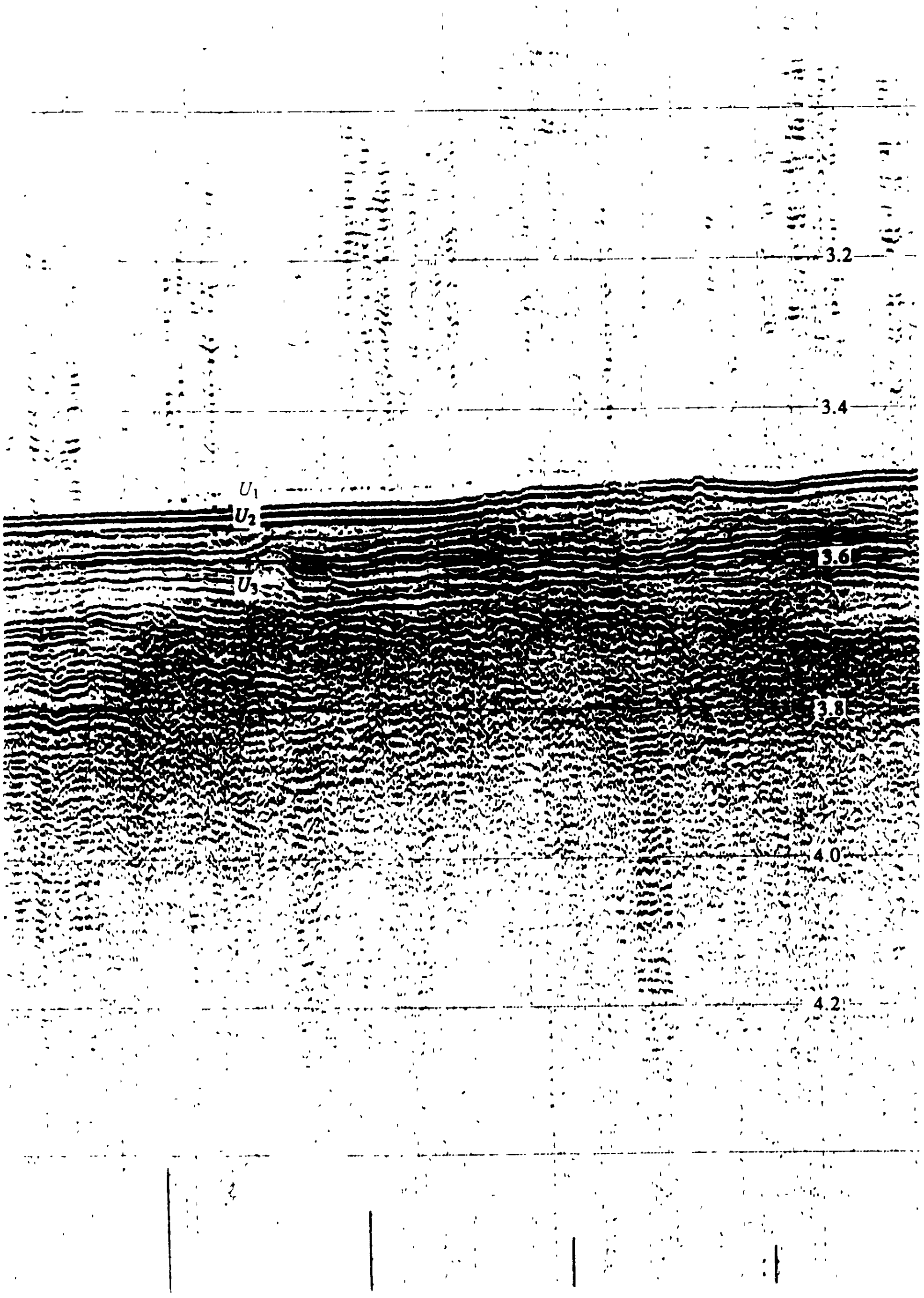

Figure 3.11. Single channel seismic profile of sediments south of Motu One. Unit U_3 is composed of some strong reflectors, although even these are not continuous in the section. The chaotic nature of U_3 is masked by the smooth turbidite flows of U_2 and U_1 and cannot be seen in the SEABEAM bathymetry. Numbers on horizontal lines are seconds of two-way travel time.

sediments is absent. The seafloor is covered by an acoustically opaque cap that shows no internal layering, and is overlain only by the thin transparent layer. The SEABEAM swath shows that this area is studded by small volcanic cones, and a dredge haul from one of these cones yielded a pillow lava [*Natland and McNutt,* 1987]. The initial stages of Marquesan volcanism would seem to conform to *Menard*'s [1956] second model: the initial volcanism occurred over a widespread area, forming a lava plain, and did not coalesce into a few central vents until later in the sequence. The lava carapace is illustrated in Figures 3.4 and 3.12, where it can be seen extending to the north wall of the Marquesas fracture zone ridge. To the south of the ridge, the seafloor is covered by a thick sedimentary layer, and as can be seen in Figure 3.13. The acoustic character of these sediments is obviously very different from that of the carapace to the north. The dating of samples from the island chain [*Duncan and MacDougall,* 1974] indicates that the Marquesas hotspot presently lies below the fracture zone ridge, which is consistent with the abrupt change in seafloor cover from one side of the fracture zone to the other.

3.4. DISCUSSION

As discussed by *Natland and McNutt* [1987] and as suggested by this compilation of seismic data, the progression of mid-plate volcanism in the Marquesas differs from Hawaii in several respects. One difference is quite obviously of constancy: there is no chain of atolls and guyots to the northwest of the main island group. A second difference is the expression of the initial stages of volcanism. The submarine 'Loihi' stage [*Clague and Dalrymple,* 1987] of Hawaii occurs on the flanks of the previous dome, whereas in the Marquesas the initial volcanism occurs in the form of a volcanic carapace, and any sizeable edifices grow in relative isolation from their predecessors. There may in fact be an initial carapace stage in Hawaii, but it has not yet been detected. The tholeiitic shield volcanoes of Hawaii stand so high that the subsequent volcanoes may always be erupting from the flanks of the previous domes [*Natland and McNutt* , 1987]. A third difference is in the expression of the balance between the

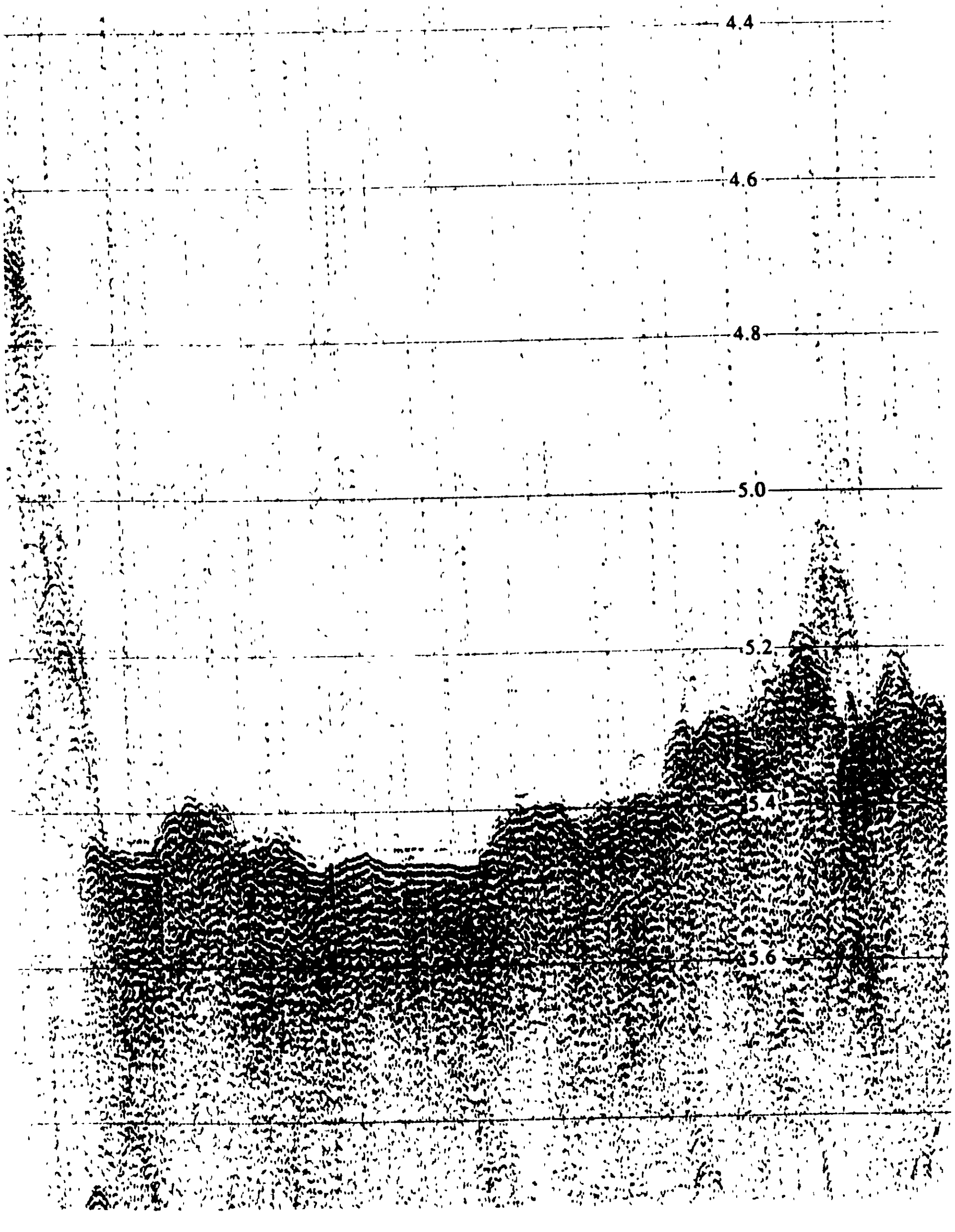

Figure 3.12. Single channel seismic profile of the carapace volcanics and the north wall of the Marquesas Fracture Zone Ridge. The thin transparent cover can just be seen over the opaque cover of the carapace. Irregular features are small cones, from one of which a pillow lava was recovered. Numbers on horizontal lines are seconds of two-way travel time. Handwritten notations are the time marks and comments from the watchstanders during the cruise itself.

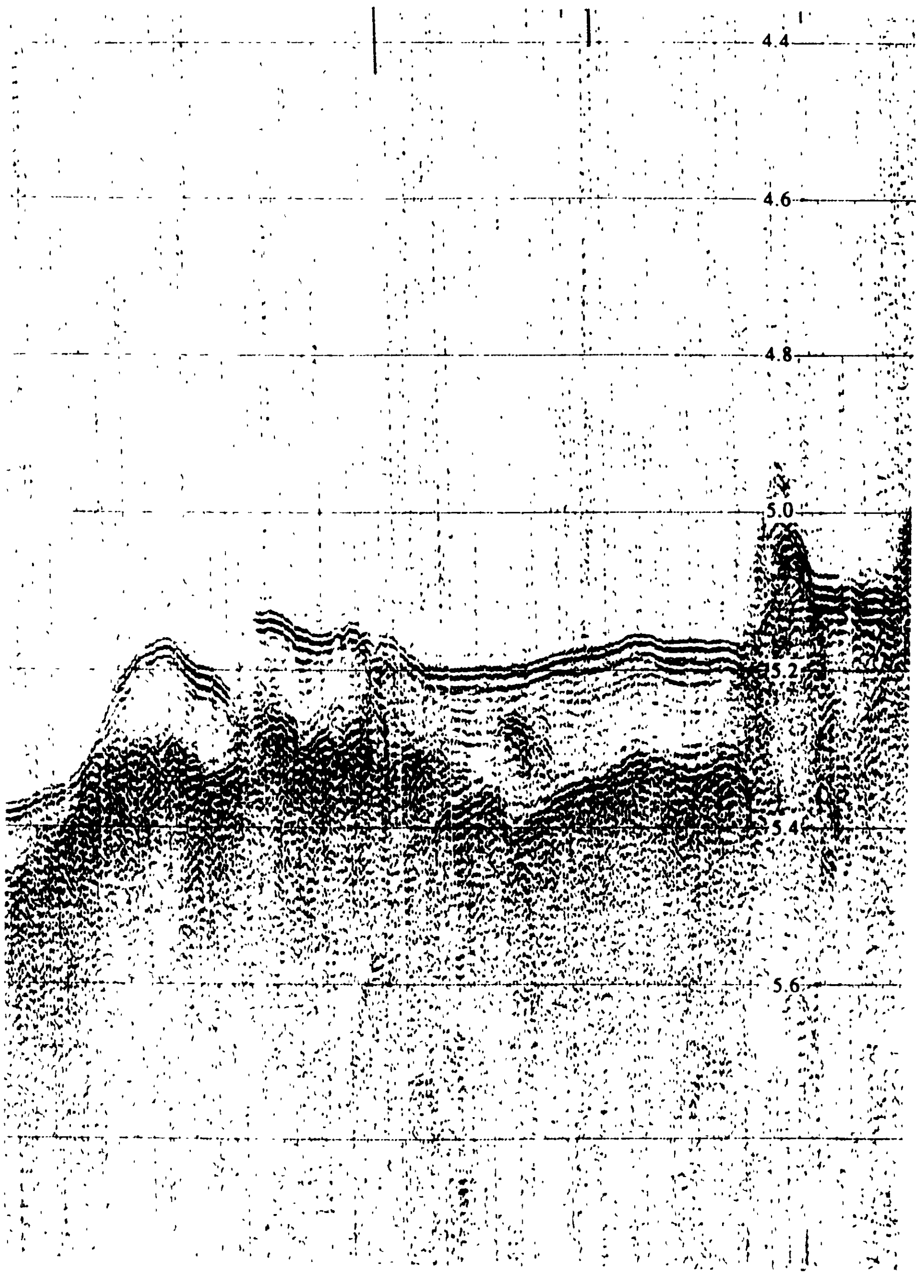

Figure 3.13. Single channel seismic profile of the pelagic sediments and the south wall of the Marquesas fracture zone ridge. The thin transparent cover can just be seen over the reverberative cover of the sediments. The fracture zone ridge clearly separates two acoustically different seafloors, which are interpreted to reflect the southernmost extent of Marquesan volcanism. Numbers on horizontal lines are seconds of two-way travel time. Handwritten notations are the time marks and comments from the watchstanders during the cruise itself.

subsidence of the islands and the infilling of the moat. In Hawaii, a moat remains even after sedimentary infilling, while in the Marquesas, the sedimentation has been sufficient to completely fill the flexural moat, leaving no expression in the bathymetry. Whereas the pattern of onlapping and offlapping units in Hawaii reflects the rate of sedimentation versus subsidence, the complete infilling of the moat in the Marquesas by mass wasting has changed some of the characteristics of the units clearly seen in Hawaii by *Rees et al.* [1991].

3.4.1. Volcanic stages and apron development

The second stage of volcanism in the Marquesas is similar to that of Hawaii: large domes or 'shields' are built from a few major centers, depressing the original seafloor beneath the weight of the growing volcanic structure. This stage is estimated to last approximately 1.6 My based on dated samples from most of the islands, although the terminology used by *Brousse et al.* [1990] may include the late alkalic stage, in which case the shields could be built in as little as 300,000 to 750,000 years. The processes of eruption and mass wasting are most active during this period, and the base of the unit with the chaotic character is presumed to have been deposited during this period, as in Hawaii [*Rees et al.,* 1991]. This unit exhibits onlap in Hawaii as the volume of deposited sediments increases [*Rees et al.,* 1991]. Unfortunately the present seismic data could not image the base of this unit in the Marquesas.

The shield building stage is followed by a capping phase, as in Hawaii, with the difference that in the Marquesas the top of the are domes below sea level [*Natland and McNutt,* 1987]. The capping phase of alkalic to tholeiitic composition produces the emergent portions of the islands, which rise from approximately 3000 meters depth to heights of 1000 m or more above sea level in approximately 0.2 My [*Brousse et al.,* 1990]. In the later stages, the larger islands develop calderas as their magma supplies wane, and subaerial erosion begins to cut deep valleys into the islands. Mass wasting continues in the form of large slumps and debris slides.

While mass wasting continues long after the capping phase, the amount is lessened by the decreasing amount of material available. The island is no longer being built faster than it is being eroded away, and the emergent portion begins to shrink. The moat infill should reflect this stage by a gradual lessening in the rate of sediment deposition. In Hawaii, this is seen in the progressive offlap of smooth sediment layers from the upper parts of the section that lie over the arch [*Rees et al.*, 1991], whereas in the Marquesas the U_3 unit exhibits only local offlapping, possibly an indication that the local sedimentation rate decreased.

The final volcanic stage is actually a waning of activity, after an elapsed time of about 1.5 My. Some volcanic activity is known to extend 0.5 to 1 Ma more, for example on Ua Huka and Ua Pou, but the volume of these events is extremely small [*Brousse et al.*, 1990]. Little to no new material is added to the islands themselves, although it should be noted that the biogenic and erosional sedimentation continues, and the apron is added to throughout and after this period. The final layers of the apron are derived exclusively from the turbidite flows originating on the steeper flanks, and can be expected to be composed of calcareous material mixed with the erosional detritus from the continued dissection of the islands. In Hawaii, these deposits are represented by the ponded unit which is constrained to the deeps of the moat [*Rees et al.*, 1991], whereas in the Marquesas the absence of a moat allows the turbidites to flow all the way to the dams created by the uplifted abyssal hills on the crest of the flexural arch. The transition between the offlapping and ponded units that is clear in Hawaii is not so clear in the Marquesas because the moat has already filled by this point, and *Rees et al.*'s [1991] stages 3b and 4, the offlapping and ponded unit stages, are in fact merged in the continuous U_2 unit of the Marquesas. The final stages of deposition are expressed as the smooth turbidite cover that *Menard* [1956] observed.

While the eruptive stages of a volcano as defined by the Hawaiian model certainly do not absolutely define the units observed in the moat, there is a good temporal correlation between the estimated volumes erupted during the volcanic stages and the observed volumes in the moat as observed in Hawaii [*Rees et al.*, 1991]. The volcanic activity may peak within the first million years of eruption, but the mass wasting continues long after the volcanoes are quiescent, albeit at a reduced rate.

Since the apron is present essentially all the way to the Marquesas fracture zone, its development must be extremely rapid. There is of course some 'along moat' contribution to the formation of the apron from the preceding islands. The contribution of the turbidites originating from the older islands can be bounded by the lateral extent of the apron, approximately 250 km. This distance provides an estimate for an overlapping contribution: turbidites originating from Nuku Hiva and Lawson Bank are probably not contributing to the apron below Fatu Hiva, but it is possible that the flanks of Ua Pou, Tahuata and Motane have shed sediments into this area for more than 4 My, the age of an older sample from Ua Pou. This type of lateral infilling of the moat has been identified in Hawaii, spreading the sediments to distances of at least 100 km along the moat [*Moore et al.*, 1989; *Rees et al.,* 1991].

3.4.2. Catastrophic collapses

There is strong evidence that some debris slides in the Hawaiian islands occurred very quickly. That these events involved thousands [*Moore et al.*, 1989] and possibly tens of thousands [*Rees et al.,* 1991] of cubic kilometers of basalt is impressive enough, but the fact that these events may have occurred in a matter of minutes is rather frightening. While the evidence for these events in Hawaii is of a geological and geophysical nature, there is some evidence from traditional and cartographic histories of the Marquesas that may point to a catastrophic collapse in recent times. Early maps of Fatu Huku by Cook in 1774 and by Hergest in 1792 show Fatu Huku as having a size comparable to Ua Pou or Ua Huka, while a later map by Porter in shows Fatu Huku as it is today, a tiny islet [*Brousse et al.,* 1990; *Barsczus, pers. comm.*]. There are also stories in the native lore of a large disaster around 1800 or so that correspond to the interval between the visits by the respective explorers [*Barsczus, pers. comm.*]. While these tantalizing pieces of evidence point to a sudden collapse of a large volcanic edifice, the *Crossgrain 2* shiptrack unfortunately passes over 50 km to the north of the island. The SEABEAM data show no highly irregular terrain characteristic of debris flows as seen in Hawaii during this closest approach, although this is not surprising since the scarp in the known bathymetry appears to face the west, implying that any failure along this scarp would flow parallel to the shiptrack rather than under it. Later shiptracks, such as line MARQ 10 of the *Ewing* cruise EW9103 should show typically chaotic bathymetry and seismic sections in the sections to the west of Fatu Huku.

The best surveyed failure scarp is that of Fatu Hiva, from data gathered during *Crossgrain 2*. Figure 3.13 illustrates the bathymetry around Fatu Hiva and Motu Nao as compiled from the SEABEAM swaths of the area. The island itself is crescent shaped, opening out to the west, and is composed of a concentric set of volcanoes, with the caldera of the outer volcano measuring about 8 km across. The bathymetry shows the large (>500 km^3) scar left on the northwestern quarter of the island by the collapse of the volcano, an event dated at about 1.40 Ma by *Brousse et al.* [1990]. Single channel seismic profiles in the area to the northwest of the island show an acoustically chaotic layer over a very opaque layer.

Other islands exhibiting these large failure scarps are Ua Huka and the Eiao - Hatutu complex, which both face to the south-southeast. The seismic profile of Figure 3.11 shows the chaotic cores of unit U_3 as well as many strong reflectors that are discontinuous. Sediments in this area can well have come from any of the flanks of Banc Jean Goguel, Ua Huka, Nuku Hiva, Hatu Iti, Eiao, or Hatutu, all islands or shallows that form the surrounding amphitheater. Sediments in this basin just off Eiao should be well resolved by the multichannel work of *Ewing*'s line MARQ 1, during the EW9103 cruise, and show the bottom of unit U_3.

3.4.3. Areal extent of the apron

The area inside the maximal extent of the apron is approximately 278,300 km^2, of which about 48,400 km^2 is volcanic edifice, inter-island sediment, and carapace. The apron seems to reach greater distances to the east, a phenomenon which cannot be attributed to prevailing currents, since the South Equatorial Current flows in the opposite direction, and since as mentioned above, the bulk of the shallow material is deposited by turbidites, which will not be

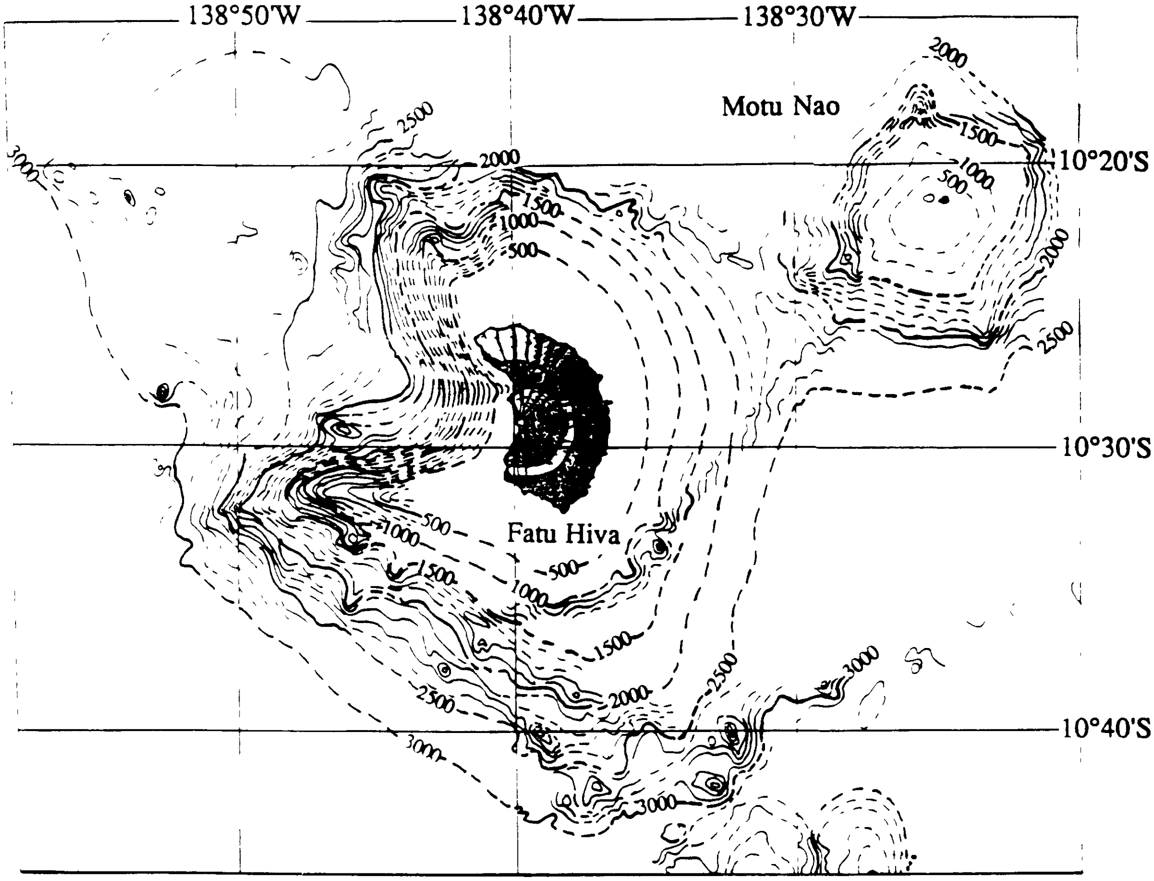

Figure 3.14. Bathymetry around Fatu Hiva and Motu Nao. Bathymetry compiled from SEABEAM plots by Jim Natland showing the prominent failure scarp in the northwestern quadrant of the island. The island itself is formed by two concentric volcanoes, the younger formed in the caldera of the older. Motu Nao, a rock to the northeast does not show any large mass wasting features similar to those on Fatu Hiva.

highly affected by water currents. The slope of the seafloor due to plate cooling is approximately 0.0006, or some 250 m over a distance of 450 km, but this slope is from east to west, in a sense opposite to the greater extent of the apron.

If the size of the apron is controlled by the uplift of abyssal hills on the flexural arch, as proposed by *Menard* [1956], then the extent of the apron should approximate the distance to the arch. In cases where there is no bathymetric expression of the moat or arch around an island load, and in the absence of gravimetric data, the extent of the apron may prove a good estimate for the distance to the flexural arch. If the geometry of the islands controls the position of the arch, then the distribution of the island load may control the extent of the apron, a question addressed in the next chapter.

3.4.4. Volume of apron sediments and building cycles

Using the sediment thicknesses derived from the sonobuoy data and the area estimate above, I may estimate the volume of the sedimentary part of the apron as more than that implied by the minimum thickness, 46,000 km^3, and probably less than that implied by the greatest thickness, 310,000 km^3. Using the minimum thickness observed at the outer edges of the apron and the largest thickness at the inner edge gives an estimate of 118,000 km^3 for the volume of the apron sediments. However, as *Menard* [1956] noted, the moat infill volume cannot possibly be derived exclusively from erosion of the emergent portion of the islands themselves, but must come from a combination of material derived from the island flanks and volcanic flows. If the volume of the mass wasting events in the Marquesas ranges from essentially zero for the small events like the Papa'u slide off Hawaii (39 km^3, *Fornari et al.* 1979) to the largest slide observed yet, 34,000 km^3 (events DF3 and DF4 of *Rees et al.*, 1991), then the number of events necessary to fill the moat ranges from 3 to many tens of thousands. Quite obviously, there are not many events in the largest size range, and even though there are many, many small events, their sum does not match the volume of the larger events. Events large for the Marquesas, such as the collapse of Fatu Hiva, imply a number as high as 240 for collapses of islands during the deposition of the Marquesan apron. For Hawaii, an apron volume of 279,000 km^3 implies either 8 events on the scale of the Oahu/Molokai events preceding the overlying Nuuanu and Wailau slides, 56 events the size of the Alika and Ka Lae slides, or 280 events the size of the Wailau slide itself.

3.5. CONCLUSIONS

The refraction profiles show two layers, one with an average velocity of 3.1 km/s that thickens from 250 m in the abyssal hills to 1400 m adjacent to the volcanic pedestal, and a lower layer with an average velocity of 5.9 km/s of undetermined thickness. I interpret the top layer as pelagic sediment and turbidite flows, and the second layer as volcanic basement and earlier lava flows associated with the carapace.

The archipelagic apron around the Marquesas formed by repeated mass wasting events and turbidite flows, and extends 250 km from the islands, with ponded sediments reaching a further 50 km. The flexural moat has been completely filled, and the offlapping and ponded units observed in Hawaii by *Rees et al.* [1991] are combined into unit U_2 in the Marquesas. The area of the apron is estimated to be 230,000 km^2, which limits the sedimentary volume to about 118,000 km^3. Estimates of the volume of the mass wasting events from the Marquesas and similar events in Hawaii imply that the total number of large events involved in filling the moat may number in the hundreds for both Hawaii and the Marquesas.

The absence of any appreciable thickness of pelagic sediment or abyssal hill structure to the southeast of Fatu Hiva, coupled with the acoustically opaque character of the seafloor and the appearance of many small cones producing pillow lavas leads to the possibility that the initial stage of volcanism in the Marquesas is expressed as the formation of a lava carapace rather than an isolated structure. The abrupt change in acoustic character from the northern side of the Marquesas fracture zone to the southern side would support the contention that the hotspot is presently beneath the fracture zone ridge, even if there are presently no signs of volcanism in the form of seismic activity.

CHAPTER FOUR

THE OCEANIC LITHOSPHERE UNDER THE MARQUESAS ISLANDS

They are ill discoverers that think there is no land, when they can see nothing but sea.

Francis Bacon
Advancement of learning, vii, 5

4.1. INTRODUCTION

The previous chapters have been concerned with the processes that occur on the seafloor and in the sediments that cover the basement. To understand the behavior and properties of the basement itself, I consider its mechanical response to the weight of the islands themselves. Although it is not at first obvious, large weights on the Earth's surface are supported by viscous forces, shear stresses, and buoyancy forces. The viscous forces are time-dependent, and are present only over the timescales of the building of the islands, decaying as the islands subside. The shear stresses and the buoyancy forces are present at all times and are due to the internal strength of the crust and the displacement of underlying higher density material. The manner in which the compensation of the island load occurs depends on the mechanical properties of the lithosphere, and if the pattern of displacement can be detected, then we may gain some information on the mechanical parameters of a model for the lithosphere itself.

The displacement of the basement can be detected through either direct seismic observation or by the potential field anomalies created by the undulations of the compensating masses. Since the seismic energy of the sources used on the *Washington* was not great enough to image the basement when there was a thick sediment cover, I use the gravity data to constrain the displacements. Although the use of gravity data to constrain density distributions is well known as an example of a non-unique inverse problem, there are several constraints that make the problem tractable. First, we know the shape of the upper surface: we directly observe the bathymetry. Second, there are only certain ranges for the densities of rocks that have been observed, and we may use these as bounds on any solution. Third, if we constrain the model by specifying a particular type of compensation, then we may obtain a unique solution *for that model.* This last point is important, but often lost in the shuffle: the parameters obtained for any model are just that and no more. They are part of a model that represents a much more complicated reality. Knowing whether the model actually comes close to the real process in the Earth is part of the art in geophysics. I must choose between various models for compensation, each of which has had its parameters optimized to reduce the error of the fit to the observed data.

4.2. GRAVITY DATA

The gravity and bathymetry profiles obtained on Leg 2 are shown in Figure 4.1, along with the center-beam bathymetry from SEABEAM for the shiptrack in the vicinity of the Marquesas islands. The gravity was reduced by removing the latitudinal variation with the International Gravity Formula, and a standard Eötvös correction for the ship's velocity was applied. As there were no ties to correct for drift, all the profiles have had their mean trend removed. Residual errors in the gravity come from two main sources: residual navigation errors appear as steps, and effects from differences between the navigation and gravity filters appear as spikes (*S. M. Smith, pers. comm.*, 1988*)*. Estimates of error from a similar gravimeter on the *R/V Conrad* are 1 mgal at wavelengths of 1 to 2 km, with accuracy limited by navigation errors [*Bell and Watts*, 1986], although the scatter of the present data even without the spikes and tears indicate that this is an optimistic estimate.

Figure 4.1. Projected bathymetry and free-air gravity recorded along survey lines. Dashed lines in bathymetry plots indicate theoretical depth given by the seafloor ages from Figure 1.4 and the depth–age relationship of *Parsons and Sclater* [1977]. Larger peaks in the lines are: profile 1' – flank of Fatu Hiva; profile 2' – flank of the Lawson Bank and Hatu Iti, and the flanks of Nuku Hiva and Ua Huka; profile 3' – uncharted seamount and the flank of Eiao. Flexural moat and arch from island loading is clearly visible on profiles 2' and 3'. Profile 1' lies near to the fracture zone, and profile 4' lies outside the flexural arch (see also Figure 4.3).

Bathymetry (m) and Gravity (mgal) lines 1 & 2

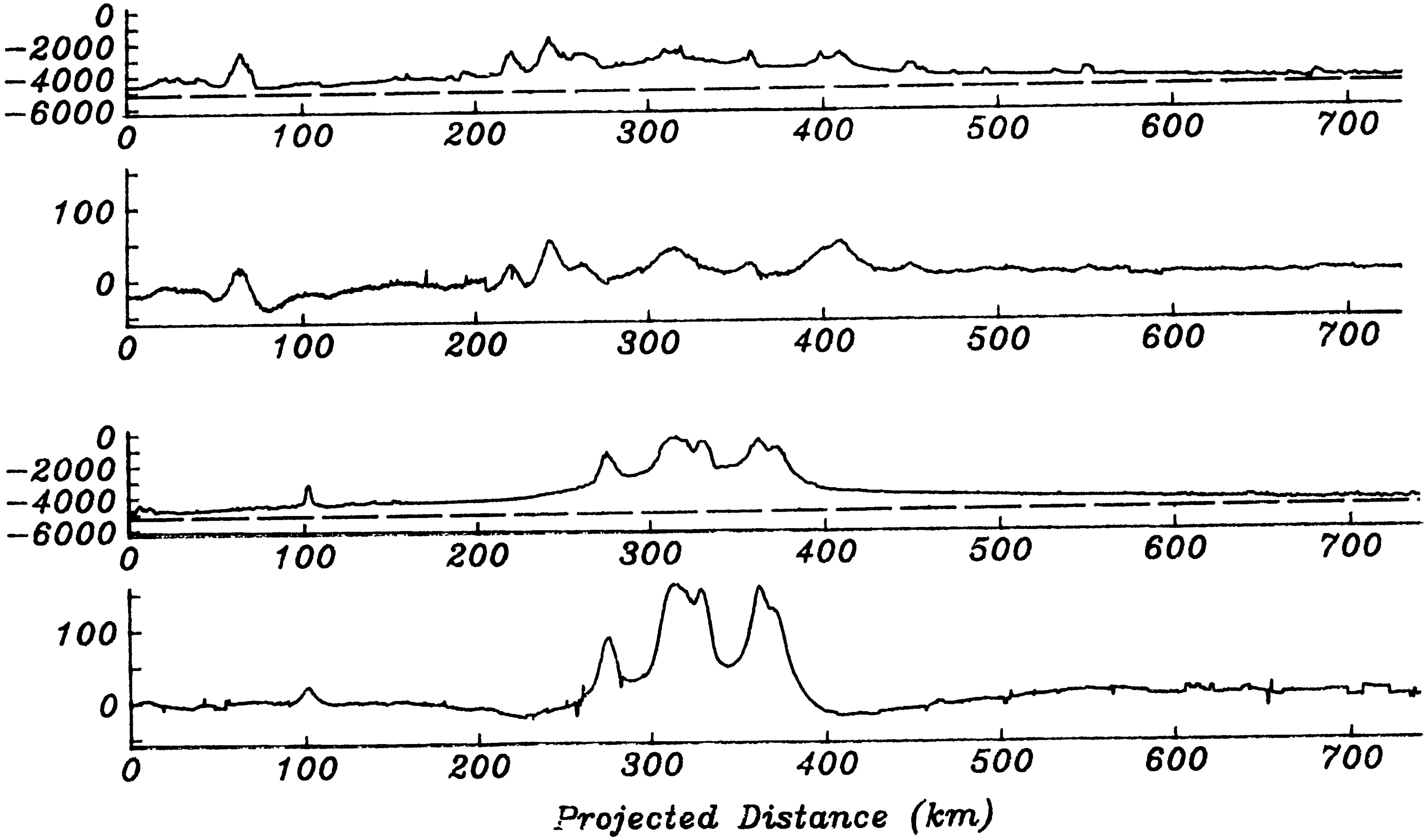

Bathymetry (m) and Gravity (mgal) lines 3 & 4

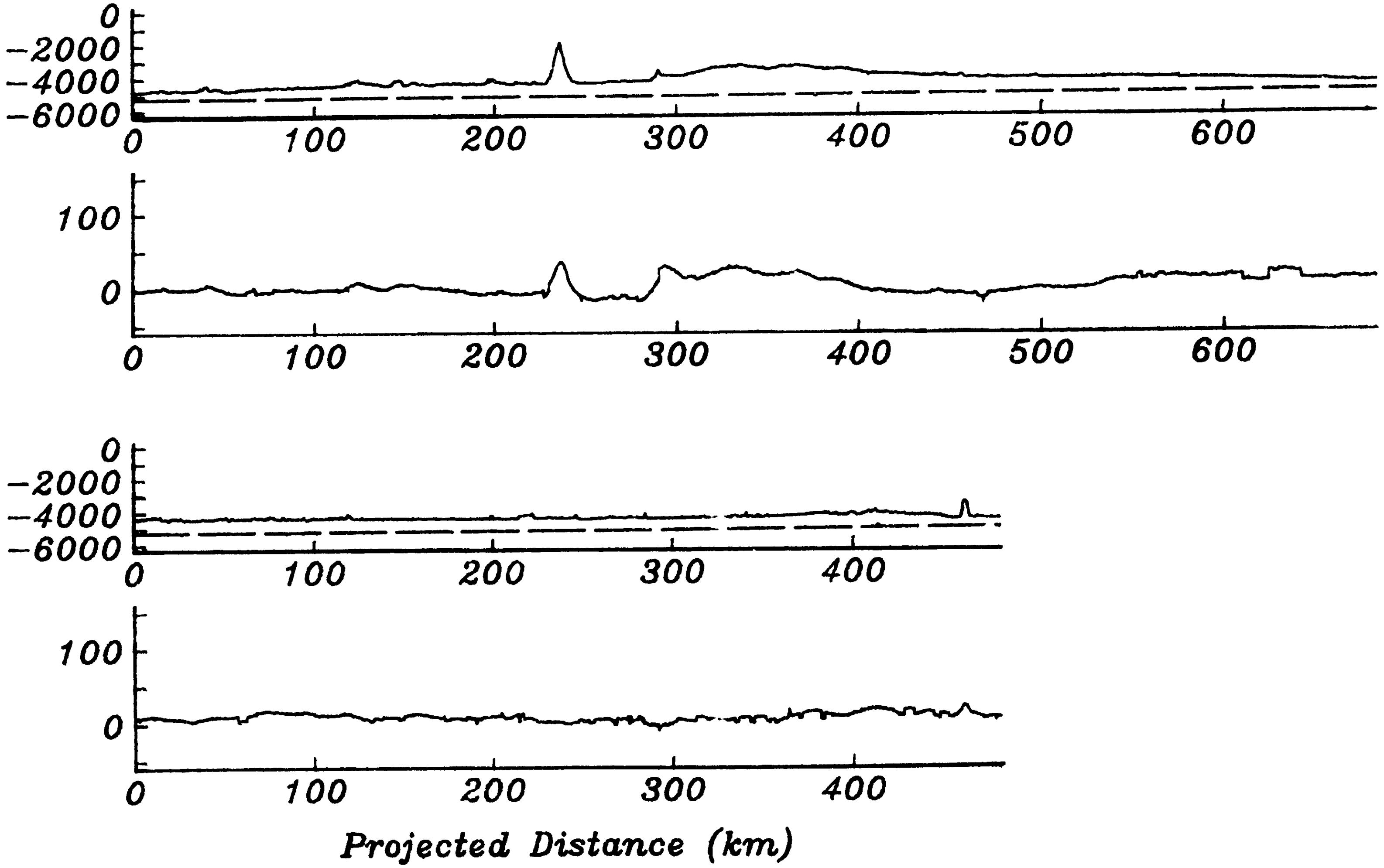

4.2.1. Adopted terminology

The terms 'lithosphere' and 'asthenosphere' are unfortunately used in much of the literature to refer to the elastic plate and the material underneath. This terminology is unfortunate because the lithosphere and asthenosphere so defined do not correspond to the usual seismic and tectonic definitions. The lithosphere drifts horizontally as a thick slab, but it responds to vertical loads as a thin plate, because while its mechanical properties on the short time-scales of earthquakes extend to depths of one hundred kilometers, the long time-scales of island loading permit the relaxation of stresses on the lower parts of the plate, effectively reducing the thickness to the elastic plate thickness we detect. A related effect of the differing time-scales is the assumption that the underlying layer is essentially a liquid. On the time-scales of island loading (millions of years), the lower part of the lithosphere is able to adjust to horizontal pressure gradients, and therefore to act as a fluid that provides a buoyancy force. This layer is not the asthenosphere of seismology or tectonics, but its fluid properties have led to its mislabelling.

I adopt the following convention when referring to the data: primed numbers refer to profiles projected normal to the islands' local trend, while unprimed numbers refer to the original survey lines. The coordinate affected is obviously only the horizontal distance, but this is an important distinction for problems dealing explicitly with horizontal wavelengths. Each of the lines is numbered in the order sailed, with the leg south of Fatu Hiva being line 1, the central leg along 9°S being line 2, the line to the northwest of Eiao being line 3, and the last leg, divided in two by a course change, being line 4a and 4b.

I have also adopted the convention of the terms 'two-' and 'three-dimensional' models. I explicitly state this because there is unfortunately no agreement in the literature for the terminology. Whereas *Ribe* [1982] considers a ridge to be a one-dimensional feature, *Watts et al.* [1985] consider it to be two-dimensional, while *Watts et al.* [1988] use the unfortunate label 'infinite dimensionality'. Since I am modelling variations in the depth dimension as well, I prefer to consider a ridge as a feature that does not vary along one of the horizontal dimensions, and so could be termed 'two-dimensional'. An isolated seamount is considered three-dimensional since its properties vary in all three directions. The primed data is used in the two-dimensional models, while the three-dimensional models need no projection. I model no infinitely dimensional objects.

4.2.2. Shipboard and satellite derived gravity

Although the bathymetry of Figure 4.1 shows no flexural arch and moat, as noted by *Menard* [1956] on the Capricorn expedition, the gravity from the *Crossgrain 2* expedition does show moat and arch structures. Even though the basement was not observable with seismic equipment, the gravity signal from the plate shows the deflection of the plate under the load of the volcanic load of the Marquesas. Where the load is greatest, along the central line (line 2), the flexural signal is greatest, while to the north, along line 3, the signal is not as strong.

The gridded gravity dataset derived from SEASAT radar altimetry [*Haxby et al.,* 1983] is shown in Figures 4.2 and 4.3. This interpolated 5 km grid shows a large anomaly over the islands, reaching 85^+ mgal over the northern island of Eiao, and shows a moat of 20^- mgal surrounding the islands. Figure 4.4 illustrates the values from this grid bilinearly interpolated onto the four profiles, along with the shipboard data. The satellite gravity field is effectively low-pass filtered because the field was calculated using the groundtrack crossover points. The ground-tracks for SEASAT are illustrated in Figure 4.5.

4.3. REVISED MAPS FOR THE MARQUESAS

Using the Navy's digital bathymetry database (DBDB5), a compilation by Karen Cianculli [*unpublished notes and map*, 1988] based on GEBCO maps [*Monti and Pautot,* 1973; *GEBCO*, 1980] and sounding sheets from various French cruises, and the data collected on leg 2 of the *Crossgrain* expedition, I have compiled a digital map of the Marquesas Islands area on a 5 km grid. This database is corrected for subsidence with plate cooling by using the magnetic isochrons of Figure 1.4 and the depth-age relation of *Parsons and Sclater* [1977] to

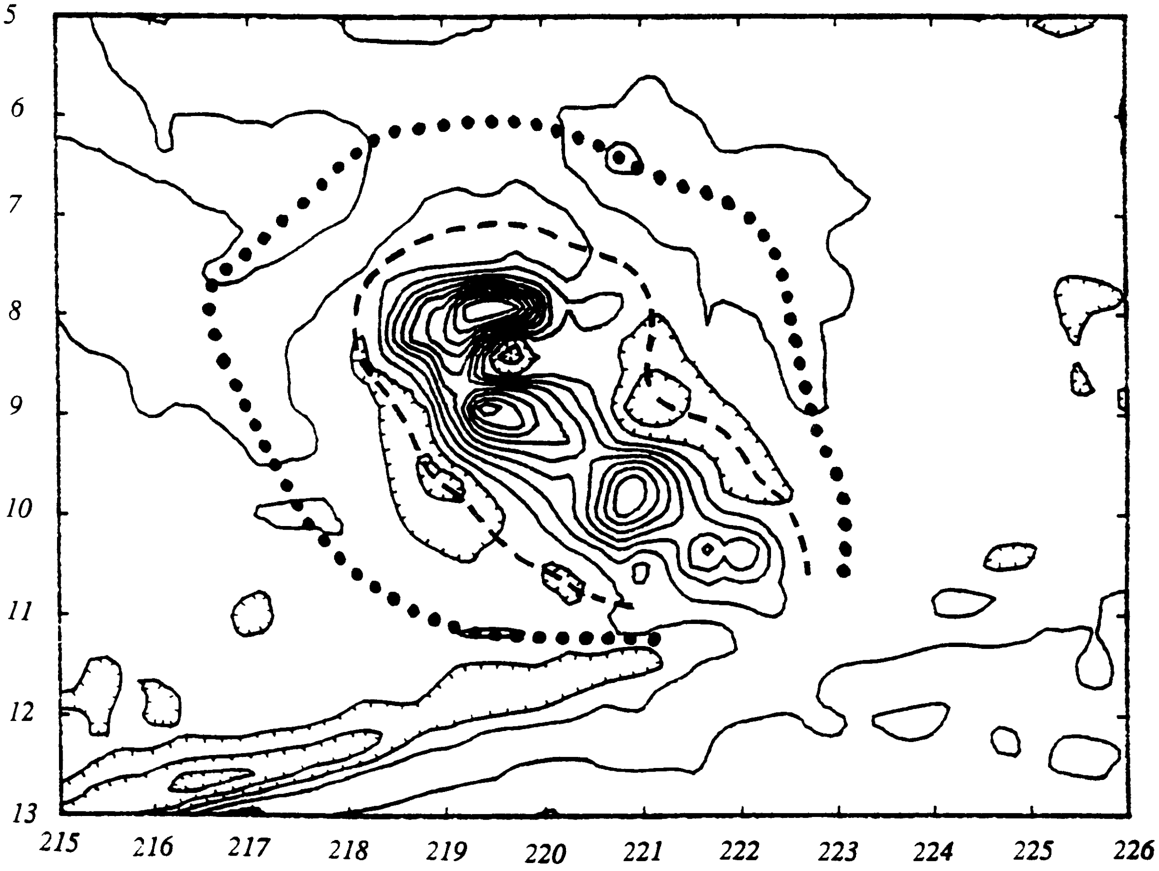

Figure 4.2. Free-air gravity field derived from SEASAT radar altimetry for the Marquesas area. Contours of 10 mgal, negative contours indicated by hachures. Crest of the flexural arch is indicated by the line of dots, and the gravity minima in the flexural moat are indicated by the dashed line, and correspond roughly to the extent of the volcanic edifice.

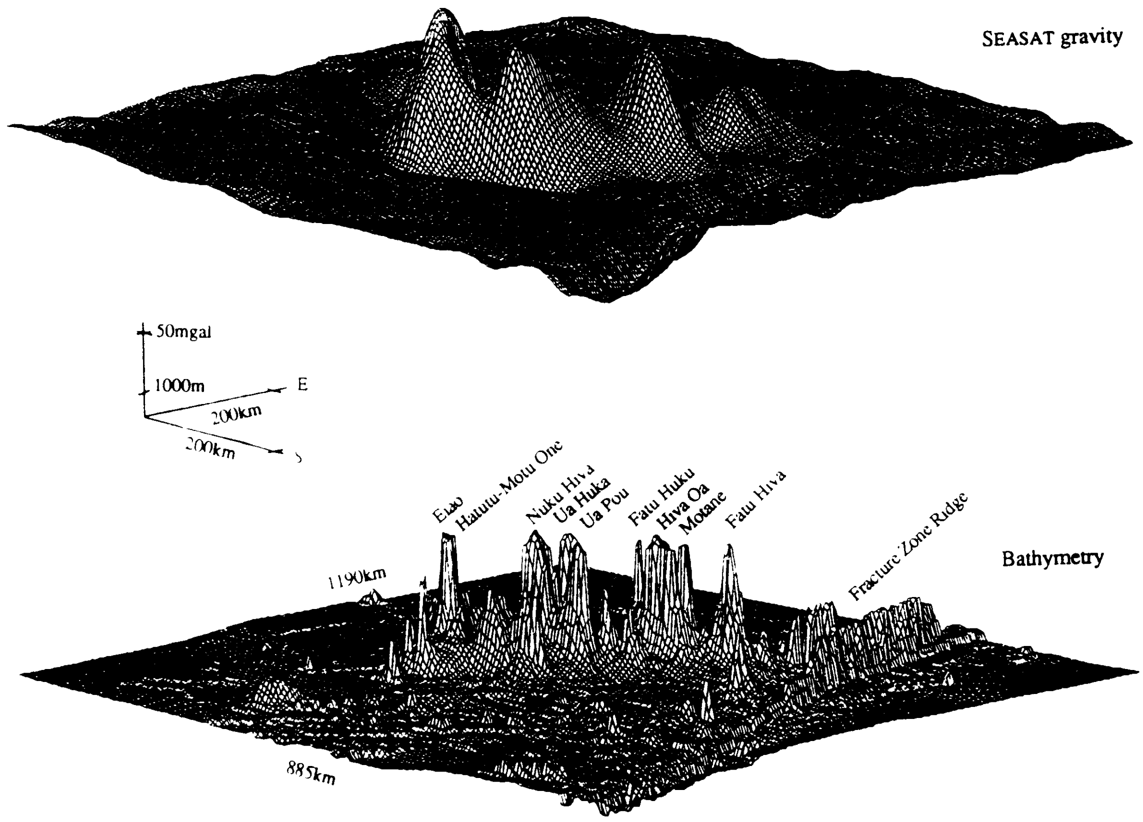

Figure 4.3. Free-air gravity and bathymetry of the Marquesas Islands area, plotted on a 5 km grid. View is from the southwest, and scale is indicated by the axes for meters of relief and milliGals of gravity. Grids are 1190 km wide in longitude, and 885 km high in latitude. Principal islands are labelled.

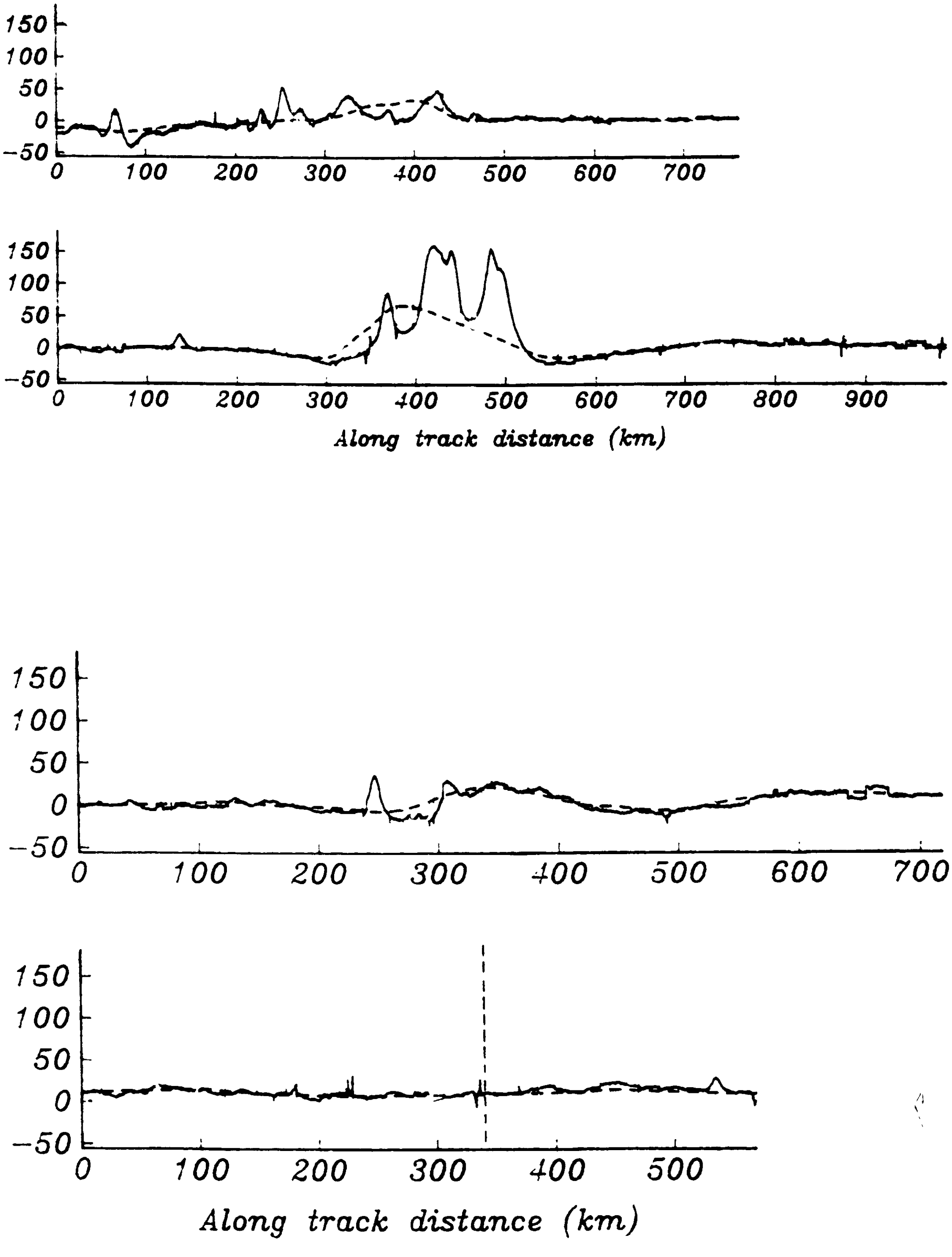

Figure 4.4. Free-air gravity along survey lines 1, 2, 3, and 4, as measured from shipboard data (solid line) and from derived SEASAT data (dashed line). Line 1 RMS difference is 11.3 mgal, line 2 RMS difference is 27.8 mgal, line 3 RMS difference is 6.7 mgal, and line 4 RMS difference is 4.3 mgal.

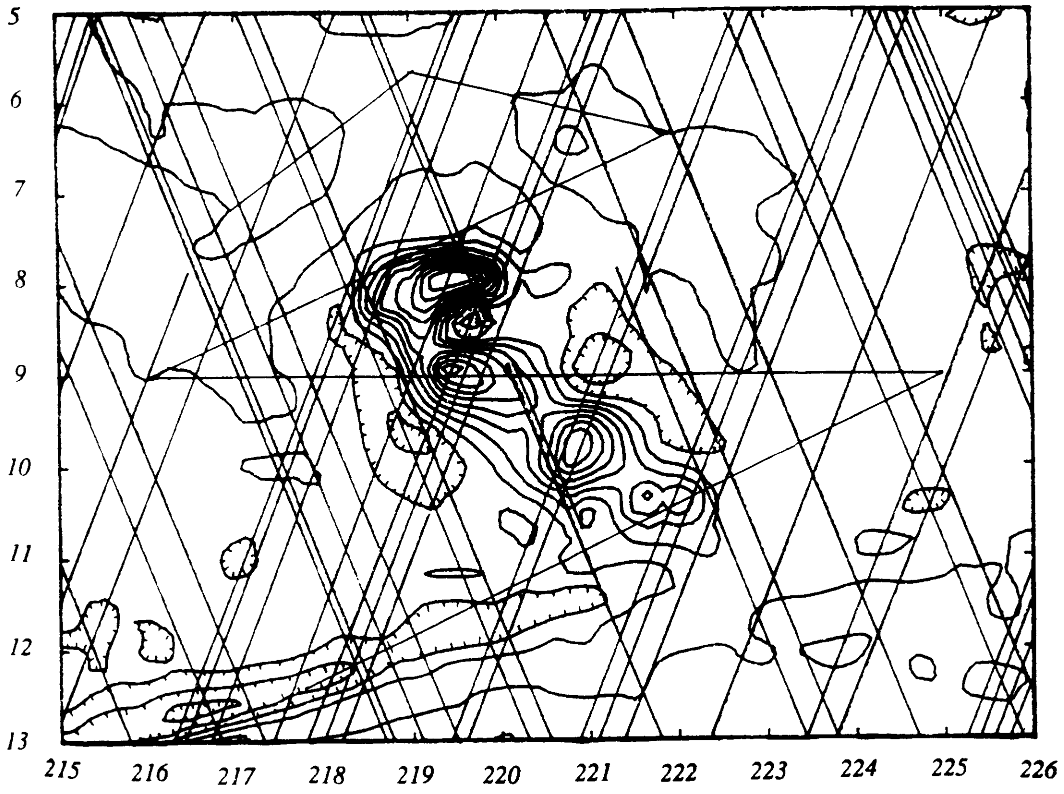

Figure 4.5. Contours of free-air gravity anomaly derived from SEASAT radar altimetry data, overlain by SEASAT ground tracks, and *Crossgrain* leg 2 survey lines. Satellite tracks ascend and descend westward. The uneven spacing of the ground track crossovers effectively filters the geoid signal which is used to produce the gravity field. Sampling of the area is especially sparse in the eastern portion.

produce a depth anomaly map for the region, which is shown as Figure 4.6. No sediment corrections were performed.

Several discrepancies between the DBDB5 dataset and the shiptrack bathymetry are observed. In general, the Marquesas rise more steeply from the abyssal plain than indicated by the DBDB5 dataset. Most contours are closer to the islands when data from the cruise is included, starting at the 4700 m isobath, and continuing to the 3700 m isobath. This is especially evident along line 2, in the central portion of the islands. The southernmost line passes over several small seamounts to the southwest and west of Fatu Hiva, and so this effect is not observed until the line reaches the 4500 m and deeper isobaths to the west. Line 3 exhibits the same sort of effect, with observed depths greater than predicted by the DBDB5 dataset between the depths of 4700 and 3700 meters. Line 4 exhibits mixed behavior: some observed depths are shallower than predicted. To the north-east of the islands, along line 4a, and to the far north-west along line 4b, the trend is as with the three previous lines: deeper bathymetry. In the center of line 4b, along the mean trend of the islands, the bathymetry is shallower than the DBDB5 depths by approximately 150 m, although since the error of the Navy dataset is unknown, this small difference may be meaningless.

4.4. GRAVITY MODELLING

Estimations of the plate thickness from gravity and bathymetric data have been made in two basic fashions. Forward modelling of the gravity, which generally involves exploring parameters in models of varying complexity until a certain level of tolerance in error is reached [*Walcott,* 1970; *Watts and Cochran,* 1974], or using the observations to produce a linear transfer function or 'admittance' between the two datasets, and then trying to interpret the admittance in terms of different mechanisms of compensation [*Neidell,* 1963; *Dorman and Lewis,* 1970; *Lewis and Dorman,* 1970; *McKenzie and Bowin,* 1976; *Banks and Swain,* 1977; *McNutt and Parker,* 1978; *Watts,* 1978; *McNutt,* 1979, 1984; *Ribe and Watts,* 1982; *Forsyth,* 1985]. I present results from both approaches.

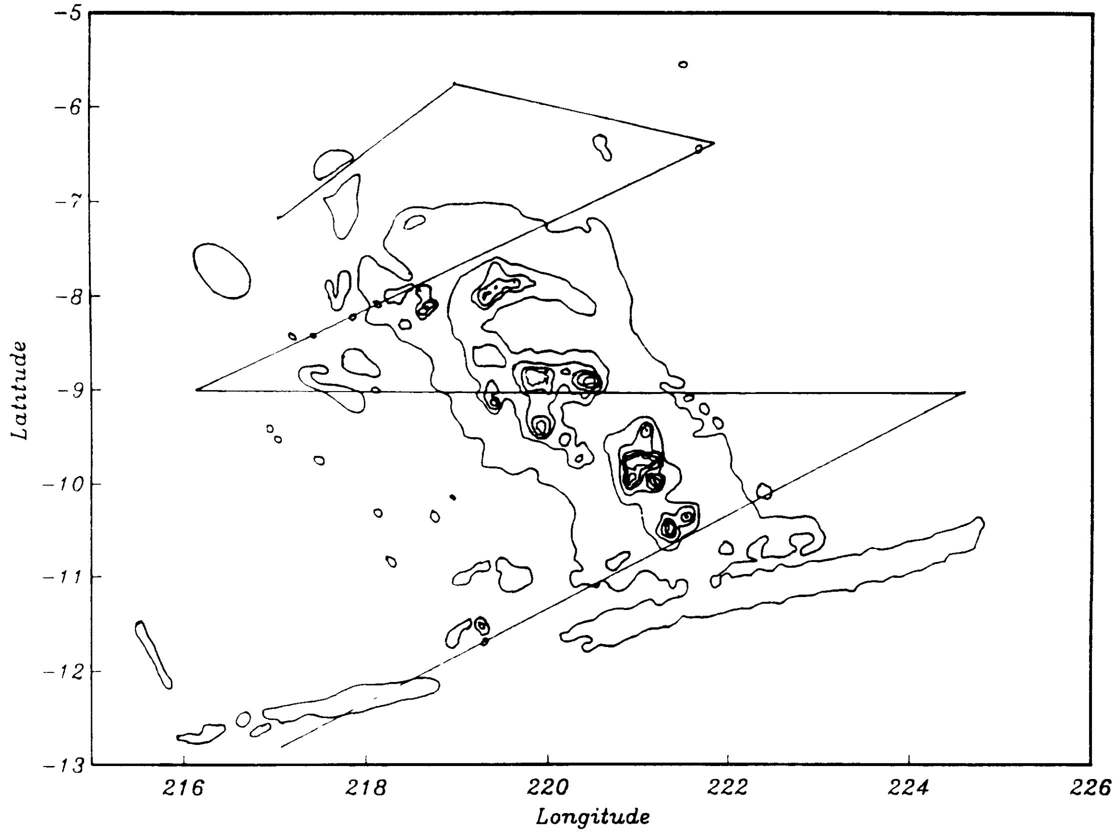

Figure 4.6. Depth anomaly for the Marquesas Islands area. The anomaly is the topography remaining after the bathymetry is corrected for subsidence due to plate cooling. No sediment correction has been performed. Geophysical survey lines are indicated by a solid line. Contour interval of 1000 meters.

4.4.1. Local compensation

To account for the less than expected deflection of plumb bobs by the Himalayas during a survey of India in the mid 1800's, two models of compensation were proposed by *Airy* [1855], and *Pratt* [1855]. Airy's model was analogous to an iceberg floating on the ocean: the Himalayas were proposed to have deep, low density roots that extended into the denser mantle, providing the displacement necessary for the hydrostatic restoring force. The greater the topography, the deeper the roots. Pratt, in contrast, proposed that the density of the mountains themselves would vary laterally: the higher the topography, the lower the density, and the lower the topography, the higher the density. Both of these models share the property that at a certain depth, all columns have the same cumulative mass. This depth can be more generally defined as the equilibrium hydrostatic pressure depth. Models like these, which have a restoring force that arises from changes directly beneath the load, are termed 'local' compensation models.

The two models share a large problem in that there is no way to realistically account for changes in the topography that occur through processes of erosion or volcanic eruption. In Airy's model, the addition or loss of topography would cause a vertical motion of the underlying column, and while vertical motions are known to take place, there is no evidence for this type of motion around *every* topographic feature. Pratt's model requires a change in the density throughout the column, and while chemical changes at depth do occur through the actions of groundwater and phase changes, again there is no evidence that this occurs everywhere.

4.4.2. Regional compensation

Multi-channel seismic profiles clearly show the basement dipping under the large load of the Hawaiian islands [*ten Brink and Watts*, 1985; *Watts et al.*, 1985; *Watts and ten Brink*, 1989]. In the Marquesas area, the basement deepens towards the islands before it is lost in the noise of the single-channel profiles approximately 200 km from the load. The amount of material in the apron has been sufficient to obscure the deflection of the seafloor, filling in the moat that is observed around larger islands.

Observing the moat and flexural bulge surrounding Hawaii, *Vening Meinesz* [1948] postulated that the load of the islands was being supported by the down-bowing of the plate. While the ultimate source of the restoring force in this model is still hydrostatic, the weight of the island mass is distributed over a wider area by the internal stresses of the supporting plate, a form of compensation which came to be termed 'regional', in contrast to the 'local' mechanisms.

4.4.2.1. Plate flexure

The lithosphere may be approximated as a thin plate overlying a fluid asthenosphere which supports loads by internal elastic stresses [*Barrell*, 1914; *Gunn*, 1943]. The equation for the deflection w of the plate due to a load h is described by the fourth order equation [*Hertz*, 1884]:

$$D\nabla^4 w + \Delta\rho_1 g w = -\Delta\rho_2 g h \tag{4.1}$$

where $\Delta\rho_1$ is the density contrast between the load and the material below the plate, $\Delta\rho_2$ is the density contrast at the loaded interface, g is the acceleration due to gravity, ∇^4 represents the biharmonic operator $\left(\partial^4/\partial x^4 + 2\partial^4/\partial x^2\partial y^2 + \partial^4/\partial y^4\right)$, and D is the flexural rigidity, which can be related to the elastic plate thickness T_e through the relation:

$$D = \frac{ET_e^3}{12(1 - \nu^2)} \tag{4.2}$$

where E is Young's modulus, and ν is Poisson's ratio. Taking the Fourier transform of (4.1) gives an equation relating the load topography h, and the deflection w in the Fourier, or wavenumber domain:

$$\hat{w}(\vec{k}) = -\frac{\Delta\rho_2\, g}{D k^4 + \Delta\rho_1\, g}\,\hat{h}(\vec{k}) \tag{4.3}$$

The inverse transform of which gives the physical deflection of the plate due to the load imposed by the topography. Note that for $D = 0$, the equation is simply the Airy model.

Since this is a fourth order equation, there will be some oscillations of the plate about the unloaded position that damp out with increasing distance from the load. The oscillations are very small, with the largest positive oscillation being just over 4% of the deflection directly under the load. This oscillation is seen as the outer rise before a plate is subducted in a trench, and as the peripheral bulge around large island loads like Hawaii.

4.4.3. Flexural effects on the gravity field

The Fourier transform provides a computationally convenient form of representing the gravity produced by L density contrasts $\Delta\rho_j$ at depths z_j [*Parker,* 1972]:

$$\hat{g}(\vec{k}) = 2\pi G \sum_{j=1}^{L} \Delta\rho_j \exp(-|\vec{k}|\, z_j) \sum_{n=1}^{\infty} \frac{|\vec{k}|^{n-1}}{n!}\,\widehat{h_j^n}(\vec{k}) \tag{4.4}$$

where $\hat{g}(\vec{k})$ is the Fourier transform of the gravity anomaly, $\vec{k}$ is the vector wavenumber, with $k = |\vec{k}| = {}^{2\pi}/_{\lambda}$, G is the universal gravitational constant, and $\widehat{h_j^n}$ is the Fourier transform of the n^{th} point-by-point power of the relief h about the depth z of the j^{th} density interface. I shall henceforth use a caret to indicate the Fourier transform of a variable.

Following (4.4), the gravity anomaly from a plate loaded by topography h at depth z_t, with its compensation at some surface w at depth z_m can be expressed as:

$$\hat{g}(\vec{k}) = 2\pi G \left\{ \begin{array}{l} \Delta\rho_2 \exp(-kz_t) \sum_{n=1}^{\infty} \frac{k^{n-1}}{n!} \widehat{h^n}(\vec{k}) \\ \qquad + \Delta\rho_1 \exp(-kz_m) \sum_{n=1}^{\infty} \frac{k^{n-1}}{n!} \widehat{w^n}(\vec{k}) \end{array} \right\} \tag{4.5}$$

Substituting (4.3) in this last equation, and taking only the first term of the series, I arrive at an expression in the linear terms of the load topography:

$$\hat{g}_1(\vec{k}) = 2\pi G \left\{ \Delta\rho_2 \exp(-kz_t) - \Delta\rho_1 \exp(-kz_m) \frac{g\Delta\rho_2}{Dk^4 + g\Delta\rho_1} \right\} \hat{h}(\vec{k}) \tag{4.6}$$

Higher order estimates $\hat{g}_{n>1}$ require w to be evaluated explicitly, and are easily calculated, but are not easily expressed in a compact form. Other density contrasts can be easily included in a similar manner in this formulation, taking into account any seismic layers observed. In the present model, $\Delta\rho_1$ is the density contrast between the load and the Moho, while $\Delta\rho_2$ is the density contrast between the load and water, and h and z_t are both observable from the SEABEAM data. Other values used are as listed in Table 4.1. The greatest density contrasts are found at the seafloor and the Moho, although the contrasts at the sediment-basalt boundary and the basalt-gabbro (layer 2-layer 3) boundary may also be included if desired.

The success of a relatively simple elastic beam model like the above in predicting the observed gravity over various marine and terrestrial features indicates that the compensation of these features is due to elastic behavior within a large portion of the plate. It has become customary to refer to the 'elastic plate thickness' when more accurately it is actually the *effective* elastic plate thickness, since the model parameter consists of the thickness of a purely elastic beam that

TABLE 4.1. Values of constants and parameters used in models

Constant or parameter	Value
G, universal gravitation	6.67×10^{-11} N m/kg^2
g, gravitational acceleration	9.78 m/s^2
E, Young's Modulus (basalt)	8×10^{10} Pa
ν, Poisson's ratio (basalt)	0.25
ρ_w, density of salt water	1030 kg/m^3
ρ_m, density of the mantle	3300 kg/m^3

would display the same characteristics (be they deflection or gravity). Without further ado, I shall also drop the 'effective' part, and consider the concept implicit in the phrase.

More realistic models take into account the finite yield strength of the plate, and determine the *mechanical* thickness T_m, which is larger than T_e, since the differential stress in the plate is limited by brittle failure at the top of the plate and thermally activated creep at the bottom. The depth at which the plate fails due to ductile flow is exponentially sensitive to temperature, and so may be used to indicate the depth to an isotherm defining some chosen level of stress. For geologically observed strain rates, the depth of a minimum differential stress of 50 MPa is taken to be between 550 and 600°C, and defines the mechanical thickness of the plate [*McNutt,* 1984]. For an island load the size of the Marquesas on a plate with a T_e greater than 15 km, the curvature is less than 2×10^{-7} m^{-1}, and there is little yielding, so T_e essentially equals T_m [*McNutt and Menard,* 1982].

The elastic plate thickness observed under seamount loads correlates reasonably well with the square root of the plate age at loading [*Watts,* 1978; *Watts et al.,* 1980]. Since the isotherms in a conductively cooling plate deepen with the square root of plate age, and the thickness of the plate's elastic core between the brittle and ductile failure fields is thermally controlled, I may reasonably assume that the elastic plate thickness, T_e, can be related to the isotherms controlling the elastic behavior of the plate [*Watts,* 1978; *McNutt and Menard,* 1982]. The data for most seamount loads fall between roughly the 450°C and 600°C isotherms [*McNutt,* 1984], but an anomaly exists in the south Pacific in that many of the seamount loads lie on anomalously weak lithosphere [*Calmant and Cazenave,* 1986; 1987]. *Calmant and Cazenave* [1986, 1987] include the Marquesas in this anomalous group, with the Marquesas falling on the 300°C isotherm. There are several higher estimates of the elastic plate thickness for the area, derived from various other databases, listed in Table 4.2. Given the age of the seafloor under the Marquesas as spanning 45 to 65 Ma [*Kruse,* 1988], and the ages of the islands as spanning 5.3 to 1.6 Ma [*Brousse et al.,* 1990], I would expect the elastic plate thickness at the time of loading to vary from 28 km under Fatu Hiva to 32 km under Eiao.

Since smaller values of T_e have been observed than are expected for the age of the plate, there must exist some mechanism for weakening the plate. Several models have been advanced to explain the origin of the swell surrounding the islands, the weakening of the plate, and the island volcanism itself. Simple models of 'plate thinning' involve resetting the temperatures below a certain depth to the temperature of the uppermost mantle by some unspecified method, and then conductively cooling the column [*Crough,* 1978; *Detrick and Crough*, 1978]. While this class of model can explain the depth anomaly, elastic plate thickness, heat flow, and subsidence of several hotspots, it fails to explain the ~2 km swell height of Cape Verde [*Courtney and White*, 1986; *McNutt*, 1988], and it does not elucidate the actual method by which the geotherm is altered. Convective models have been able to match observed figures for swell heights, and experiments with variable viscosity have shown that small depths of compensation for the swell can be mimicked by a shallow low viscosity zone, when in fact compensation is occurring over a much deeper column [*Robinson and Parsons,* 1988]. In this thesis, I shall not discuss chemical models for swell origin [e.g. *Jordan,* 1979]. In the absence of data directly related to thermal processes, such as heat flow measurements, estimates of the elastic plate thickness under seamount loads in combination with rheological models [e.g. *Goetze and Evans*, 1979] give us our best estimate of perturbations to the geothermal gradient in the marine lithosphere.

4.4.4. Initial estimates of T_e and $\Delta\rho$

Profiles 2' and 3', and the corresponding SEASAT derived gravity profiles in Figure 4.4 show clear moat and arch structures, while profiles 1' and 4' do not show visible flexural arches or moats in either dataset. The arches in the gravity occur at the same distance as the last appearance of the abyssal hills before they are buried under the archipelagic apron. If I assume that the moat and arch in the gravity correspond to the physical moat and arch, then I may use the characteristic wavelength of the gravity to define the flexural parameter α [*Walcott*, 1970]:

TABLE 4.2. Past elastic thickness estimates and compensation depths for the Marquesas Islands area

Area[a]	T_e, km	z_c, km	Dataset/Method	Reference
	18		GEOS3	*Cazenave et al.*, 1980
		30±40	geoid admittance	*Crough and Jarrard*, 1981
	19	45[b]	geoid filtering	*Fischer et al.*, 1986
Fatu Hiva[c]	15		SEASAT geoid	*Calmant*, 1987
Nuku Hiva	14±2		"	"
Eiao[c]	21		"	"
	20		SEASAT geoid spectrum	*Black and McAdoo*, 1988
Marquesas Fracture Zone Ridge	10		shipboard gravity	*McNutt et al.*, 1989

a: Value for the elastic plate thickness is the average for the whole island group unless a specific area is listed. b: compensation depth for the Marquesas swell. c: *Calmant* [1987] remarks that these values may be the result of sampling problems.

$$\alpha = \left(\frac{4D}{g\Delta\rho}\right)^{1/4} \tag{4.7}$$

where $\Delta\rho$ is the density contrast between the load and the mantle. This expression can then be used to derive a first approximation to the parameters D and $\Delta\rho$ of a full flexural model.

I can distinguish four different characteristic distances in profiles 2' and 3', one from each side of the swell. I might expect a slight difference from the east side to the west side, since the survey lines cross seafloor of differing ages, and cross different seamount age provinces. Defining the distance from the load to the arch as x_b, from Figure 4.1 I estimate distances of 183 and 228 km for the west and east sides of profile 2', and of 204 and 219 km for the west and east sides of profile 3', within about 10 km accuracy. Following the simple arguments for a continuous plate model outlined in Appendix B, I arrive at values of 13±2 and 18±3 km for the elastic plate thickness T_e for the western and eastern sections of profile 2', and 15±1, and 17±1 km for profile 3'. A broken plate model yields the corresponding values of 20±3, 26±4, 23±1, and 25±1 km. Working with the SEASAT data of Figure 4.2, I estimate the distance from the center of the load to the crest of the arch to range between almost 275 km in the central portions to about 100 km in the southernmost areas. These figures yield values for the elastic plate thickness ranging between 25 and 7 km for a continuous plate, and 37 and 10 km for a broken plate model. While *McNutt and Menard* [1982] point out that the flexural parameter is fairly insensitive to the loading geometry, the values from (4.7) are only approximations since the flexural parameter corresponds to a purely two-dimensional load.

If I rely on the assigned uncertainties, there is no real trend discernible from one side of the islands to the other, even though in Figure 4.2 there is a fairly clear asymmetry to the gravity across the chain, with the eastern crest lying 30 to 50 km farther out. There is also no discernible trend from the northern end of the islands to the southern end, even though there is a noticeable lessening of the width in Figure 4.2 as one proceeds towards the younger end of the chain. The asymmetry across the chain is in a sense opposite to that expected from the plate age, which increases to the west. This asymmetry has also been noticed by *Fischer et al.* [1986] in the geoid, and since it is also present in the shipboard data, it cannot be ascribed to the irregularly spaced ground-tracks of the SEASAT data in Figure 4.2. The asymmetry in gravity may be due solely to the geometry of the load, a theory that can be easily tested with a three-dimensional model, done below in section 4.4.6.

4.4.5. Two-dimensional models

By using a two-dimensional approximation to the observed bathymetry, I gain several computational advantages. The greatest of these is speed. With only one horizontal dimension, the number of points used in the Fourier transforms of (4.3) and (4.5) is greatly reduced from the full three-dimensional case for the same spacing. This gain in speed can then be expended on decreasing the spacing interval, which improves the accuracy of (4.5) in areas where the depth is less than the spacing, without greatly increasing the total number of points.

The great disadvantage of the approximation is the representation of the bathymetry. The two-dimensional model can be thought of as a three-dimensional model where the bathymetry is composed entirely of parallel ridges perpendicular to the shiptrack. In this way, if a seamount of a certain height is observed directly under the ship, the two-dimensional model represents it as a ridge with the same height. The volume of the seamount, and hence its compensation and gravity signal, are overestimated. Alternatively, if the seamount lies slightly off the shiptrack, the two-dimensional model represents the seamount as a ridge of the height observed on the shoulder of the seamount. The seamount is now underestimated.

For areas where the features are indeed lineated or elongated, this is a very good approximation, and requires only a projection of the horizontal distances onto a perpendicular to the elongation. However, in areas where the features are not elongated, the above disadvantages become serious. For the lines sailed in the Marquesas I can expect that this approximation will be best in the central areas of the chain, and worst at the ends, since the island group is only about three to four times as long as it is wide.

4.4.5.1. Admittance

The portion of the gravity field that is linearly related to the topography and its compensation can be expressed using a transfer function formulation. In geophysics this function is known as the admittance, or the isostatic response function [*Dorman and Lewis,* 1970]. In the notation of (4.6):

$$\hat{g}_1(\vec{k}) = Z(k)\, \hat{h}(\vec{k}) \tag{4.8}$$

where Z is the admittance, and can be thought of as the Fourier transform of the gravity anomaly that is linearly related to a point load and its compensation. Since noise is always present in data, an estimate of Z is usually obtained by using [*Munk and Cartwright,* 1966]

$$\tilde{Z} = \frac{\left\langle \hat{g}_1 \cdot \hat{h}^* \right\rangle}{\left\langle \hat{h} \cdot \hat{h}^* \right\rangle} \tag{4.9}$$

where the brackets indicate that there is some smoothing of the spectra, in this case the cross correlation in the numerator and the normed topography in the denominator, and where * indicates the complex conjugate. The smoothing of the spectra can be accomplished by some averaging process: either averaging discrete wavenumber bands in the *k*-plane, averaging several profiles together, ensemble averaging, or windowing. I have taken a combined approach, using the Welch method of half-overlapping Hanning windowed segments [*Welch,* 1970; *Oppenheim and Schafer*, 1975], and averaging the spectra from several lines. A disadvantage of the method is that each segment is assumed to be a stationary random process, when in fact this is not the case for geological features, but this is not a serious problem with long enough windows. A great advantage of the Welch method is its speed, since Fourier transforms of many short series are many times faster than those of a few long ones. The errors in the empirical admittance function can be estimated [*Munk and Cartwright,* 1966;

Watts, 1978; *Ribe,* 1982], and are used to quantitatively distinguish between compensation mechanisms, and to determine statistically significant uncertainties. In terms of the derivation for a simple elastic plate, equation (4.8) becomes

$$Z(k) = 2\pi G\left\{\Delta\rho_2 \exp(-kz_t) - \Delta\rho_1 \exp(-kz_m)\frac{\Delta\rho_2}{Dk^4 + g\Delta\rho_1}\right\} \tag{4.10}$$

From (4.10) it may be deduced that for short wavelengths, or large k, the first term will dominate, while at long wavelengths, or small k, the second term will dominate. Essentially, small features are supported regionally, while large features are supported locally. With this definition of Z, equations (4.10) and (4.8) are mathematically identical.

The formulations in (4.6) and (4.8) are linear relationships, while (4.4) and (4.5) contain non-linear terms. Any residual misfit then represents not only the non-isostatic processes, but also the neglect of higher order terms in bathymetry. The size of the contribution from the non-linear terms is however very small. Analysis of gravity data from the continents and oceans has shown that even with relatively noise-free and highly coherent data, the linear terms are sufficient to explain the variations in gravity for all but the shallowest and roughest topography [*Lewis and Dorman,* 1970; *McNutt,* 1979].

4.4.5.2. Admittance results

The power spectra for the depth anomaly along the four profiles are shown in Figure 4.7, with the obviously low relief of profile 4' showing as very low power compared to the other profiles at wavelengths longer than 42 km. The large relief of the islands is most obvious in profile 2', at wavelengths of 250 km and more. The power spectrum for the gravity (Figure 4.8) shows a similar distribution for the power of the individual profiles, although the lack of signal in profile 4' is not as obvious.

The admittance spectrum of Figure 4.9 was calculated using the averages of the power and cross correlation spectra from only the first three profiles, and the constants in Table 4.1. I justify the omission of profile 4' for two reasons. First, the observation from Figure 4.2 that profile 4' falls entirely outside the flexural arch crest, and crosses over no portion of the load. And second, the correlation between depth anomaly and gravity is low for profile 4' at all wavelengths, as seen in Figures 4.10 and 4.11, which illustrate the low coherence and large phases for profile 4' over even the longest wavelength ranges. The inclusion of the data from profile 4' changes the admittance error significantly below wavelengths of 60 km, but it does not alter the value of the admittance itself significantly.

The signal from the compensation of the plate is contained in the coherent portion of these spectra, so I shall only consider the spectra from profiles 1', 2', and 3' at wavelengths of 55 km and longer. The weighted exponential regression shown as a dotted line in Figure 4.9 is a fit to the portion of the admittance curve that is dominated by the e^{-kz_t} term, and provides an estimate of both the average depth of the anomaly, and the mean density of the feature. Values from this fit are an average depth of 2290 m, and a density of 2350 kg/m^3, values which are both low. The low value for the average depth is due to the overemphasis of the topography in (4.9), compared to the formulation (4.8), and the low value for the density is due to the two-dimensional approximation. Similar fits to each of the separate lines yield densities of 2560, 2950, and 2160 kg/m^3, and average depths of 3.56, 2.53, and 2.76 km for lines 1, 2, and 3 respectively. This is can be interpreted as the result from a model that assumes that the anomaly is produced entirely by a density contrast at the seafloor, and so ignores any compensation mechanism.

Using a downhill simplex algorithm, I determined the weighted best fit admittance to the data from each profile and from the combination of all three profiles. The results are presented in Table 4.3, with accompanying Figures 4.12, 4.13, 4.14, and 4.15. The admittance from the combined profile, illustrated in Figure 4.12, has a best fit elastic plate thickness of 17 km, but the fits from plates with elastic thicknesses of 14 to 25 km are not significantly different.

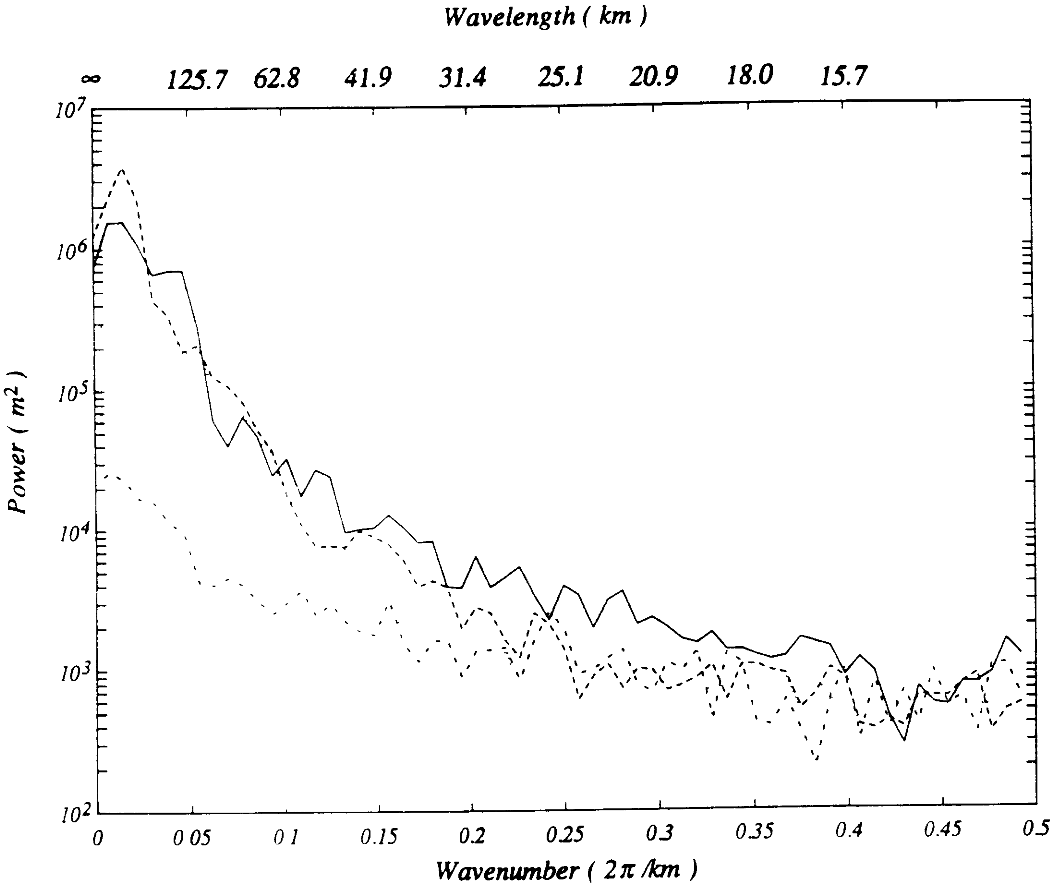

Figure 4.7. Power spectral density of the depth anomaly along profiles 1', 2', 3', and 4'. Horizontal wavenumber axis runs from $k = 0$ (infinite wavelength) to the Nyquist wavenumber, $k_N = \pi$ ($\lambda_N = 2$ km), in units of km^{-1}. Vertical axis is in units of m^2 and is the power of the depth anomaly in each wavenumber band. Spectrum 1' is indicated by the solid line, spectrum 2' by the dashed line, spectrum 3' by the dotted line, and spectrum 4' by the dash–dotted line. Spectra are determined by the Welch method. The low relief of profile 4' is visible as reduced power in the longer wavelengths, and the high relief of profile 2' is visible as a peak in the long wavelengths (270 – 400 km).

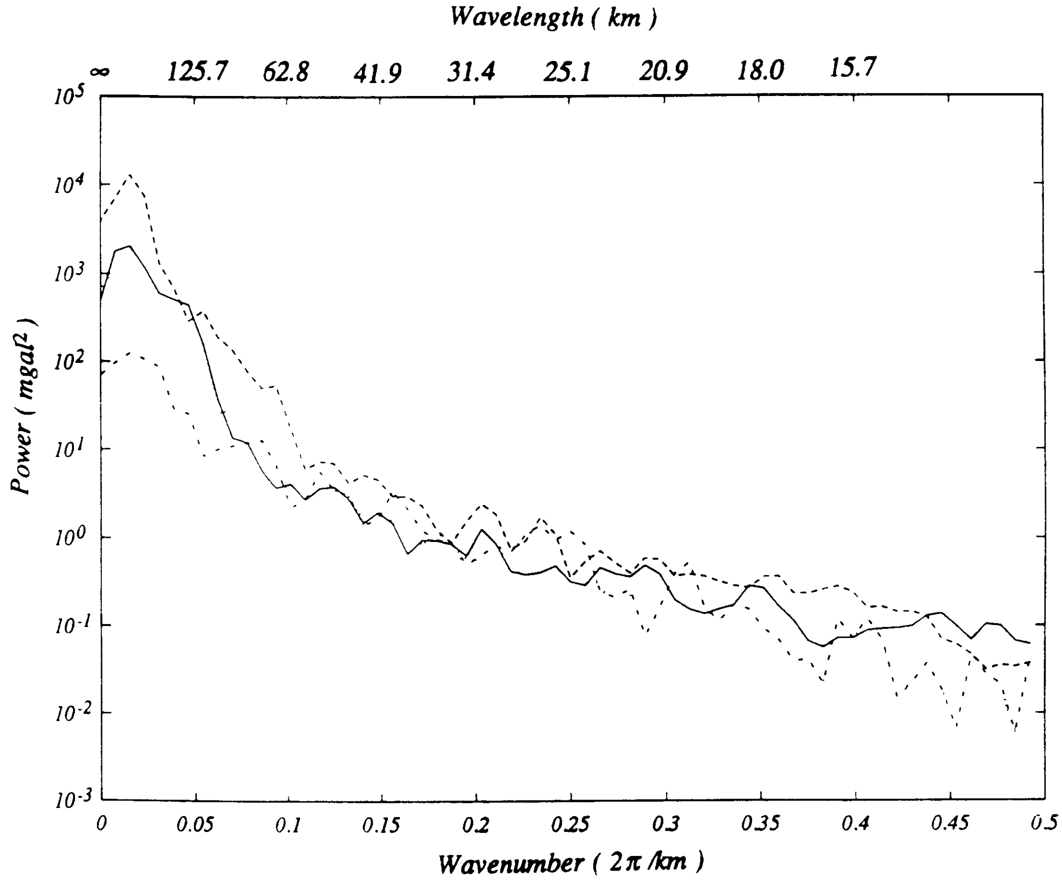

Figure 4.8. Power spectral density of the gravity anomaly along profiles 1', 2', 3', and 4'. Ordinate units are mgal^2. Profiles and units of abscissa are as in Figure 4.7.

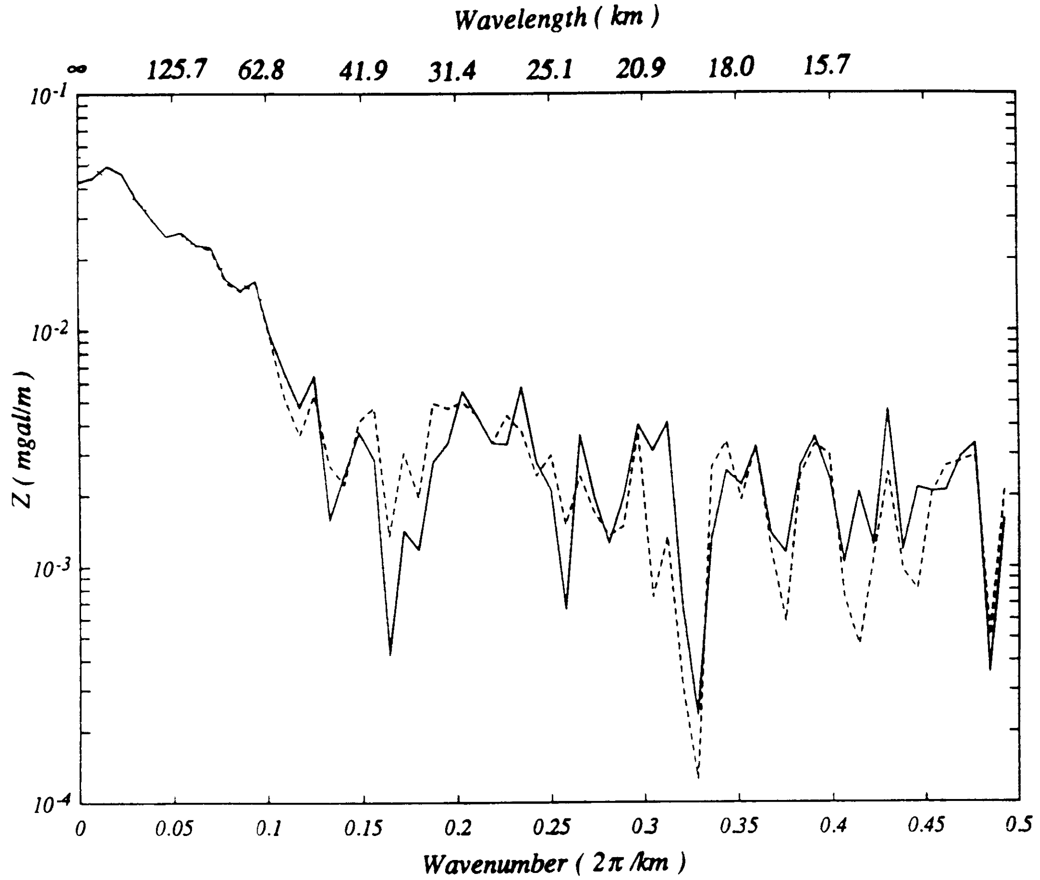

Figure 4.9. Admittance spectrum, or the amplitude of the complex transfer function between the depth and gravity anomalies in the wavenumber domain. Ordinate is in units of mgals per meter of relief, and abscissa is as in Figure 4.7. Solid line is admittance from the combination of the profiles 1', 2', and 3', while the dashed line is the admittance for the combination of all four profiles. Combinations are made by averaging the power and complex cross–correlation spectra in each wavenumber band. Dotted line is straight line fit to admittance for wavenumbers between 0 and 0.12, yielding a density for the load, ρ_c, of 2350 kg/m^3 and an average depth z_t of 2.29 km. The observed z_t for all lines combined is 3.25 km.

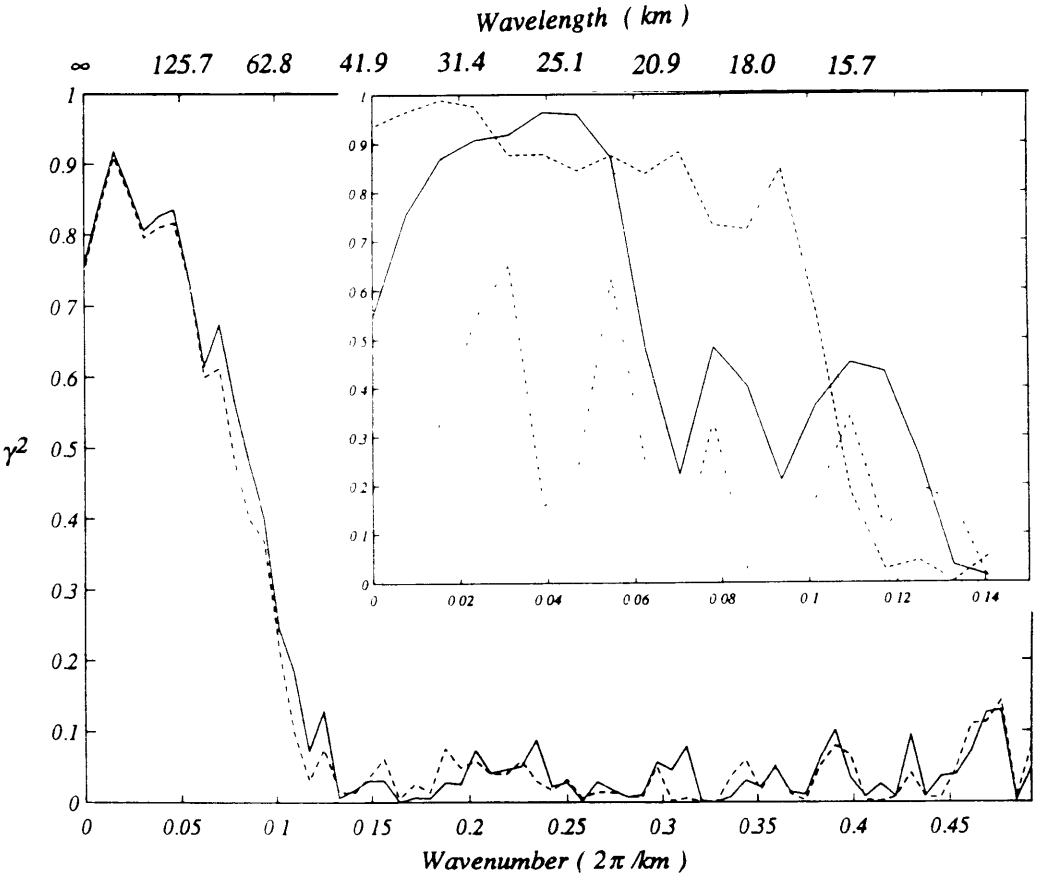

Figure 4.10. Coherence of the depth anomaly and the gravity. Solid line is coherence for the combination of the profiles 1', 2', and 3', while the dashed line is the coherence for the combination of all four profiles. High coherence is observed at wavelengths over 60 km. INSET: Coherence of individual profiles on an expanded wavenumber scale. Wavelengths range from 804.2 to 44.7 km. High coherences are observed for profiles 1'(solid), 2'(dashed), and 3'(dotted), while profile 4'(dash-dotted), which lies outside the flexural arch, does not show a high coherence pattern which is indicative of noise problems at the level of relief and gravity observed.

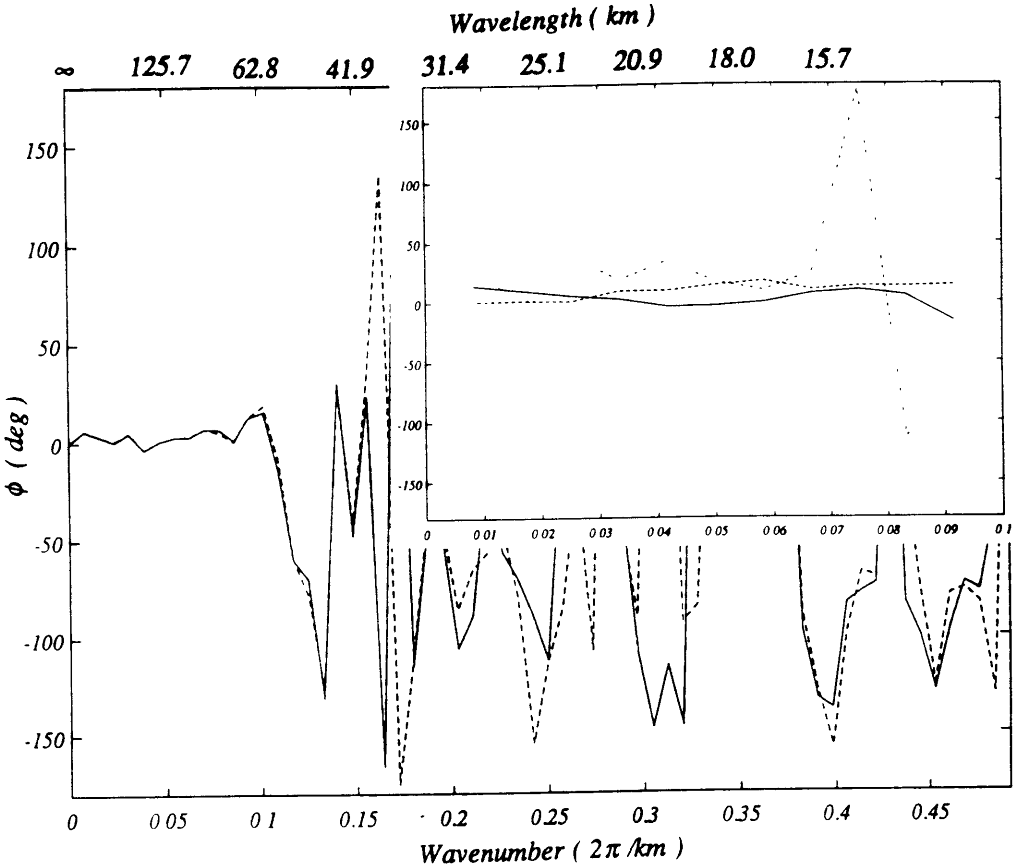

Figure 4.11. Phase of the admittance. Solid line is phase of the admittance from the combination of the profiles 1', 2', and 3', while the dashed line is the phase of the admittance for the combination of all four profiles. Phases near zero result when the admittance has a very small imaginary part, something expected for purely real signals. INSET: Phase of individual profiles on an expanded wavenumber scale. Wavelengths range from 785 to 68 km. Small phases are observed for profiles 1'(solid), 2'(dashed), and 3'(dotted), while profile 4'(dash-dotted), which lies outside the flexural arch, shows an irregular phase starting at wavelengths of 95 km, with a generally wider spread of values.

TABLE 4.3. Weighted fits to admittance values from combined and separate lines

profile	T_e (km)	σ_{T_e}† (km)	ρ_c (kg/m^3)	$\sigma_{\rho c}$ (kg/m^3)	z_m (km)	σ_{zm} (km)	z_t (km)	σ_{zt} (km)	χ_ν^2
1'	4.9	+5.3 -1.3	2366	±50	9	+16 -3	2.86	+0.14 -0.16	0.592
2'	16.9	<+200 -6.6	2731	±70	9	<+200 -30	2.19	+0.22 -0.19	1.079
3'	29.5	<+200 -15.5	2215	±70	6	<+300 -24	2.81	±0.18	1.364
1', 2'&3'	16.8	+8.7 -2.5	2560	±70	9	+38 -24	2.86	+0.22 -0.15	0.875

†: Uncertainties for T_e , z_m, and z_t are not necessarily symmetrical because of the non-linearity of the admittance function in these parameters. Uncertainties are those values that result in changes in χ_ν^2 of $1/\nu$, where ν is the number of degrees of freedom in the fit, in this case 25. Entries with the < sign indicate that values above this level produce no statistically significant change in the value of χ_ν^2 , and there is therefore no effective constraint in this direction for the parameter.

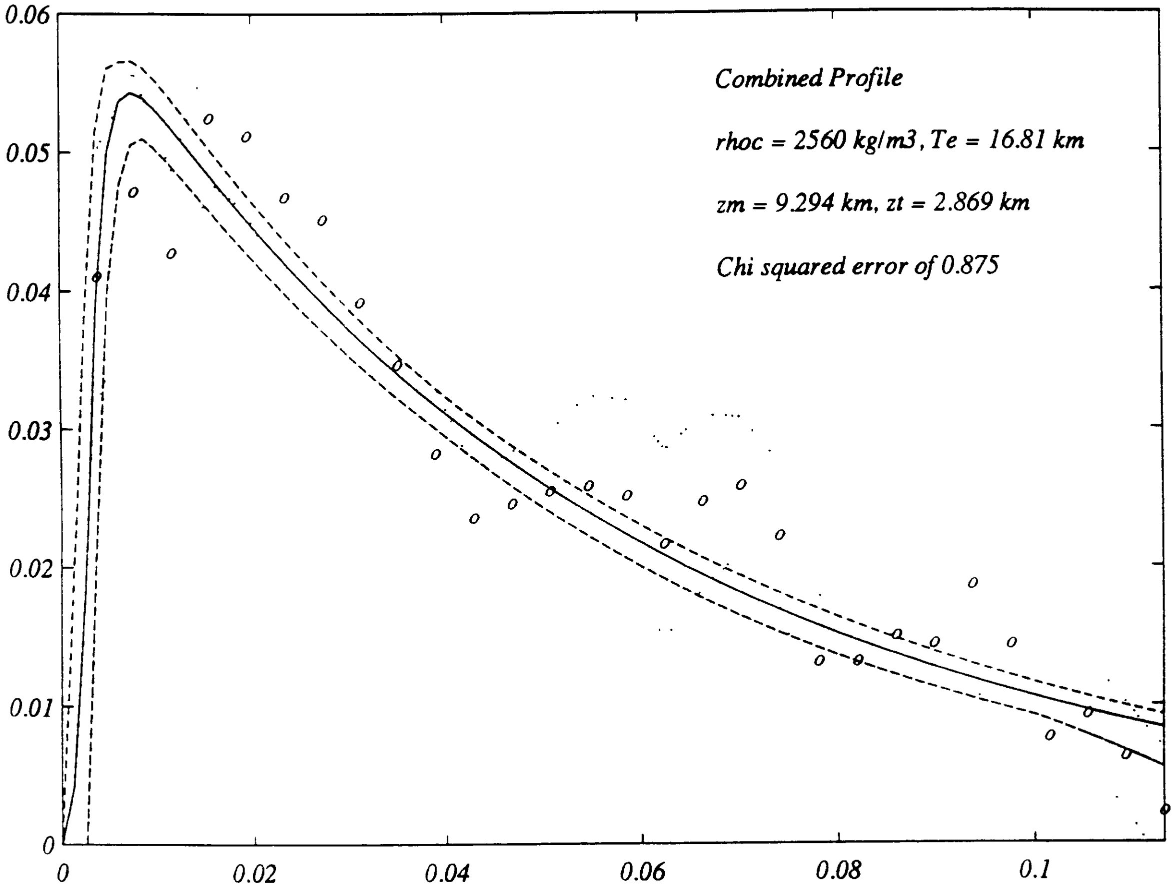

Figure 4.12. Admittance from combined profiles 1', 2', and 3' on an expanded wavenumber scale, from $\lambda = \infty$ to $\lambda = 55.5$ km. Observed admittance is indicated by the open circles, with errors indicated by the dotted lines. Theoretical admittance for the weighted best fitting parameters is indicated by the smooth curve, with the cumulative maximal uncertainty indicated by the dashed lines. All admittance curves wholly within these lines match the data at the same level of statistical significance. Non-zero admittance at $k=0$ and drop-off behavior above $k=.1$ of the lower uncertainty curve is due to the size of σ_{zm}, which allows large 'negative depths' to the Moho.

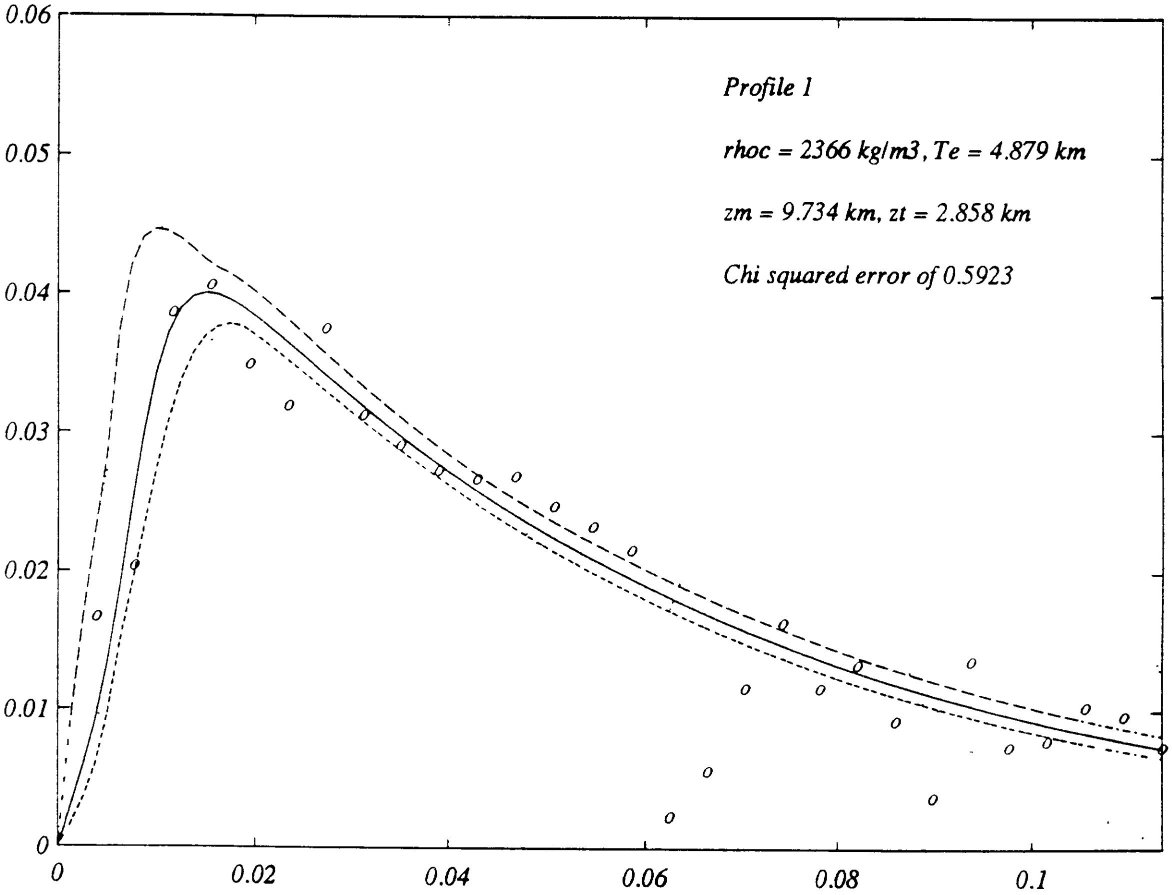

Figure 4.13. Admittance for profile 1' only, with symbols as in Figure 4.12. The density of the load, ρ_c, is low because line 1 passes to the south-east of Fatu Hiva. This is in fact a failure of the two-dimensional approximation. Observed average z_t is 3.16 km.

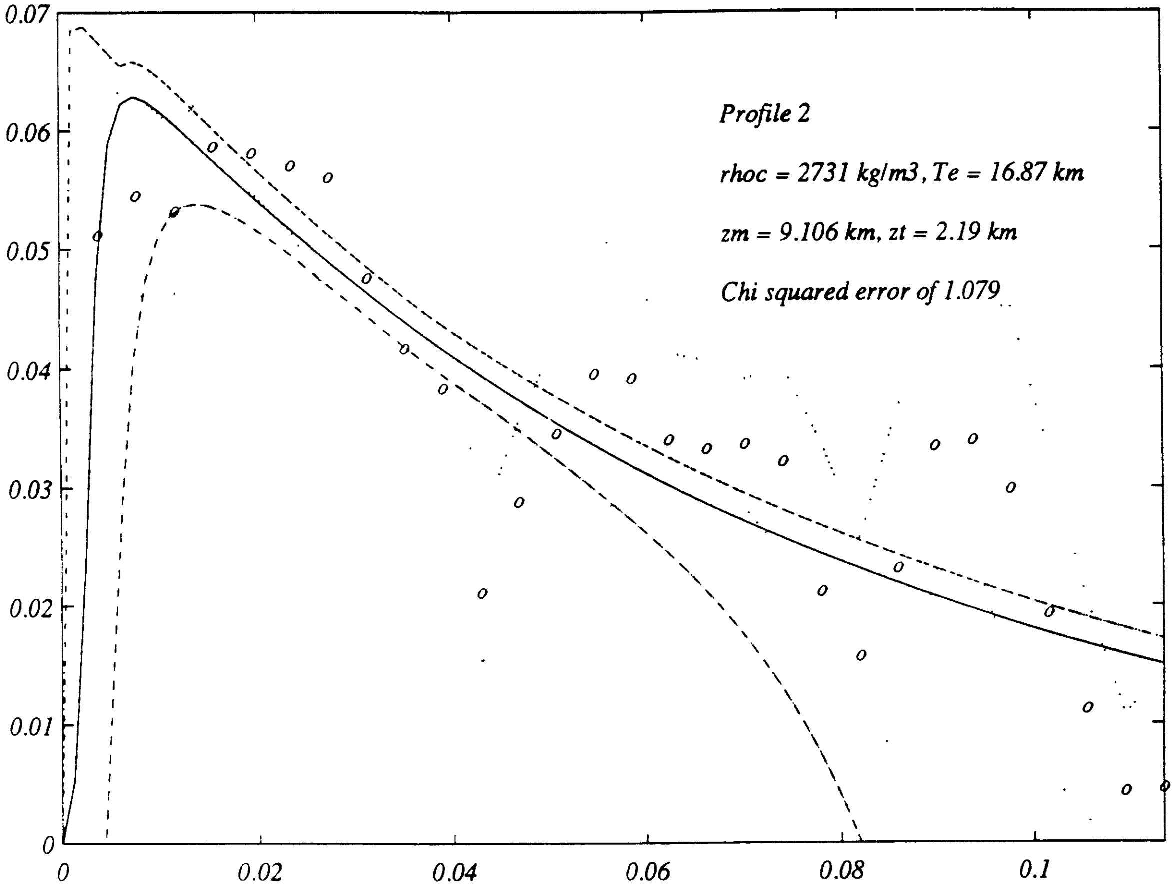

Figure 4.14. Admittance for profile 2' only, with symbols as in Figure 4.12. Load density is higher since line 2 passes over the center of the island chain, and the bulk of the island volcanic edifice. As listed in Table 4.3, T_e can only be constrained to be larger than 10.3 km by this data, since there is no statistically significant variation of χ_ν^2 for any larger value of the elastic plate thickness. Similarly, the depth to the Moho cannot be constrained in any realistic manner by the admittance. As with the uncertainties in the combined profile, the behavior of the minimal bounds are due to the large uncertainty in depth to the Moho. Observed z_t is 2.58 km.

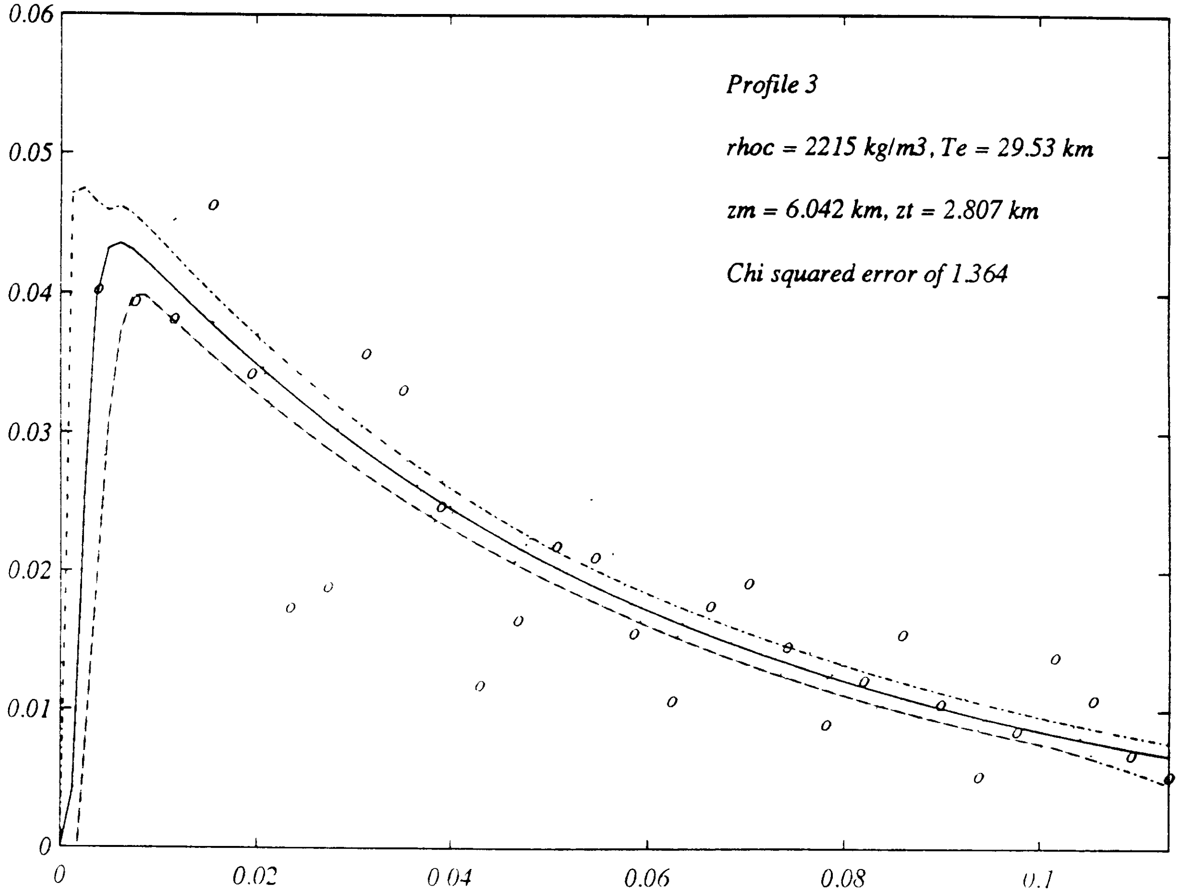

Figure 4.15. Admittance for profile 3' only, with symbols as in Figure 4.12. The elastic plate thickness can only be constrained to be greater than 4 km by the data, and the depth to the Moho is again not realistically constrained. Density is low, since line 3 crosses the moat and the infilling sediments over most of its length, to the north-west of Eiao. Observed average z_t is 3.33 km.

Each parameter has uncertainties that cause a change in the reduced chi-square error, χ_ν^2, of $1/\nu$, a statistically significant change. I have calculated the admittance for each of these uncertainty limits, and taken the extrema as the bounds illustrated in the plots. It should be noted that the tabulated uncertainties represent the projection of the uncertainties in the full parameter space onto the single dimensions of the individual parameters, rather than a joint uncertainty. Joint uncertainties are larger, and would be expressed as wider extremal bounds in the plots.

Since the weighted best fit admittance is calculated for two-dimensional features, the elastic plate thicknesses will be overestimated, and the density underestimated [*Ribe,* 1982; *Watts et al.,* 1988]. For profiles 2' and 3', the admittance data do not provide an upper bound for the elastic plate thickness. Positive variations of any size with other parameters fixed do not produce a statistically significant change in the error. The lower bounds indicated by the fits are 13 and 14 km respectively. The fit to profile 1' gives a value of between 4 and 10 km for the elastic plate thickness, with a best fit at 5 km.

Densities for the crust are linear parameters of (4.6), and so exhibit symmetric uncertainties from 50 to 70 kg/m^3, and range from 2215 kg/m^3 for profile 3', to 2730 kg/m^3 for profile 2'. As discussed above, these values vary as a result of the two-dimensional approximation. The admittance does not effectively constrain the depth to the Moho, since changes over any reasonable range (5 to 20 km) do not produce any significant change in the error. The large values for the uncertainties in the depth to the Moho lead to the possibility in the model space of negative depths to the Moho, which are expressed as a widening in the extrema with increasing wavenumber.

The observed average depth, z_t, for all profiles combined is 3.25 km, deeper than the best-fit value of 2.86 km, although the observed value is only slightly deeper than the assigned uncertainty. As discussed above, these values are biased by the formulation of the admittance estimator (4.8).

For each of the profiles, the greatest influence on the fit is exerted by the admittance estimate at the longest wavelength. Reaching longer wavelengths by altering the sampling frequency requires shorter wavenumber intervals for the admittance estimation. Unfortunately, an increase in the number of wavenumber bins implies an increase in the scatter of the spectral estimate. The only way to reduce the variance of the spectral estimates and retain the same number of wavenumber bins is to average various samples of the feature together, and this implies several crossings of the feature. The combination of the three profiles reduces the scatter of the estimate in Figure 4.12 when compared with the estimates of the single profiles, but there is still a fair amount of scatter which cannot be reduced further – there are no more profiles over the feature.

The best fits and their extrema illustrate the danger of trying to fit admittance visually. The maximum of the admittance estimate, an attractive feature for a visual fit, does not necessarily correspond to the maximum of the best fit, and while the extrema define a rather narrow band in most cases, any admittance curve wholly within the extrema is statistically indistinguishable from the best fit.

The spectral approach carries several assumptions about the sampled area that must be borne in mind. First, the compensational mechanism of the plate (whatever it might be) is assumed to be isotropic and uniform. Second, the loading ratio from above and below is assumed to be similar over the entire area, and last, the density variations of the crust are assumed to be uncorrelated with the observed bathymetry. For island loads, the third condition is violated, and the thermal contribution from a hotspot plume violates the second assumption, and probably affects the first assumption.

4.4.5.3. Forward modelling

The bathymetry observed by the center beam of the SEABEAM system was used as the database for the two-dimensional calculations of plate flexure. Free-air gravity lines were generated using a Fourier expansion of the bathymetry and Moho deflection, which was assumed to be deflected in the same manner as the plate. The free parameters were the elastic plate thickness, T_e, the density of the crust, ρ_c, and the depth to the Moho, z_m, while all other constants or quantities are as listed in Table 4.1. The Fourier expansions were taken to the order five, where contributions to the field fell below 0.8 mgal. Using the algorithm outlined in Appendix C, the variance of the fit was minimized in the space defined by the three parameters, using two sets of constraints. The first set constrained the parameters to positive values, and the second to geophysically reasonable values. Best fits in these parameters are presented in Table 4.4 and illustrated in Figures 4.16, 4.17, and 4.18.

From the table and figures it can be seen that there are some serious questions about the applicability of the two-dimensional model to this data. For profile 1', the lack of a flexural moat results in the extremely high plate thickness and low density. The model cannot produce an adequate fit to the data. Profile 2' has reasonable plate thicknesses and densities, but the depth to the Moho is unreasonable. The Moho depth is depressed to reduce the contribution of the e^{-kz_m} term, which overestimates the magnitude of the gravity moat, since the load of the islands has been increased by using the two-dimensional approximation. When the Moho is constrained to reasonable depths, the gravity moat is overestimated, as can be seen in Figure 4.17. The third profile suffers from the opposite effect: the observed gravity moat is much too large for the two-dimensional bathymetry, and the e^{-kz_m} term contribution is increased by making the Moho as shallow as possible (if the parameters are not constrained to be positive, the Moho is actually fitted at a height 17 km *above* the islands). Constraining the Moho to reasonable depths forces an under-fitting of the gravity moat, as seen in Figure 4.16.

I noted in section 4.4.5.1. that the theoretical admittance function (4.10) gave a form of (4.8) which was identical to that of (4.6), the forward modelling of the gravity. A comparison of Tables 4.3 and 4.4 quickly shows that the results differ greatly when only the parameter values themselves are considered. However, when the size of the uncertainties is considered, much of the discrepancy can be accommodated. From the range of values for the variance of the fit to profile 1', the uncertainties in the forward modelling scheme are also bound to be

TABLE 4.4. Iterated two-dimensional fits to free-air gravity.

Profile	T_e (km)	ρ_c (kg/m^3)	z_m (km)	s^2 (mgal^2)
	$0<T_e<\infty$	$0<\rho_c<\infty$	$0<z_m<\infty$	
1'	215	1690	18	45.60
2'	10	2680	45	16.72
3'	29	2340	0.	30.86
	$0<T_e<40$	$2<\rho_c<3$	$8<z_m<16$	
1'	40.	2000.	16.	80.27
2'	32	2500	16.	51.70
3'	26	2330	8.	32.64

T_e: Elastic plate thickness; ρ_c: Density of the crust; z_m: Depth to the Moho; s^2: Sample variance for the fit. Parameter entries with decimal points are at the constraining bounds.

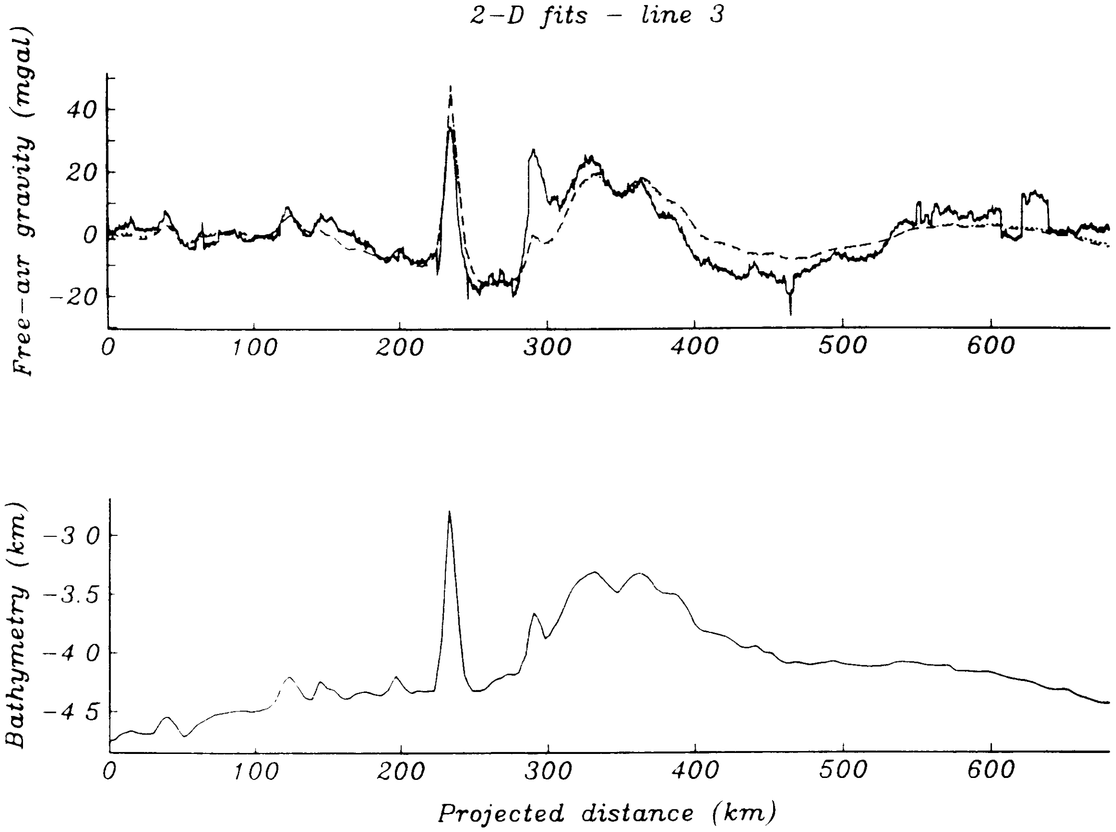

Figure 4.16. Topography and two-dimensional fit to the free-air gravity of profile 3'. The solid line is the shipboard data, the dotted line is the fit with positively constrained parameters, and the dashed line is the fit with the parameters constrained to reasonable values. Parameter values for the second fit were: $T_e = 26$ km, $\rho_c = 2330$ kg/m^3, and $z_m = 8.$ km. The figure illustrates all the problems with the two-dimensional approximation: the seamount at 230 km is modelled as a ridge, and so causes gravity overestimation, the seamount at 290 km is only represented by the bathymetry across its far shoulder, and so causes gravity underestimation, while the position of the line at the edge of the chain guarantees the underestimation of the moat.

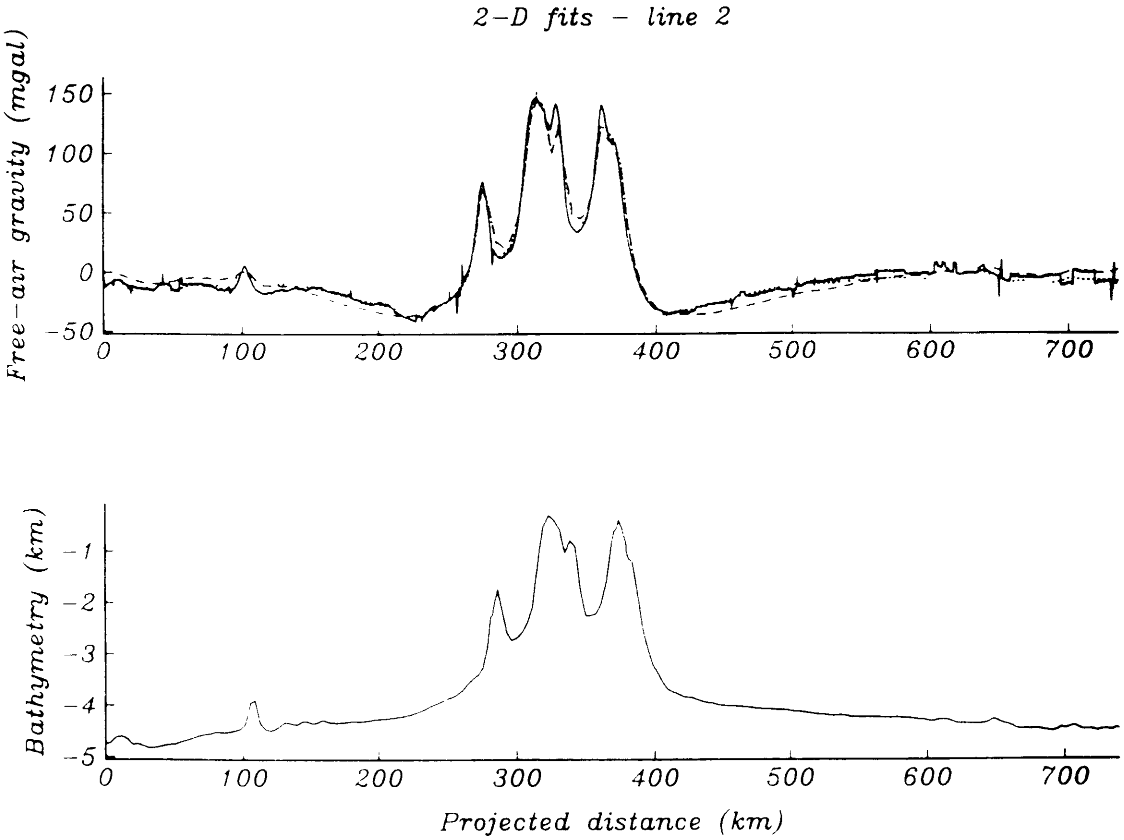

Figure 4.17. Topography and two-dimensional fit to the free-air gravity of profile 2'. The solid line is the shipboard data, the dotted line is the fit with positively constrained parameters, and the dashed line is the fit with the parameters constrained to reasonable values. Parameter values for the second fit were: $T_e = 32$ km, $\rho_c = 2500$ kg/m^3, and $z_m = 16.$ km. While the moat can be fitted with the parameters unconstrained, the required depth to the Moho is very large. Constraining the Moho to reasonable depths causes the moat to be overestimated.

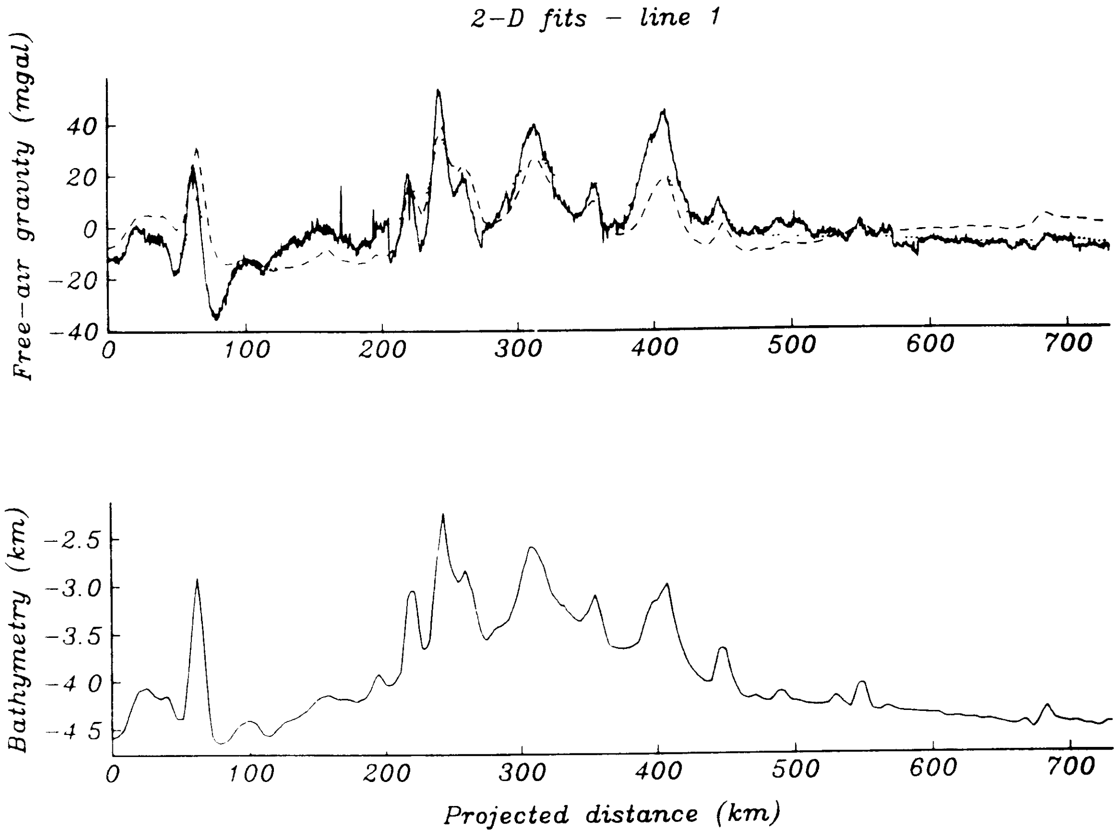

Figure 4.18. Topography and two-dimensional fit to the free-air gravity of profile 1'. The solid line is the shipboard data, the dashed line is the fit with the parameters constrained to reasonable values, while the dotted line is the fit with two extra parameters, geoid height and half-width. The parameter values are as follows: Dash - ρ_c = 2000 kg/m^3; T_e = 40 km; z_m = 16 km. Dotted - ρ_c = 1682 kg/m^3; T_e = 112 km; z_m = 42 km; N = 78 m; σ_N = 1545 km. The models cannot fit the data in any satisfactory manner.

large. The differences in the grouping of the data and the use of different minimization algorithms also contribute to the discrepancy.

To account for the possibility that the swell surrounding the islands might be contributing to the longer wavelength features of the overall gravity, fits were made with two more parameters, the height and half-width of the geoid anomaly from a regional swell. For profiles 2' and 3' this artifice collapsed to a small feature of width similar to the islands, and could no longer be interpreted as a contribution from the regional swell. For line 1', which does seem to have a longer wavelength component, the half-width remained at values near 1500 km, but the geoid height increased to over 70 m, with the other parameters behaving as before. The variance of the fit was not reduced significantly by the addition of the extra parameters, and I conclude that this model is inappropriate for profile 1'.

It is interesting to note that the observed bathymetry, even when approximated with the two-dimensional model, produces an asymmetric arch as observed in the data. The asymmetry is therefore more due to the configuration of the load than any difference in plate thickness from one side of the islands to the other. As expected, the fits from the ends of the chain are much worse than the fits from the central area. However, even the central area cannot be fitted satisfactorily within this model. I must use a full three-dimensional model to account for the geometry of the islands.

4.4.6. Three-dimensional models

The 5 km grid described in section 4.3 was used as the database for the three-dimensional calculations of plate flexure. Free-air gravity grids were generated using a Fourier expansion of the bathymetry and Moho deflection, which was assumed to be deflected in the same manner as the plate. The Fourier expansions were again taken to order five, where contributions to the field fell below 0.8 mgal. The free parameters were the elastic plate thickness, T_e, the density of the crust, ρ_c, and the depth to the Moho, z_m, while all other constants or quantities are as listed in Table 4.1. Using the algorithm outlined in Appendix C, the variance of the fit was minimized in the space defined by the three parameters, using two sets of constraints. The first set constrained the parameters to positive values, and the second to geophysically reasonable values. Results for the fits are presented in Table 4.5, and are illustrated in Figures 4.19, 4.20, and 4.21.

As with the two-dimensional modelling, line 1 cannot be fitted in any satisfactory manner by this simple model. The elastic plate thickness is again very high as the algorithm tries to match the observed gravity, which has no gravity moat corresponding to the flexure of the plate. The density is low to compensate for the lack of a negative contribution from the Moho, while the depth to the Moho is not well constrained at all. A fit without the positive constraints places the Moho at a *height* of 11 km, while similar variances are obtained for other values of z_m. Since the three-dimensional model cannot match the observed gravity for line 1, I must conclude that the model is inappropriate for this area.

For the remaining lines that do show a flexural moat, the fit is excellent. For line 2, while the free fit has a Moho depth of 29 km, a constrained fit only increases the variance by 6%. The elastic plate thickness is 16 km for both the positive and the constrained fits, with a crustal density of 2670 kg/m^3. For line 3, the improvement over the two-dimensional model is quite evident in the variance and the parameter values. While the two-dimensional model has a variance of 30.86 mgal^2 for the positively constrained fit with one of the parameters at a bound, the three-dimensional model halves the variance with all parameters still within their bounds. Even constraining the depth to the Moho to be no shallower than 8 km only changes the variance of the fit by 0.5%. In Figure 4.22 the change in variance for lines 2 and 3 is illustrated as a function of Moho depth, evaluated for the constrained parameter values.

4.4.7. Convergence of the series

In his paper on the calculation of potentials, *Parker* [1972] points out that the series (4.4) may become inaccurate when the bathymetry is shallower than the spacing of the observation points, a condition encountered with the 5 km spacing of the depth anomaly grid.

TABLE 4.5. Iterated three-dimensional fits to free-air gravity.

Line	T_e (km)	ρ_c (kg/m^3)	z_m (km)	s^2 (mgal^2)
	$0<T_e<\infty$	$0<\rho_c<\infty$	$0<z_m<\infty$	
1	129	1770	0.	50.14
2	16	2660	29	17.64
3	26	2630	4	17.34
	$0<T_e<40$	$2<\rho_c<3$	$8<z_m<16$	
1	40.	2000.	16.	73.12
2	16	2680	16.	18.69
3	23	2690	8.	17.43

T_e: Elastic plate thickness; ρ_c: Density of the crust; z_m: Depth to the Moho; s^2: Sample variance for the fit. Parameter entries with decimal points are at the constraining bounds.

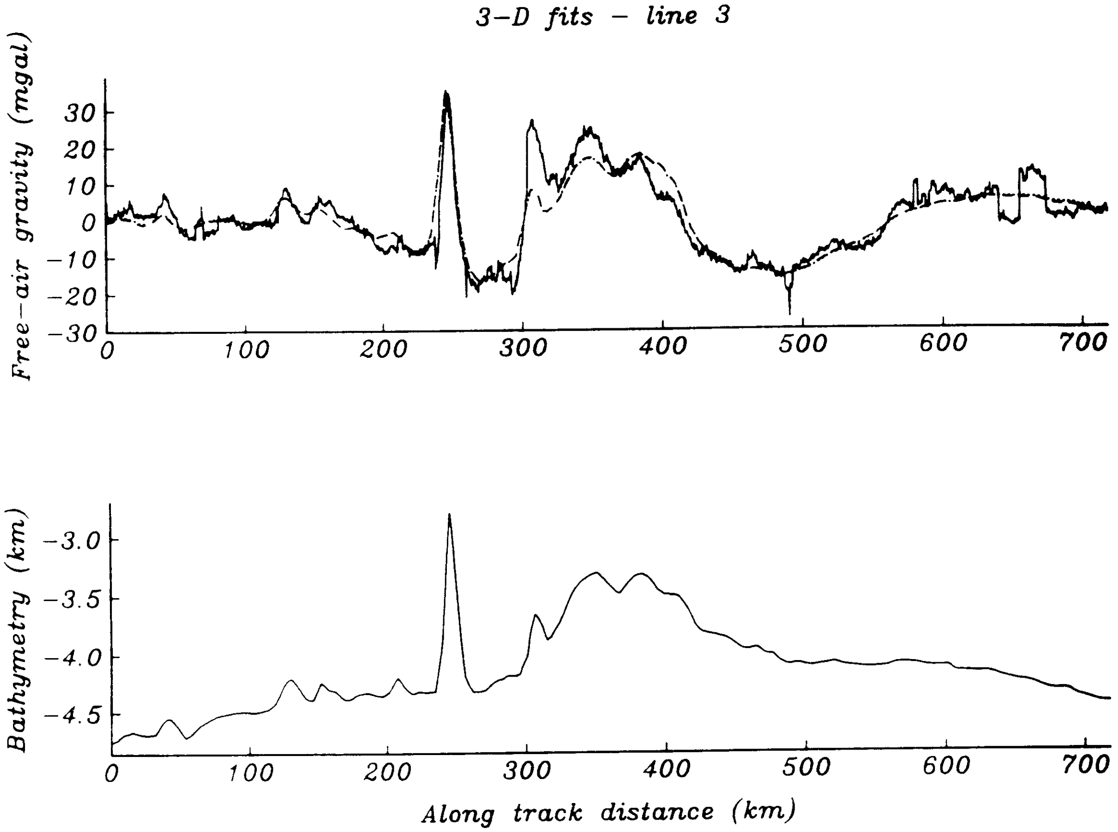

Figure 4.19. Topography and three-dimensional fit to the free-air gravity of line 3. The solid line is the shipboard data, the dotted line is the fit with positively constrained parameters, and the dashed line is the fit with the parameters constrained to reasonable values. Parameter values for the second fit were: $T_e = 23$ km, $\rho_c = 2690$ kg/m^3, and $z_m = 8.$ km. The fit to the seamount and the moat at 450 km are greatly improved over the two-dimensional fits of Figure 4.16. Main source of error is in the central region of the line, and is due to the averaging effect of the 5 km grid, which causes an underestimation of the bathymetry for the seamount at 310 kilometers distance.

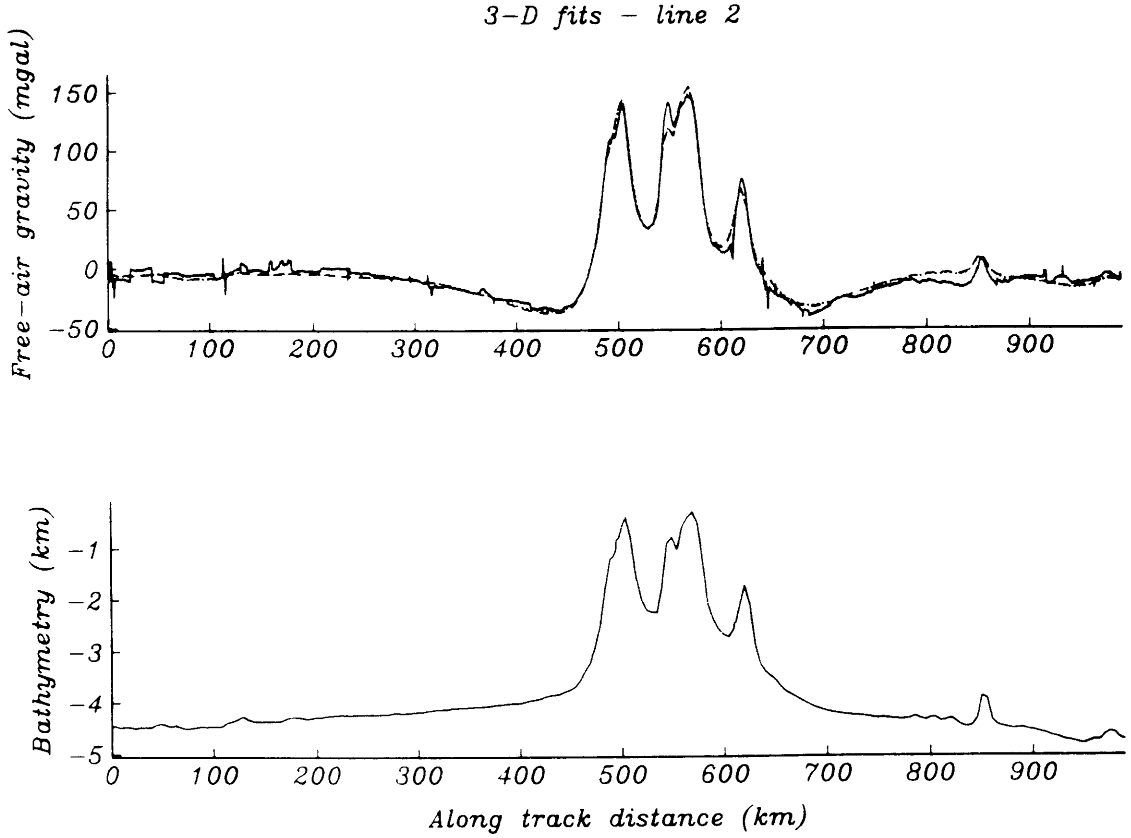

Figure 4.20. Topography and three-dimensional fit to the free-air gravity of line 2. The solid line is the shipboard data, the dotted line is the fit with positively constrained parameters, and the dashed line is the fit with the parameters constrained to reasonable values. Parameter values for the second fit were: T_e = 16 km, ρ_c = 2680 kg/m^3, and z_m = 16. km. The fit to the moat is greatly improved compared to the two-dimensional model of Figure 4.17. Residual misfit is probably due to the averaging process of the model and the 5 km grid.

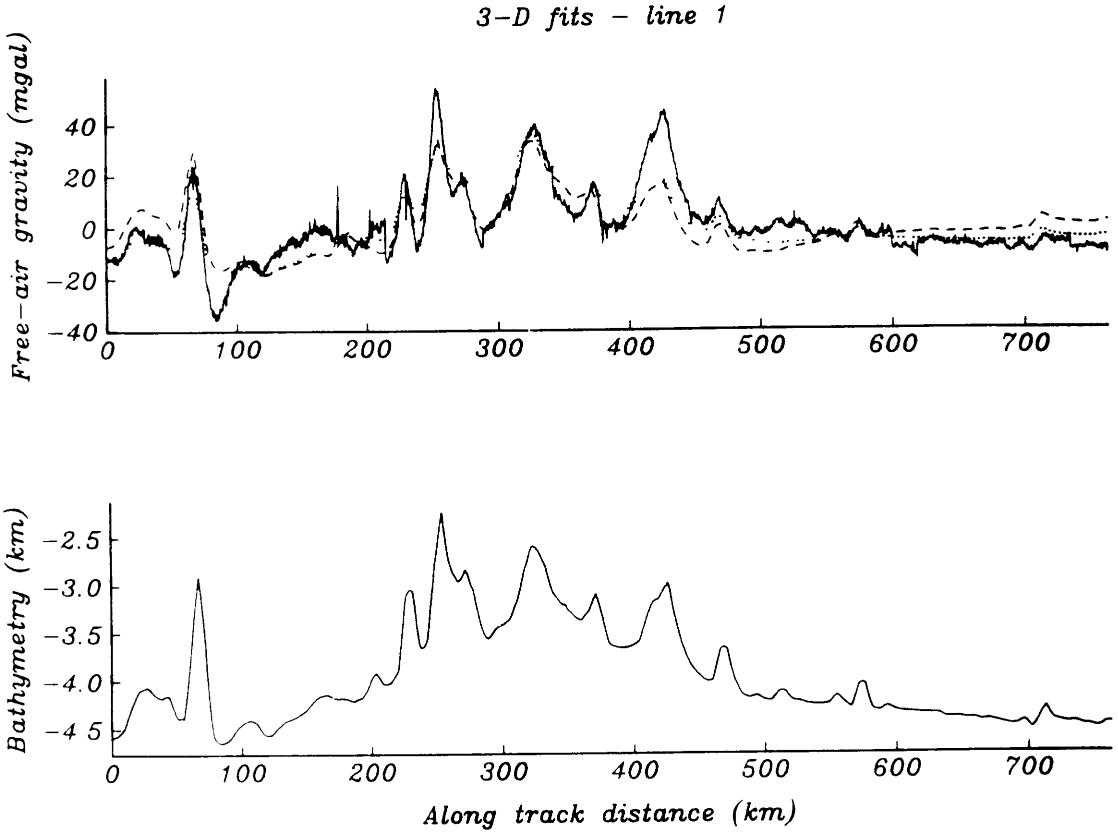

Figure 4.21. Topography and three-dimensional fit to the free-air gravity of line 1. The solid line is the shipboard data, the dotted line is the fit with positively constrained parameters, and the dashed line is the fit with the parameters constrained to reasonable values. Parameter values for the second fit were: T_e = 40. km, ρ_c = 2000. kg/m^3, and z_m = 16. km. The model cannot fit the long wavelength component of the data in any satisfactory manner.

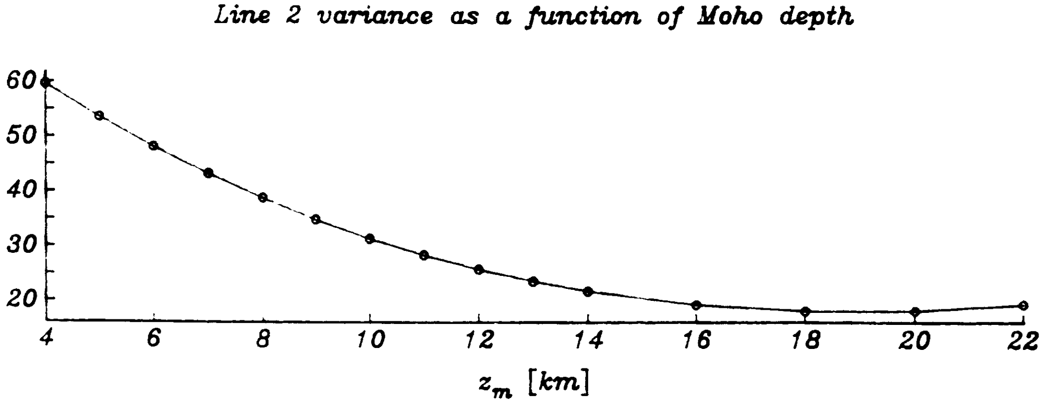

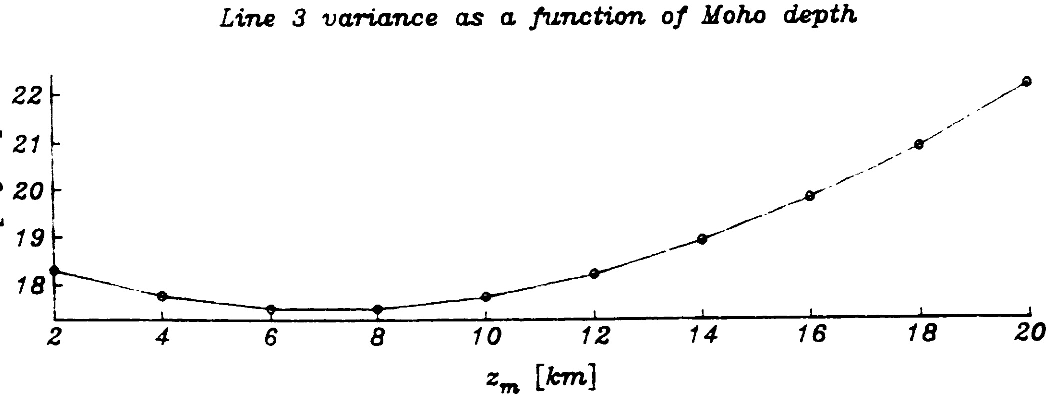

Figure 4.22. Variance of the fit to the data of lines 2 and 3 as a function of Moho depth. The small change in the variance near the minima is an indication that the fit is insensitive to the Moho depth used in the fit. The other parameters have the values as follows. For line 2: ρ_c = 2680 kg/m^3; T_e = 16 km. For line 3: ρ_c = 2690 kg/m^3; T_e = 23 km.

Furthermore, since there is emergent topography, there is no guarantee that the series will converge.

Reducing the spacing of the depth anomaly grid to the 500 m minimum depth observed along the shiptrack is impractical for two reasons: first, the control on the topography is already poor, since most of the input for the grid comes from the DBDB5 dataset, which is spaced at about 10 km. Interpolation of this data any further than the 5 km grid does not make any sense. Second, even if there was topographic information, the implied grid is over 4 million points in size, and iteration involving Fourier transforms at each step would become extremely costly.

I compared the gravity from the series with a line integral formulation for the gravity from the topography [*Talwani and Ewing,* 1960] and found that the two calculations agree within 5 mgal over the length of the central line, implying that even with the spacing of 5 km and emergent topography, the violation of the conditions for convergence is not severe enough for the series to diverge within the first few terms. As seen in Figure 4.23, the contribution from the terms at orders 5 and 6 are nearly opposite in sign, and less than 1 mgal.

4.5. DISCUSSION

In order to explain the rather strange behavior of the gravity data from line 1, I investigated several possible factors. The first of these was off-track bathymetry, which becomes more of a problem in the southern sections because of the scarcity of shiptracks in the area. The second factor to be investigated was the possibility that the Marquesas Fracture Zone is in fact unlocked, making the continuous plate assumption invalid. The third factor was the possibility that the plate is loaded from below, altering the predicted admittance and coherence patterns of gravity and topography.

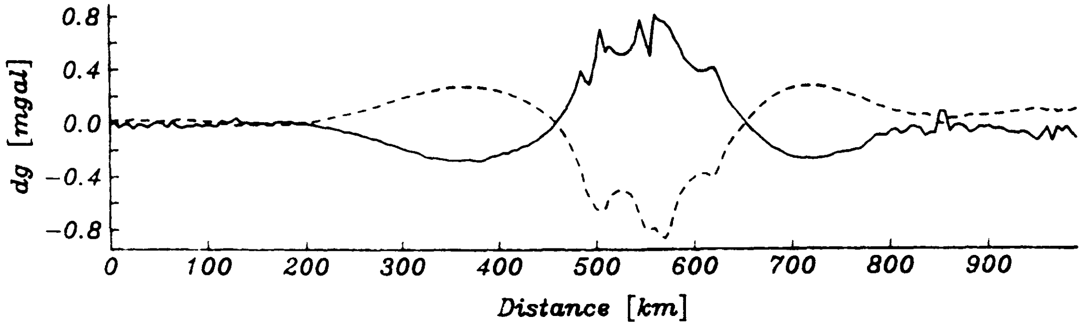

Figure 4.23. Contribution to series from the fifth and sixth terms. Calculation is from line 2 bathymetry data. Fifth term is the solid line, and sixth term is the dashed line. Contributions to the gravity anomaly fall below 0.9 mgal for the fifth term, and below 0.8 mgal for the sixth term. The two contributions are very nearly opposite, so contribution by pairs is smaller than either of the maxima.

4.5.1. Off-track bathymetry

For line 1, the amplitude of the features at 250 and 350 km can be fitted with a 20 km thick plate and a density of 2600 kg/m^3, but no combination of T_e, ρ_c, and z_m can fit the other features simultaneously without the presence of a flexural moat. The lack of flexural signal causes the minimizing algorithm to stiffen the plate and reduce the density to compensate, with the depth to the Moho becoming essentially unrestrained. To investigate the possibility of off-track bathymetry in the area, the only recourse is the thin SEABEAM swath along the line. While the swath only images about 2.5 to 3 km to either side of the center beam at the depths encountered during line 1, it is sufficient to detect several seamounts in the southwestern section that are not well represented in the center beam.

Using the labelling of Chapter 2, the seamounts are features 55, 56, 57, and 58, all of whose summits fell beyond the swath, and whose bathymetry was underestimated by >200, >400, >500, and >100 meters. These seamounts lie at the distances of 159, 172, 184, and 195 km respectively on Figure 4.21, and may explain the slight gravity high in the area of the expected moat the southwest. The only other feature greatly underestimated is seamount 81, at 409 km distance, which is underestimated by at least 200 meters, and may explain the large feature in the gravity here that the model cannot match. All other features imaged by the SEABEAM swath either lie directly beneath the shiptrack or have height discrepancies of less than 100 meters. Most of the underestimated features are on the scale of the gridding interval, and since only the center beam information was included in the new map, these features are systematically underrepresented in the digital grid. It should be noted, however, that these seamounts alone *cannot* explain the absence of the flexural moat to the southeast. The moat is expected at 500 km, where only seamount 93 is underestimated by >100 meters. Because soundings from this area are so sparse, there may well be large undiscovered seamounts just beyond the swath width which obscure the flexural low in the gravity signal.

While this effect must be present to some extent on all the other lines, all the features on the other lines are much larger, and therefore fairly well represented in the grid. The apron also tends to be more well-developed to the northwest, and buries topography less than 1 to 2 km in height with high density debris from the islands. The effect on the gravity from this type of blanketing would be to smooth out the signal, since there would only be a small density contrast at the interface with the most relief, while the highest density contrast would occur at the surface with the smallest relief. The apron has not yet fully blanketed the area of the carapace, and many high density features still contribute to the gravity signal. Bathymetry gathered after *Crossgrain 2* by the later cruises of the *Ewing* (EW9013 and EW9106) shows several large seamounts that lie just to the north of the fracture zone [*McNutt and Mutter,* 1991; *McNutt, pers. comm.*, 1991], and it is reasonable to assume that several other features in this area may have escaped detection by all three cruises.

The only underrepresented seamount on the other lines occurs on line 3 at 290 km, as feature 104. This discrepancy has already been mentioned above in the captions to Figures 4.16 and 4.19. While this seamount appears in Figure 2.4 to be well resolved, the shiptrack on line 3 passes over 9 km to the northwest of the summit. Later dredging provided the bathymetric coverage seen in the figure.

4.5.2. Locked versus unlocked fracture zones

The second possibility I explored was that of the Marquesas Fracture Zone being actually unlocked and unable to sustain shear stresses, making the continuous plate model inappropriate. Using 32 GEOSAT deflection-of-the-vertical profiles, 27 bathymetric profiles, and 9 gravity profiles that cross the Marquesas Fracture Zone, *Christeson and McNutt* [1991] suggest that the fracture zone is weak along most of its length. The possible presence of a free boundary along the fracture zone, and the proximity of line 1 to this feature led to the suggestion that I alter the plate flexure model.

I calculated the deflection of the plate using a successive-overrelaxation method described in Appendix D, relaxing from an initial configuration as calculated by a continuous plate model. The gravity resulting from this deflection of the Moho and the bathymetry was calculated using

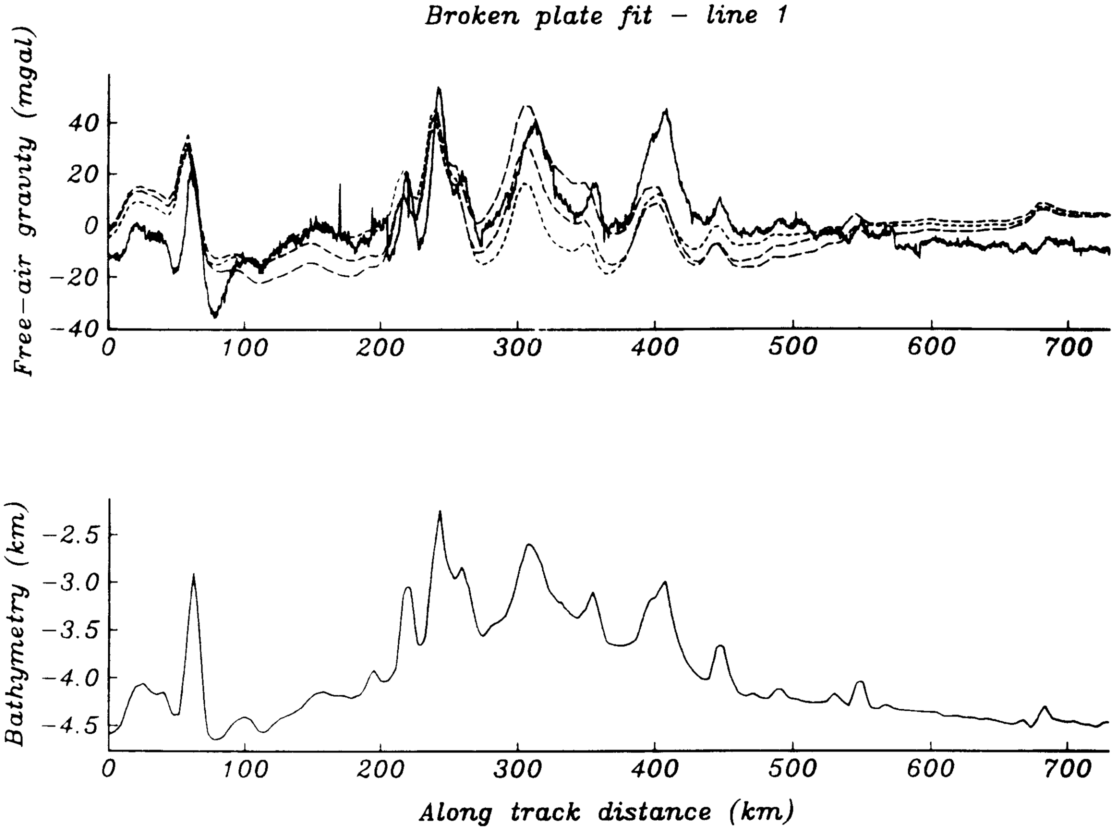

Figure 4.24. Predicted gravity from a broken plate model over line 1. Dashed lines are predicted free-air gravity for plate thicknesses of 10, 20 and 40 km, with the length of the dashes corresponding to the increasing plate thickness. All lines were calculated with ρ_c = 2590 kg/m^3, and all still show the characteristic flexural moat absent in the data.

equation (4.4), and then the profile along line 1 was extracted from the resulting grid using a simple bilinear interpolator. Three runs were completed, using a density of 2590 kg/m^3 (see below for this density) and elastic plate thicknesses of 10, 20, and 40 kilometers. As illustrated in Figure 4.24, all three runs have a conspicuous flexural moat that does not exist in the data. The presence of a free boundary at the fracture zone does not seem to substantially affect the predicted gravity along line 1. Conversely, the gravity profile of line 1 cannot be used to argue for an unlocked fracture zone. Further evidence may indicate that the Marquesas Fracture Zone is not quite as weak as suggested by *Christeson and McNutt* [1991].

The juxtaposition of seafloor of differing ages across fractures produces two effects that have been observed at other fracture zones. The first effect is the flexural alteration of the frozen scarp produced by the different cooling rates of the seafloor. The second effect is caused by the non-uniformity of the cooling rate with depth along the transform fault: the thermal bending stresses developed cause deformation of the older plate. These features have been observed at the Clarion, Clipperton, Mendocino, Murray, Pioneer, Romanche, and Udintsev Fracture Zones [*Sandwell and Schubert,* 1982; *Sandwell,* 1984; *Parmentier and Haxby,* 1986; *Wessel and Haxby,* 1990].

Figure 4.25 illustrates a model of the gravity and bathymetry predicted across a locked fracture zone corresponding to the known 12 Ma age offset at the Marquesas islands [*Kruse,* 1988], compared to the observed data during the fracture zone crossings of *Crossgrain 2*. The models were computed with the programs of *Christeson and McNutt* [1991], as modified by Alain Bonneville. The gravity model matches the observed profile as well as at any other Pacific fracture zone [*Bonneville and McNutt,* 1991], but the predicted bathymetric scarp is too small. This type of behavior is observed along much of the fracture zone surveyed during the *Ewing* cruise EW9106, with the observed scarp being too large to be consistent with the gravity within the context of the thermal stress and differential subsidence models until seafloor to the west of the Marquesas is reached [*McNutt, pers. comm.*]. The Marquesas Fracture Zone seems to conform to the differential subsidence models to the west of the islands

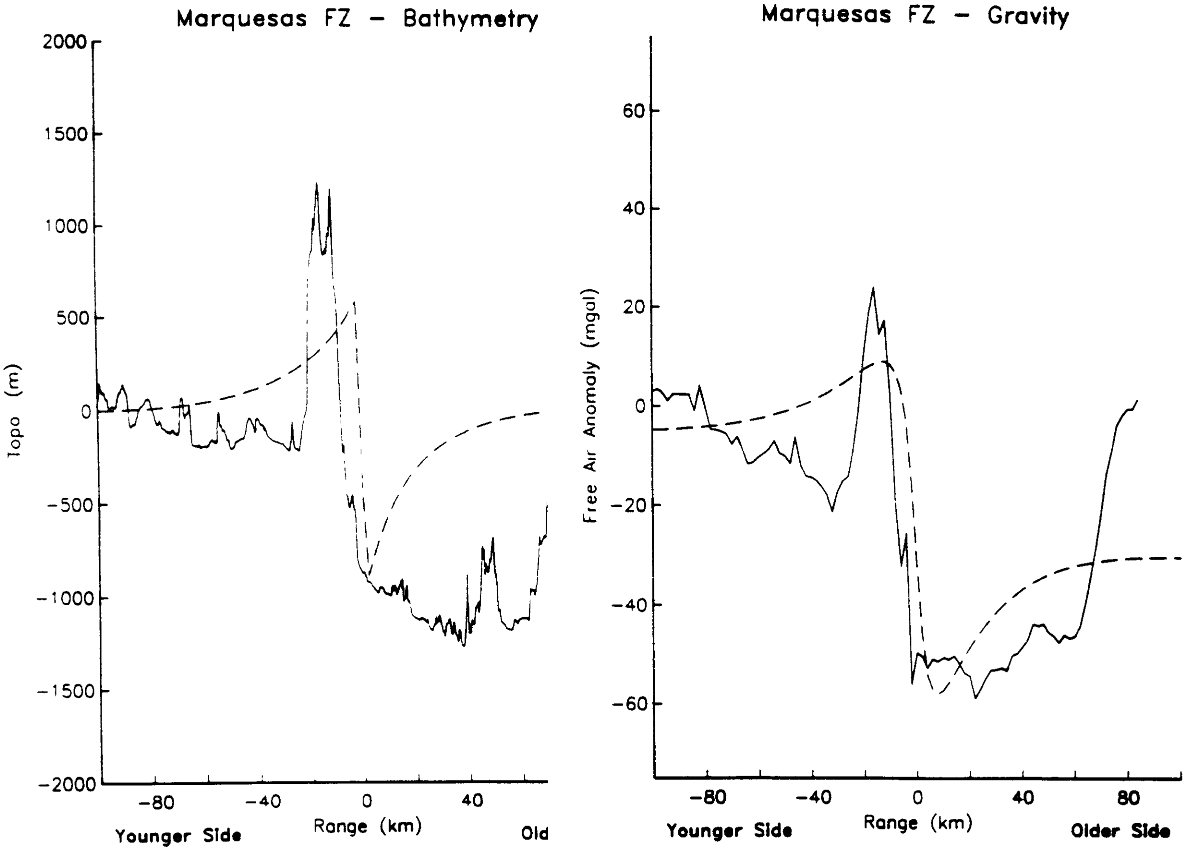

Figure 4.25. Predicted bathymetry and gravity across the Marquesas Fracture Zone. Fracture zone is modelled as locked with an age offset of 12 Ma and evolving with subsequent thermal stresses and differential subsidence modifying the profile. Rise on the older side is the flank of Fatu Hiva. As with most of the fracture zone observed to the east of the islands, the predicted bathymetry from the model is smaller than the observed.

themselves, but not to the east and possibly not directly below them. In the vicinity of the islands, the ridge feature is much larger than the age offset and subsidence models would predict.

McNutt et al. [1989] used the presence of cones on the summit of the ridge to propose that the structure was volcanic, and used the gravity data to suggest that the feature was compensated by a thin, broken plate. While the fit of Figure 4.25 is certainly worse than that of *McNutt et al.* [1989], there is an additional benefit to retaining the locked fracture zone model. As explained in Chapter 5, if the hotspot is presently under the ridge, then there is not enough time to thermally thin the lithosphere to the 10 km elastic thickness postulated by *McNutt et al.* [1989], either by conduction or direct injection of the magma into the plate. If we are willing to accept the worse fit, we do not have to explain the very thin plate thickness beneath the ridge implied by the broken plate model, since the subsidence model uses unperturbed plate thicknesses. However, the uplift of the ridge compared to its expression to the east and west of the islands remains to be explained. It is possible that volcanic intrusions in the area have thickened the crust very locally along the fracture zone, uplifting a pre-existing differential subsidence feature.

The change in shape of the gravity anomaly in Figure 4.24 near the feature at the 375 km distance mark with elastic plate thickness and the passage of the shiptrack over the center of this feature suggest that there might be a thin plate in the area. For a thin plate to display the gravity observed, there must be other loads present beyond the simple top loading models considered so far, leading to the last factor I investigated for line 1.

4.5.3. Top and bottom loading

As pointed out by *McNutt* [1983] and *Forsyth* [1985], the combination of loading a plate from above and below produces a mixed spectral response that can be mistakenly interpreted as shallow local compensation when interpreted in the context of top loading alone. As observed in Table 4.3 and in Figure 4.13, the modelling of line 1 uses a 5 km top loaded plate to fit the

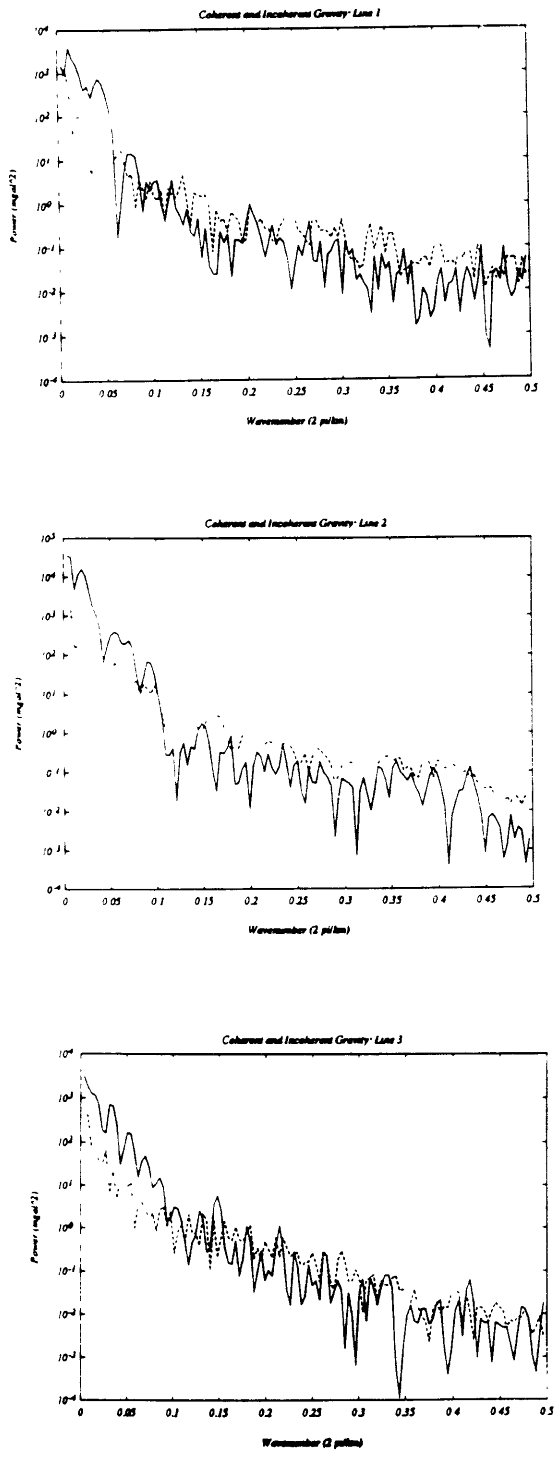

Figure 4.26. Coherent and incoherent Bouguer gravity for lines 1, 2, and 3. Solid line is the coherent portion of the gravity, while dashed line is the incoherent portion. Short wavelengths (large wavenumbers) will be mostly incoherent: small topography is not compensated by Moho deflection.

observed admittance. While some of the problem is certainly due to the three dimensional nature of the bathymetry, there may be some contribution from loads applied within the plate, or to its base.

To investigate the possibility of bottom loading, I first examine the components of the Bouguer gravity that are coherent and incoherent with the topography. On an infinitely rigid plate, there are no compensating displacements for loads at the surface or base of the plate. I expect the Bouguer gravity to be incoherent. On a plate with zero rigidity (a locally compensated system), loads placed at the surface produce roots, and loads placed at the base produce topography. I cannot distinguish which is which, and I expect the Bouguer gravity to be coherent. For a plate with intermediate rigidity, the coherent and incoherent components will both contribute, with the coherent component dominating at long wavelengths, and the incoherent component dominating at short wavelengths. The transition between the two components will occur around the characteristic wavelength for the rigidity. The wavelength at which the transition between the components occurs will then indicate the rigidity. In Figure 4.26 I illustrate the coherent and incoherent Bouguer gravity for lines 1, 2 and 3. From the fact that the power dominance transition occurs at a wavenumber for line 1 that is similar to, or slightly smaller than, that of lines 2 or 3, I may deduce that line 1 lies over an area with the same or higher average rigidity as lines 2 or 3.

To explicitly check for bottom loading, I calculate the Bouguer admittance Q, which is analogous to Z in equations (4.8) and (4.9) for the free-air admittance:

$$\hat{b}_1(\vec{k}) = Q(k)\,\hat{h}(\vec{k}) \tag{4.11}$$

which is estimated with

$$\tilde{Q} = \frac{\left\langle \hat{b}_1 \cdot \hat{h}^* \right\rangle}{\left\langle \hat{h} \cdot \hat{h}^* \right\rangle} \tag{4.12}$$

where b is the Bouguer anomaly, and all notation is as in section 4.4.5.1. This last equation (4.12) is simply the least squares estimate of the filter that produces Bouguer gravity given topography. Note that we might equivalently estimate Q by using the same least squares scheme to estimate the filter Q^{-1} in

$$\hat{h}_1(\vec{k}) = Q^{-1}(k)\ \hat{b}(\vec{k}) \tag{4.13}$$

by using the corresponding

$$\widetilde{Q^{1}} = \frac{\left\langle \hat{h}_1 \cdot \hat{b}^* \right\rangle}{\left\langle \hat{b} \cdot \hat{b}^* \right\rangle} \tag{4.14}$$

noting that this is the best estimate filter that predicts the topography given the Bouguer gravity. Substituting (4.13) into (4.14) makes it slightly easier to see that if the topography and gravity are produced by surface loads, then $1/\widetilde{Q^{1}} = \tilde{Q}$:

$$\widetilde{Q^{1}} = \frac{\left\langle 1/Q \cdot \hat{b} \cdot \hat{b}^* \right\rangle}{\left\langle \hat{b} \cdot \hat{b}^* \right\rangle} \tag{4.15}$$

This of course implies that if there are no subsurface loads, then the same $1/\widetilde{Q^{1}} = \tilde{Q}$ condition applies. In practice, *McNutt* [1983] notes that (4.14) is an unstable downward continuation with respect to noise in the short wavelengths of the gravity. Discrimination between estimates of Q is then only useful at the longest wavelengths. With this *caveat* in mind, I illustrate the estimates for Q as described above in Figure 4.27 for lines 1, 2, and 3. It can be seen that at the lowest wavenumbers, $\tilde{Q}$ and $1/\widetilde{Q^{1}}$ are equal, but tend to diverge at higher wavenumbers. The irregular behavior of the estimates above these wavenumbers is probably due to noise in the data. The estimates of $\tilde{Q}$ and $1/\widetilde{Q^{1}}$ show that at least at wavelengths over 60 km, the top loading model is essentially correct for all the lines. I cannot rule out the top loading model on the basis of these calculations, and line 1 remains mysterious.

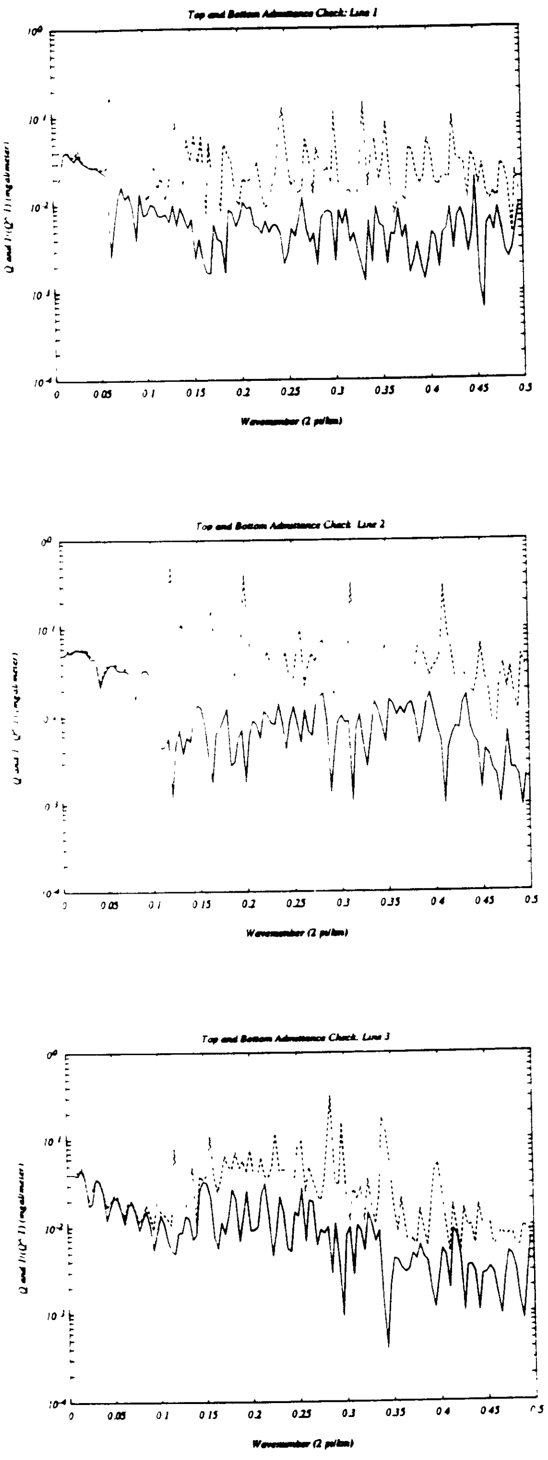

Figure 4.27. Estimates of the filters $\widetilde{Q}$ and $1/\widetilde{Q^{-1}}$ for lines 1, 2, and 3. Solid lines are for $\widetilde{Q}$ while the dashed lines are for $1/\widetilde{Q^{-1}}$. The two estimates should be equal for a plate loaded only from the top.

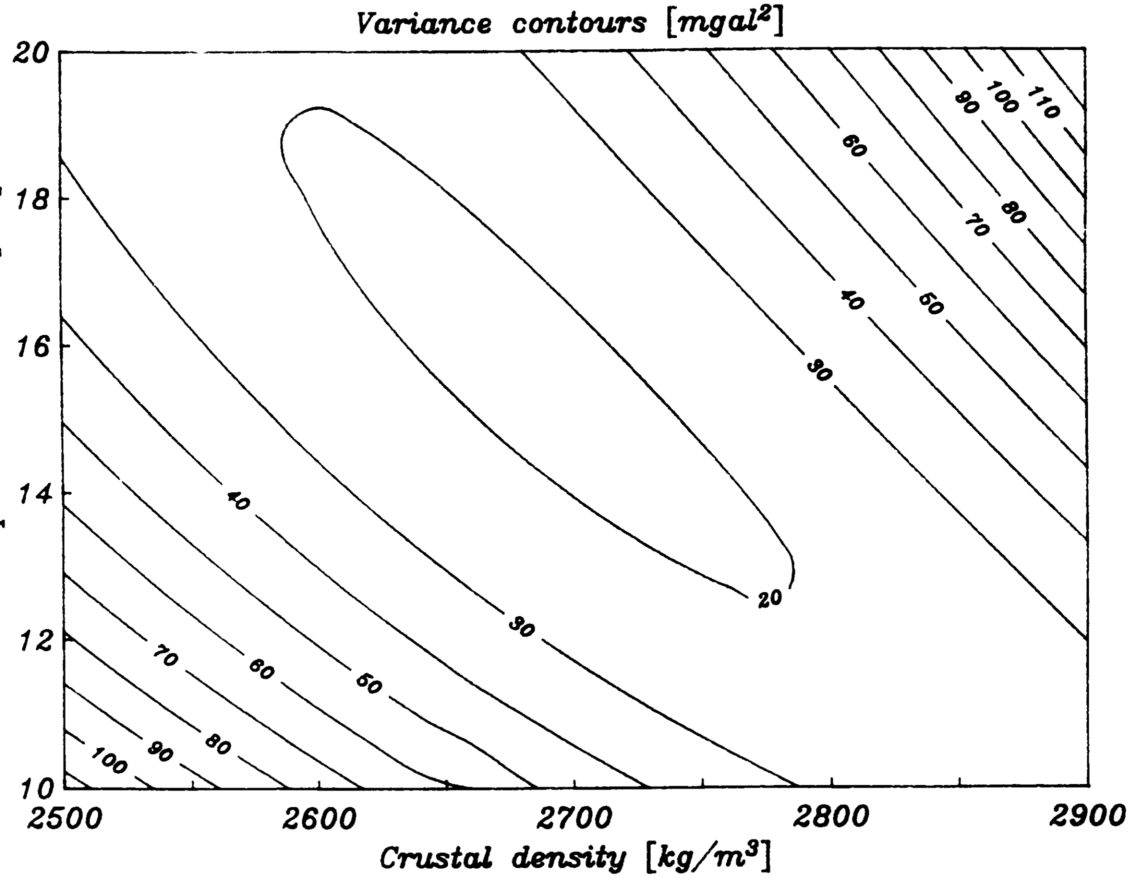

Figure 4.28. Contours of variance for line 2 in the parameter space defined by the crustal density and the elastic plate thickness, calculated for a Moho depth of 16 km. The minimum lies at ρ_c = 2680 kg/m^3, T_e = 16 km. There is a trade-off between density and elastic plate thickness, expressed as the poor resolution in that direction.

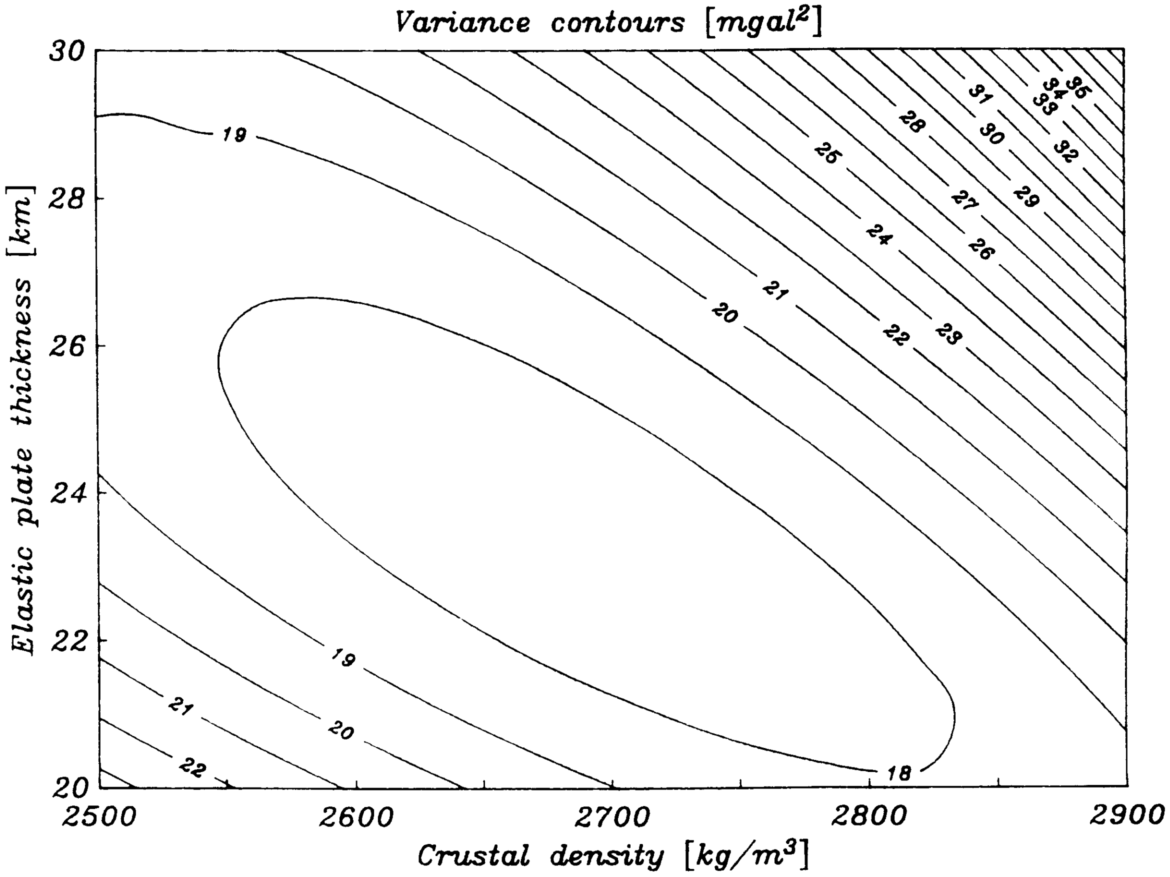

Figure 4.29. Contours of variance for line 3 in the parameter space defined by the crustal density and the elastic plate thickness, calculated for a Moho depth of 8 km. The minimum lies at ρ_c = 2690 kg/m^3, T_e = 23 km. Line 3 is not as well resolved as line 2, as could be expected from the smaller size of the signal-to-noise ratio. The density range is the same as for Figure 4.28, but the elastic plate thickness ranges from 20 to 30 km.

4.5.4. Trends in T_e

The values for the parameters in Table 4.5 suggest that there is a trend in the elastic plate thickness, with the plate weakening to the southeast. However, without some idea of the sensitivity of the two fits, I cannot say that there is not an intermediate value that fits both lines acceptably. To explore the variance function in the vicinity of the minima, I have calculated the variances over ranges above and below the preferred values of Table 4.5, and I present them in contour form on Figures 4.28 and 4.29.

There is a trade-off between the density and plate thickness requiring the plate thickness to decrease as the density increases: the greater contribution from the crust must be offset by a stronger Moho signal. This trade-off is reflected in the poor resolution in the right diagonal direction. To compare the two diagrams, I have normalized them with the value of the variance from the positively constrained fits in Table 4.5. It should be noted that this is *not* the reduced chi-squared (χ_v^2) value, since I do not have information on the error of each data point. The normalized variances would be the χ_v^2 values only if the positively constrained fit had a χ_v^2 value of one, i.e. it was a perfect fit. Since this is not so, the variances only approximate the behavior of χ_v^2, and we have no information on the absolute value of the misfit statistic. I may however try to look at the minimum normalized variance for both lines.

Illustrated in the composite Figure 4.30 is the normalized variance for both lines 2 and 3. They are shown contiguously since the elastic plate thickness ranges coincide at 20 km. The dotted line is the locus of equal levels of normalized variance for the two lines, which reaches a minimum value of approximately 1.19 at ρ_c = 2590 kg/m^3 and T_e = 20.5 km. The joint fit for the two lines is shown in Figure 4.31. This fit is to be compared with Figures 4.19 and 4.20, the corresponding fits from the minima of the individual lines. For line 2, the arch and moat from 100 to 450 km are better fitted by the weaker plate, while the moat and arch at 700 km are better fitted by the intermediate parameters. For line 3, the differences are very small, but the stronger plate fits the amplitudes slightly better.

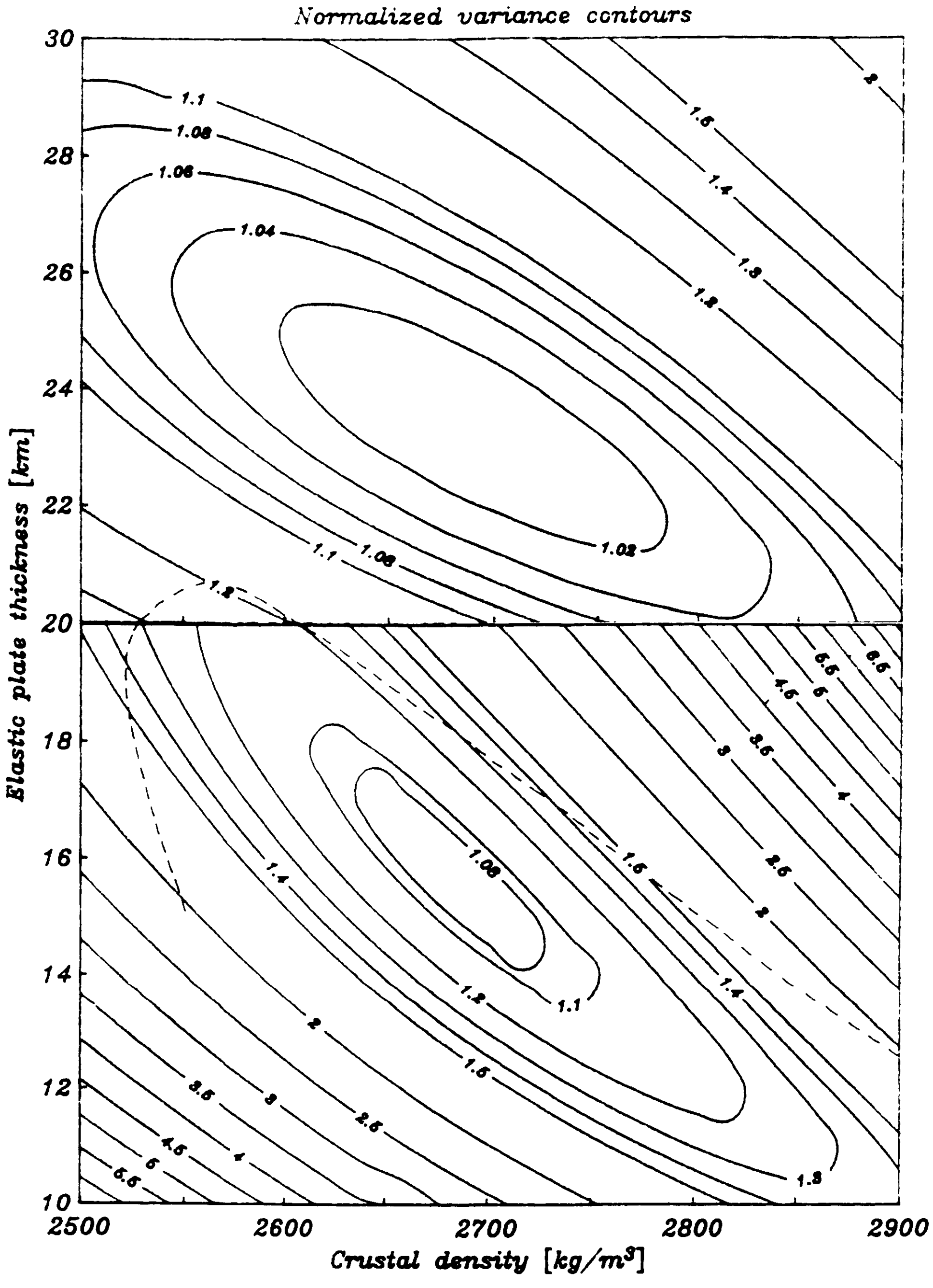

Figure 4.30. Normalized variance for lines 2 and 3, using the minima obtained in the positively constrained fits as the normalization factor. Plots are shown contiguously with an equal plate thickness at 20 km. Contour intervals are 0.02 below 1.1, 0.1 below 1.5, and 0.5 thereafter. Dashed line is the locus of equal normalized variance for both the lines, and reaches a minimum of approximately 1.19 at $\rho_c = 2590$ kg/m^3, $T_e = 20.5$ km.

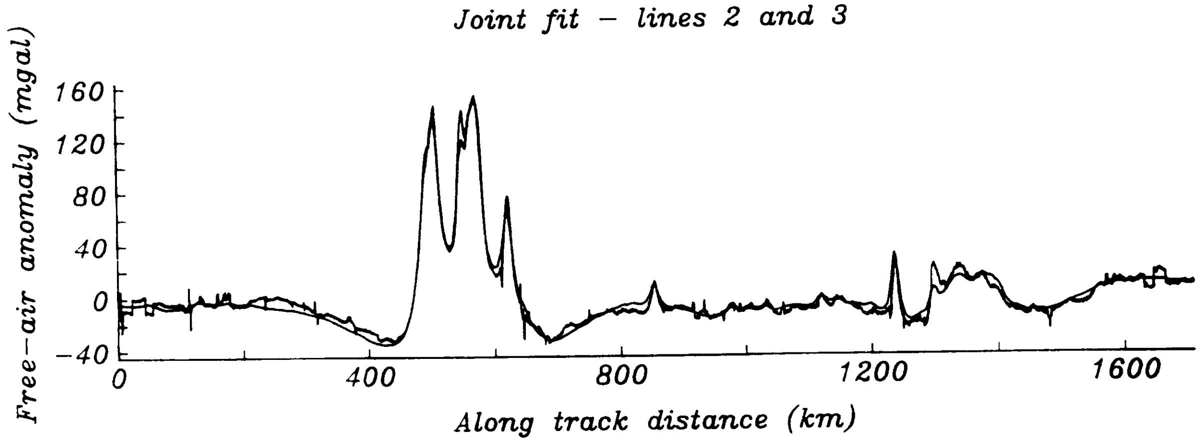

Figure 4.31. Joint fit for the data of lines 2 and 3, using the parameters of the minimum equal normalized variance point of Figure 4.30, and an average Moho depth of 15 km. The variance for the fit is 20.34 $mgal^2$. The moat is slightly overestimated for line 2, and slightly underestimated for line 3.

The parameter values for this normalized variance minimum point are actually the values obtained by minimizing all the data from lines 2 and 3 together, which is not necessarily to be expected. For the individual minimizations, the average Moho depths are allowed to be different, and the errors are weighted differently because of the separate normalizations. In the joint case, there is only one average Moho depth, 15 km, and the errors contribute equally.

It would appear that the data from lines 2 and 3 can be satisfactorily explained with an intermediate elastic plate thickness of 20 km, loaded by an average density of 2590 kg/m^3, and compensated at an average depth to the Moho of 15 km. This model has no need for a trend in the elastic plate thickness. Without better information on the thickness and density of the moat sediments, I am unwilling to ascribe the differences between the two lines exclusively to differences in the elastic plate thicknesses.

I may however draw several conclusions: first, the observed thickness agrees well with the thicknesses observed over other hotspots. From a compilation of elastic plate thicknesses for volcanos over hotspots, *Calmant and Cazenave* [1987] have derived the empirical dependence of elastic plate thickness with the age of the plate at the time of loading to be represented by $T_e = 2.7\sqrt{t_l}$, where t_l is the age at the time of loading, in Ma. For lines 2 and 3, using the ages of *Brousse et al.*, [1990] and the seafloor ages of *Kruse* [1988] this formula yields 19 and 21 km respectively. The plate under the Marquesas is neither weaker nor stiffer than under other hotspot volcanos.

Since there is no detectable opposite trend, any effects from thermal rejuvenation or visco-elastic relaxation from lower lithospheric reheating are not evident on the 1.3 My timescale separating the two areas, agreeing with the theoretical determination that visco-elastic equilibrium for this plate thickness is reached within 1 Ma for large seamount loads [*Bodine et al.*, 1981].

The value determined for the elastic plate thickness is also high for thicknesses characteristic of the Superswell. While previous studies include the Marquesas in this area of anomalously low elastic plate thicknesses, the present result indicates that although the plate is

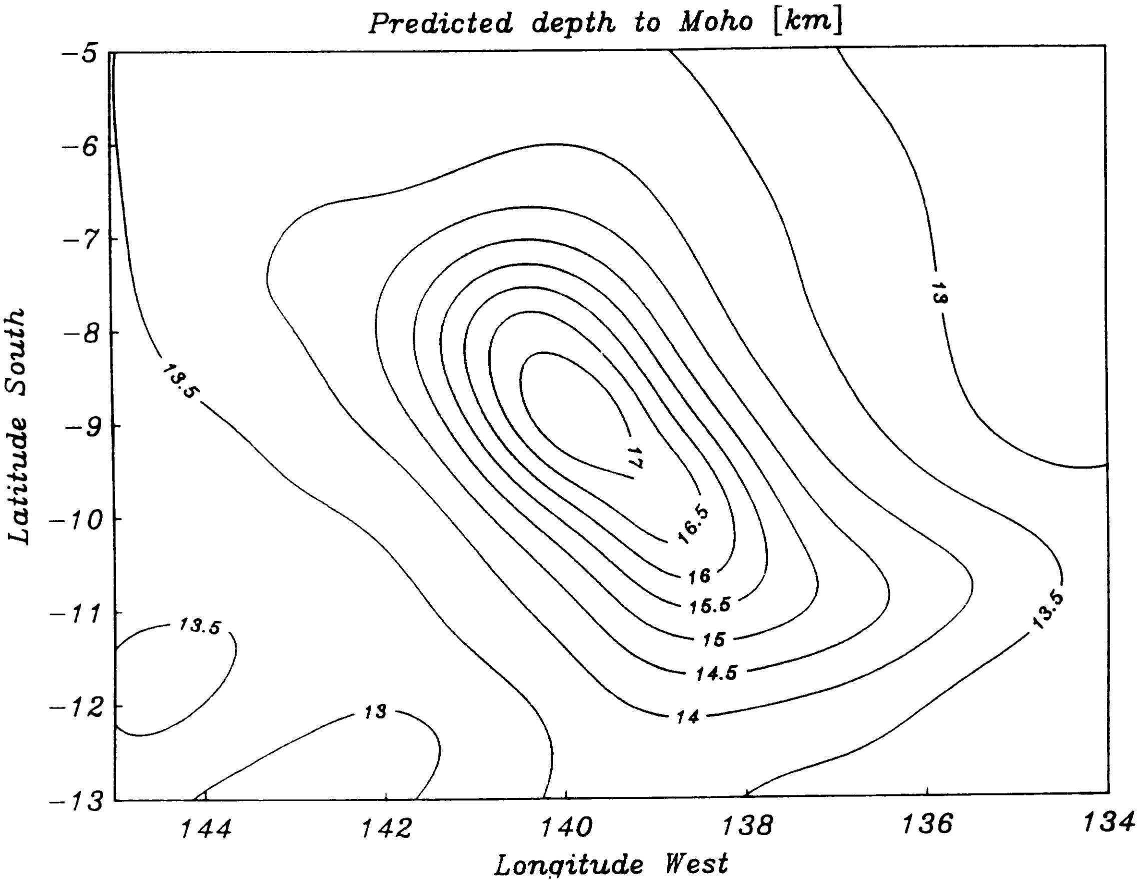

Figure 4.32. Predicted depth to the Moho for the Marquesas area. Contours are kilometers of depth to the best fitting Moho for the gravity data of lines 2 and 3, evaluated for the parameters of the minimum equal normalized variance point of Figure 4.26. Since the plate thickness is uniform, the predicted deflection is not expected to match observations near the fracture zone ridge or along line 1.

certainly weakened, it is not weakened to the 14 km value indicated by the SEASAT data analysis [*Calmant and Cazenave*, 1986; *Calmant,* 1987]. If we include the result for the elastic plate thickness of 10 km for the Marquesas fracture zone ridge [*McNutt et al.,* 1989], then the transition to Superswell type lithosphere must take place within this short distance, 250 km. *McNutt et al.* [1989] have modelled the fracture zone ridge as loading a broken plate to the north of the fracture, with Airy compensated topography to the south of the fracture (see their Figure 4). This result implies that there has been extensive weakening in the area that extends onto the older and presumably colder plate to the north.

In Figure 4.32, I show the predicted depth to the Moho for an elastic plate thickness of 20 km and a load density of 2590 kg/m^3, the values of the best fitting parameters. The depths are high, probably a result of overestimating the load in the moat and underestimating the density of the islands. The values for the depth to the Moho derived from recent multi-channel work in the area (*R/V Ewing* cruise EW9103), yet to be interpreted, should yield Moho profiles that are slightly shallower and slightly steeper near the islands, although the overall shape of the deflection must be similar to that displayed here. Closer to the fracture zone, there is very little control, and the results will probably be quite different. Gravity calculated for the best fit parameters is shown in Figure 4.33 for the whole area. The gravity is inaccurate over the southern end of the islands, but matches all profiles to the northwest of Fatu Hiva.

Using the deflection data for the best fit parameters, I may calculate the deflection of the pre-existing seafloor, and therefore estimate the amount of sediments and the amount of lava flows that make up the infill of the moat. From the sonobuoy results of Chapter 3, I know the sediments off the west flank of Nuku Hiva are about 1.4 km thick. From the deflection data, the pre-existing seafloor at this point has been depressed about 3.0 km, implying the lava flows are about 1.6 km thick in this location. If this is typical of the sediment to lave thicknesses throughout the moat, then it implies an amount of sediment almost equal to the amount of flows that constitute the moat material.

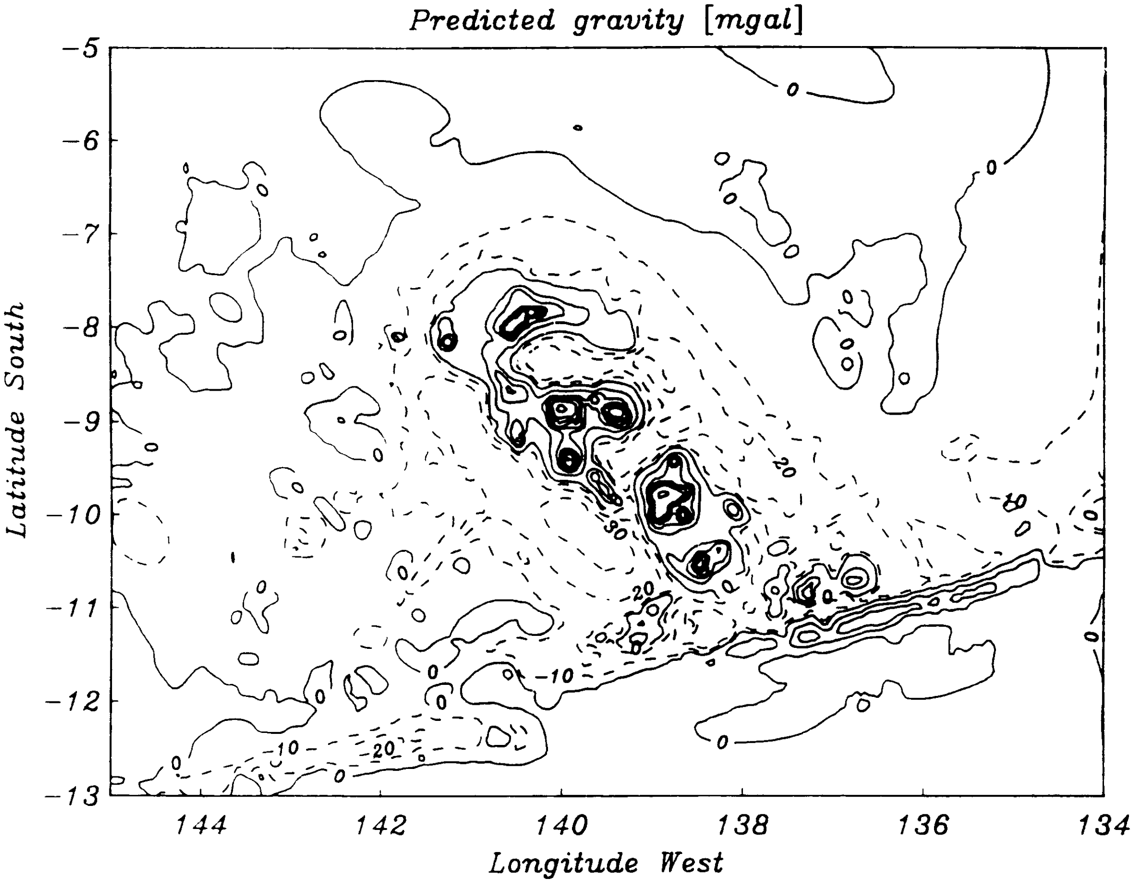

Figure 4.33. Predicted gravity for the Marquesas area. Contour intervals are 10 mgal for negative values, and 30 mgal for positive values. Values less than -30 mgal are reached in the moat off the Hiva Oa/Tahuata dome, and in the moat to the east and northeast of Ua Huka. At this contour interval, the arch is not very obvious, but it follows the general trend of the arch in the SEASAT data of Figure 4.2.

The most important density contrasts I have not considered are those produced by the sediment-lava flow interface and the contrast at the interface between seismic layers 2 and 3. At the sediment-basalt interface, the density contrast varies between 0 and 1500 kg/m^3, since the sediments can range from suspended silts with densities almost equal to water to highly compacted sediments compressed by the weight of a thick overburden. The sediment density is a function of this compaction: the deeper the sediment layer, the higher the density of the bottom-most sediments. For small sediment thicknesses, the gravity contribution from the layer is very small, while for thick sediment layers, the density contrast with the basement is small, producing the same effect. The omission of the sediment layer in gravity calculations, or rather its 'inclusion' in the crust, will then result in a density for the best fit to the gravity that represents some sort of average between the densities of the crust and the sediments. The proportion of sediments lighter than the crust in aprons is not known, but it is certain that they cannot compose the full volume of aprons from both the observed regional pelagic sedimentation rates [*Menard,* 1956] and seismic refraction experiments for Hawaii [*ten Brink and Watts,* 1985]. The density contrast at the layer 2-layer 3 transition is very small, probably less than 100 kg/m^3, and its omission results in a negligible increase in the fitted depth to the Moho.

It is important to remember that the parameters should be viewed in the context of the model, and not as absolute measures of the properties of the actual crust. The reality is undoubtedly more complex: the elastic plate thickness probably varies with position, and the density structure is certainly not uniform. The parameters represent some sort of average throughout the lines, and for the lines 2 and 3, this is sufficient to explain the data with a simple model. For line 1, the situation must be much more complex than the model, since we have tried to invoke several factors that usually complicate gravity studies to explain the data.

4.6. CONCLUSIONS

The free-air gravity from the central and northern lines of the Marquesas show a definite moat and arch structure that is not present in the bathymetry. This feature is best modelled with a 20 km three-dimensional elastic plate loaded by a density of approximately 2590 kg/m^3 in the central and northwestern areas of the chain. Together with the refraction data of Chapter 3, the deflection of the seafloor suggest that the material in the moat is about half volcaniclastic debris and pelagic sediments, and half subaqueous lava flows. There is no need to invoke a high density core to the islands as with the crustal sill complex seen in the multi-channel seismic data for Hawaii [*ten Brink and Watts*, 1985; *Watts et al.*, 1985; *Watts and ten Brink*, 1989], and there is no evidence of the sub-plate load that this type of structure implies.

The asymmetry of the gravity field about the islands can be explained by the load geometry alone, and differences in elastic plate thickness are not detectable either along the chain or across it. There appears to be no abnormal amount of reheating when the Marquesas are compared with other hotspots, and the elastic plate thickness, although reduced from unperturbed values, is not as low as the characteristic values of the Superswell to the south. The Marquesas fracture zone forms an abrupt boundary demarcating the northern extent of the anomalously shallow bathymetry of the Superswell, and apparently also delimits the extent of the weakened plate. The fracture zone may be considered locked or unlocked depending on the interpretation of the gravity over the fracture zone ridge.

The absence of any flexural moat in the gravity data from the southernmost line cannot be explained using a simple flexural model. The long wavelength component of the signal is not compatible with the observed bathymetry, implying that there must be processes that are unaccounted for in the model. The observed data cannot be accounted for by off-track bathymetry observed in the SEABEAM swath, by the presence of a free boundary at the fracture zone, or by subsurface loading of the plate. If there are large features beyond the SEABEAM swath, then these features may be altering the gravity signal significantly, and masking the flexural signal.

CHAPTER FIVE

THE THERMAL POWER OF THE MARQUESAS HOTSPOT

Many a time I have wanted to stop talking and find out what I really believed.

Walter Lippman

The analysis of data in previous chapters has yielded estimates for the sediment thicknesses and the densities of the material composing the islands and the infill of the moat. I may use these quantities to estimate the amount of energy available from the cooling of the magma, and knowing the time over which the eruption has occurred, roughly estimate a power for the process, and discuss the implication of that power for the anomalously thin plate thickness observed at the southern end of the chain under the Marquesas Fracture Zone Ridge if I accept the modelling of *McNutt et al.* [1989] for the compensation of the feature by a thin broken plate.

5.1. ERUPTED VOLUME AND AVERAGE THERMAL POWER

From a simple isostatic argument, I may estimate the amount of displaced material at the Moho that provides the restoring force that balances the load of the islands. If the volume of the load is V_l and its corresponding density is ρ_l, then the force exerted by a submerged load on the supporting plate is

$$F_l = (\rho_l - \rho_w) g V_l \tag{5.1}$$

where ρ_w is the density of the water, and g is the gravitational acceleration. Similarly for the restoring force exerted on the bottom of the plate

$$F_r = (\rho_d - \rho_i) g V_d \tag{5.2}$$

where ρ_d is the density of the displaced material, ρ_i is the density of the infill, and V_d is the volume of the displaced material. The situation is illustrated in Figure 5.1. Equating the two forces and solving for V_d gives the simple relation

$$V_d = V_l \frac{\rho_l - \rho_w}{\rho_d - \rho_i} = V_l f \tag{5.3}$$

where f is the compensation volume factor, and the total volume of the emplaced structure is then

$$V_t = V_l + V_d = V_l (1 + f) \tag{5.4}$$

which is valid for *any* compensation mechanism, since the volumes V are simply the integrals of the load topography and deflection over the area in question.

A contour plot of the factor f in (5.3) is shown in Figure 5.1 for ranges of load and infill densities between 2000 and 3000 kg/m^3, where the dotted line represents the commonly assumed simplification that the infilling material has the same density as the load. Since the infill is composed of a mix of volcanic flows and sediments, the factors should generally fall on or below this line. For the ranges usually encountered with volcanic flows and marine sediments, the factor probably ranges between 1.5 and 4.

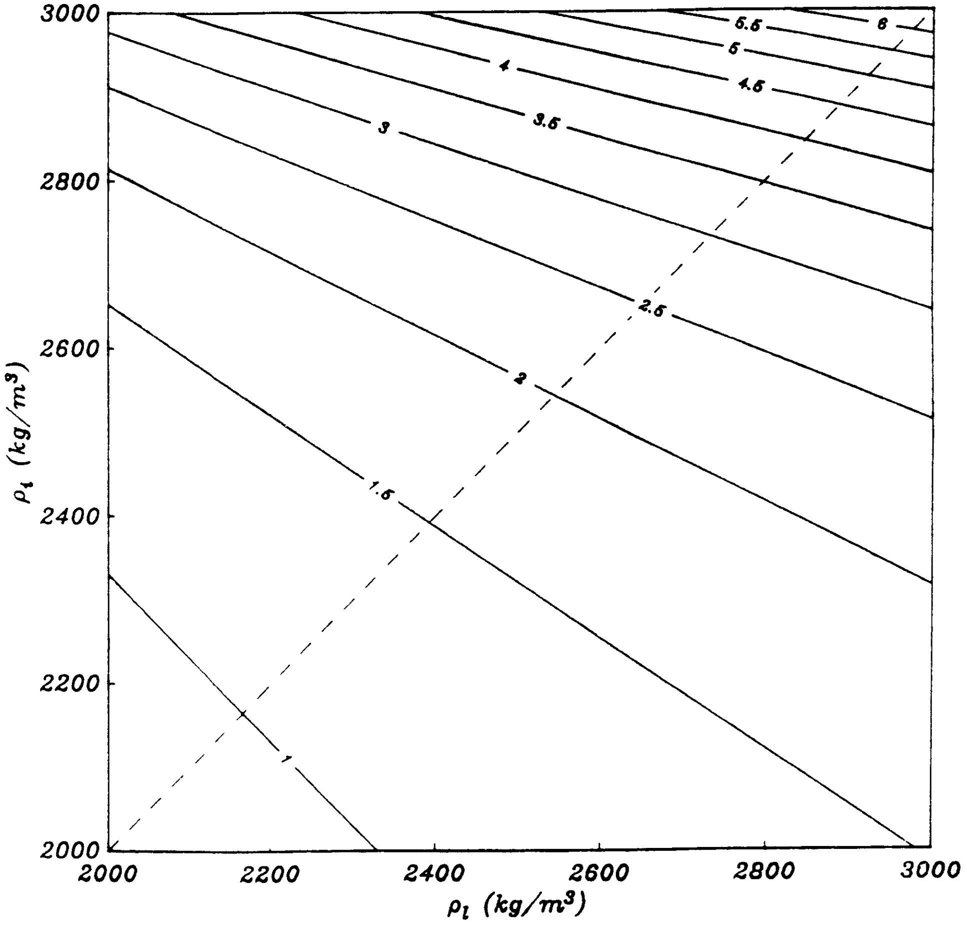

Figure 5.1. Contours of the infill factor f as a function of load and infill densities. Dashed line reflects equal densities for the load and infill, a common assumption. Since infill is generally derived from the load material and sediments, the factor will fall on or below the dashed line. For common loads, f ranges from 1.5 to 4. The total volume as a function of the load volume is $V_t = (1 + f)V_l$.

5.1.1. Total volume of erupted volcanic material

For the Marquesas, I estimated a volume for the load of 3.9×10^5 km^3 by summing all the values of the depth anomaly grid of Figure 4.6 above the 1000 m estimated height of the Marquesas swell [*Fischer et al.,* 1986], excluding the fracture zone ridge. Using 2590 kg/m^3 as the density of the load (derived in Chapter 4) and a nominal uncertainty of 100 kg/m^3, the factor ranges from about 1.8 to 2.8, giving a displaced volume of $(9\pm2)\times10^5$ km^3.

As a check, I summed the predicted deflection of the seafloor shown in Figure 5.2 in the same manner as the depth anomaly, to arrive at a volume of 8.8×10^5 km^3, within the expected range. The total volume of the edifice and moat volcanics and moat sediments is then $(1.3\pm0.2)\times10^6$ km^3. Figure 5.3 shows this total volume V_t as a function of the load density, assuming the infill density is the same as the load density. From the refraction results of Chapter 3, I assume that the sediments of the moat are derived from erupted volcanics that have eroded from the islands in mass wasting events. The sediments in the moat are then counted as material erupted.

5.1.2. Average thermal power

The available energy from the solidification of the erupted material may be calculated using

$$E_f = H_f \rho\, V_v \tag{5.5}$$

where H_f is the latent heat of basalt, 100 cal/g or 418 kJ/kg, ρ is the density of the basalt, and V_v is the volume of the erupted basalt. From the above numbers, $E_f = (1.4\pm0.2)\times10^{24}$ J.

The above material has been erupted since the onset of Eiao, or since 7.3 Ma, according to *Brousse et al.*'s [1990] estimate of the age of onset for Eiao. Using the age span above, the eruptive rate is calculated as 0.18 km^3/y. This rate may also be calculated by looking at the cross-sectional area of the islands, and multiplying by the plate velocity to get a mass flux. In Figure 5.4 I show the cross-section of profile 2', along with the corresponding deflection of

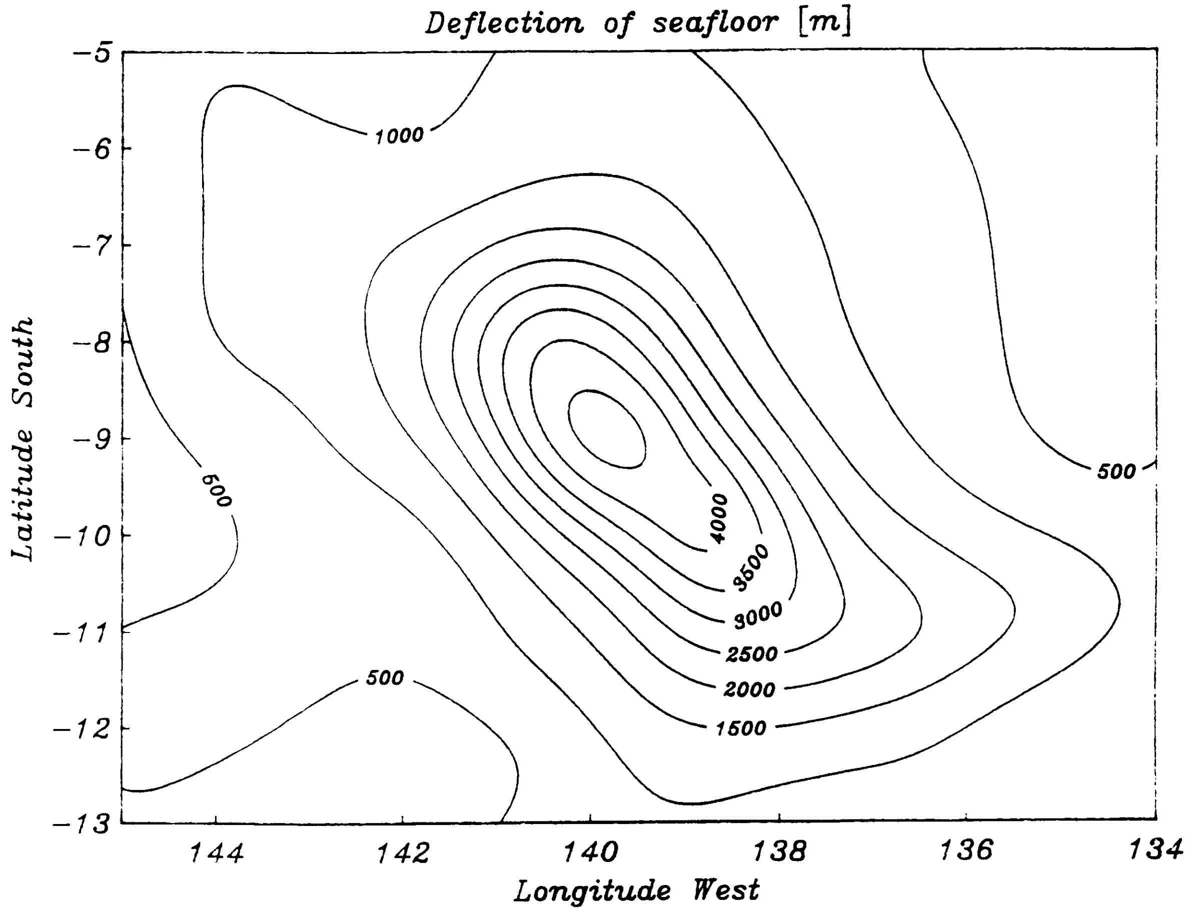

Figure 5.2. Predicted deflection of seafloor by the Marquesas island load. The maximum deflection of 4.5 km is beneath Nuku Hiva. Deflection beneath the gravity moat is 2 to 3 km. Total deflected volume is 8.8×10^5 km^3.

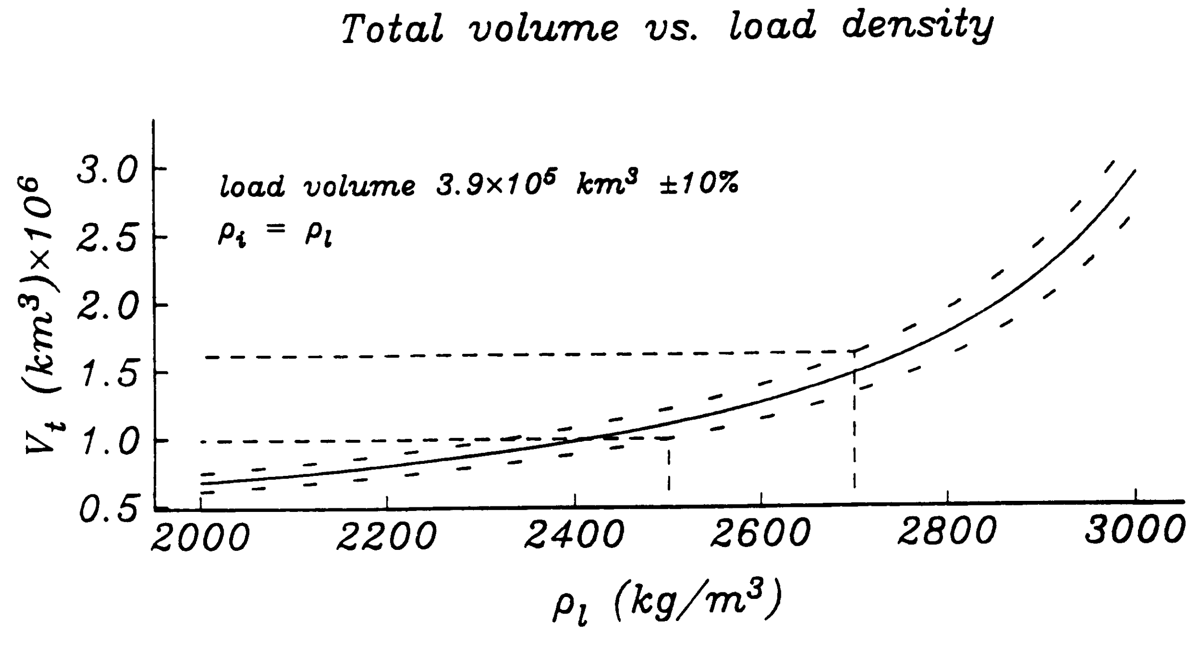

Figure 5.3. Total volume of chain and apron as a function of load density. Solid line is calculated for a load volume of 3.9×10^5 km^3, and represents the dashed line of Figure 5.1. Dashed lines are 10% uncertainty limits on the total volume V_t and the projection of the uncertainty in load density ρ_l on the volume axis. Estimated total volume is 1.3×10^6 km^3.

the pre-existing seafloor. Two estimates of the size of the tholeiitic domes are shown, with the narrow version reflecting the continuation of the slopes of the upper portions, as modelled by *Watts et al.* [1985] and *Watts and ten Brink* [1989] for Hawaii, and with the wide version reflecting the continuation of the slopes seen on the flanks of the domes, and reflecting the seismic refraction data of Chapter 3, which indicated a sediment depth of 1.4 km off the flank of Nuku Hiva. In both cases, the cross-sectional area $A + B$ is 1800 km^2 (ignoring the variable volume of the islands themselves), which when multiplied by the local plate velocity, 10 cm/y, gives a mass flux of 0.18 km^3/y, in agreement with the previous estimate. The thermal power from the solidifying volcanics is then 6.2 GW. This energy is dissipated by the quenching of the melts in water, and by conduction back into the surrounding, colder rock formed by previous eruptions. Eventually, all the energy will be dissipated into the overlying ocean.

For comparison, I present the previous results in Table 5.1 with the same order-of-magnitude estimations for Hawaii, using an estimate for the cross-sectional area through Oahu of 1600 km^2, and an average density of 2800 kg/m^3 [*Watts and ten Brink*, 1989]. Previous estimates of magma production at Kilauea are 0.11 km^3/yr [*Swanson,* 1972], 0.1 km^3/yr [*Frey et al.,* 1990], and 0.16 km^3/yr [*Watson and McKenzie,* 1991]. It is interesting to note that these two hotspots are actually more similar than might be presumed from the size of the islands themselves. Given the errors in estimating the cross sections from the figures, the two chains are probably almost indistinguishable. Even though the plate velocities and eruptive rates are similar at both locations, the size of the emergent portion of the volcanoes is strikingly different. The main difference between the two island chains is the elastic plate thickness of the plate they rest on: in Hawaii, T_e is estimated at 40 km [*Watts and ten Brink,* 1989], whereas in the Marquesas, T_e is only 20 km, which allows most of the erupted material to be hidden in the deflected trough beneath the chain. Given this similarity in fluxes, why does Hawaii burn through older (and presumably colder) crust more constantly?

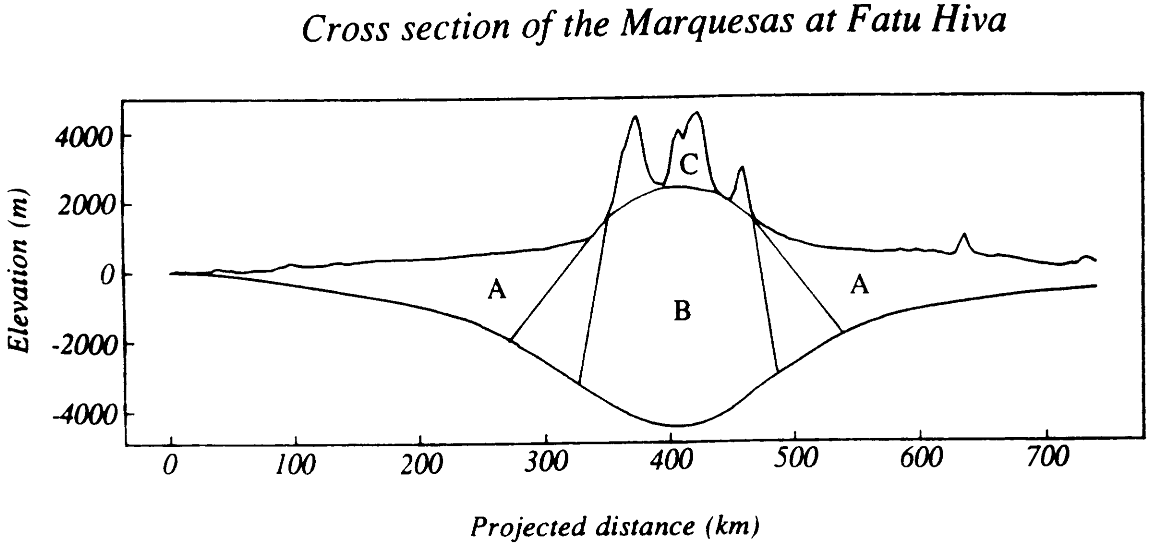

Figure 5.4. Cross section of the Marquesas at Nuku Hiva, from profile 2'. Letters stand for different components of the structure: *A*, the sediments of the moat, deposited by mass wasting; *B*, the tholeiitic shield of the volcano, with two possible shapes depending on the slope followed to the original seafloor; *C*, the alkalic capping phase, which has produced the emergent sections of the islands. The narrow shield follows the example of *Watts and ten Brink* [1989], while the wider version is more compatible with the slopes of the flanks and the observed seismic depths of the sediments in the moat.

5.2. PERTURBATION OF THE GEOTHERM

If the lithosphere beneath the Marquesas were thermally unperturbed, the 600°C isotherm would lie at approximately 30 km depth [*McNutt,* 1984]. The best fitting elastic plate thickness, 20 km, implies that the geotherm has been perturbed on the order of 10 km. Many mechanisms for weakening the plate have been proposed: rejuvenation [*Crough,* 1978], dike injection [*Withjack,* 1979], the formation of a deep crustal sill complex [*ten Brink and Watts,* 1985], lithospheric erosion [*Spohn and Schubert,* 1982; *Turcotte and Emerman,* 1983] and convective destabilization [*Parsons and McKenzie,* 1978; *Fleitout et al.,* 1986]. In the present case, a simple scaling argument shows that conduction alone will suffice to weaken the plate over the timescales that we observe for the central and northern areas.

If I ignore lateral heat conduction, the conductive timescale for a length l may be expressed as $\tau = l^2/\kappa$, where κ is the thermal diffusivity. A rough value for thermal diffusivity of basalt is 0.8 mm^2/s, or in more convenient units, approximately 8π km^2/My. Using this value, a 10 km perturbation can be produced by conduction alone within 4 My, a sufficient time for the central and northern islands. However, gravity data over the Marquesas Fracture Zone Ridge to the southeast of Fatu Hiva have been used to constrain the elastic plate thickness to a low value of 10 to 13 km [*McNutt et al.,* 1989]. The timescale for a 20 km perturbation by conduction alone is 16 My, far too long for there to be an effect presently. Within the 8 My since the start of eruptions at Eiao, the conductive perturbation can only have been 14 km, yielding an effective elastic plate thickness of 16 km. With only 4 km of difference between the elastic plate of the central and northern areas, it is very difficult to detect any trends in reheating, as was demonstrated in Chapter 4. The suggestions of extremely low elastic thickness in the southeast would require some other explanation.

The volcanism south of Fatu Hiva is present only in the form of the carapace, some activity from cones [*McNutt, pers.comm.*] and the fracture zone ridge. The hotspot seems to have diminished or even ceased its surface activity, suggesting that the magma that would have formed the next edifice in the island chain may be distributed in the lithosphere below the carapace and ridge. The effect of injecting all the thermal energy from the cooling and solidifying magma may be estimated and I may then determine whether this is a viable mechanism for perturbing the geotherm enough to weaken the lithosphere to the values suggested for the fracture zone ridge.

If the magma is injected into the overlying lithosphere at its melting temperature and it solidifies without contact with water, then the energy E_f calculated above is distributed wholly in the lithosphere. Taking the local plate velocity u_0 to be 10 cm/y, and the width of the hotspot w to be approximately 200 km, the amount of heat per unit area becomes

$$Q_f = \frac{P_f}{u_0 w} = 9.7\times10^{12}\ \mathrm{J/m^2} \tag{5.6}$$

where Q_f refers to the fact that this is energy from the heat of fusion only. If the specific heat of the lithosphere is 1.381 kJ/kgC°, and the heat is distributed through a 125 km thick thermal plate, then the average temperature change throughout the column is

$$\overline{\Delta T} = \frac{Q_f}{C_p m} = 21^\circ\mathrm{C} \tag{5.7}$$

where m is the mass per unit area of the column. While this temperature change is enough to produce 64 m of thermal expansion in the column, it is not enough to produce the 480°C change at the 10 km depth required by the gravity data. If we replace w by the value appropriate for the width of the swell, 1200 km, then the temperature change is reduced to 3.5°C, and the contribution to the swell height is less than 13 meters.

Even if the magma is injected well above the melting temperature, for example with 250 to 300°C of excess temperature from thermal plume models [*Sleep,* 1987; *Liu and Chase,* 1989; *Sleep*, 1990; *Watson and McKenzie,* 1991], and assuming that the specific heat of the magma is similar to that of the lithosphere, the corresponding figures in the calculation above are only increased by a factor of two, and the resultant temperature change $\overline{\Delta T} = 42°C$ is still not sufficient to weaken the lithosphere. The uplift produced by this temperature change is 158 m over the width of the hotspot. If w is altered as above to the dimensions of the swell, only 26 m of uplift can be attributed to the cooling and solidification of magma within the lithosphere. The power from both cooling and solidification are indicated in Table 5.1, with the subscript c for 'cooling'.

Injection of magma at the same rate as observed in the islands is therefore insufficient to produce the suggested change in elastic plate thickness beneath the ridge. The observed T_e may simply be preserved from the original 12 My offset along the transform fault, which yields a predicted T_e of 14 km. Other processes, associated with the plume itself or the fracture zone and its interaction with the Superswell lithosphere may be contributing to the effect. I discount lithospheric erosion since any model that erodes material quickly enough requires an excessively high heat flux [*McNutt,* 1984].

5.3. PRESENT LOCATION AND ACTIVITY OF THE MARQUESAS HOTSPOT

A crude estimate of the hotspot's present location can be made by extrapolating the trend of the average dates of collected samples from the islands to zero age. This approach leads to an estimate that lies under the fracture zone ridge, within 60 km (see Fig. 2A of *Brousse et al.,* 1990). It is important to clarify exactly what is meant by 'the position' of the hotspot. If we define this as the locus of the average age of erupted volcanics, then this is an accurate estimate. However, if we define the location as the estimated position of the first eruptions, then the present location must be some 40 km to the southeast of the fracture zone ridge. This estimate is arrived at by assuming a 0.4 My period for the construction of the islands. If a further allowance is to be made for the plume material to penetrate the lithosphere, the position must be even farther to the southeast.

As noted in Chapter 3, there is no evidence of any volcanic activity to the southeast of the fracture zone ridge in the areas sailed on *Crossgrain 2*. There is evidence for recent volcanism

TABLE 5.1. Volume Flux and Power of Marquesas and Hawaii Hotspots

Quantity	Marquesas (at Nuku Hiva)	Hawaii (at Oahu)
Cross-section, A	1800 km^2	1600 km^2
Volume flux, Q_v	0.18 km^3/y	0.16 km^3/y
Mass flux, Q_m	14.7 Mg/s	14.3 Mg/s
Fusion Power, P_f	6.2 GW	5.9 GW
Cooling Power, P_c	12.3 GW	11.7 GW

to the southeast of Fatu Hiva, but north of the fracture zone, in the form of hyaloclastite breccias and basaltic glass dredged during the *Ewing* cruise EW9106 [*McNutt, pers. comm.*]. There are also two small seamounts to the southeast of the ridge, Tua Ivi Nao at 12°05'S 136°42'W, 800 m high, and another small seamount at 11°35'S 136°32'W, 500 m high. These features (numbers 85 and 86 in Chapter 2) unfortunately remain undated.

The volume of the ridge and its compensating volume, using a broken plate model and a density of 2600 kg/m^3 [*McNutt et al.,* 1989], is estimated to be about 3×10^4 km^3, or an amount eruptible at previous rates within 166,000 years. Using the youngest date from Fatu Hiva, 1.38 Ma, that leaves about 2.2×10^5 km^3 unaccounted for if previous rates are upheld.

If there is volcanic activity under the ridge, there should also be some seismic activity. Over 40,000 events in the swarm around the new seamount Mehetia in the Society Islands have been detected by a network in the Societies [*Talandier and Okal,* 1987]. Strictly speaking, it is not fair to expect the same number of events from the Marquesas: there is a network bias in the numbers. However, *T* phases from MacDonald seamount are regularly detected by the Society network, which is equidistant from the Marquesas [*Talandier and Okal*, 1984], although MacDonald is abeam the local island trend rather than athwart, like the Marquesas, which have the Tuamotus between them and the network in the Societies. Of two events detected between 1913 and the present, one (12.0°S -140.3°E, 08/11/1969) has been relocated to the Line islands and the other (9.47°S -140.07°E, 02/10/1988, $m = 4.4$) has been located 5 km beneath the south flank of Ua Pou [*Wysession et al.,* 1991]. There appears to be no seismicity in the ridge area.

5.4. CONCLUSIONS

Using the volume of the load and an isostatic balance argument, the volume of the islands and their compensating mass is estimated as 1.3×10^6 km^3. The volume of volcanic material erupted during the 6.1 My of activity in the archipelago is estimated as 8.3×10^5 km^3. Using a cross-sectional area of 1800 km^2 estimated from predicted deflection profiles, the magma production rate is estimated at 0.18 km^3/yr, which is similar to estimates for the production rate estimated for Hawaii. Since the plate velocity and the magma production rate are similar for both chains, the vast difference in observed size must be attributed to the difference in plate strength below the islands. Most of the Marquesas lava production has subsided below the waves, and below the pre-existing seafloor. The power available from the cooling and solidification of the lavas from both island chains is estimated at 12 GW. Conduction alone is sufficient to reheat the plate underlying the central and northern islands within the eruptive timescales appropriate for these areas, but the 10 km plate thickness suggested for the fracture zone ridge area cannot be explained by conduction alone. The amount of heat from the cooling and solidification of lavas injected into the lithosphere beneath the ridge is insufficient to weaken the plate to the observed thickness.

APPENDIX A

CIRCULAR ERROR ANALYSIS

Truth lies within a little and certain compass, but error is immense.

Henry St, John, Viscount Bolingbroke
Reflections upon Exile

Although Gauss developed his theory of errors for the analysis of astronomical and terrestrial surveying measurements, which are fundamentally spherical data, he assumed that the geometry within which the measurements were made was Euclidean, or flat. In essence, Gaussian error theory incorporated the flat earth approximation. In order to define meaningful statistics for a set of observed azimuths, it is necessary to explicitly account for the geometric nature of the space within which the set is distributed. In this appendix I shall discuss only circular spaces and not spherical ones. For reasons explained below, it is interesting to note that the circular case is actually the more numerically complex. As is usual, there is no standard notation in the literature. I have tried to follow the notation of *Batschelet* [1981] and *Pearson and Hartley* [1972], whose works contain many tables to which this appendix refers.

A.1. CIRCULAR, OR PERIODIC VARIABLES

Many common observations are circular variables. Measurements of angles or directions are obviously of this type. The cycles of time: hour of day, month of the year, etc. are circular. Since all circular variables are periodic, there would seem to be only a semantic difference between mathematicians and statisticians in the definition of the basic properties of these variables.

While *linear* variables can be distributed on the interval [$-\infty$, ∞], *circular* variables are distributed on the interval [0, 2π], or equivalently [$-\pi$, π]. Even though these smaller intervals are contained in the infinite interval, the distinguishing quality of circular variables is their *periodicity*. Note that vectors can be expressed in polar form $\overrightarrow{(r,\theta)}$ as variables of a mixed type: their length r is linear, while their azimuth θ is circular. Lines can also be expressed as circular data, although there is a basic ambiguity in azimuth. This difference leads to the definition of two circular variable types: *vector* and *axial*. Vector circular data can be interpreted simply as a set of vectors of unit magnitude. Whereas a vector datum would plot as a single point, each axial datum would plot as a pair of dots on the unit circle separated by 180°.

Vector data can be clustered about a certain directions, or *modes*. If axial data is clustered, it will necessarily produce modes and *anti-modes*. We shall be interested in both unimodal and bimodal distributions, in their mean directions, and in the certainties of the estimates.

A.2. THE MEAN DIRECTION OF A CIRCULAR DISTRIBUTION

It can be easily demonstrated that the linear ideas of means and averages give nonsensical answers to data that are inherently periodic. We are given, say, a 7 element direction dataset, Φ:{90°,90°,90°,90°, 270°, 270°, 270°} (in degrees rather than radians, for simplicity) . The set defines directions that lie along a single line, and so should yield a mean along the same line. However, if we perform the simple linear mean calculation on these angles

$$\overline{x} = \frac{1}{N} \sum_{i=1}^{N} x_i \tag{A.1}$$

we arrive at a mean of 167°, which does *not* lie on the line. On the interval [$-\pi$, π] the set becomes Φ:{90°,90°,90°,90°, -90°, -90°, -90°}, and the mean is calculated as 13°, which is different from the previous mean. The mean depends on the interval we choose.

Say we rotate our set by 90°, to Φ':{ 0°, 0°, 0°, 0°,±180°,±180°,±180°} (the signs depending on our interval). The mean, ±60°, again depends on the interval. Furthermore, if we rotate the mean by -90°, back to the original orientation, we get 150° or 30°. It seems that the mean also depends on rotations. To complicate the matter further, these means do not agree with those we calculated from the original dataset, 167° and 13°. These are definitely undesirable properties for a mean.

Despite the above results, finding the mean direction of a circular distribution is intuitive. If we define ψ_i as the angle between the unknown mean and the *i*th observation, then for a set of *N* observations, we desire to maximize the sum

$$S = \sum_{i=1}^{N} \cos \psi_i \tag{A.2}$$

where we maximize rather than minimize, since this is a sum of cosines.

In terms of a fixed axis, for example the 0° azimuth, the mean direction can be described by its as yet unknown azimuth $\overline{\varphi}$. Relative to the fixed axis, our set of *N* observations have the azimuths φ_i. The ψ_i are then expressible simply as

$$\psi_i = \varphi_i - \overline{\varphi} \tag{A.3}$$

and the sum *S*, when differentiated with respect to $\overline{\varphi}$ and subjected to the extremal condition $dS/d\overline{\varphi} = 0$ becomes

$$\frac{d}{d\overline{\varphi}} \sum_{i=1}^{N} [\cos\varphi_i \cos\overline{\varphi} - \sin\varphi_i \sin\overline{\varphi}] = 0 \tag{A.4}$$

or

$$\tan \overline{\varphi} = -\frac{\sum \sin \varphi_i}{\sum \cos \varphi_i} \tag{A.5}$$

and this last expression can be recognized as the tangent of the angle formed by the resultant sum of N unit vectors $\boldsymbol{e}_i = \overrightarrow{(1,\varphi_i)}$ in the observed directions. The length of this resultant vector, R, is simply

$$R = \left(\sum_{i=1}^{N} \cos \varphi_i\right)^2 + \left(\sum_{i=1}^{N} \sin \varphi_i\right)^2 \tag{A.6}$$

The mean azimuth is then simply the azimuth of the unit vector sum of all the observed azimuths, and the length of this vector sum is R. The mean direction, $\overline{\varphi}$, is the mode of the data.

We also define the mean vector, $\boldsymbol{m}$, or the *first moment*, as

$$\boldsymbol{m} = \overrightarrow{(r,\overline{\varphi})} = \frac{1}{N} \sum_{i=1}^{N} \boldsymbol{e}_i \tag{A.7}$$

where

$$r = R/N \tag{A.8}$$

so $0 \leq R \leq N$, and $0 \leq r \leq 1$. If all the φ_i are equal, then $R = N$, $r = 1$, and $\overline{\varphi} = \varphi_i$. Note that the first moment of the sample is a vector quantity.

The sample angular variance s^2 and the sample angular deviation s can be found from

$$s^2 = \frac{1}{N} \sum_{i=1}^{N} 2[\, 1 - \cos(\varphi_i - \overline{\varphi})] \tag{A.9}$$

A.3. Binning Effects

When we convert the observations φ_i into frequency counts, they are binned in an integer degree interval. The statistics that are derived from binned data are biased relative to a continuous sample, but this can be corrected for by a simple factor.

If we have k bins over the circle, defined by their mid-points φ_k, then we may define the *class length* $\lambda = 2\pi / k$ and the corrected mean vector length r_c

$$r_c = cr\,; \;\; c = \frac{\lambda/2}{\sin \lambda/2} \tag{A.10}$$

When binning is fine and the class length is small, then this correction factor is very nearly unity. For my purposes, all data was measured at 1° intervals, yielding a correction factor of 1.000012692, essentially unity. For some applications, I bin in 5° and 10° intervals, and the correction factors are 1.00031738 and 1.001270368, again essentially unity. All estimates are corrected for binning effects, and the symbol r_c is implied when I use r.

For a sample Φ of n observations φ_i binned into k bins φ_k, there are k sample frequencies $n_1, n_2, \ldots, n_k$. Their sum is obviously N. In terms of the binning count, the mean vector $\boldsymbol{m}$ is simply

$$\boldsymbol{m} = \frac{c}{N}\left(\overrightarrow{\sum_{j=1}^{k} n_j \cos \varphi_j \,,\; \sum_{j=1}^{k} n_j \sin \varphi_j}\right) \tag{A.11}$$

and the mean angle $\overline{\varphi}$ is the same, since c drops out of the fraction A.5.

A.4. The von Mises Distribution

In order to perform statistical tests on circular samples, it is necessary to have models for the parent distributions from which the samples were drawn. Certain types of distribution allow estimates of the confidence intervals for the parameters to be calculated, and are useful models in various tests of significance. In linear error analysis, the Gaussian distribution plays a very important role in the Central Limit Theorem as the limit distribution as the number of samples tends to infinity. There is a similar distribution for the circular case that possesses many of the same properties as the normal distribution. It is not surprising that this circular distribution can be derived from the linear normal distribution.

Rather than the familiar Gaussian, or 'normal' probability density function

$$g(x\,;\mu,\sigma^2) = \frac{1}{\sigma\sqrt{2\pi}}\exp\left[-\frac{1}{2}\frac{(x-\mu)^2}{\sigma^2}\right] \tag{A.12}$$

where the standard deviation σ and the mean μ, are the only two parameters, or moments, necessary to describe the model, we use the von Mises distribution [*von Mises,* 1918; *Fisher,* 1953]. This distribution exhibits some very useful properties in circular space, just as the normal distribution does in linear space. The parameters are invariant under rotations and under the choice of interval, and more usefully, for a given set of observations, the maximum likelihood estimates for the parameters of the parent distribution are the statistics derived from the dataset. The probability density function, or pdf, is

$$v(\varphi\,;\theta,\kappa) = \frac{1}{2\pi\ \mathrm{I}_0(\kappa)}\exp\left[\kappa\cos(\varphi-\theta_1)\right] \tag{A.13}$$

where φ is the angle between a sample observation and the true mean θ_1 of the parent set, and κ, the concentration parameter, is a measure of how tightly the data is distributed about θ_1, much as σ functions in the normal distribution, describing the dispersion about μ. The normalization factor contains the modified Bessel function I_0, which arises from the condition requiring the integral of the pdf to be unity over the interval $[0, 2\pi]$.

(*Aside*: It is this normalization that makes the circular space numerically more difficult than the spherical space. If we were integrating over the sphere, the differential d*A* would be have the extra factor of $\sin\varphi$, which makes the integration of the exponential function trivial. Rather than the modified Bessel function, we would have a hyperbolic sine. This fact cost me *much* time, so beware. More details on spherical statistics are found in *Watson* [1983], and *Fisher et al.*[1987]. Either of these two names will generate a host of references, since there are two Fishers who have proved fundamental to the field, and Watson continues to publish unabated.)

As κ tends to infinity, v approaches G, with κ behaving as the invariance, or $1/\sigma^2$, and as κ tends to zero, v approaches the uniform circular distribution with pdf

$$u(\varphi) = \frac{1}{2\pi} \tag{A.14}$$

which, although very simple, provides an important null hypothesis against which to test an azimuthal dataset.

A.4.1. Best estimates for κ, θ_1, and μ

The von Mises distribution has the useful property that the statistics r, $\overline{\varphi}$, and m derived from the sample are the maximum likelihood estimates $\hat{\rho}_1$, $\hat{\theta}_1$, and $\hat{\mu}_1$ for the parameters of the parent distribution, ρ_1, θ_1, and μ_1. The subscripts refer to the fact that these refer to the first moment of the distribution. For small sample numbers N, there is however a bias on r, giving an overestimate. For $N \leq R^{1/2}$, the best estimate of the concentration parameter is $\breve{\kappa} = 0$, while for $N > R^{1/2}$, we must solve the transcendental equation

$$\frac{\mathrm{I}_1(\breve{\kappa})}{\mathrm{I}_0(\breve{\kappa})} = r\,\frac{\mathrm{I}_1(Nr\breve{\kappa})}{\mathrm{I}_0(Nr\breve{\kappa})} \tag{A.15}$$

for $\breve{\kappa}$ [*Schou,* 1978], where

$$\mathrm{I}_{\nu}(\kappa)=\left(\frac{\kappa}{2}\right)^{\nu}\sum_{n=0}^{\infty}\frac{(\kappa^{2}/4)^{n}}{n!\,\Gamma(n+\nu+1)} \tag{A.16}$$

is the series for the modified Bessel function of order ν. For a fit of a von Mises distribution to the sample, an iterative algorithm is used to obtain the best estimate $\tilde{\kappa}$ appropriate for the value of r.

A.4.2. Confidence intervals for the estimates of θ_1 and κ

Given r and $\overline{\varphi}$, and a certain confidence level α, we wish to determine the confidence intervals for θ_1 and κ, $\delta\theta_1$ and $\delta\kappa$. There exists no simple expression for the confidence intervals, so I have used Table 5.2.2 of *Batschelet* [1981], and Table 57 of *Pearson and Hartley* [1972] for $\delta\theta_1$, and Charts 5.3.1, 5.3.2 and 5.3.3 of *Batschelet* [1981] and Table 56 of *Pearson and Hartley* [1972] for κ. The confidence intervals are another example of the spherical case being simpler than the circular, since closed form expressions for the confidence intervals do exist for the spherical case.

A.4.3. Higher order moments of distributions

In section A.2, I mentioned that the first moment $\boldsymbol{m} = \overrightarrow{(r,\overline{\varphi})}$ is the mean vector. This is analogous to the linear case where the n-th moments of a distribution $f(x)$ are given by

$$\mu_n = \int_{-\infty}^{\infty} x^n f(x)\, dx \tag{A.17}$$

except here the quantities are scalars. In the circular case, the moments are described in terms of the trigonometric functions:

$$\mu_n = \left(\int_0^{2\pi} \overrightarrow{\cos n\varphi\, f(\varphi)\, d\varphi,\ \int_0^{2\pi} \sin n\varphi\, f(\varphi)\, d\varphi} \right) \tag{A.18}$$

where it can be seen that the higher moments are also vectors, with each component generated by the trigonometrically weighted integral. In polar coordinates, the moments are expressed as

$$\mu_n = (\overrightarrow{\rho_n, \theta_n}) \tag{A.19}$$

where the subscripts refer to the order of the moment. The higher order moments of a sample are easily calculated: the original angles φ_i are doubled to $2\varphi_i$ for the second moment, trebled to $3\varphi_i$ for the third moment etc., and then calculations analogous to those for the first moment are carried out to determine ρ_n and θ_n. The components must be corrected for the multiplicative factor n simply by a division.

Note that for bimodal data, doubling the angles removes the first harmonic, and the new dataset is unimodal. Tripling a trimodal sample removes the second harmonic, and converts the data into a unimodal form. Thus any number of modes or harmonics can be reduced to the unimodal case.

A.5. TESTS FOR RANDOMNESS

To determine whether a sample is uniformly distributed on the circle, two statistical tests are common, the Rayleigh test and the V-test. Because of its simplicity, the Rayleigh test is the more used, but the V-test is more powerful when there is some reason to suspect that a specific mode actually exists. Both tests have the null hypothesis H_0 that the parent population of the sample is uniformly distributed. We are testing the possibility that the observed sample could result *purely as a matter of chance* from a uniform parent distribution.

A.5.1. The Rayleigh Test

The Rayleigh test relates the magnitude of the mean vector, r, to a P-value, or the smallest significance level by which we can reject the hypothesis that the sample is in fact random. The test assumes that axial data has been converted into unimodal data by doubling all angles observed, and that all statistics have been corrected for grouping, as in A.9. For a uniformly distributed dataset, r will have an expectation value of zero, and the value obtained from the data can be compared with this. Critical values for Rayleigh's test are found in *Batschelet's* [1981] Table H. For a dataset of N higher than 200 observations, I use his Table 4.2.1, with the test statistic $z = Nr^2$. We may also use the fact that for $N \geq 20$, $2R^2/N$ is approximately distributed under the uniformity hypothesis as χ^2 with two degrees of freedom [*Pearson and Hartley,* 1972].

A.5.2. The V*-test*

When a certain mode θ_0 is expected *a priori*, a more powerful test of randomness is the V-test [*Greenwood and Durand,* 1955]. Given the mean angle of a sample, $\overline{\varphi}$, and the length of the mean vector r, we test the component of r along θ_0,

$$v = r\cos(\overline{\varphi} - \theta_0) \tag{A.20}$$

and the test statistic is then

$$u = v\sqrt{2N} \tag{A.21}$$

whose expectation value for a uniform distribution is zero. It is assumed that all binning corrections have been made, and that axial data has been doubled to form a unimodal version. The critical values for the statistic u are found in *Batschelet's* [1981] Table I. A common misuse of this method involves testing whether $\overline{\varphi}$ deviates significantly from θ_0, which this test is not capable of discriminating. It is purely a randomness test. Confidence intervals for $\overline{\varphi}$

should be used for the purpose of detecting deviations from specific angles or from other estimated modes.

A.6. CIRCULAR-LINEAR CORRELATION

It is often desired to test whether a particular variable is a function of a periodic variable. There are two basic approaches, equally powerful, one requiring slightly more computation. We may convert a fitted sinusoidal form to a linear problem and proceed as usual with linear tests of significance for the value of the correlation coefficient r, or we may use a more direct method that uses the correlations of the trigonometric functions.

A.6.1. 'Linearizing' the problem

If we assume we have fit the data with a sinusoid of the form

$$y = M + A\cos(\varphi - \varphi_0) \tag{A.22}$$

then we may set

$$x_i = \cos(\varphi_i - \varphi_0) \tag{A.23}$$

and then

$$y = M + Ax \tag{A.24}$$

is the simple linear problem.

A.6.2. The Nr^2 test

We calculate a combined correlation coefficient using the correlations of the trig functions:

$$r_{yc} = \mathrm{corr}(y, \cos\varphi), \quad r_{ys} = \mathrm{corr}(y, \sin\varphi), \quad r_{cs} = \mathrm{corr}(\cos\varphi, \sin\varphi) \tag{A.25}$$

and then

$$r^2 = \frac{(r_{yc}^2 + r_{ys}^2 - 2r_{yc}r_{ys}r_{cs})}{(1 - r_{cs}^2)} \tag{A.26}$$

and the statistic Nr^2 is distributed approximately as χ^2 with two degrees of freedom for $N > 20$.

APPENDIX B

ERRORS IN ESTIMATIONS OF T_e

> *(On decimal points:) I never could make out what those damned dots meant.*
>
> Winston S. Churchill, quoting his father, Lord Randolph Spencer Churchill
> *Lord Randolph Churchill, ii, 84*

Simple estimations of the flexural rigidity D, or equivalently the elastic plate thickness T_e, using the linear load approximation and the distance from the load to the crest of the flexural bulge, x_b, are of course subject to errors in the estimation of x_b, and therefore subject to errors in the projections of the profiles. I investigate the size of these errors by investigating the relations between these quantities.

Walcott [1970] defined the flexural parameter α as a length scale in the solution to the homogeneous version of the flexure equation (4.3):

$$\alpha = \left(\frac{4D}{g\Delta\rho}\right)^{1/4} \tag{B.1}$$

where g is the acceleration of gravity, and $\Delta\rho$ is the density contrast between the material above and below the plate. Solving for D,

$$D = \frac{\lambda'^4 g\Delta\rho}{4} \tag{B.2}$$

where

$$\lambda' = \lambda \cos(\theta) \tag{B.3}$$

and θ is the angle of the projection, and λ is the unprojected length estimate for α found from the measured x_b, using

$$\lambda = \begin{cases} \frac{x_b}{\pi}, & \text{continuous plate} \\ \frac{4x_b}{3\pi}, & \text{broken plate} \end{cases} \tag{B.4}$$

Using the relation between elastic plate thickness and flexural rigidity (equation 4.2), I arrive at an expression for T_e in terms of λ':

$$T_e = \left(\frac{3\lambda'^4 g \Delta\rho (1 - \nu^2)}{E} \right)^{1/3} \tag{B.5}$$

from which I calculate the derivative

$$\frac{dT_e}{d\theta} = -\frac{4}{3} \left(\frac{3\lambda^4 g \Delta\rho (1 - \nu^2)}{E} \sin^3\theta \, \cos\theta \right)^{1/3} \tag{B.6}$$

and the ratio

$$\frac{dT_e}{T_e} = -\frac{4}{3} \tan\theta \, d\theta \tag{B.7}$$

A similar derivation for a finite change in projection angle, $\Delta\theta$, yields the relation

$$\frac{\Delta T_e}{T_e} = \left(\frac{\cos(\theta + \Delta\theta)}{\cos(\theta)} \right)^{4/3} - 1 \tag{B.8}$$

This function is plotted in figures B.1 and B.2, over the ranges of θ and $\Delta\theta$ used in the projections of the survey lines 1, 2, 3, and 4b. From figure B.1 it can seen that as expected, the change in predicted elastic plate thickness increases both with increasing projection angle, and with changes about that projection angle. For the four projection angles used, the change in elastic plate thickness is clearly seen in figure B.2, and it can be seen that for changes up to

10° about the projection angle used for each line, the change in the estimated elastic thickness varies from ~5% for line 4b, to ~32% in the case of line 4a. The errors in estimating x_b come from the estimates of x_b and from noise in the gravity data, while the errors in T_e come from x_b and the choice of projection angle. With the general shape of the Marquesas edifice widening to the north-west, estimates for the mean trend of the islands tend to vary over several degrees, and so the angle θ for the projections used can vary over the same amount. I have chosen to use the orthogonal projection about a trend N42°W by estimating the mean trend of the elongate axis for the majority of the contours. Figures for the mean trend vary from N40°W [*Brousse et al.*, 1990], to N52°W [*Duncan and McDougall*, 1974]. The last trend describes the alignment of only the southwestern-most centers, and so is probably not representative of a 'mean' direction, and the figure N48°W is used implicitly for the the fit to the age data, and represents the trend of a great circle through Fatu Hiva and Eiao [*Duncan and McDougall*, 1974]. Variations of up to 6° produce changes in T_e of up to 20%, but only from estimates projected from line 4a. The estimates with visible flexural signals from lines 1, 2, and 3, all projected at angles of less than 45°, would show changes in T_e of less than 15% for the same 6° variations of projection angle.

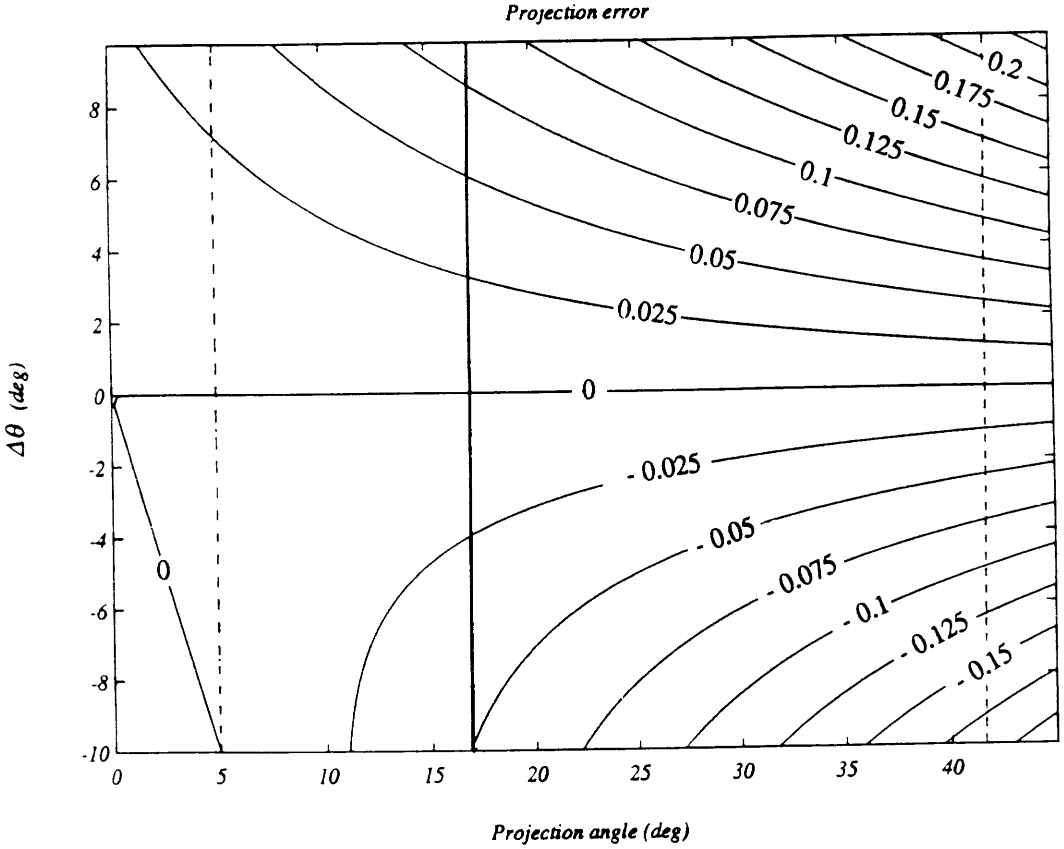

Figure B.1. Projection errors as function of variations $\Delta\theta$ about the projection angle θ, contours of $\Delta T_e/T_e$. Vertical lines indicate the projections used for profiles: dot-dash, 5° projection of line 4b; solid, 17° projection of lines 1 and 3; dashed, 42° projection of line 2 (θ used was 138° to reverse the profile). The 54.5° projection of line 4a is off scale. Oblique line from $\Delta\theta$ = 0 to θ = 5 is a zero contour.

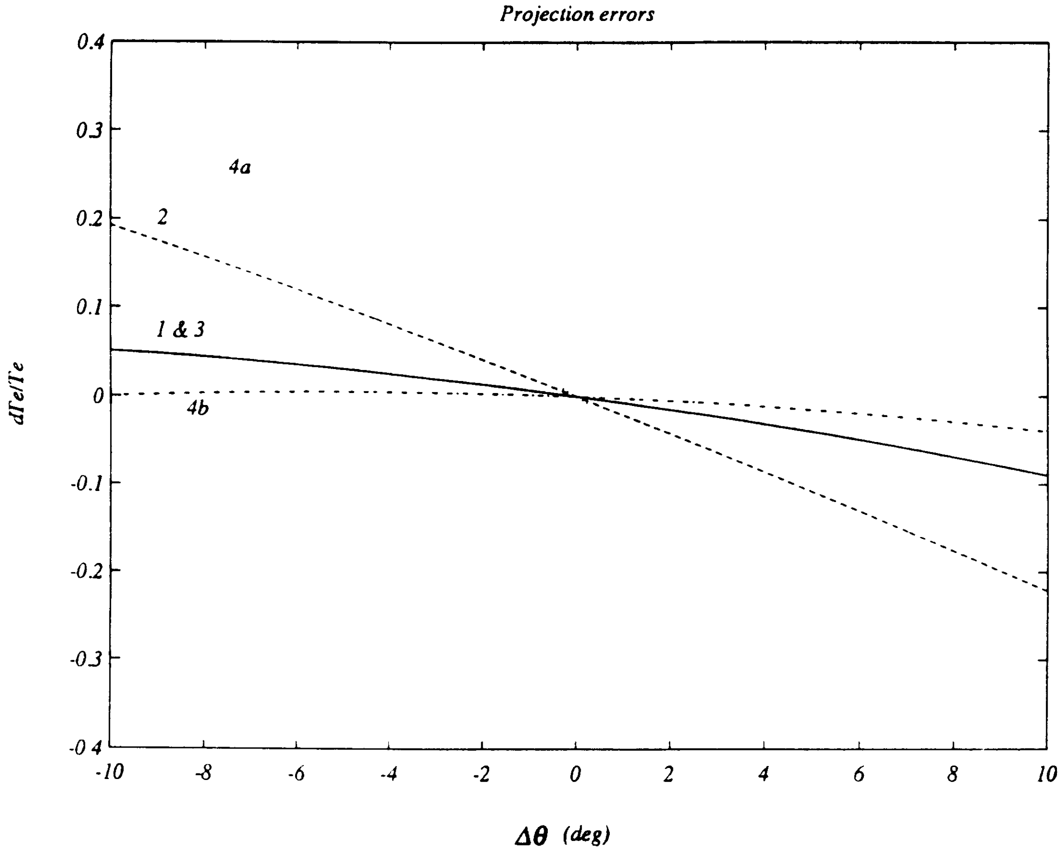

Figure B.2. Relative error as a function $\Delta T_e/T_e$ as a function of variation about the projection angle. Ordinate corresponds to contours in the previous figure, and the line styles correspond to the lines in the previous figure. The relative error is a measure of the change in estimated elastic plate thickness with changes in the projection angle.

APPENDIX C

"XI-SQUARED"

Nunca dije tal cosa.
I never said such a thing.

Borges
The Second Encyclopædia of Tlön. Vol. XI Hlaer to Jangr

The root mean square (RMS) formulation is a standard method for quantitative estimates of fit. As several authors have noted, this formulation emphasizes higher amplitudes at the expense of fitting wavelengths [*Watts,* 1978; *Smith et al.,* 1989]. In order to explicitly fit the phase of the data as well as the amplitude, I adopt a complex chi-squared formulation:

$$\Xi^2 = \sum_{i=1}^{N} \left| \frac{\Delta\hat{g}_i}{\hat{\sigma}_i} \right|^2 = \sum_{i=1}^{N} \frac{\Delta\hat{g}_i \, \Delta\hat{g}_i^*}{\hat{\sigma}_i^2} \tag{C.1}$$

and

$$\Delta\hat{g}_i = \hat{g}_i - \hat{g}(k_i) \tag{C.2}$$

where $\Delta\hat{g}_i$ is the difference between the Fourier transform of the data to be fitted, $\hat{g}_i$, and the Fourier transform of the model, $\hat{g}(k_i)$, and k_i is the discrete version of the wavenumber k, $\hat{\sigma}_i$ is the weighted data error vector, * indicates complex conjugation, and the summation is taken over the N wavenumber bins of the discrete transform. I use the notation Xi-squared, Ξ^2, to distinguish it from its real counterpart, chi-squared, χ^2. Note that we calculate the norm of the differences, rather than the difference of the norms, so the phase information is not discarded.

The error σ_i is easily weighted, since the weighting correction for the Fourier transform convention I have chosen is simply:

$$\widehat{\sigma}_j = \frac{d\Delta\hat{g}_j}{d\Delta g_j}\,\sigma_j = \frac{d}{d\Delta g_j}\frac{1}{\sqrt{2\pi}}\int_{-\infty}^{\infty}\Delta g_j e^{ikx}\,dx\,\sigma_j = \frac{\sigma_j}{\sqrt{2\pi}} \qquad \text{(C.3)}$$

where I have used the index *j* rather than *i* because of the imaginary exponent in the transform. This is simply a multiplication by a constant, and the constant could therefore be omitted from the search for minima, as can be easily verified. Non-linear transformations of the data will not yield a constant multiple, and I let the notation on the error vector reflect this by retaining the caret. If the uncertainties in the data are not known, they may be approximated from the data by calculating the sample variance for the fit to the model. The procedure is identical, but the σ are all equal and drop out. We may then minimize the variance of the fit to the data.

I seek to minimize Ξ^2 in the parameter space defined by the model. For *P* parameters *a*, the minima are defined by the elementary conditions:

$$\frac{\partial \Xi^2}{\partial a_j} = 0 \quad \text{and} \quad \frac{\partial^2 \Xi^2}{\partial a_j^2} > 0 \qquad \text{(C.4)}$$

Taking the derivatives of Ξ^2:

$$\frac{\partial \Xi^2}{\partial a_j} = \sum_{i=1}^{N} \frac{-2}{\widehat{\sigma}_i^2}\left\{\mathrm{Re}(\Delta\hat{g}_i)\,\mathrm{Re}\left(\frac{\partial}{\partial a_j}\hat{g}(k_i)\right) + \mathrm{Im}(\Delta\hat{g}_i)\,\mathrm{Im}\left(\frac{\partial}{\partial a_j}\hat{g}(k_i)\right)\right\} \qquad \text{(C.5)}$$

$$\frac{\partial^2 \Xi^2}{\partial a_k\,\partial a_j} = \sum_{i=1}^{N} \frac{-2}{\widehat{\sigma}_i^2}\left\{\begin{matrix}\mathrm{Re}(\Delta\hat{g}_i)\,\mathrm{Re}\left(\frac{\partial^2}{\partial a_k\,\partial a_j}\hat{g}(k_i)\right) - \mathrm{Re}\left(\frac{\partial}{\partial a_k}\hat{g}(k_i)\right)\mathrm{Re}\left(\frac{\partial}{\partial a_j}\hat{g}(k_i)\right) + \\ \mathrm{Im}(\Delta\hat{g}_i)\,\mathrm{Im}\left(\frac{\partial^2}{\partial a_k\,\partial a_j}\hat{g}(k_i)\right) - \mathrm{Im}\left(\frac{\partial}{\partial a_k}\hat{g}(k_i)\right)\mathrm{Im}\left(\frac{\partial}{\partial a_j}\hat{g}(k_i)\right)\end{matrix}\right\} \qquad \text{(C.6)}$$

$$\frac{\partial^2 \Xi^2}{\partial a_j^2} = \sum_{i=1}^{N} \frac{-2}{\hat{\sigma}_i^2} \left\{ \begin{array}{c} \mathrm{Re}(\Delta\hat{g}_i)\, \mathrm{Re}\left(\frac{\partial^2}{\partial a_j^2}\hat{g}(k_i)\right) - \mathrm{Re}\left(\frac{\partial}{\partial a_j}\hat{g}(k_i)\right)^2 + \\ \mathrm{Im}(\Delta\hat{g}_i)\, \mathrm{Im}\left(\frac{\partial^2}{\partial a_j^2}\hat{g}(k_i)\right) - \mathrm{Im}\left(\frac{\partial}{\partial a_j}\hat{g}(k_i)\right)^2 \end{array} \right\} \tag{C.7}$$

Where Re and Im refer to the real and imaginary parts respectively, and $\mathrm{Re}(x)^2$ refers to the square of the real part of x. The parameters are

$$a_1 = \rho_c \qquad a_2 = D \qquad a_3 = z_m$$

where ρ_c is the density of the crust, D is the flexural rigidity, and z_m is the depth to the Moho, in the model:

$$\hat{g}(k) = -2\pi G \left\{ (\rho_c - \rho_w)\exp(-kz_t) \; - \; (\rho_m - \rho_c)\exp(-kz_m)\frac{g(\rho_c - \rho_w)}{Dk^4 + g(\rho_m - \rho_c)} \right\} \hat{h}(k) \tag{C.8}$$

give the straightforward but tedious derivatives:

$$\frac{\partial \hat{g}}{\partial \rho_c} = -2\pi G \left[\exp(-kz_t) - g\exp(-kz_m) \left\{ \frac{g(\rho_m - \rho_c)(\rho_c - \rho_w)}{\left(Dk^4 + g(\rho_m - \rho_c)\right)^2} + \frac{(\rho_m - 2\rho_c + \rho_w)}{Dk^4 + g(\rho_m - \rho_c)} \right\} \right] \hat{h} \tag{C.9}$$

$$\frac{\partial \hat{g}}{\partial D} = -2\pi G\, gk^4 \exp(-kz_m) \frac{(\rho_m - \rho_c)(\rho_c - \rho_w)}{\left(Dk^4 + g(\rho_m - \rho_c)\right)^2} \hat{h} \tag{C.10}$$

$$\frac{\partial \hat{g}}{\partial z_m} = -2\pi G\, gk \exp(-kz_m) \frac{(\rho_m - \rho_c)(\rho_c - \rho_w)}{Dk^4 + g(\rho_m - \rho_c)} \hat{h} \tag{C.11}$$

$$\frac{\partial^2 \hat{g}}{\partial \rho_c^2} = 4\pi G\, g\exp(-kz_m) \left\{ \frac{g^2(\rho_m - \rho_c)(\rho_c - \rho_w)}{\left(Dk^4 + g(\rho_m - \rho_c)\right)^3} + \right.$$

$$\frac{g(\rho_m - 2\rho_c + \rho_w)}{\left(Dk^4 + g(\rho_m - \rho_c)\right)^2} - \frac{1}{Dk^4 + g(\rho_m - \rho_c)} \Bigg\} \hat{h} \tag{C.12}$$

$$\frac{\partial^2 \hat{g}}{\partial D^2} = 4\pi G\, gk^8 \exp(-kz_m) \left\{ \frac{(\rho_m - \rho_c)(\rho_c - \rho_w)}{\left(Dk^4 + g(\rho_m - \rho_c)\right)^3} \right\} \hat{h} \tag{C.13}$$

$$\frac{\partial^2 \hat{g}}{\partial z_m^2} = 2\pi G\, gk^2 \exp(-kz_m) \left\{ \frac{(\rho_m - \rho_c)(\rho_c - \rho_w)}{Dk^4 + g(\rho_m - \rho_c)} \right\} \hat{h} \tag{C.14}$$

$$\frac{\partial^2 \hat{g}}{\partial \rho_c \partial D} = \frac{\partial^2 \hat{g}}{\partial D \partial \rho_c} = -2\pi G\, gk^4 \exp(-kz_m) \Bigg\{ \frac{2g(\rho_m - \rho_c)(\rho_c - \rho_w)}{\left(Dk^4 + g(\rho_m - \rho_c)\right)^3} +$$

$$\frac{(\rho_m - 2\rho_c + \rho_w)}{\left(Dk^4 + g(\rho_m - \rho_c)\right)^2} \Bigg\} \hat{h} \tag{C.15}$$

$$\frac{\partial^2 \hat{g}}{\partial \rho_c \partial z_m} = \frac{\partial^2 \hat{g}}{\partial z_m \partial \rho_c} = -2\pi G\, gk \exp(-kz_m) \Bigg\{ \frac{g(\rho_m - \rho_c)(\rho_c - \rho_w)}{\left(Dk^4 + g(\rho_m - \rho_c)\right)^2} +$$

$$\frac{(\rho_m - 2\rho_c + \rho_w)}{Dk^4 + g(\rho_m - \rho_c)} \Bigg\} \hat{h} \tag{C.16}$$

and finally

$$\frac{\partial^2 \hat{g}}{\partial D \partial z_m} = \frac{\partial^2 \hat{g}}{\partial z_m \partial D} = 2\pi G\, gk^5 \exp(-kz_m) \left\{ \frac{(\rho_m - \rho_c)(\rho_c - \rho_w)}{\left(Dk^4 + g(\rho_m - \rho_c)\right)^2} \right\} \hat{h} \tag{C.17}$$

where it is understood that $\hat{g}$ in the derivatives is only $\hat{g}_1$, the first term in the Fourier expansion of the gravity. The derivatives are used in (C.5) through (C.7) to search for and evaluate minima in Ξ^2. Since the numerical value of Ξ^2 was evaluated in the wavenumber domain, we evaluate the fit to the gravity data at a minimum in the complex domain using the reduced (and real) chi-square,

$$\chi_\nu^2 = \frac{\chi^2}{\nu} = \frac{\chi^2}{(N - P - 1)} = \frac{1}{(N - P - 1)} \sum_{i=1}^{N} \left[\frac{g_i - g(k_i)}{\sigma_i}\right]^2 \tag{C.17}$$

where ν is the number of degrees of freedom (number of data points N less the number of parameters P, minus one), and the sum is done in the real domain.

A similar derivation applies for the standard counterpart χ^2 in the space domain, except the gravity must be re-transformed to evaluate the error Δg for each step in the parameter space, which involves twice as many transforms as the complex formulation, and the derivatives of the error function must be evaluated empirically. Empirical calculation of the derivatives has several advantages, even though it is computationally more expensive: An arbitrary number of terms n in $\hat{g}_n$ can be easily taken in the expansion, for either the Ξ^2 or χ^2 formulation, and the derivatives can be calculated for as many parameters as required by the model.

Non-linearity of chi-squared in the parameters is not a problem in the numerical sense, and neither is the finding of minima, but the *global* minimization of a function with local minima, of which this is one, is a problem that has generated a vast amount of literature (see *Press et al.* [1986] for a discussion). Fortunately, we have some *a priori* constraints for our parameters: positivity, and physically significant numbers. To locate minima, we use three methods: a variable grid search algorithm, a gradient expansion algorithm, and a downhill simplex method. The downhill simplex method is reliable but computationally intensive, so we do not use it for global searches, but use it to confirm the results of the first two methods.

The grid search minimizes each parameter cyclically, but the minimum located can be influenced by the initial parameter vector and the permutation order of the parameters. To partially cope with these problems, we vary both the initial parameter vector and the permutation order. A more efficient search uses the information from the derivatives, or gradients, minimizing each parameter simultaneously. This method is the most effective as far as number of iterations to a minimum, but it is of course still sensitive to the initial parameter vector.

APPENDIX D

SUCCESSIVE OVERRELAXATION

Quis accurate loquitur, nisi qui vult putide loqui?
For who studies to speak too accurately, that does not design to perplex his audience?

Seneca
Epist., 117

The equation for the deflection of a plate supported on a fluid may be expressed as [*Hertz*, 1884]:

$$D\nabla^4 w + \Delta\rho_1 g w = - \Delta\rho_2 g h \tag{D.1}$$

where D is the flexural rigidity, w is the deflection of the plate, $\Delta\rho_1$ is the density contrast between the load and the underlying material and $\Delta\rho_2$ is the density contrast between the load and the surrounding material.

To model the deflection w of the plate, I used a standard 13 point approximation for the biharmonic operator ∇^4:

$$\nabla^4 w_{0,0} = \left(\frac{\partial^4 w}{\partial x^4} + 2\frac{\partial^4 w}{\partial x^2 \partial y^2} + \frac{\partial^4 w}{\partial y^4} \right)_{0,0}$$

$$= \frac{1}{(\Delta x)^4} \begin{bmatrix} 20 w_{0,0} \\ - 8(w_{1,0} + w_{0,1} + w_{-1,0} + w_{0,-1}) \\ + 2(w_{1,1} + w_{1,-1} + w_{-1,1} + w_{-1,-1}) \\ + (w_{0,2} + w_{2,0} + w_{-2,0} + w_{0,-2}) \end{bmatrix} + O\left((\Delta x)^2\right) \tag{D.2}$$

where the subscripts indicate the relative position of the points to the origin of the approximation, and Δx is the spacing of the points on the grid. If all the terms in the square brackets other than the (0,0) term are represented by F, then after some rearranging, (D.1) becomes

$$w_{0,0} = \frac{\frac{\Delta \rho_2 g (\Delta x)^4}{D} h_{0,0} - F}{f + \frac{\Delta \rho_1 g (\Delta x)^4}{D}} \tag{D.3}$$

where $h_{0,0}$ is the load height at the same point as $w_{0,0}$, and F and f are adjusted to normalize the points when $w_{0,0}$ lies within two points of a boundary (f is 20 in the interior).

If w is a solution to the equation, then we have the ideal situation

$$- w_{i,j} + \frac{\frac{\Delta \rho_2 g (\Delta x)^4}{D} h_{i,j} - F}{f + \frac{\Delta \rho_1 g (\Delta x)^4}{D}} = 0 \tag{D.4}$$

for all i and j in the grid. However, the usual case is that w is only an approximation, and there is a residual $r_{i,j}$:

$$- w_{i,j} + \frac{\frac{\Delta \rho_2 g (\Delta x)^4}{D} h_{i,j} - F}{f + \frac{\Delta \rho_1 g (\Delta x)^4}{D}} = r_{i,j} \tag{D.5}$$

The successive-overrelaxation (SOR) method uses this residual and a convergence factor ω to generate the next approximation to w in the iterative scheme:

$$w_{i,j}^{(k+1)} = w_{i,j}^{(k)} + \omega\, r_{i,j}^{(k)} \tag{D.6}$$

where $\omega \leq 2$, and k is the number of the iteration. There will be a value of ω that gives the fastest convergence for each particular problem, and a crude method of finding an approximation to this optimal value consists of minimizing the absolute value of the residual after a fixed number of iterations as a function of ω. For this particular problem the maximum absolute residual is minimized after 20 iterations by $\omega = 1.11108$, and this value was used for all subsequent iterations. Figure D.1 shows the maximum absolute residual after twenty iterations as a function of ω, with a very clear minimum.

All runs were taken to 1000 iterations, where the maximum absolute residual had fallen below 0.2 meters. The value of the maximum absolute residual for a run is shown in Figure D.2, and is typical of all runs. The reduction in size of residual is about ten-fold for each ten-fold increase in number of iterations, a situation which becomes rapidly expensive.

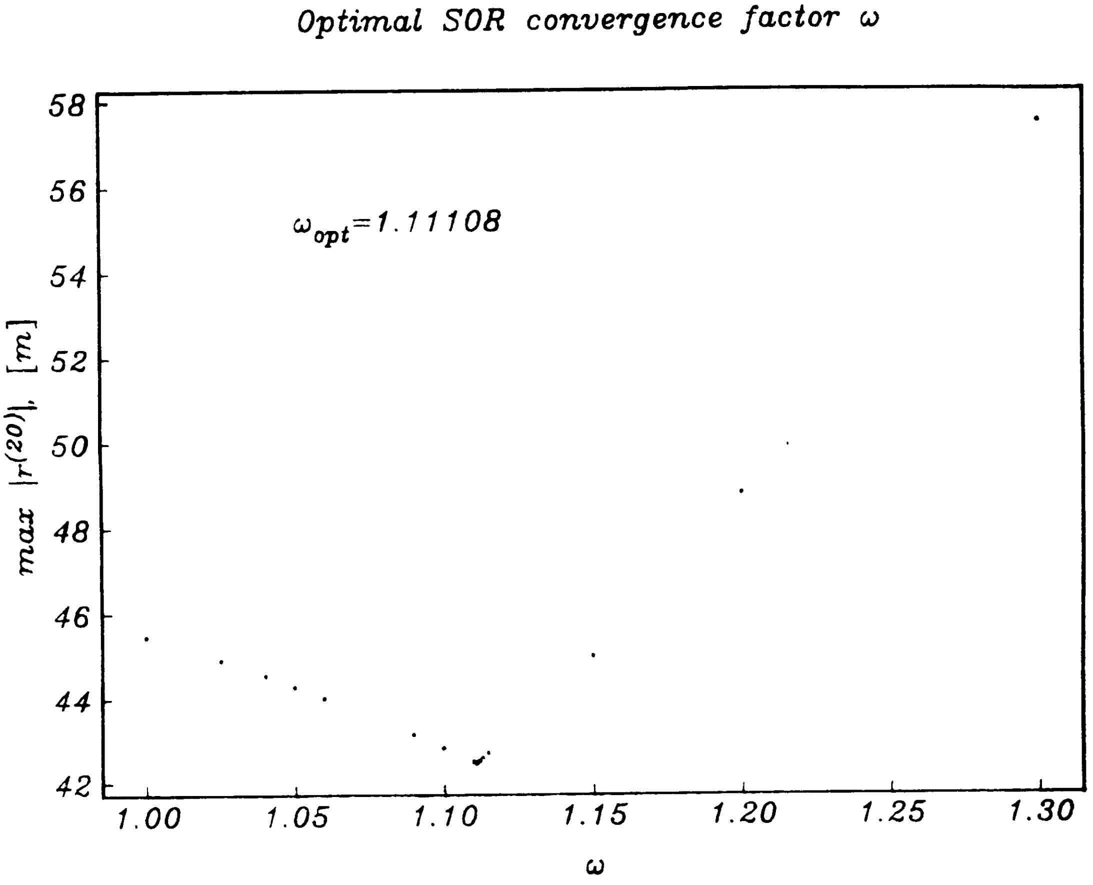

Figure D.1. Variation of the maximum absolute residual as a function of ω. After twenty iterations the minimum residual is found at $\omega_{opt} = 1.11108$.

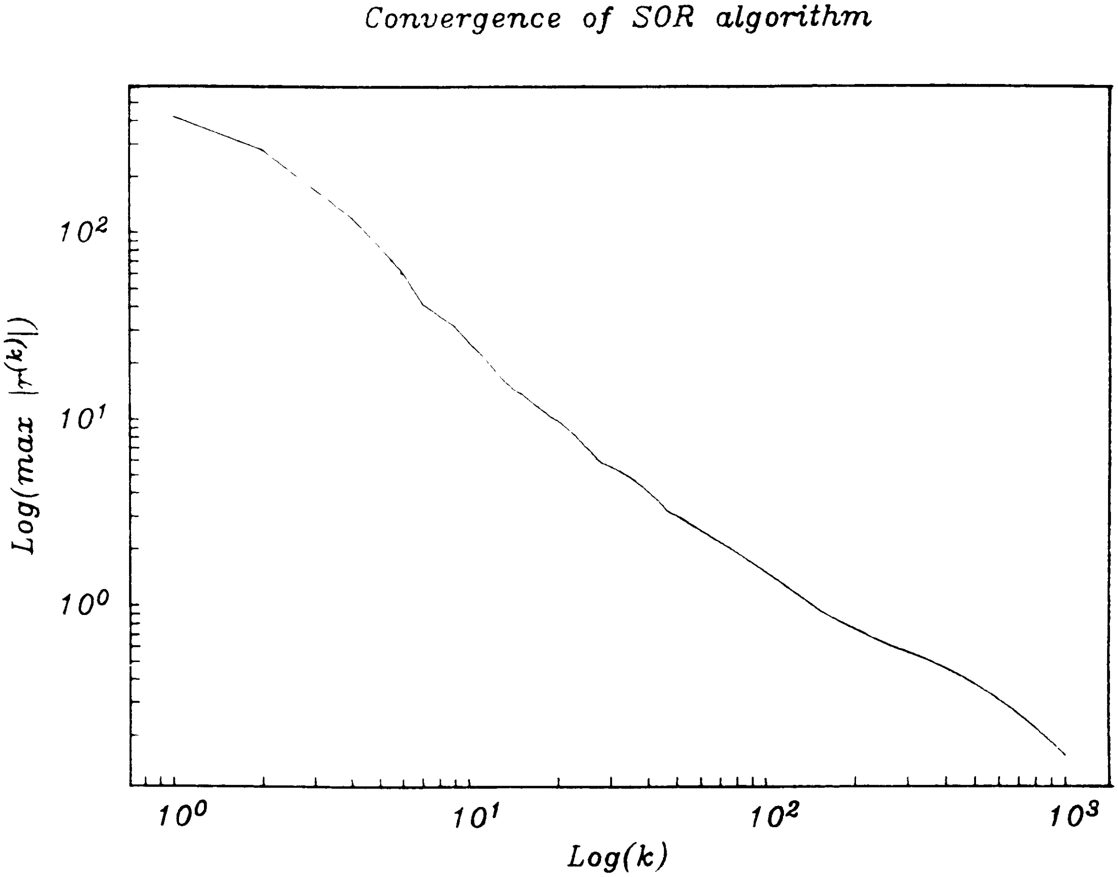

Figure D.2. Convergence of SOR algorithm. There is about a 10-fold decrease in residual size for each 10-fold increase in number of iterations. All runs were stopped after 1000 iterations.

REFERENCES

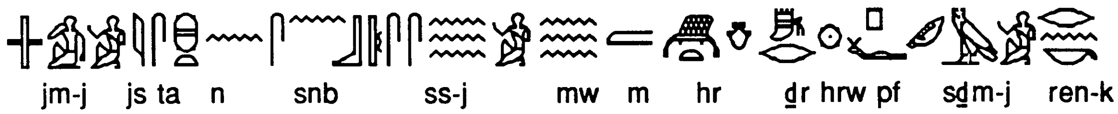

I have eaten the bread of health and drunk the water of joy since the day I heard thy name.
Miscellaneous exercise, Gardiner

Airy, G.B., On the computation of the effect of the attraction of mountain masses, Phil. Trans. R. Soc. Lond., 145, 101-104, 1855.

Banks, R.J., and C.J. Swain, The isostatic compensation of East Africa, *Proc. R. Soc. London, Ser. A, 364*, 331-352, 1978.

Barrell, J., The strength of the earth's crust, 8, Physical conditions controlling the nature of lithosphere and asthenosphere, *J. Geol., 22*, 425-443, 1914.

Batschelet, E., *Circular Statistics in Biology*, 371 pp., Acad. Press, London, 1981.

Bell, R., and A.B. Watts, Evaluation of the BGM-3 sea gravity meter system on board the "R/V Conrad", *Geophysics, 51*, 1480-1493, 1986.

Berggren, W.A., D.V. Kent, J.J. Flynn, and J.A. Van Couvering, Cenozoic geochronology, *Geol. Soc. Am. Bull., 96* (11), 1407-1418, 1985.

Black, M.T., and D.C. McAdoo, Spectral analysis of marine geoid heights and ocean depths: constraints on models of lithospheric and sublithospheric processes, *Mar. Geophys. Rev., 10*, 157–180, 1988.

Bodine, J.H., M.S. Steckler, and A.B. Watts, Observations of flexure and the rheology of the ocean lithosphere, *J. Geophys. Res., 86*, 3695-3707,1981.

Bonneville, A., Structure de la lithosphère, in *Le volcanisme de la Réunion - Monogaphie,* edited by J.-F. Lénat, 1-18, Centre de Recherches Volcanologiques, Observatoire du Physiqe du Globe de Clermont, Université Blaise Pascal, Clermont-Ferrand, 1990.

Bonneville, A., and M.K. McNutt, Volcanic versus tectonic controls on the relief along the great Pacific fracture zones (abstract), *EOS, Trans. Am. Geophys. Union, 72*, 519, 1991.

Bonneville, A., J.-P. Barriot, and R. Bayer, Evidence from geoid data of a hotspot origin for the Southern Mascarene Plateau and Mascarene Islands (Indian Ocean), *J. Geophys. Res., 93,* 4199-4212, 1988.

Brousse, R., and H. C. Bellon, Age du volcanisme de l'île d'Eiao, au nord de l'archipel des îles Marquises, *C. R. Acad. Sci., D 278*, 827-830, 1974.

Brousse, R, H.G. Barsczus, H. Bellon, J.-M. Cantagrel, C. Diraison, H. Guillou, and C. Léotot, Les Marquises (Polynésie française): volcanologie, géochronologie, discussion d'un modèle de point chaud, *Bull. Soc. Géol. France, 8,* 933-949, 1990.

Calmant, S., The elastic thickness of the lithosphere in the Pacific Ocean, *Earth Planet. Sci. Lett., 85,* 277–288, 1987.

Calmant, S., and A. Cazenave, The effective elastic lithosphere under the Cook–Austral and Society islands, *Earth Planet. Sci. Lett., 77,* 187–202, 1986.

Calmant, S., and A. Cazenave, Anomalous elastic thickness of the oceanic lithosphere in the south–central Pacific, *Nature, 328,* 236–238, 1987.

Capricorn Expedition, *Shipboard Report,* Ref. 53-15, University of California, Scripps Institute of Oceanography, La Jolla, Ca., 1953.

Cazenave, A., B. Lago, K. Dominh, and K. Lambeck, On the response of the oceanic lithosphere to seamount loads from GEOS3 satellite radar altimeter observation, *Geophys. J. R. Astron. Soc., 63,* 233–252, 1980.

Chase, C.G., and D.R. Sprowl, Proper motion of hotspots: Pacific plate, EOS, *Trans. Am. Geophys. Union, 65,* 1099, 1984.

Christeson, G.L., and M.K. McNutt, Geophysical constraints on the shear stress along the Marquesas Fracture Zone, *J. Geophys. Res.,* in press, 1991.

Clague, D.A., and G.B. Dalrymple, The Hawaiian-Emperor volcanic chain, part 1, Geologic evolution, in *Volcanism in Hawaii, U. S. Geol. Surv. Prof. Pap., 1350,* vol. 1, 5-54, 1987.

Courtney, R.C., and R.S. White, Anomalous heat flow across the Cape Verde rise: evidence for a thermal plume in the Earth's mantle, *Geophys. J. R. Astron. Soc., 87,* 815–868, 1986.

Cox, A., and D.C. Engebretson, Change in motion of Pacific plate at 5 Myr BP, *Nature, 313,* 472-474, 1985.

Crough, S.T., Thermal origin for mid–plate hot–spot swells, *Geophys. J. R. Astron. Soc., 55,* 451–459, 1978.

Crough, S.T., and R.D. Jarrard, The Marquesas–Line swell, *J. Geophys. Res., 86,* 11763–11771, 1981.

Dana, J.D., *Characteristics of volcanoes,* 399 pp., University Press, John Wilson, Cambridge, Mass., 1890.

Delorme, H., P. Bachèlery, P.A. Blum, J.-L. Cheminée, J.-F. Delarue, J.-C. Delmond, A. Hirn, J.-C. Lépine, P. Vincent, and J. Zlotnicki, March 1986 episodes at Piton de la Fournaise volcano (Réunion Island), *J. Volcanol. Geotherm. Res., 36,* 199-208, 1989.

Detrick, R.S., and S.T. Crough, Island subsidence, hot spots, and lithospheric thinning, *J. Geophys. Res., 83*, 1236–1244, 1978.

Dietz, R.S., H.W. Menard, and E.L. Hamilton, Echograms of the Mid-Pacific Expedition, *Deep-Sea Research, 1*, 258-272, 1954.

Dorman, L.M., and B.T.R. Lewis, Experimental isostasy, 1, Theory of the determination of the Earth's isostatic response to a concentrated load, *J. Geophys. Res., 75*, 3357-3365, 1970.

Duffield, W.A., L. Stieltjes, and J. Varet, Huge landslide blocks in the growth of Piton de la Fournaise, La Réunion, and Kilauea volcano, Hawaii, *J. Volcanol. Geotherm. Res., 12*, 147-160, 1982.

Duncan, R.H., and I. McDougall, Migration of volcanism with time in the Marquesas Islands, French Polynesia, *Earth Planet. Sci. Lett., 21*, 414-420, 1974.

Fischer, K.M., M.K. McNutt, and L. Shure, Thermal and mechanical constraints on the lithosphere beneath the Marquesas swell, *Nature, 322*, 733–736, 1986.

Fisher, N.I., T. Lewis and B.J.J. Embleton, *Statistical Analysis of Spherical Data*, 329 pp., Cambridge University Press, Cambridge, 1987.

Fisher, R.A., Dispersion on a sphere, *Proc. J. R. astr. Soc. London, 217*, 295-305, 1953.

Fiske, R.S., and E.D. Jackson, Orientation and growth of Hawaiian volcanic rifts: the effect of regional structure and gravitational stresses, *Proc. R. Soc. London, 329,* 299-326, 1972.

Fleitout, L., C. Froidevaux, and D. Yuen, Active lithospheric thinning, *Tectonophysics, 132*, 271-278, 1986.

Fornari, D.J., J.G. Moore, and L. Calk, A large submarine sand-rubble flow on Kilauea volcano, Hawaii, *J. Volcanol. Geotherm. Res., 5,* 239-256, 1979.

Fornari, D.J., M.O. García, R.C. Tyce, and D.G. Gallo, Morphology and structure of Loihi seamount based on Seabeam sonar mapping, *J. Geophys. Res., 93,* 15227-15238, 1988.

Forsyth, D., Subsurface loading and the estimates of the flexural rigidity of continental lithosphere, *J. Geophys. Res., 90*, 12623-12632, 1985.

Frey, F.A., and D.A. Clague, Geochemistry of diverse basalt types from Loihi seamount, Hawaii: petrogenetic implications, *Earth Planet. Sci. Letts., 66,* 337-355, 1983.

Frey, F.A., W.S. Wise, M.O. García, H. West, S.-T. Kwon, and A. Kennedy, Evolution of Mauna Kea volcano, Hawaii: petrologic and geochemical constraints on postshield volcanism, *J. Geophys. Res., 95,* 1271-1300, 1990.

Gaskell, T.F., Seismic refraction work by H.M.S. Challenger in the deep oceans, *Proc. R. Soc., Ser. A, 222*, 356-361, 1954.

GEBCO, *General Bathymetric Chart of the Oceans*, Canadian Hydrographic Office, 5th Edition, 1980.

Goetze, C., and B. Evans, Stress and temperature in the bending lithosphere as constrained by experimental rock mechanics, *Geophys. J. R. Astron. Soc., 59*, 463-478, 1979.

Greenwood, J.A., and D. Durand, The dispersion of length and components of the sum of n random unit vectors, *Ann. Math. Stat., 26*, 233-246, 1955.

Gunn, R., A quantitative evaluation of the influence of the lithosphere on the anomalies of gravity, *J. Franklin Inst., 236*, 373-396, 1943.

Haxby, W.F., G.D. Karner, J.L.LaBrecque, and J.K. Weissel, Digital images of combined oceanic and continental datasets and their use in tectonic studies, *EOS Trans. AGU, 64*, 995-1007, 1983.

Hertz, H., On the equilibrium of floating elastic plates, *Wiedemann's Ann., 22*, 449, 1884.

Holcomb, R.T., Eruptive history and long-term behavior of Kilauea volcano, in *Volcanism in Hawaii, U. S. Geol. Surv. Prof. Pap., 1350,* vol. 1, 261-350, 1987.

Jarrard, R.D., and D.A. Clague, Implications of Pacific island and seamount ages for the origin of volcanic chains, *Rev. Geophys. Space Phys., 15*, 57–76, 1977.

Jordan, T.H., Mineralogies, densities and seismic velocities of garnet lherzolites and their geophysical implications, in *The Mantle Sample: Inclusions in Kimberlites and Other Volcanics*, edited by F.R. Boyd and H.O.A. Meyer, pp. 1–14, American Geophysical Union, Washington D.C., 1979.

Jordan, T.H., H.W. Menard, and D.K. Smith, Density and size distribution of seamounts in the eastern Pacific inferred from wide-beam sounding data, *J. Geophys. Res., 88*, 10508-10518, 1983.

Klein, F.W., R.Y. Koyanagi, J.S. Nakata, and W.R. Tanigawa, The seismicity of Kilauea's magma system, *U. S. Geol. Surv. Prof. Pap., 1350,* vol. 2, 1019-1185, 1987.

Kruse, S. E., Magnetic lineations on the flanks of the Marquesas swell: implications for the age of the seafloor, *Geophys. Res. Lett., 15*, 573-576, 1988.

LaBrecque, J.L., D.V. Kent, and S.C. Cande, Revised magnetic time scale for late Cretaceous and Cenozoic time, *Geology, 5*, 330-335, 1977.

Lénat, J.-F., Structure at Dynamique internes d'un volcan basaltique intraplaque océanique: le Piton de la Fournaise (Ile de la Réunion), Ph.D. Thesis, Université de Clermont II, Clermont, 1987.

Lénat, J.-F., and P. Labazuy, Morphologies et structures sous-marines de la Réunion, in *Le Volcanisme de la Réunion - Monogaphie,* edited by J.-F. Lénat, 43-74, Centre de

Recherches Volcanologiques, Observatoire du Physiqe du Globe de Clermont, Université Blaise Pascal, Clermont-Ferrand, 1990.

Lewis, B.T.R., and L.M. Dorman, Experimental isostasy, 2, An isostatic model for the U.S.A. derived from gravity and topographic data, *J. Geophys. Res., 75*, 3367-3386, 1970.

Lipman, P.W., J.P. Lockwood, R.T. Okamura, D.A. Swanson, and K.M. Yamashita, Ground deformation associated with the 1975 magnitude 7.2 earthquake and resulting changes in the activity of Kilauea volcano, *U. S. Geol. Surv. Prof. Pap., 1276,* 45 pp., 1985.

Lipman, P.W., W.R. Normark, J.G. Moore, J.B. Wilson, and C.E. Gutmacher, The giant submarine Alika debris slide, Mauna Loa, Hawaii, *J. Geophys. Res., 93,* 4279-4299, 1988.

Liu, M., and C.G. Chase, Evolution of midplate hotspot swells: numerical solutions, *J. Geophys. Res., 94,* 5571-5584, 1989.

Malahoff, A., Geology of the summit of Loihi submarine volcano, in *Volcanism in Hawaii, U. S. Geol. Surv. Prof. Pap., 1350,* vol. 1, 133-144, 1987.

McDougall, I., and R.A. Duncan, Linear volcanic chains—recording plate motions?, *Tectonophysics, 63*, 275-295, 1980.

McKenzie, D.P., and C. Bowin, The relationship between bathymetry and gravity in the Atlantic Ocean, *J. Geophys. Res., 81*, 1903-1915, 1976.

McNutt, M.K., Compensation of oceanic topography: an application of the response function technique to the Surveyor area, *J. Geophys. Res., 84*, 7589-7598, 1979.

McNutt, M.K., Influence of plate subduction on isostatic compensation in northern California, *Tectonics, 2,* 399-415, 1983.

McNutt, M.K., Lithospheric flexure and thermal anomalies, *J. Geophys. Res., 89*, 11180–11194, 1984.

McNutt, M.K., Thermal and mechanical properties of the Cape Verde rise, *J. Geophys. Res., 93*, 2784–2794, 1988.

McNutt, M.K., and K.M. Fischer, The south Pacific Superswell, in *Seamounts, Islands, and Atolls*, edited by Keating, B.H., P. Fryer, R. Batiza, and G. W. Boehlert, 405 pp., Geophysical Monograph 43, American Geophysical Union, Washington, D.C., 1987.

McNutt, M.K., and H.W. Menard, Constraints on yield strength in the oceanic lithosphere derived from observations of flexure, *Geophys. J. R. Astron. Soc., 71*, 363-394, 1982.

McNutt, M.K., and J. Mutter, A one-ship multichannel seismic survey of the Marquesas and Society Islands, French Polynesia, *Cruise Report, R/V Maurice Ewing Cruise EW 91-03*, 1991.

McNutt, M.K., and R.L. Parker, Isostasy in Australia and the evolution of the compensation mechanism, *Science, 199*, 773-775, 1978.

McNutt, M.K., K.M. Fischer, S.E. Kruse and J. Natland, The origin of the Marquesas Fracture Zone Ridge and its implications for the nature of hotspots, *Earth Planet. Sci. Lett., 91*, 381-393, 1989.

Menard, H.W., Archipelagic aprons, *Bull. Amer. Assoc. Petrol. Geol., 40*, 2195-2210, 1956.

Menard, H.W., and R.S. Dietz, Submarine geology of the Gulf of Alaska, *Bull. Geol. Soc. Am., 62*, 1263-1285, 1951.

Minster, J.B., and T.H. Jordan, Present–day plate motions, *J. Geophys. Res., 83*, 5331–5354, 1978.

Monti, S., and G. Pautot, *Les Marquises*, scale 1:1 000 000, gebco sheet 297, CNEXO, 1973.

Moore, J.G., Subsidence of the Hawaiian ridge, in *Volcanism in Hawaii, U. S. Geol. Surv. Prof. Pap., 1350*, vol. 1, 85-100, 1987.

Moore, J.G., and G.W. Moore, Deposit from a giant wave on the island of Lanai, Hawaii, *Science, 226*, 1312-1315, 1984.

Moore, J.G., D.A. Clague, R.T. Holcomb, P.W. Lipman, W.R. Normark, and M.E. Torresan, Prodigious submarine landslides on the Hawaiian ridge, *J. Geophys. Res., 94,* 17465-17484, 1989.

Muller, O.H., and D.D. Pollard, The stress state near Spanish Peaks, Colorado, determined from a dike pattern, *Pure Appl. Geophys., 115*, 69-86, 1977.

Munk, W.H., and D.E. Cartwright, Tidal spectroscopy and prediction, *Phil. Trans. R. Soc. Lond., Ser. A, 259*, 533, 1966.

Nadai, A., *Theory of Flow and Fracture of Solids*, 709 pp., 2 vols., McGraw-Hill, New York, 1963.

Nakamura, K., Volcanoes as possible indicators of tectonic stress orientation - Principle and Proposal, *J. Volcanol. Geotherm. Res., 2*, 1-16, 1977.

Nakamura, K., Horizontal deviatoric stress increasing toward the trench; radial dike pattern of active volcanoes (abstract), *International Union of Geodesy and Geophysics, General Assembly Abstracts, 19(1)*, 40, 1987.

Nakamura, K., K.H. Jacob, and J.N. Davies, Volcanoes as possible indicators of tectonic stress: Aleutians and Alaska, *Pure Appl. Geophys., 115*, 87-112, 1977.

Natland, J.H., and M.K. McNutt, Submarine stages of Marquesan volcanism (abstract), *EOS, Trans. Amer. Geophys. Union, 68*, 1451, 1987.

Neidell, N.S., A statistical study of isostasy, *Geophys. Prospect., 11*, 164-175, 1963.

Officer, C.B., M. Ewing, and P.C. Wuenschel, Seismic refraction measurements in the Atlantic Ocean. Pt. IV: Bermuda, Bermuda Rise, and Nares Basin, *Bull. Geol. Soc. Am., 63*, 777-808, 1952.

Oppenheim A.V., and R.W. Schafer, *Digital Signal Processing*, 585 pp., Prentice-Hall, Englewood Cliffs, NJ, 1975.

Parker, R.L., The rapid calculation of potential anomalies, *Geophys. J. R. Astron. Soc., 31*, 447-455, 1972.

Parmentier, E.M., and W.F. Haxby, Thermal stresses in the oceanic lithosphere: evidence from geoid anomalies at fracture zones, *J. Geophys. Res., 91,* 7193-7204, 1986.

Parsons, B., and D., McKenzie, Mantle convection and the thermal structure of plates, *J. Geophys. Res., 83*, 4485-4496, 1978.

Parsons, B., and J. Sclater, An analysis of the variation of ocean floor bathymetry and heat flow with age, *J. Geophys. Res., 82*, 803-827, 1977.

Pearson, E.S., and H.O. Hartley, *Biometrika Tables for Statisticians, Volume 2*, 385 pp., Cambridge University Press, Cambridge, 1972.

Peterson, D.W., and R.B. Moore, Geologic history and evolution of geologic concepts, Island of Hawaii, in *Volcanism in Hawaii, U. S. Geol. Surv. Prof. Pap., 1350,* vol. 1, 149-189, 1987.

Pollitz, F.F., Pliocene change in Pacific plate motion, *Nature, 320*, 738–741, 1986.

Pratt, J., On the attraction of the Himalaya mountains, *Phil. Trans. R. Soc. Lond., 145*, 53-100, 1855.

Press, W.H., B.P. Flannery, S.A. Teukolsky, and W.T. Vetterling, *Numerical Recipes, The Art of Scientific Computing,* 818 pp., 3d ed., Cambridge University Press, New York, 1986.

Raitt, R.W., *The 1950 Seismic Refraction Studies of Bikini and Kwajalein Atolls and Sylvania Guyot*, Ref. 52-38, Univ. California, Marine Phys. Lab., Scripps Inst. Oceanography, La Jolla, Ca., 1952.

Rees, B.A., R.S. Detrick, and B. Coakley, Seismic stratigraphy of the Hawaiian flexural moat, *Geol. Soc. Am. Bull.*, submitted, 1991.

Ribe, N.M., On the interpretation of frequency response functions for oceanic gravity and bathymetry, *Geophys. J. R. Astron. Soc., 70*, 273-294, 1982.

Ribe, N.M., and A.B. Watts, The distribution of intraplate volcanism in the Pacific Ocean basin: A spectral approach, *Geophys J. R. Astron. Soc., 71*, 333-362, 1982.

Robinson E.M., and Parsons, B., Effect of a shallow low–viscosity zone on the formation of midplate swells, *J. Geophys. Res., 93*, 3144–3156, 1988.

Rosa, J.W.C., and P. Molnar, Uncertainties in reconstructions of the Pacific, Farallon, Vancouver, and Kula plates and constraints on the rigidity of the Pacific and Farallon (and Vancouver) plates between 72 and 35 Ma, *J. Geophys.Res., 93*, 2997-3008, 1988.

Sager, W.W., and M.S. Pringle, Paleomagnetic constraints on the origin and evolution of the Musicians and South Hawaiian Seamounts, in *Seamounts, Islands, and Atolls,* B. Keating, P. Fryer, R. Batiza, and G.W. Boehlert, eds., Geophysical Monograph #43, American Geophysical Union, Washington D.C., 1987.

Sandwell, D.T., Thermomechanical evolution of oceanic fracture zones, *J. Geophys. Res., 89,* 11401-11413, 1984.

Sandwell, D.T., and G. Schubert, Lithospheric flexure at fracture zones, *J. Geophys. Res., 87,* 4657-4667, 1982.

Schou, G., Estimation of the concentration parameter in von Mises distributions, *Biometrika, 65*, 369-377, 1978.

Sleep, N.H., Lithospheric heating by mantle plumes, *Geophys. J. R. Astron. Soc., 91,* 1-11, 1987.

Sleep, N.H., Hotspots and mantle plumes: some phenomenology, *J. Geophys. Res., 95,* 6715-6736, 1990.

Smith, D.K., and T.H. Jordan, Seamount statistics in the Pacific Ocean, *J. Geophys. Res., 93*, 2899-2918, 1988.

Smith, W.H.F., H. Staudigel, A.B. Watts, and M.S. Pringle, The Magellan Seamounts: early Cretaceous record of the South Pacific isotopic and thermal anomaly, *J. Geophys. Res., 94*, 10501-10523, 1989.

Spohn, T., and G. Schubert, Convective thinning of the lithosphere: a mechanism for the initiation of continental rifting, *J. Geophys. Res., 87*, 4669-4681, 1982.

Stearns, H.T., and G.A. Macdonald, Geology and ground-water resources of the island of Hawaii, *Hawaii Div. Hydrogr. Bull., 9,* 363 pp., 1946.

Steiger, R.H., and E. Jäger, Subcommission on geochronology: convention on the use of decay constants in geo- and cosmochronology, *Earth Planet. Sci. Lett., 36*, 359-362, 1977.

Swanson, D.A., Magma supply rate of Kilauea volcano, 1952-1971, *Science, 1975*, 169-170, 1972.

Swanson, D.A., W.A. Duffield, and R.S. Fiske, Displacement of the south flank of Kilauea volcano: the result of forceful intrusion of magma into the rift zones, *U. S. Geol. Surv. Prof. Pap., 963,* 39 pp., 1976a.

Swanson, D.A., D.B. Jackson, R.Y. Koyanagi, and T.L. Wright, The February 1969 East Rift eruption of Kilauea volcano, Hawaii, *U. S. Geol. Surv. Prof. Pap., 891,* 30 pp., 1976b.

Talandier, J., and E.A. Okal, New surveys of MacDonald seamount, south central Pacific, following volcanoseismic activity, 1977-1983, *Geophys. Res. Lett., 11*, 813-816, 1984.

Talandier, J., and E.A. Okal, Crustal structure in the Society and Tuamotu islands, French Polynesia, *Geophys. J. R. Astr. Soc., 88*, 499-528, 1987.

Talwani, M., and M. Ewing, Rapid computation of gravitational attraction of three-dimensional bodies of arbitrary shape, *Geophysics, 25*, 203-225, 1960.

ten Brink, U.S., *Lithospheric Flexure and Hawaiian Volcanism: A Multichannel Seismic Perspective*, Ph.D. Thesis, 219 pp., Columbia University, 1986.

ten Brink, U.S., Volcano spacing and plate rigidity, *Geology, 19,* 397-400, 1991.

ten Brink, U.S., and A.B. Watts, Seismic stratigraphy of the flexural moat flanking the Hawaiian Islands, *Nature, 317*, 421-424, 1985.

Tilling, R.I., R.Y. Koyanagi, P.W. Lipman, J.P. Lockwood, J.G. Moore, and D.A. Swanson, Earthquakes and related catastrophic events, island of Hawaii, November 29, 1975; a preliminary report, *U. S. Geol. Surv. Circ., 740,* 33 pp., 1976.

Timoshenko, S.P., and J.N. Goodier, *Theory of Elasticity*, 566 pp., McGraw-Hill, New York, 1970.

Turcotte, D., and S.H. Emerman, Mechanics of active and passive rifting, *Tectonophysics, 94*, 39-50, 1983.

van Andel, T.H., and D. Bukry, Basement ages and basement depths in the eastern equatorial Pacific from Deep Sea Drilling legs 5, 6, 8, 9, and 16, *Geol. Soc. Am. Bull., 84*, 2361-2370, 1973.

Vening Meinesz, F.A., *Gravity Expeditions at Sea, vol. IV*, Netherlands Geod. Comm., Delft, 1948.

von Mises, R., Uber die "Ganzzahligkeit" der Atomgewicht und Verwandte Fragen, *Physikal. Z., 19*, 490-500, 1918.

Walcott, R.I., Flexure of the lithosphere at Hawaii, *Tectonophysics, 9*, 435-446, 1970.

Watson, G.S., Goodness-of-fit tests on a circle, *Biometrika, 48*, 109-114, 1961.

Watson, G.S., *Statistics on Spheres*, 238 pp., University of Arkansas Lecture Notes in the Mathematical Sciences, vol. 6, John Wiley & Sons, New York, 1983.

Watson, S., and D. McKenzie, Melt generation by plumes: a study of Hawaiian volcanism, *J. Petrology, 32,* 501-537, 1991.

Watts, A., An analysis of isostasy in the world's oceans, 1, Hawaiian–Emperor seamount chain, *J. Geophys. Res., 83*, 5989–6004, 1978.

Watts, A.B., and J.R. Cochran, Gravity anomalies and flexure of the lithosphere along the Hawaiian-Emperor seamount chain, *Geophys. J. R. Astron. Soc., 38*, 119-141, 1974.

Watts, A.B., and U.S. ten Brink, Crustal structure, flexure, and subsidence history of the Hawaiian Islands, *J. Geophys. Res., 94*, 10473-10500, 1989.

Watts, A.B., J.H. Bodine, and N.M. Ribe, Observations of flexure and the geological evolution of the Pacific Ocean basins, *Nature, 283*, 532–537, 1980.

Watts, A.B., U.S. ten Brink, P. Buhl, and T.M. Brocher, A multichannel seismic study of lithospheric flexure across the Hawaiian-Emperor seamount chain, *Nature, 315*, 105-111, 1985.

Watts, A.B., J.K. Weissel, R.A. Duncan, and R.L. Larson, Origin of the Louisville Ridge and its relationship to the Eltanin Fracture Zone system, *J. Geophys. Res., 93*, 3051-3077, 1988.

Welch, P.D., The use of the fast Fourier transform for the estimation of power spectra, *IEEE Trans. Audio Electroacoust., AU-15*, 70-73, 1970.

Wessel, P., and W.F. Haxby, Thermal stresses, differential subsidence, and flexure at oceanic fracture zones, *J. Geophys. Res., 95,* 375-391, 1990.

Withjack, M., A convective heat transfer model for lithospheric thinning and crustal uplift, *J. Geophys. Res., 84*, 3008-3022, 1979.

Wysession, M.E., E.A. Okal, and K.L. Miller, Intraplate seismicity of the Pacific basin, 1913-1988, *Phys. Earth Plan. Inter.*, submitted, 1991.

Let's all move one place on.

Lewis Carroll
Alice in Wonderland, ch. 7

4523-50